PROCEEDINGS OF THE 20TH ANNUAL CONFERENCE ON ATMOSPHERIC TRANSMISSION MODELS, 10-12 JUNE 1997

Editors:

Gail P. Anderson
James H. Chetwynd

21 May 1998

Approved for Public Release; Distribution Unlimited

19980623 106

AIR FORCE RESEARCH LABORATORY
Space Vehicles Directorate
29 Randolph Road
AIR FORCE MATERIEL COMMAND
HANSCOM AFB, MA 01731-3010

"This technical report has been reviewed and is approved for publication"

LAILA. S. JEONG, Chief
Background Clutter Mitigation Branch

DAVID HARDY, Acting Director
Battlespace Environment Division

REPORT DOCUMENTATION PAGE

Public reporting burden for this collection of information is estimated to average 1 hour per response, including the time for reviewing instructions, searching existing data sources, gathering and maintaining the data needed, and completing and reviewing the collection of information. Send comments regarding this burden estimate or any other aspect of this collection of information, including suggestions for reducing this burden, to Washington Headquarters Services, Directorate for Information Operations and Reports, 1215 Jefferson Davis Highway, Suite 1204, Arlington, VA 22202-4302, and to the Office of Management and Budget, Paperwork Reduction Project (0704-0188), Washington, DC 20503.

1. AGENCY USE ONLY (Leave blank)	2. REPORT DATE 21 May 1998	3. REPORT TYPE AND DATES COVERED Scientific

4. TITLE AND SUBTITLE
PROCEEDINGS OF THE 20TH ANNUAL CONFERENCE ON ATMOSPHERIC TRANSMISSION MODELS, 10-12 June 1997

5. FUNDING NUMBERS
PE: 62101F
PR: 3054
TA: GD
WU: 01

6. AUTHOR(S)
Editors: GAIL P. ANDERSON
JAMES H. CHETWYND

7. PERFORMING ORGANIZATION NAME(S) AND ADDRESS(ES)
AFRL/VSBM
29 Randolph Rd.
Hanscom AFB, MA 01731-3010

8. PERFORMING ORGANIZATION REPORT NUMBER
AFRL-VS-HA-TR-98-0057
ERP, No. 1215

9. SPONSORING/MONITORING AGENCY NAME(S) AND ADDRESS(ES)

10. SPONSORING/MONITORING AGENCY REPORT NUMBER

11. SUPPLEMENTARY NOTES

12a. DISTRIBUTION/AVAILABILITY STATEMENT
Approved for public Release; Distribution Unlimited

12b. DISTRIBUTION CODE

13. ABSTRACT (Maximum 200 words)

CONTAINS THE VIEWGRAPHS AND OTHER MATERIALS FOR THE 47 PAPERS PRESENTED AT THE 20th ANNUAL ATMOSPHERIC RADIANCES AND TRANSMITTANCE HELD AT THE GEOPHYSICS DOD DIRECTORATE, PHILLIPS LABORATORY (AFMC), HANSCOM AFB, ON:
10-12 JUNE 1997

14. SUBJECT TERMS
Atmospheric Radiance   Aerosols   Climate
Atmospheric Transmittance Clouds   Remote Sensing
Atmospheric Structure   The Sun

15. NUMBER OF PAGES

16. PRICE CODE

17. SECURITY CLASSIFICATION OF REPORT	18. SECURITY CLASSIFICATION OF THIS PAGE	19. SECURITY CLASSIFICATION OF ABSTRACT	20. LIMITATION OF ABSTRACT
Unclassified	Unclassified	Unclassified	SAR

TABLE OF CONTENTS

SPECTROSCOPY/MODELING

The SUN, MEASUREMENTS and MODELING

MODTRAN APPLICATIONS

AEROSOLS

CODES and IMAGING SPECTROSCOPY

CLOUDS

PREFACE

The 20TH Annual DoD Atmospheric Radiance and Transmittance Meeting was held at the Air Force Phillips Laboratory Geophysics Directorate Science Center at Hanscom AFB from 10-12 June 1997.

47 papers and presentations were given including rememberances of the late Francis (Frank) X.Kneizys who was one of the primary movers in the Air Force's entry into this field.

Updates of the various consumer codes such as MODTRAN, MOSART etc and their applications in modelling for sensors and systems were made. Other topics addressed included Spectroscopic Techniques, Imaging Spectroscopy, Aerosols, Clouds, Earth Limb, Solar Studies, Climate, Lidar and Microwave techniques.

This volume contains the abstracts, grouped together at the front for easy perusal and, where available, hardcopy furnished by the authors. No significance should be accorded to variations between abstract and hard copy titles and/or author names.

An Author Index and a partial list of Attendees are also included.

The Editors thank the authors, and attendees for their participation.

Gail P.Anderson

Background Clutter Mitigation Branch
Battlespace Environment Division
Air Force Research Laboratory

BIOGRAPHY
Colonel Alan R Shaffer
United States Air Force

Colonel Shaffer is the Assistant for Battlespace Environments, Office of the Director, Defense Research and Engineering.

Col Shaffer was born in Dunkirk, NY, on 24 Jan 1955. He earned a B. S. in Mathematics from the University of Vermont and Air Force Commission through St Michael's College Reserve Officer Training Commissioning Program in 1976. In 1977, he earned a B. S. in Meteorology from the University of Utah, and subsequently a M. S. (with Distinction) from the Naval Postgraduate School, Monterey, CA, and a M. S. in National Resource Management from National Defense University.

In 1977, Col Shaffer was assigned to Detachment 7, 24th Weather Squadron, Mather AFB, CA, as weather forecaster, then Wing Weather Officer to both the 323d Flying Training Wing and 320th Bombardment Wing (Heavy). While supporting the 320th Bomb Wing, the unit won the Fairchild Trophy as best bomb wing in the Air Force. From Mather, Col Shaffer attended the Air Force Institute of Technology graduate education program at the Naval Postgraduate School.

Following graduation, Col Shaffer was assigned to Det 1, 2d Weather Squadron, Wright-Patterson AFB, OH as an advanced weather officer to the Air Force Foreign Technology Division, where he assessed foreign nation operational weather capabilities and the direct impact of the environment on foreign weapons systems. In 1986, Col Shaffer served an extended temporary duty as Officer in Charge, Weather Support Element, Palmerola Air Base, Honduras. While assigned to Det 1, Col Shaffer was selected as the 1986 Air Force Weather Company Grade Officer of the Year.

In 1987, he assumed command of Det 2, 7th Weather Squadron, Hanau Army Installation, Germany with concurrent duty as Weather Officer to the Commanding General, 3d Armored Division. During this tour, Det 2 was selected as the 1989 William Award winner, given to the most outstanding Air Force Weather unit. In 1990, Col Shaffer was reassigned to 5th Weather Wing, Langley Air Force Base, VA, as Chief, Operational Support Division. Upon restructure of Air Force Weather, he became Chief, Plans and Program Branch, and Deputy Chief, Weather Division, Hq Air Combat Command.

In 1993, Col Shaffer attended the Industrial College of the Armed Forces, Ft McNair, DC. Upon graduation in 1994, he was assigned to the Hq Air Force Directorate of Weather, Deputy Chief of Staff, Plans and Operations. While at Air Staff, he was Deputy Chief, Weather Plans Division; then Chief, Interagency Division; Chief, Weather Policy Division; and Chief, Weather Resources Division. He assumed his present position and rank in June 1996.

Col Shaffer's decorations include the Meritorious Service Medal with three oak leaf clusters and the Air Force Commendation Medal with one oak leaf cluster. He is married to the former Jacqueline C Sklenar, and they have one son, Eric.

The MOSART Code: 1997

by

Dr. William M. Cornette
National Imagery and Mapping Agency
Bethesda, MD 20816

Sally J. Westmoreland
Photon Research Associates, Inc.
San Diego, CA 92121

Dr. Prabhat K. Acharya, Dr. Alexander Berk, Dr. David C. Robertson
Spectral Sciences, Inc.
Burlington, MA 01803

Gail P. Anderson, Dr. William A.M. Blumberg, Dr. Laila S. Jeong
and Dr. Francis X. Kneizys
Air Force Research Laboratory
Hanscom AFB, MA 01731

Abstract

The MOderate Spectral Atmospheric Radiance and Transmittance (MOSART) code is a U.S. Government standard code with the ability to support scene and signature simulations. MOSART uses the same band model and 1 cm^{-1} resolution band parameter data base found in MODTRAN, which have been derived from the 1996 HITRAN line atlas. In the ultraviolet and visible regions, MOSART contains additional molecular absorption bands at a coarser resolution. The line-of-sight geometries include all MODTRAN3 geometries, plus some new geometries, including Observer-Source, Observer-Background, Observer-Source-Background, Earth limb, Horizontal, At-Source (i.e., Observer and Source are co-located). An X-Windows- and Motif-based MOSART Input GUI is available, as is a simple scrolling input file builder.

An extensive set of global data bases is incorporated into the code, including climatologies (e.g., diurnal surface air temperature, three etage cloud cover, cirrus presence), terrain elevation (10 arcmin resolution), water/snow composition, and ecosystem type (10 arcmin resolution). Coupled with the ecosystem and terrain elevations are composite terrain scene types with appropriate boundary layer aerosol composition. Each scene includes appropriate parameters for determining the terrain temperature for each material in the scene, together with the reflected and emitted radiances for determining the mean and standard deviation for the scene. The Global Data Base Model allows a full 3-D representation of the earth's atmosphere (i.e., altitude, latitude, and longitude) with radiative transfer varying as the line-of-sight moves within the spatially changing atmosphere.

The MOSART code is approximately 185,000 lines of ANSI FORTRAN 77 code, including about 11 utility codes and manuals (4 volumes: Installation, User's, Technical, and Software Reference Manuals). Version 1.41 of MOSART was released in September 1995. Since then, a number of modifications, upgrades, and "bug" fixes have been made.

COMPUTATIONAL METHODS APPLIED
TO THE DEVELOPMENT OF HITRAN AND HITEMP

Laurence S. Rothman

PL/GPOS
Geophysics Directorate
Hanscom AFB MA 01731

Almost three decades have passed since the GOAT (Group On Atmospheric Transmission) team convened to create the atmospheric molecular absorption database, and it is informative to review the direction of methodology that has led to the current databases, HITRAN and HITEMP. Initially, the techniques of perturbation theory, and specifically contact transformations, were applied to the molecular Hamiltonians to achieve fourth-order accuracy of energy levels. Closed-form solutions were sought, and these techniques were applied especially to the bent triatomic molecules, H_2O, O_3, and SO_2. Progress was accomplished with the discovery of simplifying generating functions and the reduction of sets of operators.[1] The dipole-moment of water vapor based on these methods is still the accepted value.[2]

However, with the computer power now available, the calculational methods of ab initio[3] and Direct Numerical Diagonalization (DND)[4] are becoming more widely used for simple molecular systems. These methods offer the capability to predict spectral properties not accessible in controlled laboratory observations, which is very desirable for long-path atmospheric transmission and hot-gas problems. In addition, the computational methods of least-squares have played a vital role in the development of HITRAN and HITEMP.

Another major factor in HITRAN and HITEMP development is the accuracy of laboratory data. Fourier transform spectrometer observations form the basis for a majority of the line-transition portion of the compilations; it is also the basis of the increasing number of cross-section files on the compilation.

1. F.X. Kneizys, J.N. Freedman, and S.A. Clough, J.Chem.Phys. 44, 2552 (1966); L.S. Rothman and S.A. Clough, J.Chem.Phys. 54, 3246 (1971).
2. S.A. Clough, Y. Beers, G.P. Klein, and L.S. Rothman, J.Chem.Phys. 59, 2254 (1973).
3. H. Partridge and D.W.Schwenke, accepted J.Chem. Phys. (1997).
4. R.B. Wattson and L.S. Rothman, J.Quant.Spectrosc.Rad.Transfer 48, 763 (1992).

HISTORY OF EOSAEL

Richard C. Shirkey

Army Research Laboratory
Information Science and Technology Directorate
Battlefield Environment Division
White Sands Missile Range, New Mexico 88002-5501

The Electro-Optical Systems Atmospheric Effects Library (EOSAEL) is a state-of-the-art computer library of computer codes describing various aspects of electromagnetic propagation and battlefield atmospheres and their effects on electro-optical sensors and systems. This paper presents the history of EOSAEL and describes events leading up to the first version, distributed in 1979, to the current version, EOSAEL 92.

THE APPLICATION OF A VUV-FT SPECTROMETER AND SYNCHROTRON RADIATION SOURCE TO MEASUREMENTS OF OXYGEN AND NO MOLECULES

K. Yoshino, J.R. Esmond, and W.H. Parkinson

Harvard Smithsonian Center for Astrophysics
Cambridge, MA 02138, U.S.A.

A.P. Thorne, J.E. Murray, G. Cox, and R.C.M. Learner
Imperial College of Science, Technology, and Medicine, London, U.K.

K. Ito, T. Imajo, and T. Matsui
Photon Factory, KEK, Tsukuba, Ibaraki 305, Japan

A.S-C. Cheung and K.W-S. Leung
University of Hong Kong, Hong Kong

We moved the IC~VUV FT spectrometer from Imperial College, London to the Photon Factory, Japan to exploit the bandwidth-limited synchrotron radiation as a background source for FT absorption spectroscopy. We have measured all absorption bands of NO in the wavelength region 195 to 160 nm with the resolution of 0.06 cm^{-1} (about a half of the Doppler widths). With resolution of 0.06 or 0.12 \wn, we extended the measurements of the Schumann-Runge bands of O2 with v' > 12 in the wavelength range 181 to 175 nm.

We will present some preliminary results of \o2 and NO measurements.

O2 PRESSURE INDUCED CONTINUUM IN THE IR

Eli J. Mlawer

Atmospheric and Environmental Research, Ind.

A recent high-resolution measurement of surface solar radiance show clear indication of continuous absorption due to the three strongest O2 X3Sg -> a3Dg transitions. The differences between these measurements and a line-by-line calculation were used to determine the properties of these continua and, for two of the bands, led to parameterizations of the spectral behavior of the absorption coefficients. The results indicate that these continuous bands remove approximately 0.8 W/m2 from the solar beam.

ACCELERATED LINE-BY-LINE CALCULATION OF ABSORPTION COEFFICIENTS WITH HIGH NUMERICAL ACCURACY

Martin Kuntz

Forschungszentrum Karlsruhe GmbH
IMK Karlsruhe, Germany

An efficient method for the calculation of spectral absorption coefficients on a line-by-line basis is presented. For each spectral line retained in the model, this method evaluates a contribution to the absorption coefficient to a predefined absolute level of accuracy. The algorithm requires the definition of a sequence of successively finer grids and interpolation from coarser to finer grids. An advantage of the method is that lines do not necessarily contribute over the entire frequency range of interest. In addition the treatment of the Voigt line shape is put onto a more rigorous basis. The absorption coefficients are finally interpolated onto a non-equidistant frequency grid which offers the prospect of improved performance modeling the radiative transfer.

IMPROVED ACCURACY INFRARED ABSORPTION DETERMINATIONS USING THE MODIFIED KUBELKA MUNK MODEL

W. G. Egan, and Q. Alexis

Natural Sciences Department
York College/CUNY
Jamaica, NY 11451

In order to further improve the accuracy of infrared aerosol optical properties determinations, a modification to the original Kubelka-Munk scattering model was made to include the effects of sample surface reflection on the determination of absorption (i.e.the Modified Kubelka Munk Model: M-K-M). The solutions to the radiative transfer equations involved for the M-K-M model are presented graphically. The results indicate that the M-K-M model generally produces somewhat less absorption than the K-M model, but comparable to the dispersion model in high absorption regions. A plot of absorption and scattering in the complex plane reveals problems with the dispersion theory when significant scattering occurs.

FASE/FASCOD4: CURRENT STATUS AND FUTURE DIRECTION

H.E. Snell

Atmospheric and Environmental Research, Inc.
840 Memorial Dr.
Cambridge, MA 02139

G.P. Anderson, J.H. Chetwynd, and S. Miller

Geophysics Directorate
Phillips Laboratory
Hanscom AFB, MA 01731

The Optical Physics Division of the Air Force Phillips Laboratory with support from the Department of Energy (DoE) Atmospheric Radiation Measurement (ARM) Program is developing a state-of-the-art line-by-lineatmospheric radiative transfer model as the successor to FASCODE (Fast Atmospheric Transmittance Code). The goal of this project is to create a computationally efficient model which contains the most up-to-date physics. The new model, known as FASCODE for the Environment, or "FASE", combines the best features of FASCODE and LBLRTM (Line-by-Line Radiative Transfer Model), the DoE's standard radiative transfer model. Upgrades to FASE include the addition of a solar spectrum module to compute the attenuated, line-of-sight solar radiance, improvement of the cloud and aerosol descriptors, based on changes made to MODTRAN (Moderate Resolution Transmittance Model), and the ability to incorporate the new heavy molecule absorption cross-section data found on the HITRAN96 database, which is of slightly different format from the previous HITRAN cross-section data. This paper addresses changes which have been made to FASCODE and LBLRTM to create FASE, gives an overview of the new capabilities, and outlines current and future development plans.

FASE-CALCULATED CONTRIBUTION AND SENSITIVITY FUNCTIONS FOR MSX SPIRIT III MWIR BANDS FOR BTH MEASUREMENTS

W. Gallery, H. Snell, C. Sarkiasian, D. Hogan

AER, Inc.

A. Zachor

Atmospheric Radiation Consultants, Inc.

J. Winick

Phillips Laboratory
Geophysics Directorate

The radiance measured at a satellite viewing the earth originates from the surface and the various levels of the atmosphere. The "contribution function" describes the relative contribution each level makes to the outgoing radiance while the "sensitivity function" describes the sensitivity of the outgoing radiance to changes in an atmospheric parameter (e.g., temperature or water vapor) at each level. Both functions are important in understanding the variations in the measured radiance along the satellite path. In this paper, both functions are defined rigorously. FASE is used to calculate both functions efficiently for the MSX SPIRIT III MWIR bands (both the radiometer bands B1 and B2 and the interferometer channel 2.) These functions are presented for various angles from nadir out to the limb and for both LTE and Non-LTE (contribution function only) cases.

FASE, FASCODE AND RADTRAN ATTENUATION DIFFERENCES IN THE MICROWAVE

Michael K. Griffin and Alan E. Lipton

Optical Effects Division
Phillips Laboratory
Hanscom Air Force Base, Massachusetts, 01731-3010

Alan G. Ling

Radex, Inc.
3 Preston Ct
Bedford, Massachusetts, 01730

Modeling radiative transfer in the microwave has become increasingly important with the wide usage of the DMSP SSM/I and SSM/T-2 microwave sensors. Current on-orbit sensor frequencies range from 19 GHz to 183 GHz; experimental airborne instrumentation will include frequencies up to 650 GHZ. The increasing interest in the full spectrum of microwave frequencies and the selection of radiative transfer models available to the user prompted this comparative study. The basic output (attenuation) from three models, RADTRAN, FASCODE and FASE were compared over the range of frequencies described above. Differences were noted and the effects these variations had on our modeling efforts were documented. Specifically, how these differences might affect our study of the sensitivity of computed microwave brightness temperature to cloud liquid water content. This presentation will highlight the model differences and discuss how these model-to-model variations might affect specific parameter estimations.

CHARACTERIZATION OF OPTICAL EXTINCTION PROFILES
USING RAMAN LIDAR TECHNIQUES

C. Russell Philbrick and Michael O'Brien

The Pennsylvania State University
Electrical Engineering Department
University Park, PA 16802

Profiles of Raman scattering, due to vibrational and rotational transitions, from a the laser transmitter of a lidar system provide a signal which can be directly interpreted as optical extinction. We have been using the Raman scatter from a Nd:YAG laser beam from the 2nd, 3rd and 4th harmonics at 532, 355 or 266 nm to obtain profiles of the optical extinction. The measurements have been made using the molecular nitrogen profiles at 607, 387 and 285 nm, which are the first Stokes vibrational Raman shifts from the Nd:YAG laser. The rotational Raman scattered radiation at 530 nm has also been used to obtain optical extinction profiles. The vertical profiles of optical extinction have been measured during several time sequences which allow a study of the evolution of cloud development. The growth, dissipation and advection of the cloud particles has been investigated using the technique. The fact that the profiles are simultaneously measured at several wavelengths allows some inference of the distribution of particle size distribution within a cloud layer. Significant variations in the relative sizes of the particles have been observed between the upper and lower regions of a cloud layer. Example results are used to show several of the features which have been observed during measurement periods. The lidar instruments which we are using to obtain the optical extinction profiles are simultaneously measuring the meteorological profiles of the water vapor and temperature. The data permit investigations of the physical process involved in the evolution of cloud optical properties.

MULTI-WAVELENGTH / TUNABLE LASER RADAR SIMULATION CODE LIDAR-PC

William E. Wilcox

W. J. Schafer & Associates
321 Billerica Road
Chelmsford, MA 08124-4191

Dennis K. Killinger

University Of South Florida
4202 E. Fowler Ave.
Tampa, FL 33620

We have developed a Laser Radar (LIDAR) simulation code which models multi-wavelength or tunable system performance over slant paths in the atmosphere. Both hard target and aerosol LIDAR systems may be modeled with the software.

The program combines high resolution spectral data from HITRAN-PC with Aerosol models from LOWTRAN 7 to predict LIDAR S/N as function of wavelength and altitude/range. Various LIDAR system parameters such as power, wavelength, telescope, and detector noise are entered into a system worksheet. Calculations are then made based on the worksheet and plotted in an interactive Windows environment.

TEMPERATURE AND TRACE GAS RETRIEVALS
FROM THE CIRRIS 1-A STRATOSPHERIC LIMB DATA
UTILIZING THE OPTIMAL ESTIMATION METHOD

Steven M. Miller and Jeremy Winick

Optical Effects Division
USAF Phillips Laboratory

Jean-Luc Moncet and Hilary E. Snell

Atmospheric and Environmental Research, Inc.

A general purpose retrieval code has been developed utilizing a derivative of FASCODE as the forward model and Rodger's optimal estimation method as the inversion algorithm. This code has been applied to stratospheric limb data taken with the CIRRIS-1A interferometer flown aboard the space shuttle in April 1991. The output of the code provides simultaneously retrieved temperature and volume mixing ratio profiles of several important trace gases and, as important, the error and the relative contributions from the measurement and the first guess profile as background information. The observation of non local thermodynamic equilibrium in the laser band of CO_2 is modeled using the Atmospheric Radiance Code, ARC, and compensated for in the data using the NLTE algorithms in FASCODE.

SCIAMACHY LIMB MODES, PRESENTATION AND PRELIMINARY SIMULATIONS

Christian Muller[1], John Burrows[2] and Albert Goede[3]

[1]Belgian Institute for Space Aeronomy, Brussels.

[2] IFE, University of Bremen.

[3]Stichting Ruimte Onderzoek Nederland, Utrecht.

SCIAMACHY is a joint project of Germany ,the Netherlands and Belgium for global atmospheric measurements. It has been selected by ESA to fly on the Envisat-1 polar platform, to be launched in 1998/1999. SCIAMACHY comprises a moderately high resolution (0.2-0.5 nm) spectrometer to observe transmitted, reflected and scattered light from the atmosphere in the UV, visible and near infrared wavelength regions over the range 240-1700 nm, and in 2 selected regions between 2.0 and 2.4 micron. The goal is to allow small optical absorptions (as small as 2E-4 in some regions of the spectrum) to be detected.

While the SCIAMACHY instrument is mainly known for its nadir mode where it will improve on the existing GOME (Global Ozone Measuring Experiment), it has also been designed with a sophisticated limb mode including solar occultation, lunar occultation and measurement of limb radiances between 100 km of altitude and the surface. This mode has no previous equivalent in space-borne earth observation experiments. Requirements for the direct models allowing to simulate this limb mode will be presented.

Simulations of the infrared channels occultation modes will also be shown. The spectral intervals were chosen essentially for nadir sounding of tropospheric columns of N2O, CH4 and CO with the limitation of using state of the art non cryogenic detectors. However, simulations show that occultation data will be relevant for the determination of the lower stratosphere vertical distribution of these gases and water vapor. This property makes it a new tool for the understanding of the troposphere-stratosphere exchange mechanisms.

ADEOS/ILAS MEASUREMENT OF THE POLAR STRATOSPHERE

Tatsuya Yokota

National Institute for Environmental Studies
16-2 Onogawa, Tsukuba, Ibaraki 305 Japan

The Advanced Earth Observing Satellite (ADEOS) has been successfully launched on August 17, 1996. Improved Limb Atmospheric Spectrometer (ILAS) is a grating spectrometer aboard ADEOS. ILAS is designed to measure stratospheric minor constituents and parameters with a solar occultation technique around the polar region for both hemispheres.

Vertical profiles of temperature, pressure, and aerosol extinction coefficient are determined from the visible channel covering the 753 ~ 784 nm for O_2 molecular absorption. ILAS has also observed spectral feature of ozone Wulf band absorption in this spectral range. To estimate the Wulf band contribution to the transmittance spectra, cross-section data from MODTRAN3.5-beta are used in the calculation.

Profiles of O_3, CH_4, N_2O, HNO_3, H_2O, NO_2, CFC-11, CFC-12, and aerosols are simultaneously obtained from the IR channel (6.2 ~ 11.8 mm). In the ILAS data retrieval code, HITRAN database is used for the absorption cross section calculation. O_2 continuum calculation around 6 mm has referred to the method in the FASCODE. The method of CKD2.1 from Dr. S. A. Clough is used for the H_2O continuum calculation. As for the cross-section calculation of CFC-11, CFC-12, and N_2O_5, pseudo-line parameters from Dr. G. C. Toon are used.

ILAS has operationally observed polar stratosphere from late-November 1996. Preliminary results of the ILAS measurement will be presented here.

CIRRIS-1A LIMB SPECTRAL MEASUREMENTS ON MESOSPHERIC OZONE

D. K. Zhou,[1] M. G. Mlynczak,[2] G. E. Bingham,[1]
J. O. Wise,[3] AND R. M. Nadile[3]

[1]Space Dynamics Laboratory
Utah State University
Logan, Utah

[2]Atmospheric Sciences Division
NASA Langley Research Center
Hampton

[3]Geophysics Directorate
Phillips Laboratory
Hanscom AFB, Massachusetts

Infrared spectral radiance measurements were made by the Cryogenic Infrared Radiance Instrumentation for Shuttle (CIRRIS 1A) during one flight of the space shuttle Discovery (28 April to 6 May, 1991). Observations were made for both the nighttime and daytime. The radiance from the ozone 9.6 mm band region shows a significant difference between night and day in the mesosphere. Band-to-band and scan-to-scan spectral analyses (in the wavenumber region of 1010 - 1140 cm-1) were made using the Strategic High-Altitude Radiance Code (SHARC) model to separate the contributions from ozone fundamental bands, hot bands, and the CO_2 band in this spectral region. A spectrally integrated ozone fundamental u3 band radiance profile was used to retrieve its excited state density. The excited state density in conjunction with the modeled vibrational temperature was used to estimate the total ozone density. The ozone abundance derived from the SHARC model and the Simplified Single Mode (SSM) ozone model were compared. The error sources and accuracy of the estimated ozone abundance were discussed. The night/day ozone ratio of the CIRRIS 1A measurements demonstrates evidence of a non-LTE mesospheric ozone diurnal variation. The photolysis rate affiliated with the daytime ozone photo-dissociation was estimated. The mesospheric ozone heating rates were estimated for CIRRIS 1A nighttime and daytime observations.

LIMB AND BELOW-THE-HORIZON SPECTRA MEASURED BY THE MSX SPIRIT III INTERFEROMETER; COMPARISON TO SAMM TEMPLATE SPECTRA

Alexander S. Zachor

Atmospheric Radiation Consultants, Inc.

R. R. O'Neil, H. A. B. Gardiner and J. J. Gibson

Phillips Laboratory
Geophysics Directorate
Hanscom AFB, MA

The SPIRIT III interferometer spectrometer aboard the MSX satellite has six channels that collectively are capable of measuring terrestrial emissions over the wavelength range 2.6-28 mm at 2 cm^{-1} spectral resolution. Data has been acquired from nadir to 200 km tangent height. Automated analysis of these observations includes the computation of "template" spectra which are predictions based on the SAMM code. We describe the interferometer's capabilities and construction of templates, and present samples of measured spectra and comparison template spectra.

PURE ROTATION EMISSIONS FROM MESOSPHERIC OH OBSERVED USING THE SPIRIT III INTERFEROMETER ABOARD THE MSX SATELLITE

P.S. Armstrong[2], S.J. Lipson[1], R.R. O'Neil[1], H.A. Gardiner[1],
A. Zachor[3], M. Kendra[4], J.J. Gibson[1], J.A. Dodd[2],
D.L. Vititoe[1], W.A.M. Blumberg[1], K. Farnham[4], and T. Woolston[5]

[1]Phillips Laboratory Geophysics Directorate, Hanscom Air Force Base, MA 01731

[2]Stewart Radiance Laboratory, 139 Great Road, Bedford, MA 01730

[3]ARC, Inc., 59, High Street, Acton, MA 01720

[4]Radex Inc., 3 Preston Court, Bedford, MA 01730

[5]Utah State University, Logan, UT 84322

Pure rotation emissions from NLTE (Non-Local Thermodynamic Equilibrium) OH(X2P) have been observed in earthlimb-viewing geometry using the SPIRIT III interferometer aboard the MSX satellite. Emission lines from rotational levels with N»30 have been identified in the LWIR (approximately 10-13 mm) wavelength region, representing over 2 eV of rotational energy. These observations are consistent with earlier measurements made during the CIRRIS 1A Space Shuttle experiment, and provide a valuable comparison made under differing aeronomic conditions. Simultaneous measurements of OH fundamental band emissions were also made using SPIRIT III, thus permitting the characterization of vibrational distributions for both LTE and NLTE OH rotational populations. The calibrated spectral data, obtained using detectors with vertical footprints of about 4-6 km, permit the determination of absolute line-of-sight column densities through the mesopause layer. These observations provide important information on the dynamics of OH, a significant chemical species and IR emitter responsible for cooling of the mesopause region. Results from a limb measurement on 8 October 1996 over Bear Lake, Utah will be reported. Ground-based OH measurements were also recorded at Bear Lake and Logan, Utah.

OVERVIEW OF THE 15 MM CO2 LIMB EMISSION FROM MSX

J.O. Wise, R. O'Neil, H. Gardiner, J.R. Winick, and R.H. Picard

Geophysics Directorate
Phillips Laboratory
Hanscom AFB, MA

P.P. Wintersteiner
Arcon Corporation
Waltham, MA

M. Kendra
Radex, Inc.
3 Preston Ct
Bedford, Massachusetts, 01730

Sample 15 mm limb emission data from the MSX SPIRIT III sensor is presented for tangent heights from 65 to 150 km. The data were measured by band D (13.5-15.9 mm FWHM) of the radiometer. Band D consists of 4 columns of 192 pixels each. The columns are oriented vertically in the limb viewing measurements and extend over an altitude range of 60 km in a single measurement. Spatial resolution of 300 m is achieved in the limb views. The spacecraft has superb pointing capabilities and nearly constant tangent height altitudes are maintained during the measurements, nominally 30 minutes in duration. The data were collected for various geophysical conditions during 1996 and 1997. The emissions are examined for their dependence on latitude and season, as well as from dissipation of energy from tidal and gravity waves. Of particular interest is the behavior of the characteristic knee at approximately 108 km. At this altitude the emission can fluctuate significantly due to variations in atomic oxygen, CO2, and temperature, and may provide important clues to the species and temperature variability between 100-150 km.

STRATOSPHERIC WAVE OBSERVATIONS FROM MSX: A NEW SOURCE OF STRUCTURE IN 4.3-MM DOWNLOOKS FROM SPACE

R. H. Picard, E. M. Dewan, R. O'Neil, H.A.B. Gardiner, J. Gibson,
J. R. Winick, J. Brown, G. P. Anderson,
Phillips Lab / Geophysics,Bedford, Mass.
E. R. Hegblom, N. A. Grossbard, E. Richards,
Boston College ISR, Chestnut Hill, Mass W. O. Gallery,
Atmospheric Environmental Research Cambridge, Mass.
A. S. Zachor, Atmospheric Radiation Consultants, Acton, Mass.
P. P. Wintersteiner, ARCON Corp., Waltham, Mass.
U. B. Makhlouf, Stewart Radiance Laboratory, Bedford, Mass.
J. Gruninger, Spectral Sciences, Inc., Burlington, Mass.

Much MSX radiometer data from the 4.3-mm spectral region, dominated by CO_2 n3 band emission features, shows evidence of significant structure arising in the cloud-free atmosphere. This occurs in both below-the-horizon (BTH) and above-the-horizon (ATH) data-gathering modes. In particular, wavelike structures are seen in these MSX mid-wave infrared bands in BTH mode at large near-horizon nadir angles. The structures are observed in both the narrow B1 band imagery (4.22- 4.36 mm), which is confined to the heart of the strongest n3 band, and the wide B2 band imagery (4.24-4.45 mm), which has extended response on the long-wave side encompassing hot and isotopic bands. Both filters have very steep edges resulting in high out-of-band rejection. This wavelike structure is contrasted with the structure resulting from clouds. Data taken on a number of day and night collections over East Asia and the Indian Ocean are examined for the presence of wave structure. In particular, the days of 17 Aug and 13 Nov and the night of 2 Oct 96 are analyzed in some detail. The wavelike structures appear to have fractional radiance modulation of a few percent and scales of 15-200 km, consistent with atmospheric gravity wave (GW) scales. Moreover, power spectral densities of the radiometer time series indicate they obey power laws consistent with expectations from the theory of saturated GW spectra and radiative response theory. The 2 Oct and 13 Nov show particularly dramatic circular wave patterns, indicating point-source wave generation events. High cloud tops observed in GMS 5 satellite LWIR images at the appropriate location and time identify specific convective storms as likely sources. These MSX results constitute the first definitive infrared observations of GW's from space and implicate such waves as important sources of BTH structure.

MODTRAN SW AND VNIR RADIANCES AND FLUXES

A. Berk, L.S. Bernstein, P.K. Acharya,

Spectral Sciences Inc.
99 S. Bedford Street, Suite No. 7
Burlington, MA 01803

G.P. Anderson

Geophysics Directorate
Phillips Laboratory
Hanscom AFB, Massachusetts

The Correlated-k (CK) option of MMODTRAN4 partitions band mode transmittances into Beer's Law components for proper implementation of multiple scattering algorithms. Comparisons between CK and standard band model short-wave (SW) and visible/near-infrared (VNIR) spectral fluxes at the surface, the tropopause and the top of the atmosphere will be presented to benchmark the level of error introduced by neglect of Beer's Law. Results will be presented at two calculation step sizes, for clear and cloudy skies, and using simple 2-stream and discrete ordinate (DISORT) N-stream multiple scattering methods. An upgrade to the MODTRAN band model, important for O2 band at 0.76μm, will also be presented.

RECENT UPGRADES TO MODTRAN - NEW SOLAR IRRADIANCE DATABASES, INCLUSION OF NOVAM, VERSATILE FREQUENCY INPUTS AND INCLUSION OF INSTRUMENT SCANNING FUNCTIONS

P. Acharya, A. Berk, L. Bernstein and D. Robertson

Spectral Sciences Inc.
99 S. Bedford Street, Suite No. 7
Burlington, MA 01803

G.P. Anderson and J. Chetwynd

Phillips Laboratory/GPO
Hanscom AFB, MA 01731

Recent upgrades are intended to make MODTRAN a more accurate, convenient and versatile atmospheric modeling tool. The current default solar irradiance database due to Kurucz was corrected in the 310-340 nm region using measured data. Several other datasets are also made available to the user. The user can also use his/her own data residing in a file. Examination confirms that the corrected Kurucz data is still the best overall among all currently available datasets. MODTRAN can now be run using frequency inputs which are in wavenumber, nm or micron. Additionally, there is now the capability of obtaining radiance and transmittance which are convolved with an appropriate instrument scanning function. Several choices of scanning functions are available including an user-defined option. This upgrade is helpful to users who would like to model satellite data which are gathered as a function of wavelength and have undergone instrument degradation. All upgrades are accomplished while maintaining strict compatibility of TAPE5 with earlier versions of the code. Work is currently in progress to incorporate NOVAM (Navy Oceanic Vertical Aerosol Models) into MODTRAN.

SOLAR ULTRAVIOLET IRRADIANCE AND ITS VARIATION

Giuliana de Toma, Gary J. Rottman, Thomas N. Woods

**Laboratory for Atmospheric and Space Physics
Boulder, Colorado**

Solar ultraviolet irradiance, especially at wavelengths below 300 nm, is strongly absorbed by the Earth's middle atmosphere, where is the dominant source of energy. Knowledge of the amount of solar energy deposited in the atmosphere and its variation with time is important for atmospheric studies.

The Solar Stellar Irradiance Comparison Experiment, SOLSTICE, on the UARS satellite makes daily observations of solar spectral irradiance in the wavelength region from 120 to 420 nm. The UARS observations start in late 1991, near the peak of solar cycle 22, and continue to the present solar minimum condition. During this period two types of variation are most notable in SOLSTICE data: the 27-day variations related to the rotation period of theSun and the longer term variability associated with the 11-year solar cycle.

In this paper, the SOLSTICE irradiance measurements are reviewed with particular emphasis on variability. For the period 1991-1996, we report a variation of about a factor of two at Lyman alpha and a variation of about 6% near 200 nm, gradually decreasing to less than 1% near 300 nm.

COMPARISON OF RSS MEASUREMENTS WITH MODTRAN

Lee Harrison, QILONG MIN, and Joe Michalsky

Atmospheric Sciences Research Center
State University of New York, Albany

The Rotating Shadowband Spectroradiometer (RSS) is a new instrument that provides spectral direct, diffuse, and total horizontal irradiances with a 512 CCD-array over the wavelength range from 350 nm to 1075 nm. We compare the measured spectra from the RSS to that taken by collocated MFRSR and MODTRAN-3.5 calculations. The measurements from both instruments (RSS and MFRSR) agree within 2%. The model calculated direct-horizontal irradiances show very good agreement with the measurements. However, the model substantially overpredicts the diffuse-horizontal if the standard "rural aerosol" model is applied. If instead we use MODTRAN's "urban aerosol" properties for the asymmetric factor and single scattering albedo, the discrepancy can be eliminated. The spectral signatures of discrepancy suggest that the scattering treatment of the diffuse irradiance and uncertainties about aerosol microphysics might be the potential reasons for "clear-sky anomaly".

SOLAR SPECTRAL MEASUREMENTS: A UNIQUE DATASET

ALEXANDER F. H. GOETZ[1,2], Kathleen B. Heidebrecht [1], and Bruce Kindel [1]

[1] Center for the Study of Earth From Space/CIRES

[2] Department of Geological Sciences
University of Colorado
Boulder, CO 80309

A database has been created containing high temporal (one per minute) solar irradiance and radiance measurements taken in Boulder, CO during September and October, 1996 and Petersham, MA in June, 1996. The measurements were made under a variety of sky conditions. The data were measured with an ASD-FR instrument that has a spectral range from .4-2.5 microns, resolution of 3-10 nm, and a sampling interval of 2 nm. The data quality is good and is in high agreement with MODTRAN simulations. A large effort was made to get an absolute calibration for the instrument and to validate the data against independent measurements. Digital photographs of the sky will be taken coincident with the spectral measurements planned for the spring and summer of 1997. The data will be stored in a commercial database and available to other researchers.

This page intentionally blank

MWIR ATMOSPHERIC CORRECTION ALGORITHM

Hsiao-hua K. Burke, J. William Snow, Kristine E. Rhoades
John Kerekes, Mike P. Jordan and Carolyn Upham

MIT Lincoln Laboratory
244 Wood Street
Lexington, MA 02173

Currently there are mid-wavelength infrared (MWIR) space assets being used for surface characterization. An effort was undertaken to reconstruct surface emitted MWIR radiance from satellite measurements using readily available atmospheric information. A new surface radiance retrieval algorithm based on MWIR satellite data (GOES Imager Channel 2 alone) was developed. It is demonstrated that retrieval accuracy can be improved by using existing NOAA operational products, specifically the 'Eta' prediction model output, combinedwith the state-of-science atmospheric radiative transfer model (MODTRAN). Various test cases were investigated. Significantly, the retrieval of sea surface temperature over ocean at nighttime is shown to have a bias of 0.1 K and rms of 0.5 K. In this presentation, additional cases of land surfaces as well as daytime conditions are also illustrated. Analysis of environmental parameter sensitivities and comparisons of results between LWIR and MWIR will be discussed.

APPLICATION OF MODTRAN TO SEA SURFACE
TEMPERATURE RETRIEVAL SIMULATION

D. Hogan, W. Gallery

AER, Inc.

Sea surface temperatures (SST) are traditionally measured from satellites using radiometer bands in the 8 to 12 and the 3 to 5 micrometer window regions. In-situ measurements of SST's are correlated with simultaneous satellite radiance measurements to develop regression equations relating the measured radiances to the SST. These regression equations are then applied to routine satellite radiance measurements to obtain operational SST's.

We have used MODTRAN to simulate the radiance for a proposed satellite radiometer. A dataset of globally representative atmospheric profiles of temperature and water vapor (the TIGR dataset) was split into training and validation datasets. The training set was used with MODTRAN to calculate the simulated radiances and the coefficients for several multi-linear regression models. The validation set was used to derive the error statistics for the regression models. Several models were tested, including various linear and non-linear terms. Finally, the models were tested against a simulated scene calculated using an independent model. Results of these simulations will be presented.

USE OF MODTRAN IN PERFORMANCE AND ANALYSIS CAPABILTIY FOR EARTH OBSERVATION SYSTEMS (PACEOS) SIMULATION SOFTWARE

Steve Marusa and Rafael Rivera

Lockheed Martin Missiles and Space

PACEOS has been under development over the past ten years by heritage Lockheed Martin personnel primarily at Valley Forge PA under IR&D funding PACEOS is an engineering tool used primarily in the design and development of satellite remote sensing systems. PACEOS consists of a series of modules that are run in sequence. The modules simulate the data flow from its source at the earth's surface and/or atmosphere through the sensor and focal plane, the platform and onboard processing, the downlink, ground processing, and extraction of information by the end user. Once the procedures are set up for a given system, the effects of changes in any of the scene, sensor, platform, or data handling parameters can easily be assessed by comparison of the values extracted from algorithms, such as EDR algorithms, with the known input scene conditions.

This paper discusses the use of MODTRAN in the scene generation portion of PACEOS. It includes sections on:

- PACEOS generation of MODTRAN input files
- cloud layer radiance and transmission models within a scene
- variations in scene conditions using non-homogeneous atmospheric profiles across the scenes
- generation of scenes from material data, varying albedo/emissivities or varying temperatures
- options to select different environmental conditions while running PACEOS
- output consistency comparisons on the Sun and DEC Alpha workstations
- generation of the scene at the sensor aperture

Sample results for a variety of conditions will be shown.
We are currently upgrading PACEOS to use MODTRAN3.5 version 1.2 from MODTRAN3.

BOMB DAMAGE ASSESSMENT THROUGH SPECTRAL/RADIOMETRIC ANALYSIS OF PLUME CO2 EMISSIONS

William E. Wilcox & Larrene K. Harada

W. J. Schafer & Associates
321 Billerica Road
Chelmsford, MA 08124-4191

We have developed a technique to assess underground facility bomb damage by measuring CO_2 emissions from the plume of the bomb's explosion. Spectral measurements of various explosions have been made using a CIGARS spectrometer with a high rep rate (60Hz) and moderate resolution (3cm-1) spectrometer in the 3-5 micron band.

The resulting spectra show a strong CO_2 emission feature which correlates to the combustion of bomb fuel products and provides information on the type of explosion being observed.

The analysis requires MODTRAN simulations of atmospheric transmission and background radiance, as well as HITRAN/HITEMP calculations of CO_2 emission at high temperature.

ANALYSIS OF VISIBLE TRANSMISSOMETER DATA IN THE COASTAL SURF ZONE

Michael Zugger and C.R. Philbrick

The Pennsylvania State University
Electrical Engineering Department
University Park PA 16802

The optical propagation conditions in coastal environments are highly variable due to the complex interaction of the maritime conditions with either urban or rural atmospheres. The breaking surf is a generator of aerosol particles, which brings further uncertainty to the description of the optical propagation path over the surf zone. This propagation path may affect the performance of several types of sensors and operational systems.

In this presentation, the data obtained using an optical transmissometer during a recent campaign at Scripps Oceanographic Institution will be described. The instrument was operated along a diagonal path across the surf zone between the shore and locations on the Scripps pier. Measurements taken using the two instruments allow a comparison and correlation of the transmittances. These transmittances will be correlated with temperature profiles from a vertical array of sensors in the surf zone, as well as information on wind and surf conditions. Transmission data will also be compared with predictions of atmospheric models. This first report on the results will also discuss the design of the visible transmissometer. The data was taken as part of the Navy's Electro-Optical Propagation Assessment in the Coastal Environment (EOPACE) program during the period 24 March to 11 April 1997.

TEMPORAL AND SPATIAL CHARACTERISTICS OF SURF-ZONE PLUMES

Christophe F. Bas and C. Russell Philbrick

The Pennsylvania State University
Electrical Engineering Department
University Park PA 16802

One of the goals of the investigation, Electro-Optical Propagation Assessment in the Coastal Environment (EOPACE), is to enhance our understanding of the impact that surf generated aerosols have on the propagation of optical radiation through coastal regions. A bi-static lidar system uses a fan beam to illuminate the atmospheric region above the surf which permits measurements of the vertical and horizontal extent of aerosol plume structures. The scattered radiation is imaged by two sensitive CCD cameras. Three measurement phases of the experiment have provided data on the surf generated coastal plumes at two locations and under a range of different meteorological conditions. The spatial and temporal characteristics of these "coastal plumes" are described.

This page intentionally blank

34

USE OF ATMOSPHERIC AND SIMULATION MODELS
FOR IMAGING SENSOR EVALUATIONS

S.J. Westmoreland, F.C. Mertz

Photon Research Associates Inc.
5720 Oberlin Dr.
San Diego, CA 92121

W.M. Cornette

National Imagery and Mapping Agency
4600 Sangamore Rd., MS D-33
Bethesda, MD 20816

As part of evaluating remotely sensed data, atmospheric effects must be removed or otherwise accounted for. In this paper we document a process for integrating atmospheric model results with sensor spectral response to (1) remove atmospheric effects from image data or (2) add atmospheric effects to surface measured spectra for comparison with at-sensor measurements. The environment developed for this process permits interactive visualization and assessment of atmospheric effects on both measured and modeled data. Examples from sensor evaluation and calibration analyses are presented including comparisons of measured and modeled radiance and tranmission data generated by MOSART and MODTRAN, effectiveness of atmospheric removal for sensor calibration, and sensitivity analyses of spectral response to variation in atmospheric parameters.

INFRARED SPECTRAL DATA ANALYSIS AND REMOTE SENSING USING PATTERN RECOGNITION ALGORITHMS

S.J. Lipson, R.B. Lockwood, D.L. Vititoe, C.L. Allred, and W.A.M. Blumberg
Phillips Laboratory, Geophysics Directorate, Hanscom AFB, MA

P.S. Armstrong
Stewart Radiance Laboratory, Bedford, MA

M.P. Jacobson, S.L. Coy, and R.W. Field
Massachusetts Institute of Technology, Cambridge, MA

In remote sensing of atmospheric spectra, the complexity of analyzing data may be compounded by extreme departures from thermodynamic equilibrium and by spectral overlaps, temporal variation, and lack of knowledge of line-of-sight effects. We have developed algorithms for the analysis of infrared spectra taken under these conditions, and applied them to the study of highly vibrationally and rotationally excited carbon monoxide observed in atmospheric simulation experiments. The data were taken using the cryogenic-background LABCEDE facility at the Phillips Laboratory. Mixtures of CO, Ar, and N2 were irradiated with a pulsed electron beam, and the resulting time-resolved infrared CO spectra were obtained with a Michelson interferometer capable of 2 cm-1 resolution. The spectra were highly self-absorbed in the v=1-0 band, but not in the highly vibrationally and rotationally excited bands. The complex, overlapped, self-absorbed spectra were analyzed using pattern recognition algorithms, and excellent agreement between data and fit was obtained. Vibrational basis sets (patterns) were obtained both from synthetic spectral models and from the XCC (Extended Cross-Correlation) method. A global fit using this combined model was performed, in which the time dependence of the known basis sets and the XCC patterns was determined. Applications of this method include remote sensing of environments in which the optical properties of the line of sight are poorly known, where spectroscopic basis sets are unavailable, or where spectra change with time or viewing angle, such as in the aurora or other highly structured atmospheric scenes.

COMPARISON OF THE INFRARED RADIATION MEASUREMENTS WITH CALCULATIONS USING LOWTRAN CODE

Beiying Wu* *

Institute of Atmospheric Physics
Beijing 100029
China

A field experiment was carried out in Xinxiang, China in 1993 to validate the LOWTRAN code. An pyrgeometer measured The infrared downward and upward radiative fluxes at the surface level for the wavelength greater than 4 micron. An infrared thermometer measured the brightness temperature of the sky. Atmospheric temperature, relative humidity, wind speed and direction, visibility and cloud type and amount at the surface level as well as the profiles measurements by a tether balloon system were recorded. Radiosonde was also released in the morning, afternoon and evening at the Zhengzhou station about 100km south of Xinxiang. Observations were conducted every hour for one week. The LOWTRAN code was used to calculate the downward and upward radiative fluxes and the brightness temperature of the sky at various observation direction using the observed atmospheric properties. This paper compares the calculation with observations and analyzes the cause of the difference between them.

* Visitor of Atmospheric Chemistry Division, National Center for Atmospheric Research, Boulder 30807.

MICROWAVE TRANSMISSION IN LIQUID WATER CLOUDS: UNCERTAINTIES AT LOW TEMPERATURES

Alan E. Lipton and Michael K. Griffin

Optical Effects Division
Phillips Laboratory
Hanscom Air Force Base, Massachusetts, 01731-3010

Alan G. Ling

Radex, Inc.
3 Preston Ct
Bedford, Massachusetts, 01730

For many years, the standard for modeling the attenuation of microwave radiation by cloud liquid water has been to rely on the Ray model for the dielectric properties of water, while employing the Rayleigh absorption approximation. The Ray model is used in the FASE and RADTRAN radiative transfer codes. Recently, Liebe, Manabe, and Hufford have developed models for the dielectric properties of water using two relaxation terms, in contrast to the single term used by Ray. The models of Ray and of Liebe, Manabe, and Hufford yield very similar values of attenuation for temperatures above 10 degrees Celsius, within the frequency range of 0 to 250 GHz. At lower temperatures, however, there are substantial spectral differences between attenuation values produced by the different models. Considering that liquid water can occur at temperatures as low as -40 degrees Celsius, the model differences indicate significant uncertainties in cloud remote sensing results derived with the aid of the models.

ECRIN'96 : AN AIRBORNE CAMPAIGN FOR THE RADIANCE MEASUREMENT OF STRATOCUMULUS CLOUDS

P. Simoneau[1], C. Malherbe[1], A. Boischot[1], G. Durand[1], B. Rosier[1], A. Delannoy[1]
P. H. Flamant[2], J. Pelon[3], L. Sauvage[2], H. Dirand[2]

[1] Office National d'Etudes et et Recherche Aérospatiale
Palaiseau, France

[2] Laboratoire de Météorologie Dynamique
Ecole Polytechnique, Palaiseau, France

[3] Service d'Aéronomie du CNRS
Université Pierre et Marie Curie, Paris, France

ECRIN'96 (étude du Champs Radiatif Infrarouge des Nuages) has been achieved for the correlative measurement of the infrared radiation coming from low altitude clouds, in situ measurements, and lidar measurements on clouds. The experiment took place in Britanny near Brest (West coast of FRANCE) in October 96 with the participation of 3 aircraft : a Caravelle operated by the Centre d'Essai en Vol, a turboprop Fokker-27 so called ARAT (Avion de Recherche Atmosphérique et Télédétection) and a turboprop MERLIN 4 operated by Météo-France.

The aircraft were instrumented with the following sensors :
- an airborne infrared cryogenic spectrometer and an infrared imager loaded on the Caravelle for radiance measurements
- an airborne Lidar for the sounding of high altitude clouds and microphysic measurements, loaded on the Fokker-27
- microphysic and thermodynamic sensors for in-situ measurements, mounted on the Merlin 4
- fluxes sensors mounted on the Fokker-27 and the ARAT

The measurement strategy and preliminaries results (radiance spectra, lidar measurements and in-situ microphysic measurements) are presented.

ATMOSPHERIC CORRECTION THROUGH TRANSMISSIVE CLOUDS

J. William Snow, Hsiao-hua K. Burke, Michael P. Jordan,
Daniel C. Peduzzi and Kristine E. Rhoades

MIT Lincoln Laboratory
244 Wood Street
Lexington, MA 02173

From space, the extraction of surface parameters by using IR sensors has long been impeded by clouds. When clouds are present, retrieval is not performed and thus surface information is unavailable. The high frequency of occurrence of clouds calls for technology development to minimize this shortcoming. In particular, transmissive clouds offer the greatest potential since statistically their global coverage extends to more than 20%, and typically they are less than 0.5 in optical depth, which makes the correction of surface radiances more tractable.

A methodology for the determination of the atmospheric conditions indicative of cloud presence and derivation of its physical thickness was developed based on water vapor and temperature profiles. Transmissive clouds are identified and parameterized, enabling correct surface radiance to be retrieved. A surface radiance retrieval algorithm based on GOES MWIR satellite data which utilizes readily available atmospheric information and MODTRAN is used. The results of surface radiance retrieved through these transmissive cloud cases are encouraging - the derived surface temperature bias and rms were shown to be 0.1 K and 1.0 K, respectively.

ENVIRONMENTAL TRANSMISSION EFFECTS WITHIN A DISTRIBUTED SIMULATION

Joel B. Mozer, Thomas R. Caudill, Capt. Mark M. Edwards

USAF Phillips Laboratory
Geophysics Directorate
Optical Effects Division
Hanscom AFB, MA 01731

Steven A. Ayer and Guy P. Seeley

Radex, Inc.
3 Preston Ct
Bedford, Massachusetts, 01730

Distributed simulation is an increasingly important part of the modeling and simulation activities in the DoD due to diminishing development and training budgets relative to the sophistication of modern weapon systems. A crucial, but often ignored, component of this type of simulation is the effect of the natural environment on an engagement scenario. For example, the impact of atmospheric constituents such as clouds, wind, fog, and haze are not typically included in a weapon system simulation. However, the existence of these constituents in a real system can mean the difference between a weapon being successful, or completely useless in a given situation.

We have developed a prototype capability to generate and disseminate atmospheric data within a Distributed Interactive Simulation (DIS) environment. This capability utilizes a variety of models and simulations to generate the appropriate 3D atmospheric constituent data using a combination of satellite analysis algorithms, mesoscale numerical weather prediction model diagnostics, and Phillips Laboratory's Cloud Scene Simulation Model (CSSM). The transmission effects of the simulated environment on a weapon system are determined via a modified version of the Electro-Optical Tactical Decision Aid (EO/TDA) program. This paper details the construction of this prototype capability and outlines the needs for this type of activity to be effective in future simulations.

GLOBAL WARMING STABILIZATION MODELS:
VEHICLE EMISSIONS, REFIGERANTS, AND DEFORESTATION

Steven Dupree, Paul Yeaman, Robert Alwine, and Jefferey Campbell

Worcester Polytechnic Institute
Worcester, MA

Evidence clearly indicates that global warming is an observable phenomenon likely to be linked to human activity. If this phenomenon continues at its current rate, the effects could be disastrous for humankind and all life on Earth. As one of the major superpowers of the world, and one of the most technologically advanced, it is the responsibility of the United States to lead the efforts to reduce global warming. This project considers some possible reduction methods, including various policy changes and legislative actions, evaluating each in terms of effectiveness as well as cost. A final comparison leads to a recommendation of a set of policies which will curb the effects of global warming in as cost effective a manner as possible.

MODTRAN4: Simulating Atmospheric Radiation Budgets in the Middle Atmosphere:

G.P. Anderson, J.H. Chetwynd, A. Berk,
L.S. Bernstein, H.E. Snell, A. Ratkowski,

Phillips Laboratory
Geophysics Directorate
Hanscom AFB, MA

E.P. Shettle
Naval Research Laboratory
Washington, DC

The new MODTRAN4 band model, with its correlated-k Beer's Law algorithm, can efficiently and correctly calculate the scattering and absorption signatures of realistic molecular, aerosol and cloudy environments in the lower and middle atmosphere. The current approach for molecular scattering accommodates line overlap and partial correlations between both molecular species and the solar irradiance, while maintaining band model spectral resolution at 2 to 15 cm^{-1}. This new level of evolution and validation will permit improved syntheses and analyses of actinic (direct plus scattered) solar and thermal energy sources and their flux divergence within the stratosphere and troposphere.

Rapid calculation of IR cooling rates for a variety of thermal and constituent profiles demonstrates the flexibility of the approach and the sensitivity to latitudinal and dynamic variability. Validation is provided through two avenues. The first involves direct comparisons with line-by-line calculations, as exemplified by FASE (the line-by-line algorithm jointly developed from FASCODE by DoD and DOE) which provides the molecular standard for layer effective optical depths, single scattering albedos, and transmittances. This enables the more primitive MODTRAN4 algorithm to be refined for both more flexible spectral resolution and efficient/accurate determination of these essential layer quantities necessary for multiple scattering applications; e.g. DISORT. The second validation step centers on comparisons against a variety of measurements, mostly airborne visible and IR up-welling radiances, including both clear and clouded skies. A particular attempt will be made to examine the impact of polar stratospheric clouds.

Optical Effects Division

DoD Atmospheric Radiance and Transmittance Codes
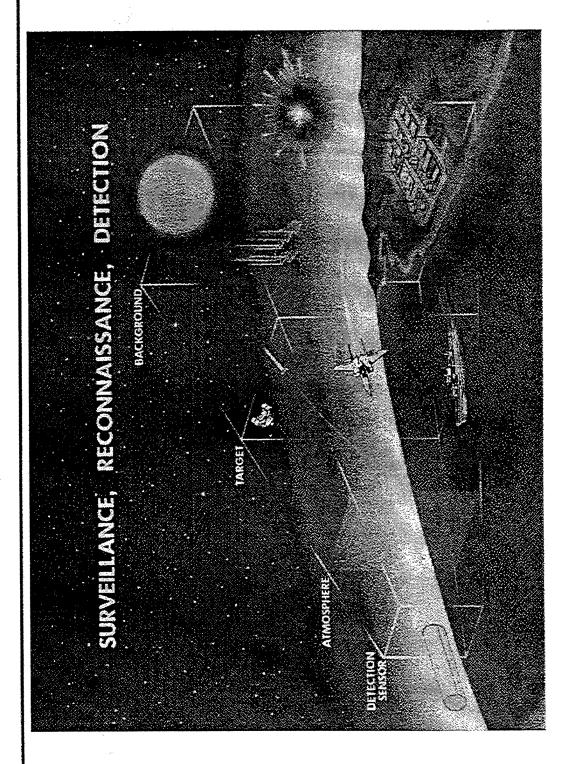
Presented To

20th Annual Review Conference of Atmospheric Transmission Models

Briefer

Dr. Laila S. Jeong

Phillips Laboratory

Geophysics Directorate

10 June 1997

Atmospheric Transmission and Radiance Backgrounds

SURVEILLANCE, RECONNAISSANCE, DETECTION

Optical Backgrounds Models for Systems Engineering

SWIR Cloud/Terrain Scene

- Spectral Radiance LOS Codes
  - MODTRAN 3.5, 4.0 (Low altitude)
  - FASCODE 3P (Low altitude)
  - MOSART 1.41, 1.5 (Low altitude)
  - SHARC 3.0 (High altitude)
  - SAMM 1.0 (All altitude)

- Spatial Structure Codes
  - SMT 1.2 (Cloud/Terrain)
  - CBSD 1, 2 (Celestial)
  - SHARC 4.0/SIG 1.0 (High altitude)
  - SMT 1.3 (Cloud/Terrain)
  - SAMM 2.0 (All altitude)
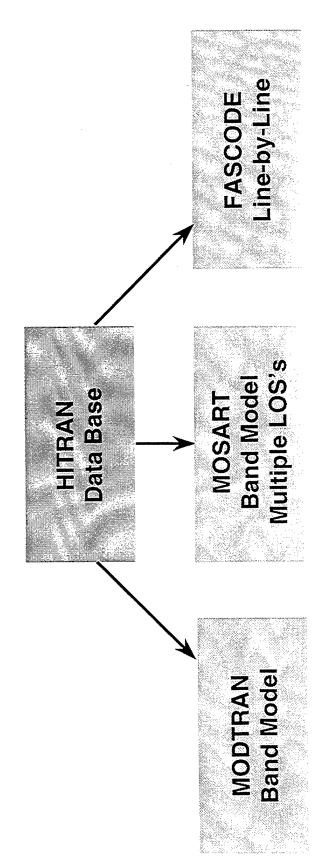
- Integrated Codes
  - PLEXUS 2.1b, 3.0, 4.0

MWIR Earthlimb Scene

97TransMtg.3
5/15/98

46
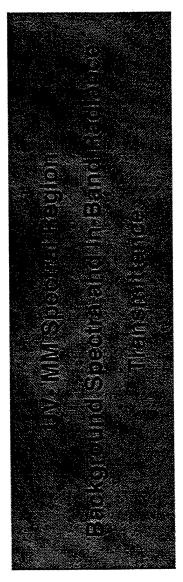
Low Altitude
Atmospheric Codes
MODTRAN, MOSART, and FASCODE

HITRAN Data Base

FASCODE Line-by-Line

MOSART Band Model Multiple LOS's

MODTRAN Band Model

Low Altitude Atmospheric Code Validation

Path Characterization

Measurements

FASCODE

MODTRAN

MOSART

97TransMtg.5
5/15/98
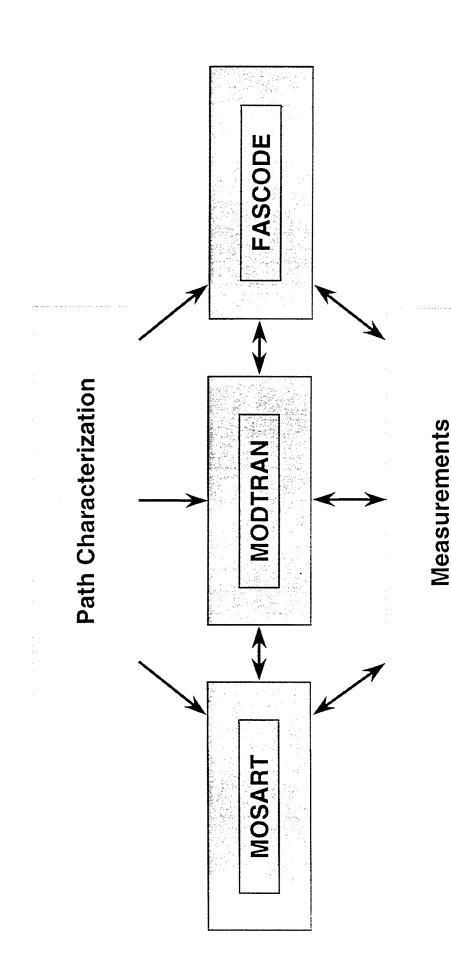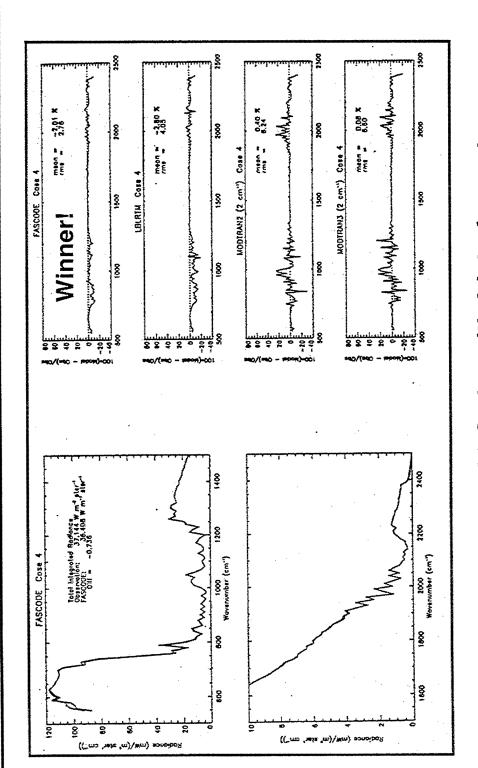
FASCODE and MODTRAN
Validation

Intercomparison of 8 Codes with 3 Interferometer
Measurements for Climate Change Modeling
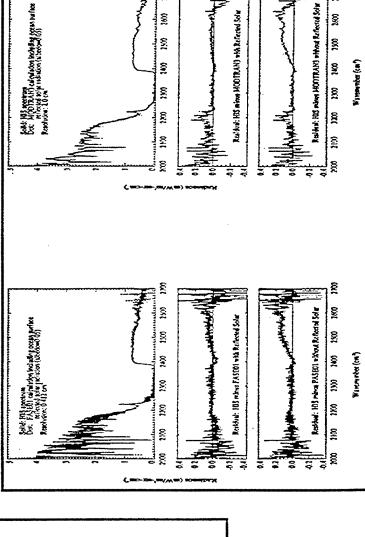
FASCODE and MODTRAN Validation

Comparison of FASCODE and MODTRAN with HIS Data

Comparison of FASE with Interferometer Data for ARM

50
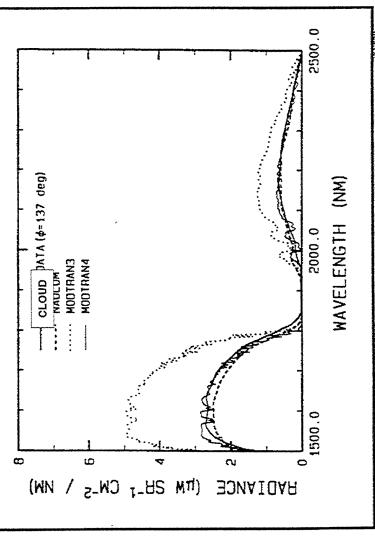
MODTRAN Upgrades
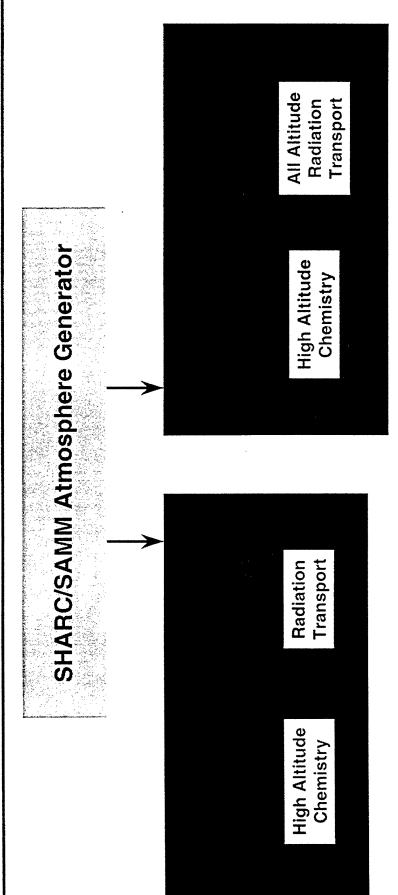
- *MODTRAN 3.5* - Provided capability for flexible description of clouds and aerosols

  - All clouds and aerosols described by user-provided cloud top, cloud bottom, layer thickness, opacity (or default values)

- *MODTRAN 4.0* - Implementing improved description of multiple scattering in clouds and aerosols

  - correlated-k technique
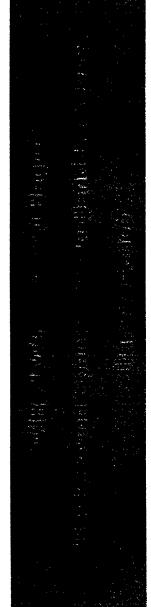
Comparison of Codes with Cloud Data from Airborne Spectrometer

CLOUD DATA (φ=137 deg)
····· MODTRAN
······ MODTRAN3
—— MODTRAN4

RADIANCE (μW SR⁻¹ CM⁻² / NM)

WAVELENGTH (NM)

High Altitude
Atmospheric Codes
SHARC 3 and SAMM 1

SHARC/SAMM Atmosphere Generator

All Altitude
Radiation Transport

High Altitude
Chemistry

Radiation
Transport

High Altitude
Chemistry

AIR FORCE RESEARCH LABORATORY

AIR FORCE MATERIEL COMMAND

High Altitude Atmospheric Code Validation

Research Models
ARC/AARC
Rotational NLTE

Species Profiles
NLTE Chemistry
Radiation Transport
Non-Local Coupling

SHARC 1 - 3

SAMM 1

Space - Based
Measurement Data

SPIRE, FWI, SPIRIT 1,
CIRRIS1A, HIRS2, *MSX,
MSTI-3*

Radiation
Transport

FASCODE
MODTRAN

97TransMtg.10
5/15/98

SHARC and SAMM Validation
Using FASCODE and MODTRAN

SAMM - MODTRAN Comparison
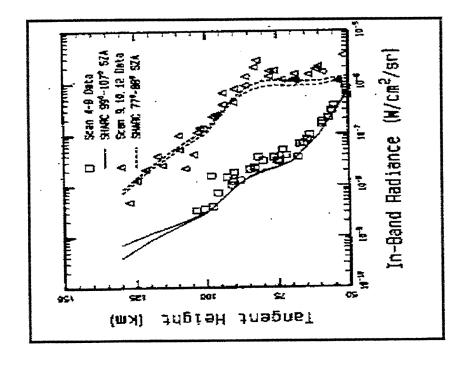
SHARC - FASCODE Comparison

SHARC 3 Validation Using SPIRE Data
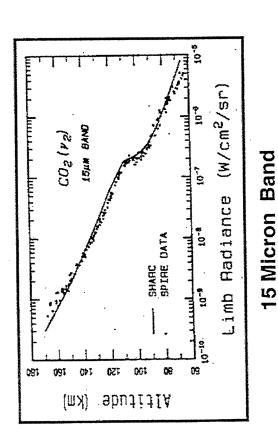
4.3 Micron Band - Terminator

4.3 Micron Band - Daytime

15 Micron Band

SAMM Validation
Using CIRRIS 1A Data

8 - 12 Micron Band

8 - 18 Micron Band

5 - 7 Micron Band

6 - 9 Micron Band

2.6 - 3.3 Micron Band

4.1 - 4.5 Micron Band

97TransMtg.13
5/15/98

56
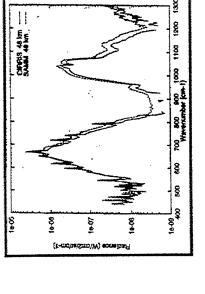
SAMM Validation
Using CIRRIS 1A Data

48 km Tangent Height

23 km Tangent Height

13 km Tangent Height

111 km Tangent Height
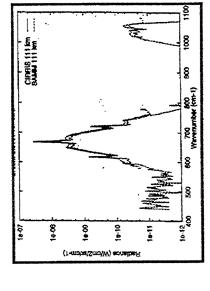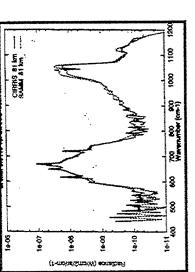
81 km Tangent Height

67 km Tangent Height

97TransMtg.14
5/15/98
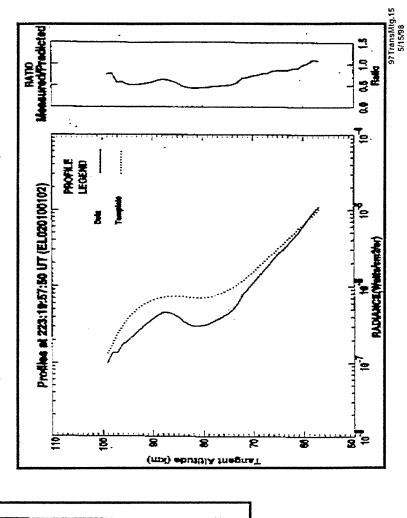
SAMM Validation Using MSX Data
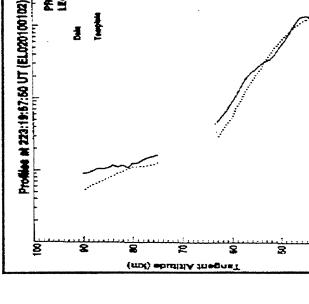
A (6.77 - 10.84 Micron) Band

B1 (4.22 - 4.36 Micron) Band

97TransMtg.15
5/15/98

Atmospheric MWIR
Background Global Variability
HIRS/2 - SAMM Data Comparison

HIRS CHANNEL 17 (DAY 33, FEB)

HIRS/NADIR
HIRS/OFF-NADIR
SHARC/NADIR
SHARC/OFF-NADIR

HIRS CHANNEL 17 (DAY 130, MAY)

HIRS/NADIR
HIRS/OFF-NADIR
SHARC/NADIR
SHARC/OFF-NADIR

10-Day Average February 1995

NOAA 12, HIRS/2, 4.23μm

10-Day Average May 1995

NOAA 12, HIRS/2, 4.23μm
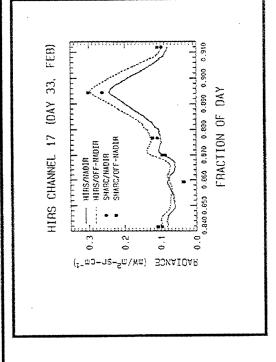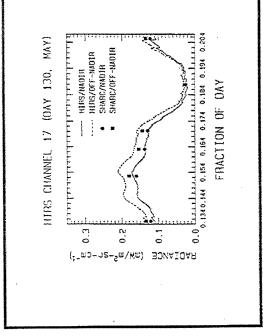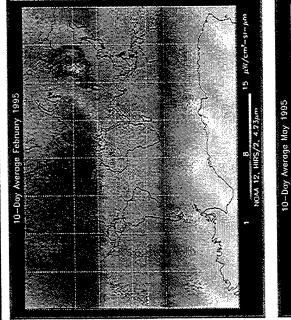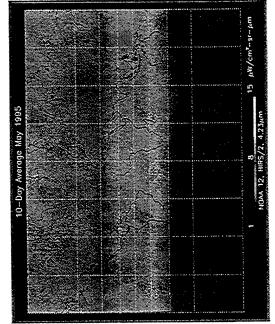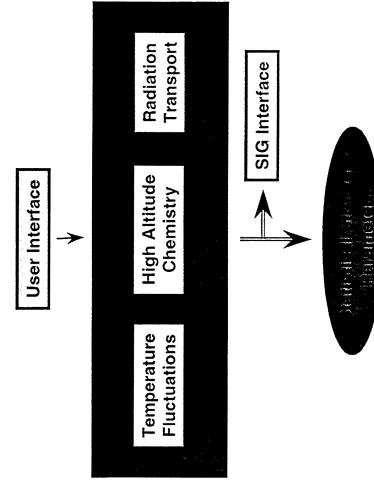
SHARC 4.0

Synthetic High Altitude Radiance Code

User Interface →

Temperature Fluctuations | High Altitude Chemistry | Radiation Transport

SIG Interface

Capabilities

- Calculates statistical structure parameters for SWIR-LWIR background scenes

- Traceable to temperature/density fluctuations

- Applicable to arbitrary viewing geometries

Provide statistical structure parameters for SWIR, MWIR, MLWIR, and LWIR background scenes containing stochastic structure

SIG 1.0
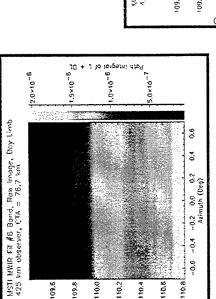
SHARC Image Generator
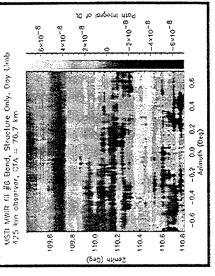
Daytime Earthlimb Structure - 4.3 Micron Band

MSTI MWIR Fil #6 Band, Structure Only, Day Limb
425 km observer, CTA = 76.7 km

Stochastic Structure Only

MSTI MWIR Fil #6 Band, Raw Image, Day Limb
425 km observer, CTA = 76.7 km

Deterministic + Stochastic Structure

Capabilities

- Calculates SWIR, MWIR, MLWIR, and LWIR spatially-structured atmospheric background scenes

- Applicable to limb, nadir, and off-nadir viewing geometries

- Incorporates both fast and high fidelity structuring techniques
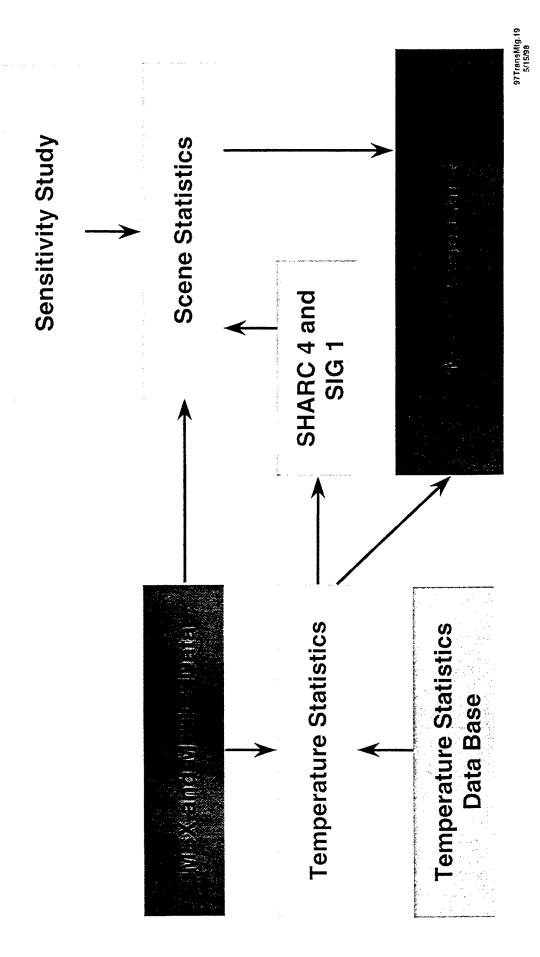
Simulate atmospheric background clutter with sufficient accuracy to meet SBIRS design requirements

97TransMtg.18
5/15/98

Atmospheric Background Model Assessment

Sensitivity Study

Scene Statistics

SHARC 4 and SIG 1

Temperature Statistics

Temperature Statistics Data Base
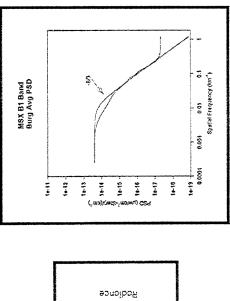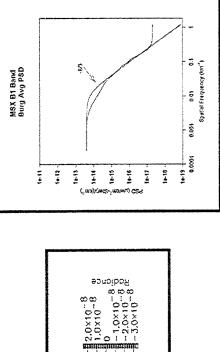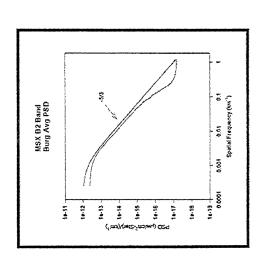
Atmospheric Background Model Validation Using MSX Data

MSX B1 Band
Burg Avg PSD

MSX B2 Band
Burg Avg PSD

BTH Narrow MWIR Band Data
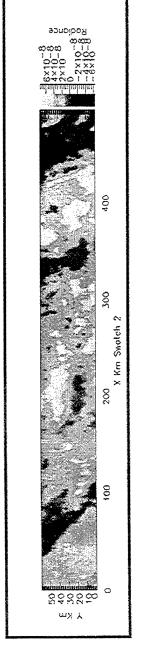
BTH Broad MWIR Band Data

97TransMtg.20
5/15/98

63

SAMM 2.0

SHARC and MOSART Merged

Planned Capabilities

- Calculates all-altitude SWIR, MWIR, MLWIR, and LWIR background scenes containing spatial structure

- Traceable to temperature/ density fluctuations

- Applicable to arbitrary viewing geometries

MOSART 1.4 Low-Altitude Radiance and Transmission

SHARC 4.2 All-Altitude Stochastic Structure Parameters

SIG 2.0 All-Altitude Stochastic Structure
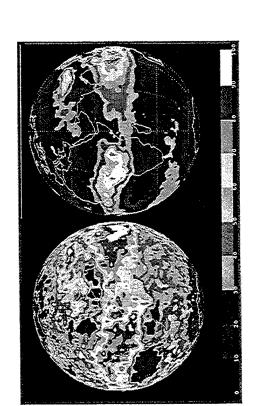
Simulate all-altitude atmospheric background clutter with sufficient accuracy to meet SBIRS design requirements

Cloud/Terrain Background Scene Models

SBIRS Model Toolkit v1.2

Capabilities

- Provides cloud and terrain background scenes using upgraded stand-alone version of integrated CLDSIM and GENESSIS

- Provides cloud-at-altitude frequencies of occurrence using CLOUDVIS data base
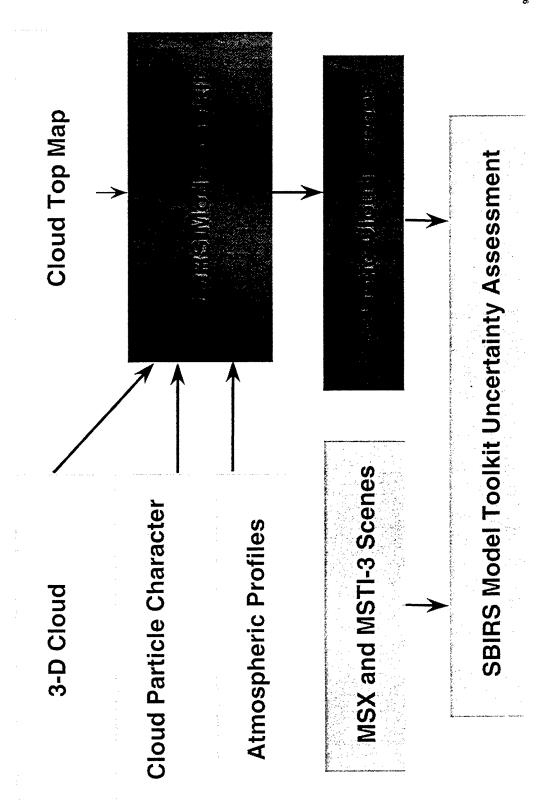
Simulate cloud and terrain background clutter with sufficient accuracy to meet TMD and NMD design requirements

65

SBIRS Model Toolkit Assessment Using MSTI-3 and ARES Data

Cloud Top Map

3-D Cloud

Cloud Particle Character

Atmospheric Profiles

MSX and MSTI-3 Scenes

SBIRS Model Toolkit Uncertainty Assessment
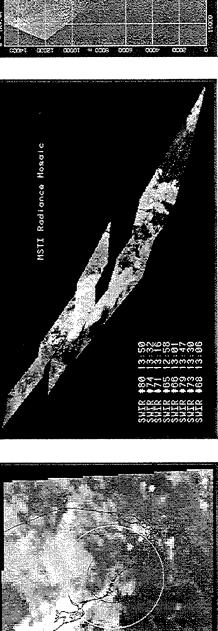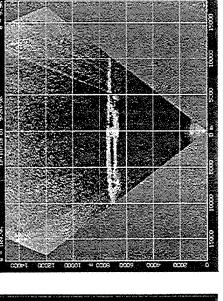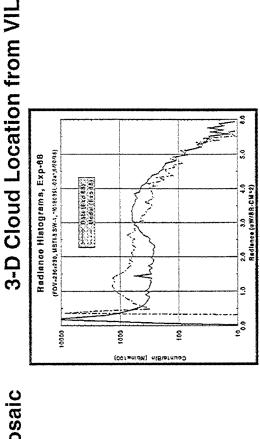
SBIRS Model Toolkit Assessment Using MSTI-3 Data

3-D Cloud Location from VIL

Radiance Histogram Comparison

MSTI-3 Stare Points

SWIR Scene Mosaic
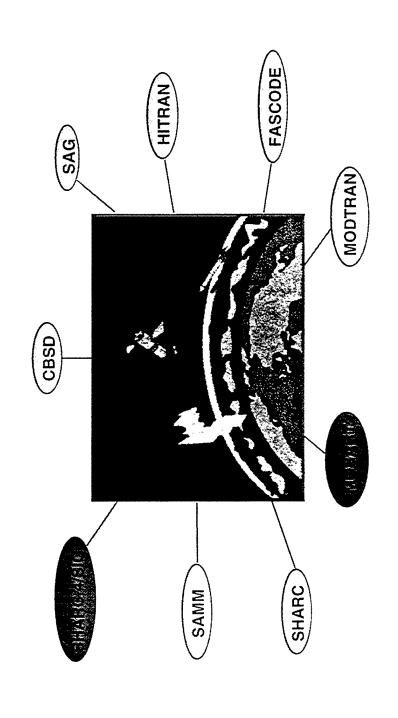
Measured and Modeled SWIR Scenes

67

PLEXUS 2.1b

Phillips Lab Expert Unified Software

SAG

HITRAN

FASCODE

MODTRAN

CBSD

SAMM

SHARC

- Single point access to PL IR atmospheric and celestial background codes
- Embedded expert system to facilitate code applications by non-expert users

PLEXUS 3.0/3.0 NI
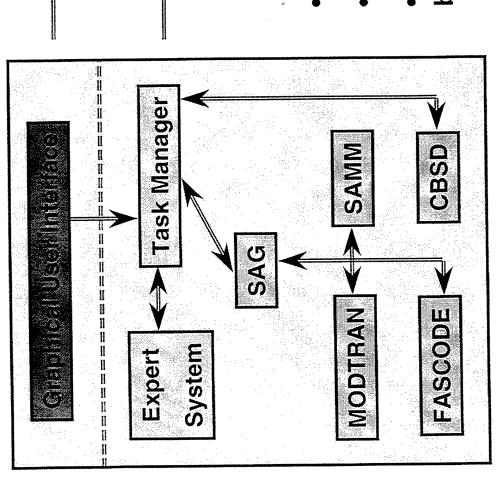
Phillips Lab Expert Unified Software

- Version 3.0 with GUI for PC applications

- Version 3.0 NI "atmospheric object" for platform independent applications

- Fully modular code architecture
- C++ GUI
- SAMM code for all-altitude background simulations

Graphical User Interface

Task Manager

Expert System

SAG

SAMM

CBSD

MODTRAN

FASCODE

97TransMtg.26
5/15/98
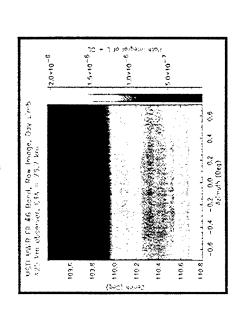
PLEXUS 4.0/4.0 NI

Phillips Lab Expert Unified Software

SHARC 4.0
Non-Stationary
Stochastic Structure
Descriptors

→

SIG1.0
Structuring
and
Scene Rendering

→

MSTI-3
ATH
SWIR
Scene
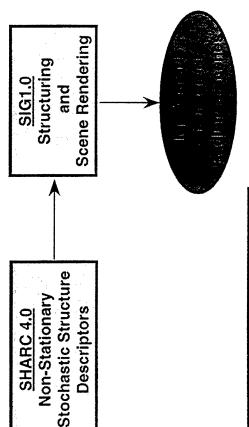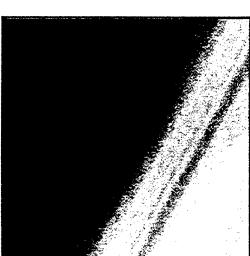
Planned Capabilities

• Simulate high-altitude spatially structured backgrounds

• Multiple structuring techniques for arbitrary viewing geometries

• Scene rendering

SHARC 4.0/SIG 1.0
MWIR Earthlimb Scene

70
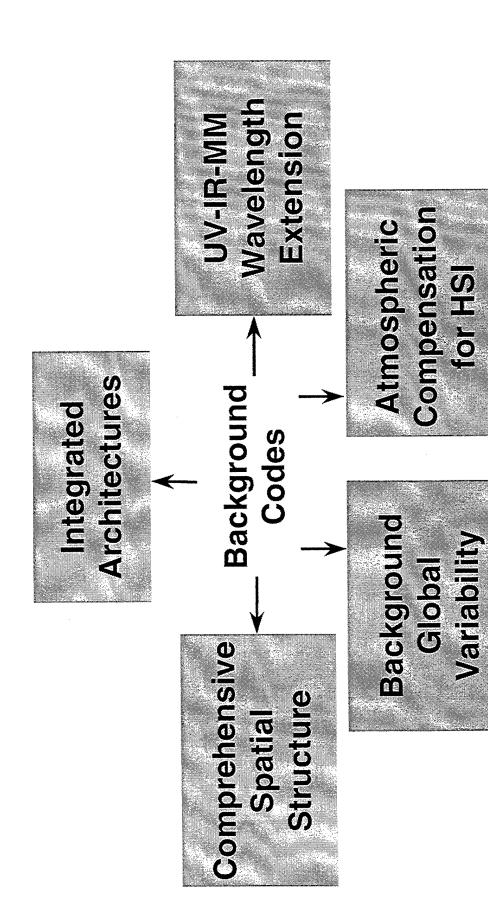
New Directions for Optical Background Codes

Integrated Architectures

UV-IR-MM Wavelength Extension

Background Codes

Comprehensive Spatial Structure

Atmospheric Compensation for HSI

Background Global Variability

Summary

- DoD standard atmospheric transmission and radiance background codes

- Unique, integrated Air Force program of optical background measurements and codes to provide validated radiance profiles and background scenes

- Key emphasis on technology transition to SMC, AF, and DoD military weapon system development

- Important role in defining environmental requirements for systems and battlespace simulations

The MOSART Code

Dr. William M. Cornette
National Imagery and Mapping Agency

Dr. Prabhat K. Acharya
Dr. Alexander Berk
Dr. David C. Robertson
Spectral Sciences, Inc.

Gail P. Anderson
Dr. William A.M. Blumberg
Dr. Laila S. Jeong
Dr. Francis X. Kneizys
Air Force Research Laboratory

Sally J. Westmoreland
Photon Research Associates, Inc.

9 June, 1997

20th Annual Atmospheric Transmission Conference
10-12 June 1997, Hanscom AFB, MA

1

73

The status of MOSART, along with these upgrades will be presented. Version 1.50 is planned for release in mid-August 1997, with a major upgrade for Version 2.00 planned for March 1998. The plans for both of these releases will be presented, together with information on how to obtain the code and who to contact for technical information and "bug" reporting.

Introduction

The MOderate Spectral Atmospheric Radiance and Transmittance (MOSART) code is a U.S. Government standard code with the ability to support scene and signature simulations. It grew out of a merging of the MODTRAN and APART codes with some additional capabilities added. Recommended platforms are workstations (SGI, Sun, HP, DEC Alpha), although it will run on a high end PC (e.g., 200 MHz, 64 Mb RAM, 50-100 Mb of free disk space). It has been thoroughly tested on machines that use the IEEE 754 floating point standard (e.g., SGI, Sun, HP), but there may be some minor numerical bugs encountered on VAX/VMS machines due to the hard underflow (i.e., one known case crashed on a VAX but ran on the other IEEE 754-compliant machines: the fix was simple and was purely numerical).

Except for DISORT, MOSART Version 1.50 contains all MODTRAN 3.5 capabilities and has been compared against it for a number of conditions by Spectral Sciences, Inc. and Photon Research Associates, Inc. The version of the DISORT code in MODTRAN 3.5 is still under beta testing and further work is on-going at Spectral Sciences, Inc. (SSI) and at the Air Force Research Laboratory, Hanscom AFB, MA. As soon as it is approved by Air Force Research Laboratory, it will be incorporated into MOSART.

As with MODTRAN, MOSART uses a 1 cm^{-1} resolution set of band parameters derived from the 1997 HITRAN line atlas, including the latest change to partition the 1 cm^{-1} region into four sections for better representation of the continuum. Based on comparisons with degraded spectral created by the line-by-line code FASCODE, the actual resolution of both MODTRAN and MOSART are slightly greater than 1 cm^{-1} and are usually advertised as 2 cm^{-1}. In the UV/ Visible region, a few more molecular absorption bands are included at a coarser resolution, and the multiple scatter model is different.

The viewpath geometries include all MODTRAN3 geometries, plus some new geometries, including Observer-Source, Observer-Background, Observer-Source-Background, Earthlimb, Horizontal, At-Source (i.e., Observer & Source are co-located). The user can specify a number of different parameters (e.g., observer altitude, source altitude, and range; observer altitude/latitude/longitude and tangent point latitude/longitude -- or tangent altitude, for a couple of examples), any potential geometry is capable of being requested. An X-Windows/Motif Input GUI is available, as is a simple scrolling input file builder. However, once the user becomes familiar with the input file structure (it is self-documenting with full text descriptions of the inputs being included in the input file), an editor like vi or emacs is quite adequate.

MOderate Spectral Atmospheric Radiance and Transmittance (MOSART) Computer Code

MOSART
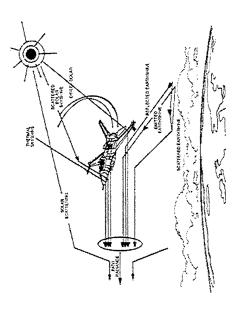
A Government-Standard Model for Predicting the Radiative Environment for

Target Signature and Background Scene Generation

- Observables-Driven Architecture
- MODTRAN Molecular Absorption
- Three-Flux Multiple Scattering
- Turbulence & Sky Noise
- Forward In-Scatter
- Global Data Bases
  – Atmospheres
  – Climatologies
  – Terrain Altitude
  – Ecosystems/Terrain Type
- Terrain
  – Contrast
  – Structured
  – Bidirectional/Directional
- Hydrometeors
  – Clouds (Water/Ice)
  – Fog
  – Rain
  – Snow

9 June, 1997

20th Annual Atmospheric Transmission Conference
10-12 June 1997, Hanscom AFB, MA

2

75

MOSART has been installed and tested on a number of machine, including:

- SGI (IRIX)
- Sun (OS & Solaris)
- HP 9000
- Data General
- IBM 3094 (VM/CMS) (Early Version)
- High End PCs (Lahey & Microsoft compilers)
- DEC VAX/VMS & Alpha 3000
- Prime (Early Version)

Although installed and tested, a numerical representation problem exists on DEC machines. The problem is related to DEC's non-compliance with IEEE Standard 754, and is easily fixable, once time is available on this type of machine.

To install MOSART (values are for a SGI machine), 50-100 Mbytes of Disk Space is required, along with a FORTRAN 77 Compiler (ANSI X3.9-1978); libraries satisfying MIL-STD 1753 is helpful, but not necessary. A requirement for X-Windows/MOTIF is optional (for GUI only).

To date, the MOSART code has been utilized by a number of simulations and applications, including:

- Synthetic Scene Generation Model (SSGM) BMDO/NRL/PRA

- Environment Effect in Distributed Interactive Systems (E^2dis) DMSO/NRL/PRA/SSI
- Flexible Infrared Signature Tools (FIST) RL/NAIC/PRA
- SPIRITS (in development) PL/SSI
- SAMM2 (in planning) PL/SSI
- Scene Simulators:
  - GENESSIS (PRA)
  - CLDSIM (PRA)
  - GCI Toolkit (PRA)
  - SensorVision (PSI)
  - CloudScape (Visidyne)

One question that a number of users raise is why two codes (i.e., MODTRAN and MOSART) and which one should be used. MODTRAN is a small, efficient code with representative environmental conditions (e.g., six model atmospheres) that performs point-to-point or point-to-space calculations. MODTRAN uses line-of-sight radiative transfer (i.e., a "soda straw" viewpoint). MOSART, on the other hand, has access to

- global environmental conditions and climatologies

- global terrain altitude, scene, and material data bases

and provides output to support scene simulation and signature models. MOSART calculates a comprehensive radiative environment, but is rather large and is not very fast. Each code has its own purpose.

Code Status

The current (i.e., as of June 1997) version of the MOSART code is Version 1.41, which was delivered in September 1995. This version of MOSART has been approved for public release, distribution unlimited by Air Force Public Affairs and Ballistic Missile Defense Office; release by Phillips Laboratory is pending code modifications, "bug" fixes, and upgrades. The MOSART documentation has been released as PL-TR-94-2244 (4 Vols) in May 1996. The documentation consists of:
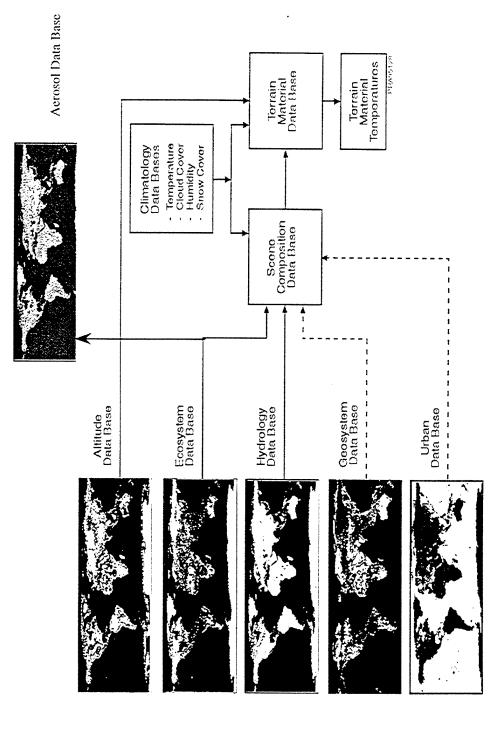
1. Installation Reference Manual
2. Users' Reference Manual
3. Technical Reference Manual
4. Software Reference Manual

As of June 1997, Version 1.41 has undergone significant testing and evaluation by several users, resulting in some general clean-up, "bug" fixes and code modifications, documentation corrections, clarifications (resulting from questions from various users), and an explanation of FTNCHEK warnings. The major upgrades that have been implemented since the initial September 1995 release are:

1. calculation of ephemeris time improved
2. User-Defined atmospheres upgraded
3. snow/ice in temperate climates removed
4. consistency in fractions vs. %
5. oxygen continuum factor (MODTRAN 3 compatibility)
6. molecular concentration normalization (User-Defined)
7. additional checking of user input
8. "To Space" output
9. numerical "closeness" on machines with 64-bit register arithmetic

MOSART Environmental Data Bases

MOSART

Aerosol Data Base

Altitude Data Base

Ecosystem Data Base

Hydrology Data Base

Geosystem Data Base

Urban Data Base

Climatology Data Bases
- Temperature
- Cloud Cover
- Humidity
- Snow Cover

Scene Composition Data Base

Terrain Material Data Base

Terrain Material Temperatures

9 June, 1997

20th Annual Atmospheric Transmission Conference
10-12 June 1997, Hanscom AFB, MA

4

Code Description

- **MOSART**
- **Installation Utilities**
  - FPTEST
  - INSTDB
- **File Utilities**
  - ASCBIN
  - CRFILE
  - MRFLTR
  - PLTGEN (NCAR)
- **UNIX Utilities**
  - Makefiles
  - Directory Set Up
  - X-Windows/Motif Input Builder GUI
  - C++ Driver

- **Ancillary Codes**
  - BBTEMP
  - FACET
  - FANTOM
  - SCNGEN
  - TERTEM
  - VISUAL
- **Test Cases (11)**
- **Data Bases**
  - MODTRAN Molecular
  - SAG/NRL Atmospheres
  - Global Terrain/Ecosystem
  - Global Climatology

Computer Requirements

- **MOSART has been installed and tested on:**
  - SGI (IRIX)
  - Sun (OS & Solaris)
  - HP 9000
  - Data General
  - High End PCs (Lahey & Microsoft compilers)
  - IBM 3094 (VM/CMS) (Early Version)
  - DEC VAX/VMS & Alpha 3000
  - Prime (Early Version)

- **Although installed and tested, a numerical representation problem exists on DEC machines**
  - Problem is related to DEC's non-compliance with IEEE Standard 754
  - Problem is easily fixable, once time is available on these machines

- **50-100 Mbytes of Disk Space is Required**

- **FORTRAN 77 Compiler (ANSI X3.9-1978)**
  - MIL-STD 1753 is helpful
  - X-Windows/MOTIF is Optional (for GUI only)

9 June, 1997

6

Usage on Other Programs

- **Synthetic Scene Generation Model (SSGM)**
  - BMDO/NRL/PRA
- **Environment Effect in Distributed Interactive Systems (E^{2}dis)**
  - DMSO/NRL/PRA/SSI
- **Flexible Infrared Signature Tools (FIST)**
  - RL/NAIC/PRA
- **SPIRITS (in development)**
  - PL/SSI
- **SAMM2 (in planning)**
  - PL/SSI
- **Scene Simulators**
  - GENESSIS (PRA)
  - CLDSIM (PRA)
  - GCI Toolkit (PRA)
  - SensorVision (PSI)
  - CloudScape (Visidyne)

9 June, 1997

20th Annual Atmospheric Transmission Conference
10-12 June 1997, Hanscom AFB, MA

Code Status

MOSART

- **Current Version 1.41 Delivered Sep 1995**
  - Approved for Public Release, Distribution Unlimited by Air Force Public Affairs and Ballistic Missile Defense Office
  - Release by Phillips Laboratory is Pending
  - Code Modifications, Bug Fixes, and Upgrades Available

- **Documents released as PL-TR-94-2244 (4 Vols)**
  - » Installation Reference Manual
  - » Users' Reference Manual
  - » Technical Reference Manual
  - » Software Reference Manual
  - Available Date: May 1996

20th Annual Atmospheric Transmission Conference
10-12 June 1997, Hanscom AFB, MA

8

82

Version 1.41: June 1997
(Upgrades)

MOSART

— Calculation of Ephemeris Time Improved

— User-Defined Atmospheres

— Snow/Ice in Temperate Climates Removed

— Consistency in Fractions vs. %

— Oxygen Continuum Factor (MODTRAN 3 Compatibility)

— Molecular Concentration Normalization (User-Defined)

— Additional Checking of User Iinput

— "To Space" Output

— Numerical "Closeness" on Machines with 64-bit Register Arithmetic

Version 1.50: Aug 1997
(Upgrades)

MOSART

- **Forward Scattering Algorithm (Testing)**

- **Terrain Temperature Algorithm**
  - New Algorithm (In Progress)
  - Wind through Material (e.g., Grass, Scrub, Tree) (Done)
  - Transmissive Layers (In Progress)
  - Air Gap (Done)
    - » Multiple Reflections
    - » Free Convection

- **Multiple Resolution Calculations (Done)**

- **Full MODTRAN 3.5 Compatibility (except for DISORT)**
  - MOLBMP96 Regular Molecular Data Base (Done)
  - CFCBMP96 Heavy Molecular Data Base (Done)
  - Adjustable Clouds (Done)

20th Annual Atmospheric Transmission Conference
10-12 June 1997, Hanscom AFB, MA

11

84

Version 2.00: Mar 1998
(Potential)

MOSART

- 3-D Atmosphere Characterization
  - Model-driven & User-defined
  - Broken Cloud Fields
  - Global Humidity Data Base (available)
- Diffuse Transmission (Off-Axis, Single Scatter) through Clouds
- Analytic (Robertson) Model of Skyshine
- Microwave/Millimeter Wave Capability
- Multiple, Overlapping Sensor Response Curves
- Higher Resolution/Expanded Terrain Material Data Base
  - New materials/higher resolution
  - FACC interface
- Global Snow Cover & Sea Ice Data Bases (available)
- Cooling Rate Calculations
- More Flexible Input File Structure

▨ Exists

12

9 June, 1997

Feature and Attribute Coding Catalogue

USAR

- **A: Culture**
  - Extraction
  - Disposal
  - Processing Industry
  - Power Generation
  - Fabrication Industry
  - Associated Industrial Structures
  - Commercial
  - Institutional/Governmental
  - Residential
  - Agriculture
  - Recreational
  - Miscellaneous Features
  - Storage
  - Transportation - Railroad
  - Transportation - Roads
  - Associated Transportation
  - Air Traffic Services
  - Communication/Transmission
  - Airport

- **B: Hydrography**
  - Coastal Hydro
  - Ports and Harbors
  - NAVAIDS
  - Dangers/Hazards
  - Depth Information
  - Bottom Features
  - Tide and Current Information
  - Inland Water
  - Miscellaneous Inland Water.
  - Snow/Ice

- **C: Hypsography**
  - Relief Portrayal

- **D: Physiography**
  - Exposed Surface Material
  - Landform

9 June, 1997

Feature and Attribute Coding Catalogue

- **E: Vegetation**
  – Cropland
  – Rangeland
  – Woodland
  – Wetlands
  – Miscellaneous Vegetation

- **F: Demarcation**
  – Boundaries/Limits/Zones (Topographic)
  – Boundaries/Limits/Zones (Aeronautical)
  – Boundaries/Limits/Zones (Hydrographic)

- **G: Aeronautical Information**
  – Air Route
  – Aerodrome

- **I: Cadastral**
  – Areas
  – Reference points
  – Special Characteristics

- **S: Special Use** (Dataset-specific)
  – Terrain Analysis Dataset
  – Background Display Dataset
  – Transportation and Logistics Dataset
  – Aeronautical Information Dataset
  – Toponymic Dataset
  – Simulation Dataset
  – Dataset Development

- **Z: General**
  – Annotation
  – Control Points
  – Magnetic Variation
  – Miscellaneous
  – Background Features

9 June, 1997

20th Annual Atmospheric Transmission Conference
10-12 June 1997, Hanscom AFB, MA

14

Points of Contact

- **To Obtain Code:**

  Dr. Laila S. Jeong (AFRL/GPOS)

  (617) 377-3671

  jeong@plh.af.mil
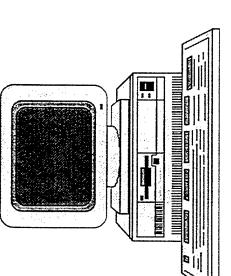
- **Technical Questions:**

  Dr. William M. Cornette (NIMA/SRT)

  (301) 227-3492

  CornetteW@nima.mil

- **Bug Reports:**

  Ms Sally J. Westmoreland (PRA)

  (619) 455-9741

  mosart@photon.com

9 June, 1997

20th Annual Atmospheric Transmission Conference
10-12 June 1997, Hanscom AFB, MA

17

A personal message:

While we all miss Frank Kneizys, we all miss him differently.

His calm manner and great intellect propelled the codes for
over a decade. Without Frank there would be no MODTRAN. He realized
how important it is to have a moderate resolution quick code.

Frank also co-claimed responsibility for the birth of FASCODE. He
even had back-of-the-napkin sketches of the original deconvolution. The
collaboration between Tony Clough and Frank on the invention of FASCODE
appeared to be a constant struggle towards excellence in science, and sometimes
even a constant struggle. Tony and Frank worked so well together.

The Geophysics Lab has products to be proud of because of their work.
Each year hundreds of new people discover that most of their problems
have already been solved. About 500 copies of MODTRAN are picked up from
our web site each year.

Frank's death came as a great shock to us. We saw him not long before
his death and he seemed fine. I miss him most as a friend. Someone to walk
with during lunch, trading jokes and stories of family. He was one of my
mentors and my friend. He can never be replaced. I will always remember him.

Jim Chetwynd

aer

PHILLIPS LABORATORY

Frank Kneizys:

Reflections on a Colleague and Friend

Tony Clough

Atmospheric and Environmental Research, Inc.

9 June 1997

Characterized by

Integrity

Humor

Intelligence

Kindness

Modesty   (to a fault ??)

Faithfulness

Breadth of Interest

Unflappable

Highly Principaled

Frank's Contribution to our Language:

It's a Louis

Good Enough for Government Work

First Check the Spark Plugs

Scooped Again

Blowout Patch

New Cement

Back of the Envelope / Front of the Napkin

Quantum Mechanical Engineering

People that Interested Him

Moe Berg

Bill Lee

Earl Weaver
} Baseball

Heisenberg

Dirac

94

Coriolis Interaction in the ν_1 and ν_3 Fundamentals of Ozone

Shepard A. Clough and Francis X. Kneizys

Air Force Cambridge Research Laboratories, Bedford, Massachusetts

(Received 4 October 1965)

The ν_1 and ν_3 vibration rotation spectrum of $^{16}O_3$ in the 9.0-μ region has been analyzed. The two vibrational states are coupled through a Coriolis term, $iY_{13}P_y$, and a second-order distortion term, $-X_{13}(P_zP_z+P_zP_z)$, in the Hamiltonian. The interaction has been treated by numerically diagonalizing the secular determinant for the two states with the coupling included. The effect of the interaction on the intensities has been considered and absorption contours calculated in satisfactory agreement with experiment. With the distortion parameters fixed to the ground-state values the following constants have been obtained: $\nu_1=1103.15_7$, $A_1=3.556_9$, $B_1=0.4427_3$, $C_1^*=0.3926_9$, $A_3=3.500_4$, $B_3=0.4412_6$, $C_3^*=0.3909$, $Y_{13}=-0.46_6$, and $X_{13}=-0.009_8$ cm^{-1}. The value of the dipole-moment ratio,

$$\left(\frac{\partial M_z}{\partial Q_3}\bigg|_0 Q_3\right)\bigg/\left(\frac{\partial M_z}{\partial Q_1}\bigg|_0 Q_1\right),$$

is 10.0±1.5.

Reduction of the Fourth-Order Asymmetric-Rotor Hamiltonian

F. X. Kneizys, J. N. Freedman,* and S. A. Clough

Air Force Cambridge Research Laboratories, Bedford, Massachusetts

(Received 1 November 1965)

By use of the angular-momentum commutation relations, the fourth-order asymmetric-rotor Hamiltonian for molecules of orthorhombic symmetry has been considerably simplified. The number of rotational coefficients has been reduced to 19: three coefficients of second power, six coefficients of the fourth power, and 10 coefficients of sixth power in the angular momentum.

1. INTRODUCTION

IN a recent series of papers,[1-3] Chung and Parker, using the formalism of Nielsen, Amat, and Goldsmith,[4-8] have explicitly derived the fourth-order contribution of all terms in the asymmetric-rotor Hamiltonian. From their results, it is now possible for the first time to give theoretical significance to coefficients up to the sixth power in the angular momentum. The results of Chung and Parker were obtained by applying symmetry arguments to the coefficients of the asymmetric-rotor Hamiltonian. In this paper, we show that by use of the angular-momentum commutation relations, the asymmetric-rotor Hamiltonian of orthorhombic symmetry can be reduced to a simpler form. The reduced Hamiltonian simplifies computation of rotational energies and makes data analysis of higher-order rotational constants practical.

2. HAMILTONIAN FOR THE ORTHORHOMBIC POINT GROUPS

The Hamiltonian of an asymmetric rotor of orthorhombic symmetry in the III^r representation[9] is of the following form:

$$H^\dagger = h_v{}^{\dagger *} + \mathfrak{A} P_x{}^2 + \mathfrak{B} P_y{}^2 + \mathfrak{C} P_z{}^2$$
$$+ \tfrac{1}{4} \sum_{\alpha\beta\gamma\delta} (\tau_{\alpha\beta\gamma\delta} + \rho_{\alpha\beta\gamma\delta}) P_\alpha P_\beta P_\gamma P_\delta$$
$$+ \sum_{\alpha\beta\gamma\delta\epsilon\eta} [\alpha\beta\gamma\delta\epsilon\eta] P_\alpha P_\beta P_\gamma P_\delta P_\epsilon P_\eta, \quad (1)$$

where $h_v{}^{\dagger *}$, $\mathfrak{A}$, $\mathfrak{B}$, $\mathfrak{C}$, $\tau_{\alpha\beta\gamma\delta}$, and $\rho_{\alpha\beta\gamma\delta}$ are those of Chung and Parker[1] and $[\alpha\beta\gamma\delta\epsilon\eta]$ are the sixth-power distortion coefficients of Chung and Parker.[2,3] The term $h_v{}^{\dagger *}$ represents the vibrational contribution to the Hamiltonian; $\mathfrak{A}$, $\mathfrak{B}$, and $\mathfrak{C}$ are the effective rotational con-

* Present address: Department of Physics, University of Chicago, Chicago, Illinois.
[1] K. T. Chung and P. M. Parker, J. Chem. Phys. 38, 8 (1963).
[2] K. T. Chung and P. M. Parker, J. Chem. Phys. 43, 3865 (1965).
[3] K. T. Chung and P. M. Parker, J. Chem. Phys. 43, 3869 (1965).
[4] M. Goldsmith, G. Amat, and H. H. Nielsen, J. Chem. Phys. 24, 1178 (1956).
[5] M. Goldsmith, G. Amat, and H. H. Nielsen, J. Chem. Phys. 27, 838 (1957).
[6] G. Amat and H. H. Nielsen, J. Chem. Phys. 27, 845 (1957).
[7] G. Amat and H. H. Nielsen, J. Chem. Phys. 29, 665 (1958).
[8] G. Amat and H. H. Nielsen, J. Chem. Phys. 36, 1859 (1962).
[9] G. W. King, R. M. Hainer, and P. C. Cross, J. Chem. Phys. 11, 27 (1943). In order to be consistent with the formalism of Chung and Parker, the III^r representation has been used throughout this work. However, the results of this paper can be generalized to any representation by the appropriate reidentification of the rotational constants with x, y, z axes in the manner discussed by King, Hainer, and Cross.

stants to fourth order; $\tau_{\alpha\beta\gamma\delta}$ have the definition of the second-order distortion constants of Kivelson and Wilson[10]; and $\rho_{\alpha\beta\gamma\delta}$ are the fourth-order corrections to $\tau_{\alpha\beta\gamma\delta}$. For the case of orthorhombic symmetry, there are nine independent $\tau_{\alpha\beta\gamma\delta}$,[10] 15 nonvanishing $\rho_{\alpha\beta\gamma\delta}$,[1] and 105 $[\alpha\beta\gamma\delta\epsilon\eta]$.[2]

By the use of the commutation relations for angular momentum,

$$P_\alpha P_\beta - P_\beta P_\alpha = -i\hbar P_\gamma \quad (2)$$

(where α, β, γ are in cyclic order), and with the appropriate redefinition of coefficients, considerable simplification can be made in the Hamiltonian. The transformed Hamiltonian consists of three coefficients of second power, six coefficients of the fourth power,[11] and 10 coefficients of sixth power in the angular momentum.[12] The new form of $H^\dagger$ is

$$H^\dagger = h_v{}^{\dagger *} + A P_x{}^2 + B P_y{}^2 + C P_z{}^2$$
$$+ T_1 P_x{}^4 + T_2 P_y{}^4 + T_3 P_z{}^4 + T_4(P_y{}^2 P_z{}^2 + P_z{}^2 P_y{}^2)$$
$$+ T_5(P_z{}^2 P_x{}^2 + P_x{}^2 P_z{}^2) + T_6(P_x{}^2 P_y{}^2 + P_y{}^2 P_x{}^2)$$
$$+ \Phi_1 P_x{}^6 + \Phi_2 P_y{}^6 + \Phi_3 P_z{}^6 + \Phi_4(P_x{}^2 P_y{}^4 + P_y{}^4 P_x{}^2)$$
$$+ \Phi_5(P_y{}^2 P_x{}^4 + P_x{}^4 P_y{}^2) + \Phi_6(P_y{}^2 P_z{}^4 + P_z{}^4 P_y{}^2)$$
$$+ \Phi_7(P_z{}^2 P_y{}^4 + P_y{}^4 P_z{}^2) + \Phi_8(P_z{}^2 P_x{}^4 + P_x{}^4 P_z{}^2)$$
$$+ \Phi_9(P_x{}^2 P_z{}^4 + P_z{}^4 P_x{}^2) + \Phi_{10}(P_x{}^2 P_y{}^2 P_z{}^2 + P_z{}^2 P_y{}^2 P_x{}^2), \quad (3)$$

where

$$A = \mathfrak{A} + \tfrac{1}{4}\hbar^2(3\tau_4 - 2\tau_5 - 2\tau_6 + \rho_7 - \rho_8 - \rho_9$$
$$+ \rho_{10} + \rho_{11} - \rho_{12} - \rho_{15}) + \hbar^4 \Phi_{17},$$
$$B = \mathfrak{B} + \tfrac{1}{4}\hbar^2(3\tau_8 - 2\tau_9 - 2\tau_7 - \rho_7 + \rho_8 - \rho_9$$
$$- \rho_{10} + \rho_{12} + \rho_{13} - \rho_{14}) + \hbar^4 \Phi_{18},$$
$$C = \mathfrak{C} + \tfrac{1}{4}\hbar^2(3\tau_7 - 2\tau_8 - 2\tau_9 - \rho_7 - \rho_8 + \rho_9$$
$$- \rho_{11} - \rho_{13} + \rho_{14} + \rho_{15}) + \hbar^4 \Phi_{19},$$
$$T_1 = \tfrac{1}{4}(\tau_1 + \rho_1) + \hbar^2 \Phi_{11},$$
$$T_2 = \tfrac{1}{4}(\tau_2 + \rho_2) + \hbar^2 \Phi_{12},$$
$$T_3 = \tfrac{1}{4}(\tau_3 + \rho_3) + \hbar^2 \Phi_{13},$$
$$T_4 = \tfrac{1}{4}(\tau_4 + 2\tau_7 + \rho_4 + \rho_7 + \tfrac{1}{2}\rho_{10} + \tfrac{1}{2}\rho_{11}) + \hbar^2 \Phi_{14},$$
$$T_5 = \tfrac{1}{4}(\tau_5 + 2\tau_8 + \rho_5 + \rho_8 + \tfrac{1}{2}\rho_{12} + \tfrac{1}{2}\rho_{13}) + \hbar^2 \Phi_{15},$$
$$T_6 = \tfrac{1}{4}(\tau_6 + 2\tau_9 + \rho_6 + \rho_9 + \tfrac{1}{2}\rho_{14} + \tfrac{1}{2}\rho_{15}) + \hbar^2 \Phi_{16}. \quad (4)$$

[10] D. Kivelson and E. B. Wilson, Jr., J. Chem. Phys. 20, 1575 (1952).
[11] W. B. Olson and H. C. Allen, Jr., J. Res. Natl. Bur. Std. (U.S.) Ser. A 67, 359 (1963).
[12] L. Pierce, N. DiCianni, and R. H. Jackson, J. Chem. Phys. 38, 730 (1963).

2552

Convolution algorithm for the Lorentz function

Shepard A. Clough and Francis X. Kneizys

An algorithm for the accelerated convolution of the Lorentz function with spectral line-data has been developed. The method involves the decomposition of the Lorentz function into subfunctions spanning finite domains. The subfunctions are convolved independently with line data at appropriate sampling intervals. The spectral absorption is obtained by superposition of the independent convolutions. A criterion for the specification of the sampling interval is described.

Atmospheric spectral transmittance and radiance: FASCOD1B

S. A. Clough, F. X. Kneizys, L. S. Rothman, W. O. Gallery

Air Force Geophysics Laboratory
Hanscom Air Force Base, Massachusetts 01731

Abstract

A model and computer code, FASCODE1 (Fast Atmospheric Signature Code) has been developed for the line-by-line calculation of radiance and transmittance with particular applicability to the earth's atmosphere. An algorithm for the accelerated convolution of line shape functions (Lorentz, Voigt and Doppler) with spectral line data is used. The contribution from continuum absorption is included in the model. The method is described and applications of the present code, FASCOD1B, are presented.

Air Mass Computer Program for Atmospheric Transmittance/Radiance Calculation: FSCATM

W. O. GALLERY
F. X. KNEIZYS
S. A. CLOUGH

9 March 1983

OPTICAL PHYSICS DIVISION   PROJECT 7670

AIR FORCE GEOPHYSICS LABORATORY

HANSCOM AFB, MASSACHUSETTS 01731

AIR FORCE SYSTEMS COMMAND, USAF

Line Shape and the Water Vapor Continuum

S.A. CLOUGH, F.X. KNEIZYS and R.W. DAVIES

Atmospheric and Environmental Research, Inc., Cambridge, MA 02139 (U.S.A.)
Air Force Geophysics Laboratory, Hanscom AFB, MA 01731 (U.S.A.)
GTE Laboratories, Waltham, MA 02154 (U.S.A.)

(Received May 1, 1988; accepted June 1, 1989)

ABSTRACT
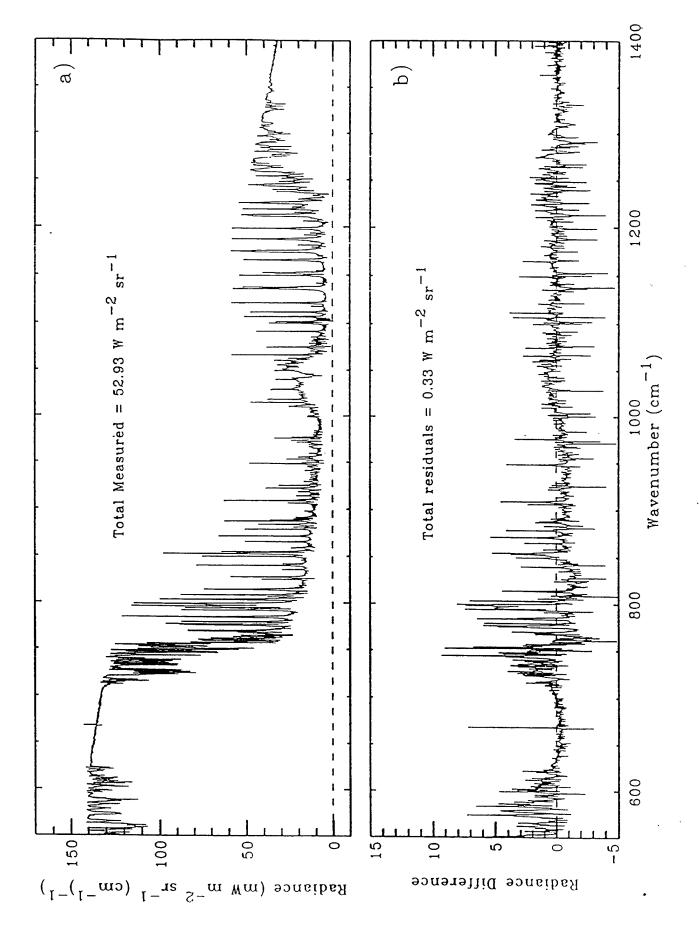
Clough, S.A., Kneizys, F.X. and Davies, R.W., 1989. Line shape and the water vapor continuum. Atmos. Res., 23: 229–241.

A formulation is developed in which the contribution of the far wings of collisionally broadened spectral lines to the water vapor continuum absorption is established. The effects of deviations from the impact (Lorentz) line shape due to duration of collision effects are treated semi-empirically to provide agreement with experimental results for the continuum absorption and its temperature-dependence. The continua due to both water–water molecular broadening (self-broadening) and water–air molecular broadening (foreign broadening) are discussed. Several atmospheric validations of the present approach are presented.

Atmospheric Continuum Absorption of Oxygen in the Near Infrared

Eli J. Mlawer, Shepard A. Clough, and Patrick D. Brown
Atmospheric and Environmental Research, Inc., Cambridge, Massachusetts

Thomas M. Stephen, Joseph C. Landry, Aaron Goldman, and Frank J. Murcray
Physics Department, University of Denver, Denver, Colorado

a) Total Measured = 52.93 W m^{-2} sr^{-1}

b) Total residuals = 0.33 W m^{-2} sr^{-1}

Radiance (mW m^{-2} sr^{-1} (cm^{-1})$^{-1}$)

Radiance Difference

Wavenumber (cm^{-1})

102

Reports of Discrepancies between Measurement and Models in the Shortwave

Clear sky

◆ Barker and Li (1995): 25 W/m^2

◆ Arking (1996): 25 W/m^2 - differences correlated with water vapor column amount

◆ Kato et al. (1997): 5-10 W/m^2 - direct beam; 15-20 W/m^2 - diffuse beam

Cloudy sky
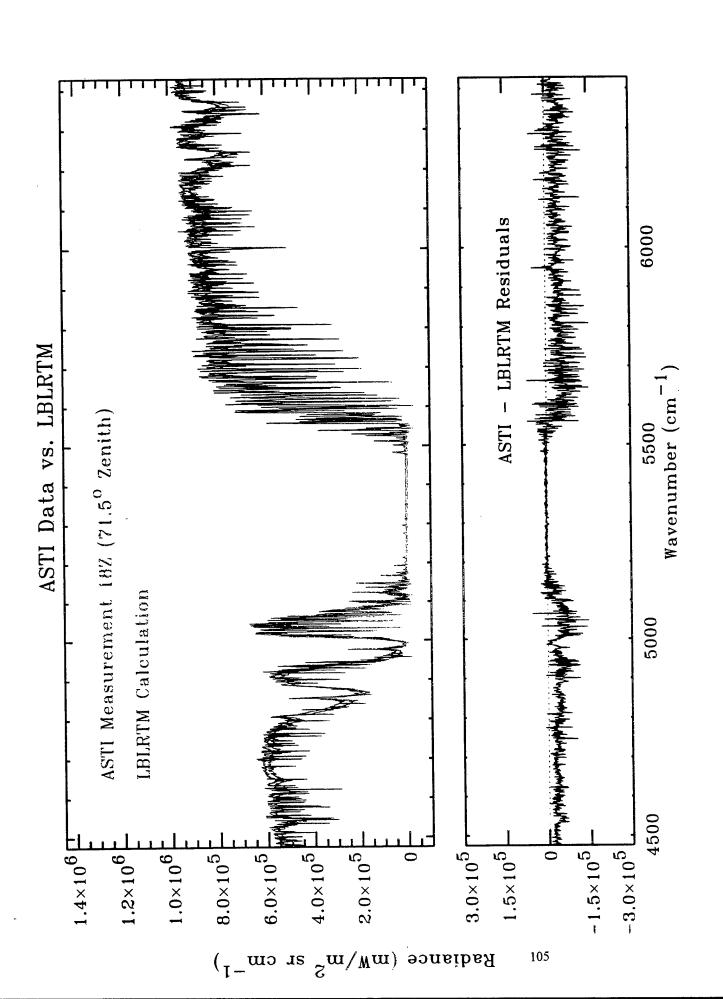
◆ Cess et al. (1995): 25 W/m^2 - consistent at all latitudes
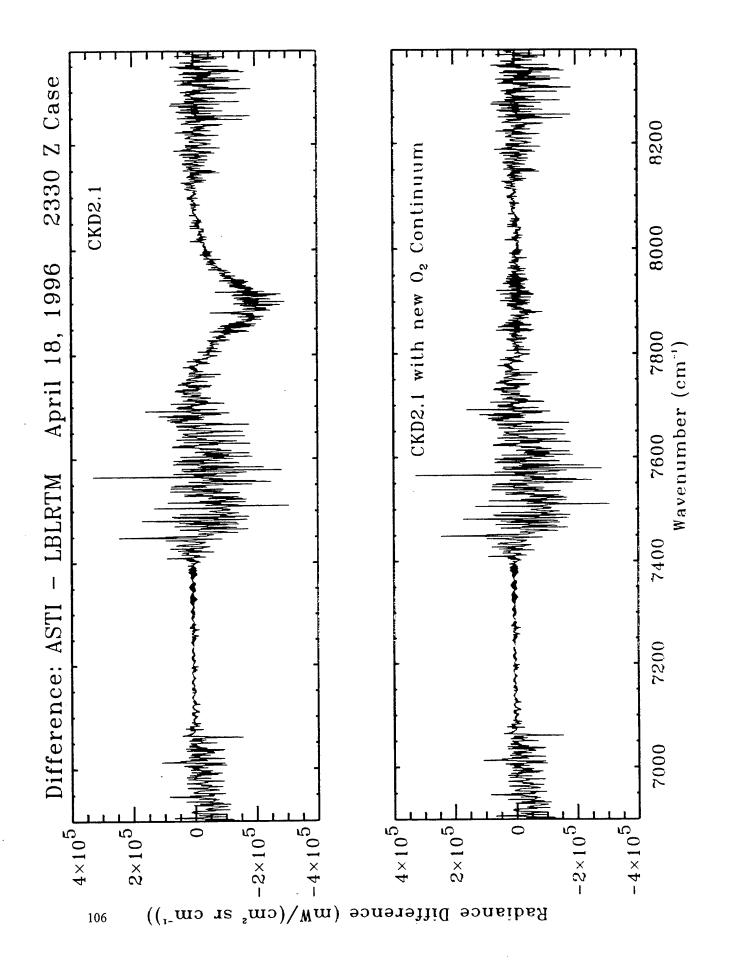
◆ Li et al. (1995): smaller effect than in Cess et al., varying with latitude, time of year
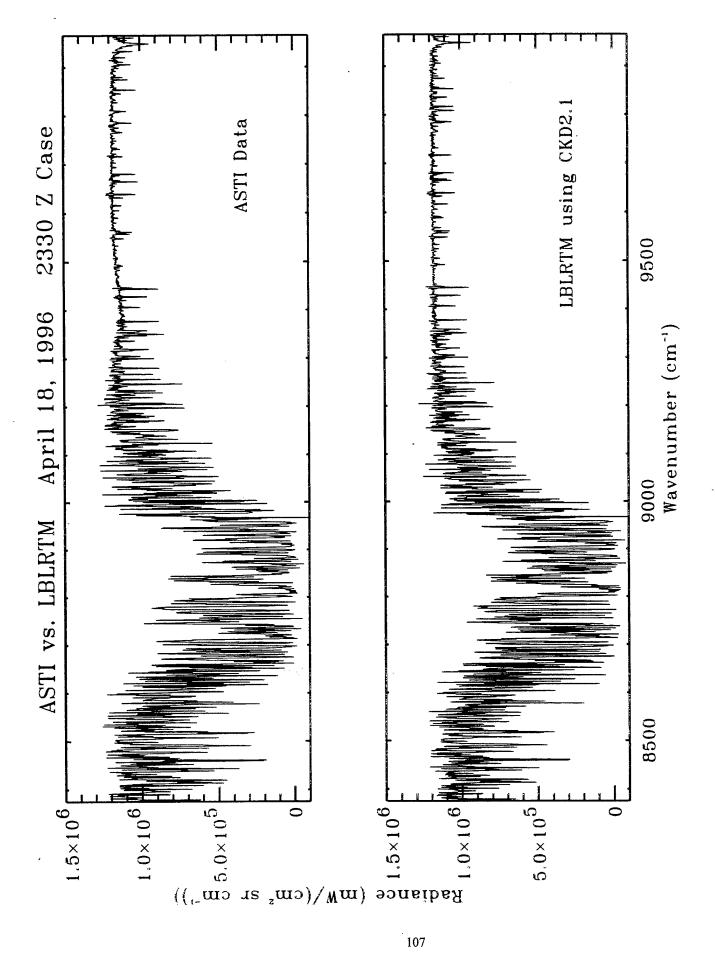
◆ Francis et al. (1997): "no evidence of enhanced cloud absorption"

103
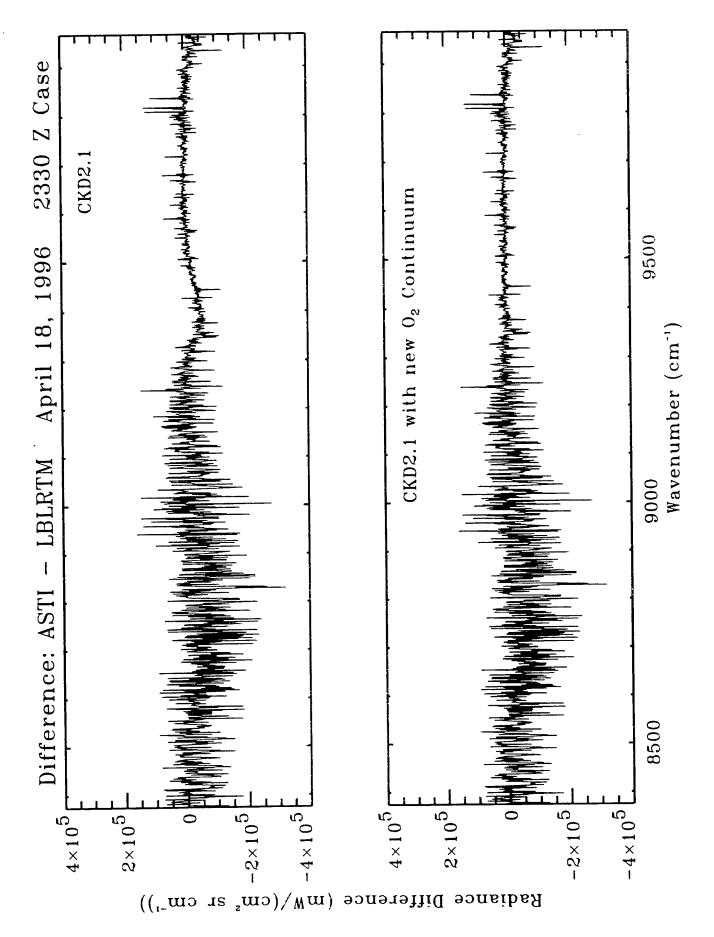
Absolute Solar Transmittance Interferometer (ASTI)
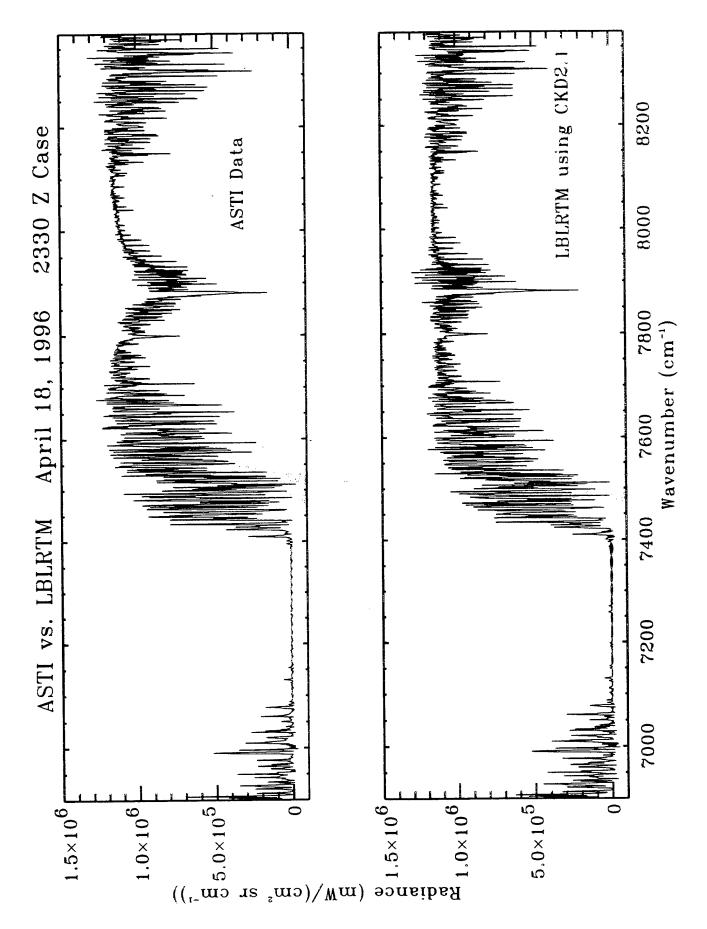
- Developed at the University of Denver (F. Murcray)

- Same type of interferometer as Atmospheric Emitted Radiance Interferometer (AERI)

- Spectral range: 2000-10000 cm^{-1}

- Spectral resolution: 0.6 cm^{-1} (HWHM)

- Measures spectral radiance from narrow field of view (central 16% of solar disk)

- Calibrated using tungsten lamp with maximum temperature of 2800 K

ASTI Data vs. LBLRTM

ASTI Measurement 18Z (71.5° Zenith)

LBLRTM Calculation

ASTI − LBLRTM Residuals

Wavenumber (cm^{-1})

Radiance (mW/m^2 sr cm^{-1})

105

Difference: ASTI − LBLRTM   April 18, 1996   2330 Z Case

CKD2.1

CKD2.1 with new O_2 Continuum

Wavenumber (cm⁻¹)

Radiance Difference (mW/(cm² sr cm⁻¹))

ASTI vs. LBLRTM   April 18, 1996   2330 Z Case

ASTI Data

LBLRTM using CKD2.1

Radiance (mW/(cm² sr cm⁻¹))

Wavenumber (cm⁻¹)

Difference: ASTI – LBLRTM   April 18, 1996   2330 Z Case

CKD2.1

CKD2.1 with new O_2 Continuum

Wavenumber (cm^{-1})

Radiance Difference ($mW/(cm^2$ sr cm^{-1}))

ASTI vs. LBLRTM   April 18, 1996   2330 Z Case

ASTI Data

LBLRTM using CKD2.1

Radiance (mW/(cm² sr cm⁻¹))

Wavenumber (cm⁻¹)

Properties of the continuum and discrete absorption bands due to the three strongest O_2 $a^1\Delta_g \leftarrow X^3\Sigma_g^-$ transitions

Band center	Continuum bands only (determined by least-squares fit)				Discrete bands only [Gamache et al., 1997]
	*Peak absorption coefficient, cm^2/molec	*Band intensity, cm^{-1} (cm^2/molec)	Half width, cm^{-1}	Solar flux absorbed, W/m^2	Band intensity, cm^{-1} (cm^2/molec)
7882 cm^{-1} (0←0)	3.17×10^{-26}	3.81×10^{-24}	50	0.57	[†]3.692×10^{-24}
9366 cm^{-1} (1←0)	6.56×10^{-27}	1.15×10^{-24}	76	0.21	[††]1.280×10^{-26}
6326 cm^{-1} (0←1)	4.98×10^{-27}	1.64×10^{-25}	17	0.05	[††]2.755×10^{-28}

* for atmospheric abundances, normalized to 296K and 1 atm.
[†] both $^{16}O^{16}O$ and $^{16}O^{18}O$
[††] only $^{16}O^{16}O$

Conclusions

1. No evidence of large discrepancies between ASTI radiances and LBLRTM calculations for spectral range 3000-10000 cm^{-1}

2. Solar flux absorbed by three strongest $a^1\Delta_g \leftarrow X^3\Sigma_g^-$ continuum bands of O_2 is 0.42 W/m^2 (global average)

3. Unmodeled (i.e. continuum) absorption due to O_2 in near infrared, visible, and near ultraviolet regions is unlikely source of 'shortwave anomaly'

20th Annual DoD Atmospheric Radiance and Transmittance Meeting,
Hanscom AFB, 10-12 June, 1997

Accelerated line-by-line calculation
of absorption coefficients with high
numerical accuracy

Martin Kuntz
Institut für Meteorologie und Klimaforschung
Forschungszentrum Karlsruhe

    ⊚ Introduction

    ⊚ Efficient calculation of the Voigt profile function

    ⊚ Determination of frequency spacing

    ⊚ Summation of spectral lines

    ⊚ Performance

    ⊚ Conclusion

Introduction

In practice calculating absorption coefficients proves to be the dominant computational expense of a line-by-line radiative transfer model (requires up to 90 % of execution time).

$$\sigma_g(T,p,\nu) = \rho_g \sum_{n=1}^{N_g} \underbrace{A_{gn}(T)}_{\text{line strength}} \quad \underbrace{\Phi_{gn}(T,p,\nu)}_{\text{profile function}}$$
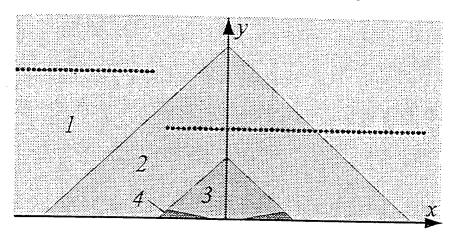
Three questions that need to be clarified

◉   How to calculate the profile function most efficiently? (which algorithm?)

◉   Where to calculate the profile function most efficiently? (at which sampling points?)

◉   How to perform the summation most efficiently?

Efficient calculation of the Voigt profile function

Humlicek-Algorithm:

- Divides x,y-space into several regions where complex rational polynomials are adequate within a given error

Optimizations:

- Reduce if-inquiries applying a recursive algorithm
  before: $\sim 2\,n$ afterwards: $\sim 2\,log_2\,n$

- Calculate only the real part of the complex Voigt profile function
  before: $\sim 75\,Flops$ afterwards: $\sim 19\,Flops$

- Automatically switch to the calculation of the Lorentzian function where permissible

- Accelerated calculation if y remains constant
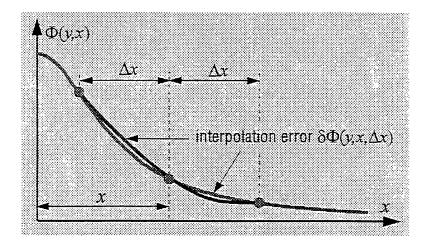
Performance:

- Factor: ~ 4.7 for rel. accuracy: $\sim 2\,10^{-6}$
  Factor: ~ 6 for rel. accuracy: $\sim 10^{-4}$

Determination of frequency spacing

idea: Calculate each spectral line as accurate as necessary in view of the desired absolute accuracy and interpolate the intermediate values, e.g. by a second order polynomial.

problem: Interpolation error $\delta\Phi(y, x, \Delta x)$ depends on the distance from line center x and the frequency spacing Δx
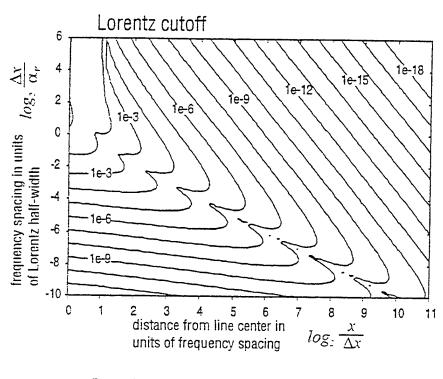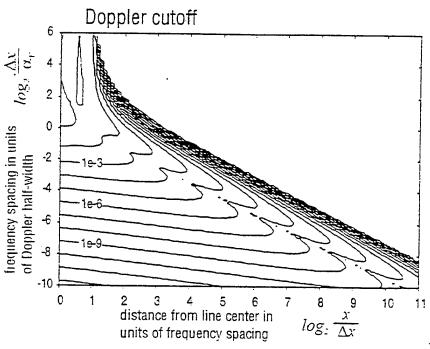
solution:
⊛ Determine the highest permissible interpolation error for a given line while retaining an absolute accuracy $\delta\sigma$
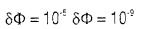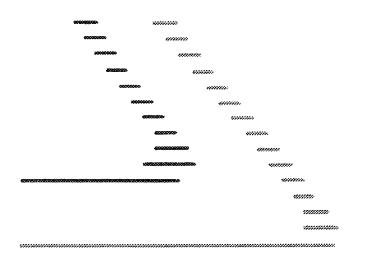
$$\delta\Phi_{gn}(y, x, \Delta x) = \frac{\delta\sigma}{\rho_g A_{gn}}$$

⊛ Determine Δx in such a way that the permissible interpolation error $\delta\Phi$ is not violated!

Determination of frequency spacing

Lorentz cutoff

distance from line center in units of frequency spacing

$log_2 \frac{x}{\Delta x}$

Doppler cutoff

distance from line center in units of frequency spacing

$log_2 \frac{x}{\Delta x}$

$$\delta\Phi = 10^{-5} \quad \delta\Phi = 10^{-9}$$

$$\delta\Phi = 10^{-5} \quad \delta\Phi = 10^{-9}$$

117

Determination of frequency spacing

Voigt cutoffs for different parameters y
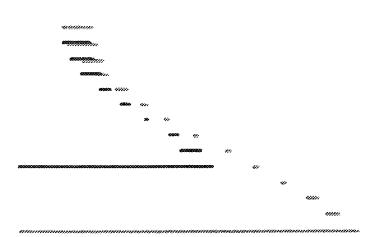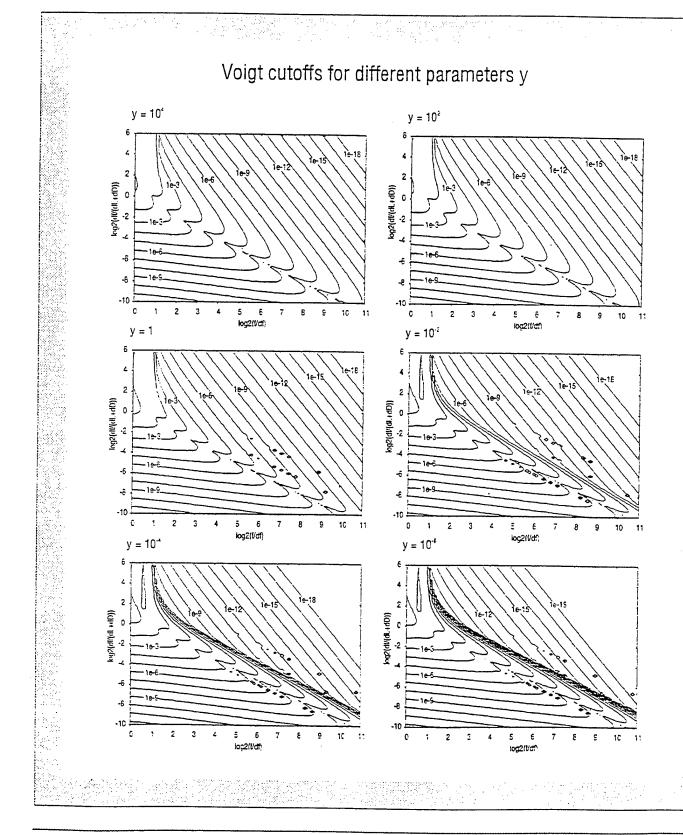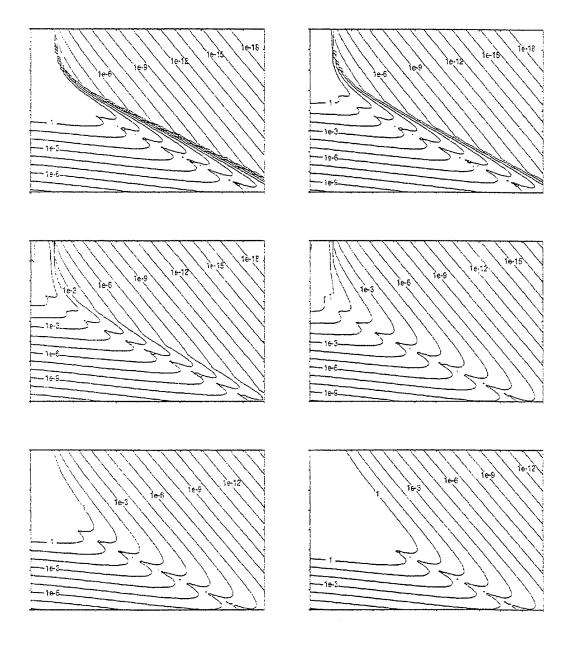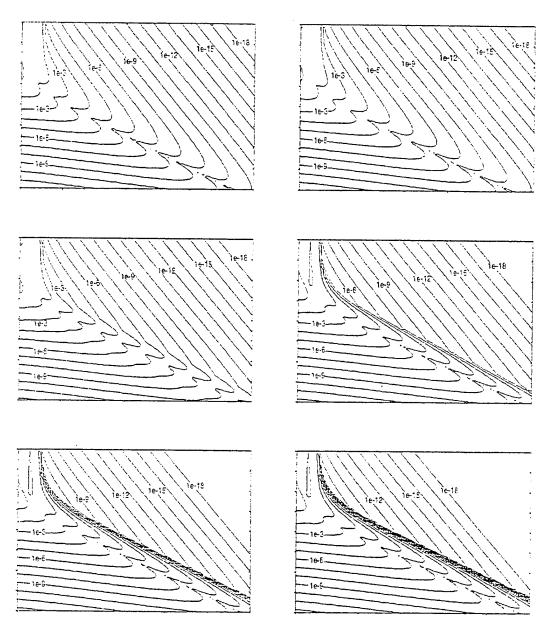
Approximation by Sparks
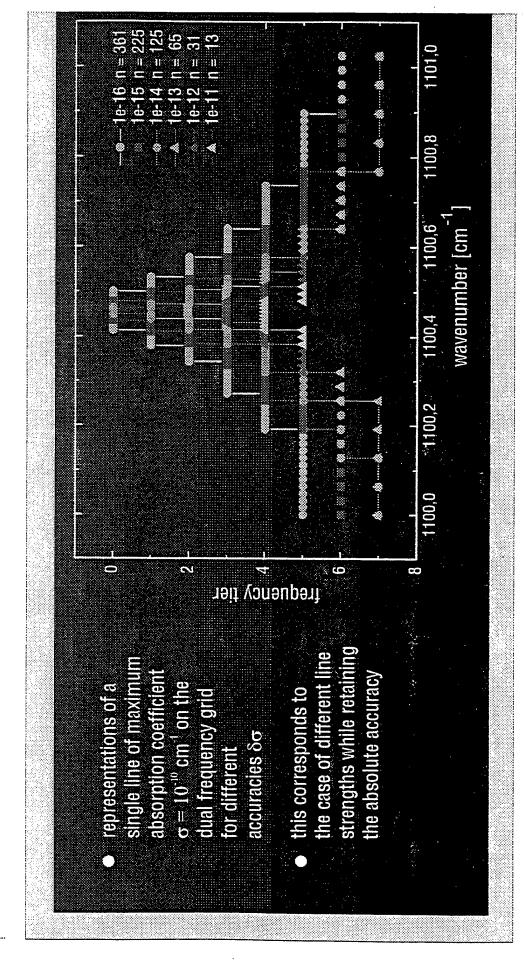
Combination of Doppler and Lorentz cutoffs
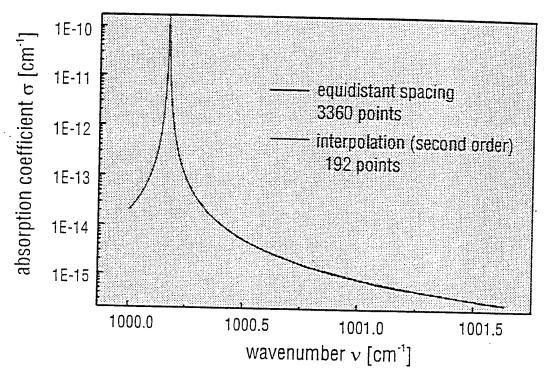
Forschungszentrum Karlsruhe
Technik und Umwelt

Determination of frequency spacing

- representations of a single line of maximum absorption coefficient $\sigma = 10^{-10}$ cm^{-1} on the dual frequency grid for different accuracies $\delta\sigma$

- this corresponds to the case of different line strengths while retaining the absolute accuracy
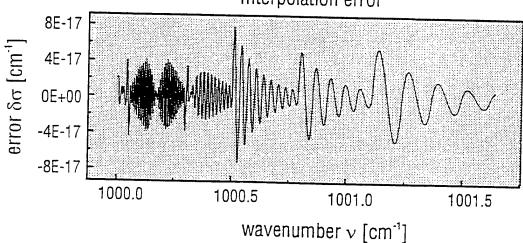
Determination of frequency spacing

Absorption coefficient

Legend:
- equidistant spacing 3360 points
- interpolation (second order) 192 points

Interpolation error

Kuntz IMK-AME 106
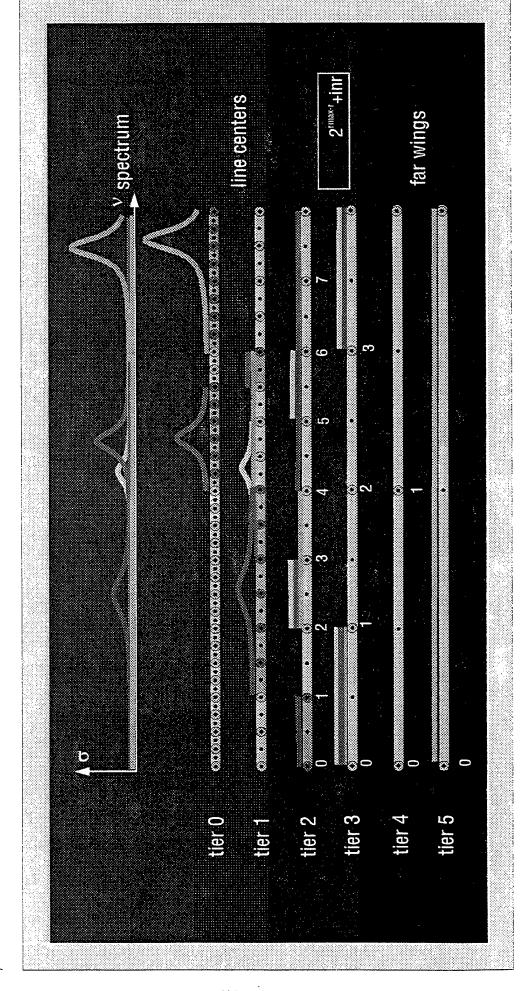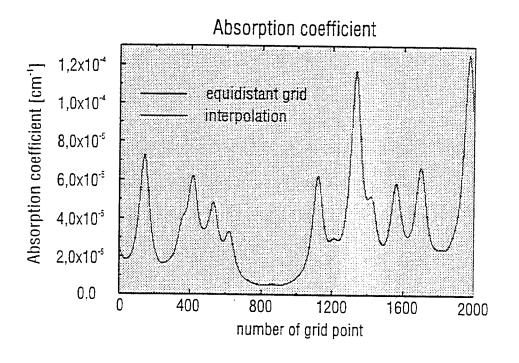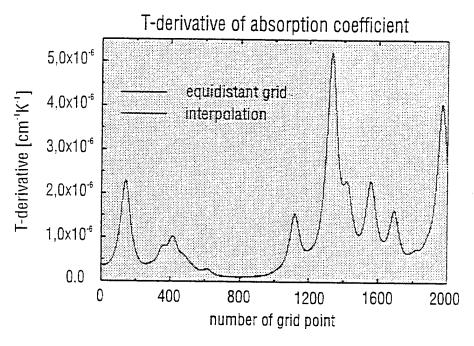
Forschungszentrum Karlsruhe
Technik und Umwelt

Summation of spectral lines

Summation of spectral lines

Absorption coefficient

T-derivative of absorption coefficient

Performance

- Microwindow of width $1\,cm^{-1}$

- 10 000 lines +/-5 cm^{-1} around the microwindow
  of which ~ 5000 lines were calculated

- Accuracy: $\delta\sigma = 10^{-9}cm^{-1}$

height	$\Delta\nu = 5\,10^{-4}\,cm^{-1}$		$\Delta\nu = 1\,10^{-4}\,cm^{-1}$	
	equidistant	new	equidistant	new
12km	142.6s	1.43s	218.4s	1.48s
24km	157.7s	1.48s	391.7s	1.59s
36km	158.0s	1.54s	745.3s	2.23s
48km	148.7s	1.43s	632.7s	2.15s
60km	128.5s	1.31s	432.7s	1.71s
72km	---	---	253.8s	1.31s

- Calculations performed with different accuracies
  ($\Delta\nu = 1\,10^{-4}cm^{-1}$, height = 72km)

accuracy	time	memory
$10^{-9}\,cm^{-1}$	1.31s	48.9%
$10^{-10}cm^{-1}$	2.03s	77.7%
$10^{-11}cm^{-1}$	2.72s	92.6%
$10^{-12}cm^{-1}$	3.46s	98.0%
$10^{-13}cm^{-1}$	4.39s	99.5%

Conclusion

Advantages:

◎ each spectral line is calculated as accurate as necessary in view of the desired numerical accuracy

◎ numerical accuracy can be varied continuously during running time (e.g. can be easily increased in an iterative procedure)

◎ it is in principle possible to calculate error bars

◎ algorithm may be readily applied to alternative line shape models

◎ increasing the spectral resolution does not necessarily imply a higher computational workload (only some additional interpoations)

◎ improved algorithm for the calculation of the Voigt profile function

◎ improved frequency spacing for the representation of the Voigt profile function

◎ T-derivative of absorption coefficient is calculated simultaneously

◎ sampling intervals can be varied continuously

◎ nonequidistant (quasi-equidistant) frequency spacing
     - saving of valuable computer memory
     - improves computational efficiency of the radiative transfer

Disadvantages:

◎ rather complicated algorithm

◎ one additional parameter to specify

IMPROVED ACCURACY INFRARED ABSORPTION DETERMINATIONS USING THE MODIFIED KUBELKA MUNK MODEL

W. G. Egan, and Q. Alexis

Natural Sciences Department
York College/CUNY
Jamaica, NY 11451

In order to further improve the accuracy of infrared aerosol optical properties determinations, a modification to the original Kubelka-Munk scattering model was made to include the effects of sample surface reflection on the determination of absorption (i.e.the Modified Kubelka Munk Model: M-K-M). The solutions to the radiative transfer equations involved for the M-K-M model are presented graphically. The results indicate that the M-K-M model generally produces somewhat less absorption than the K-M model, but comparable to the dispersion model in high absorption regions. A plot of absorption and scattering in the complex plane reveals problems with the dispersion theory when significant scattering occurs.

(a)
$$\dot{R}_{\parallel} = \left(\frac{E_{r\parallel}}{E_{i\parallel}}\right)^2 = \left\{\frac{(\hat{m}_{i'}/\hat{m}_i)^2 \cos\hat{\theta}_i - [(\hat{m}_{i'}/\hat{m}_i)^2 - \sin^2\hat{\theta}_i]^{1/2}}{(\hat{m}_{i'}/\hat{m}_i)^2 \cos\hat{\theta}_i + [(\hat{m}_{i'}/\hat{m}_i)^2 - \sin^2\hat{\theta}_i]^{1/2}}\right\}^2 .$$

$$E_{r\parallel}/E_{i\parallel} = r e^{i\phi}$$
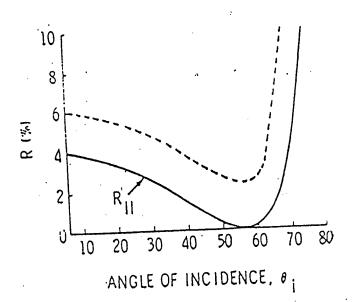
(b)
$r = |\hat{R}|^{1/2}$. The Kramers–Kronig relation links $\ln r$ to ϕ,

$$\phi(v_0) = \frac{2v_0}{\pi} \int_0^{\infty} \frac{\ln r}{v^2 - v_0^2} \, dv$$

(c)

Viewgraph I: a) Vector form of Fresnel's reflection equation
    b) Kramers-Kronig relation
    c) Plot of Kramers-Kronig relation in complex plane
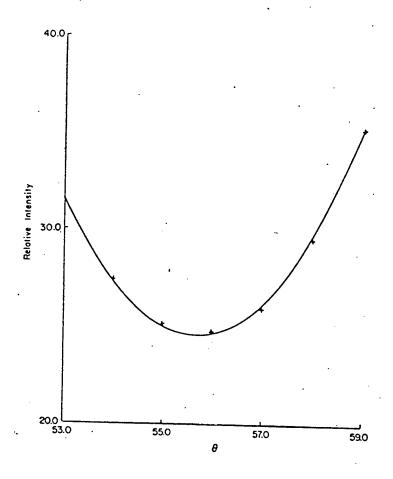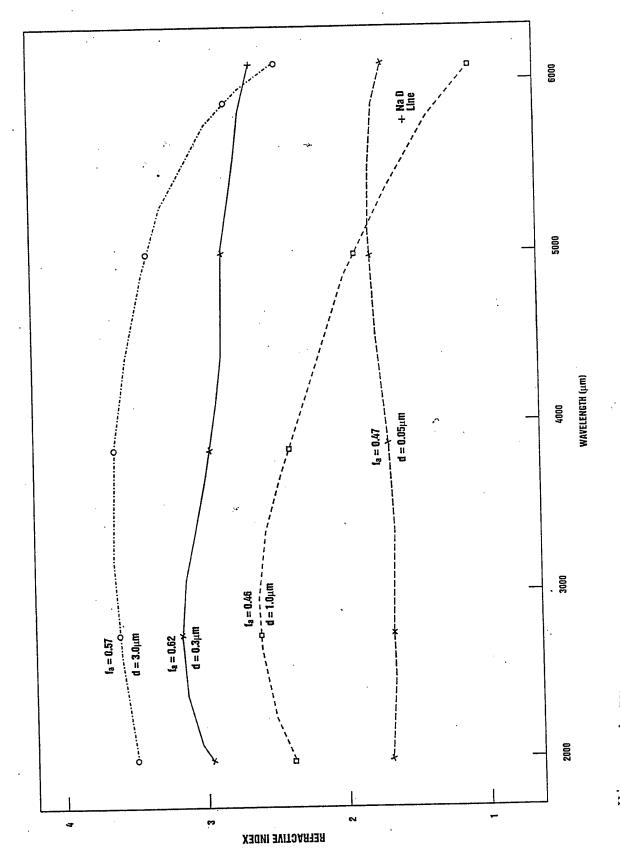
Viewgraph II: Idealized polarized reflectance from a surface:
Lower curve goes to zero at Brewster angle;
upper curve does not go to zero because of scattering
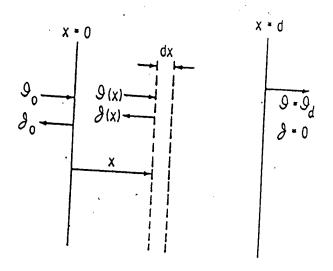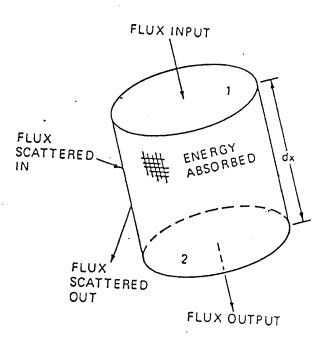
Viewgraph III: Experimental measurement of polarized reflectance
from a powdered sample of limonite ($\lambda = 0.31\mu$m);
because of scattering reflection does not go to
zero.

Viewgraph IV: Refractive indices of powdered Al_2O_3 determined by Brewster angle technique; NaD line of bulk is shown; refractive indices are a function of wavelength and particle sizes.

Viewgraph V: Upper: Geometry of original one-dimensional Kubelka-
Munk (K-M) theory
Lower: Geometry of 6-flux Modified-Kubelka-Munk
(M-K-M) theory.
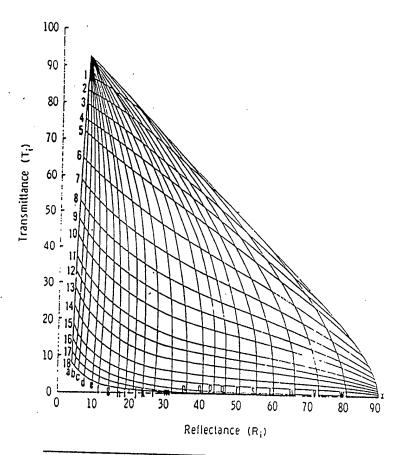
Index	Γ	Index	β	Index	Γ	Index	β
1	0.1	a	1.0	13	2.3	m	0.28
2	0.2	b	0.96	14	2.7	n	0.24
3	0.3	c	0.86	15	3.2	o	0.20
4	0.4	d	0.76	16	3.7	p	0.18
5	0.5	e	0.68	17	4.2	q	0.16
6	0.7	f	0.60	18	5.0	r	0.14
7	0.9	g	0.54			s	0.12
8	1.1	h	0.48			t	0.10
9	1.3	i	0.44			u	0.08
10	1.5	j	0.40			v	0.06
11	1.8	k	0.36			w	0.04
12	2.0	l	0.32			x	0.02

$$\Gamma = 2[\alpha(\alpha + 2\sigma)]^{1/2}d$$

$$\beta = [\alpha/(\alpha + 2\sigma)]^{1/2}$$

Viewgraph VI: Graphical solutions of M-K-M theory for index of refraction of 1.5; Transmittances (T) and Reflectances (R) are determined on powder sample embedded in Potassium Bromide matrix:enter graph with T and R; determine β and Γ ; calculate scattering (σ) and absorption (α) from lower equations.
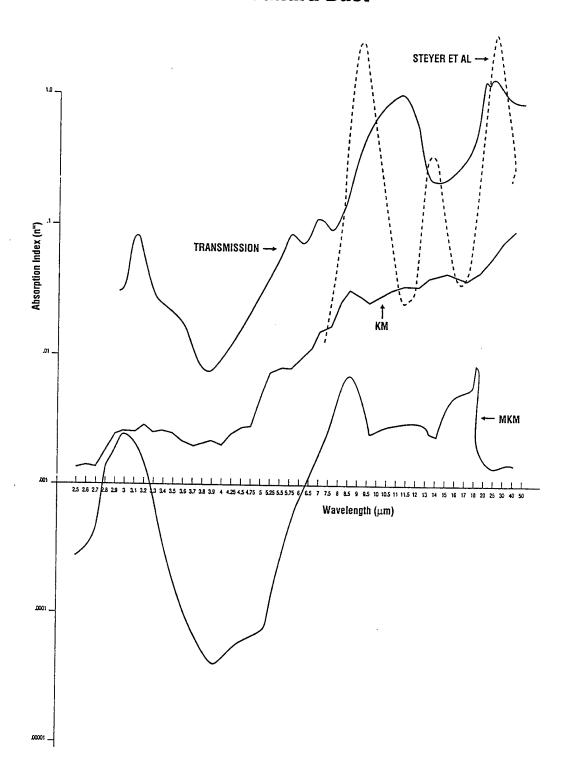
TABLE IV-2 Corning CS1-64 Glass Data Analysis

		Powder				Sintered bubble glass			
		KM		Modified KM		KM		Modified KM	
	Bulk								
$\lambda_{\mu m}$	α (cm^{-1})	α^b (cm^{-1})	s (cm^{-1})	α^b (cm^{-1})	s (cm^{-1})	α (cm^{-1})	s (cm^{-1})	$\dot{\alpha}$ (cm^{-1})	s (cm^{-1})
0.400	0.16	7.8	161	2.8	442	1.6	9.5	0.72	23
0.600	9.2	27.1	152	11.6	377	8.3	2.2	13.8	5.0
0.907	0.21	2.8	188	1.15	477	1.7	3.8	1.09	9.1
1.5	0.52	8.2	135	3.2	340	2.9	3.1	2.3	8.3

^{b} Corrected for volume fraction.
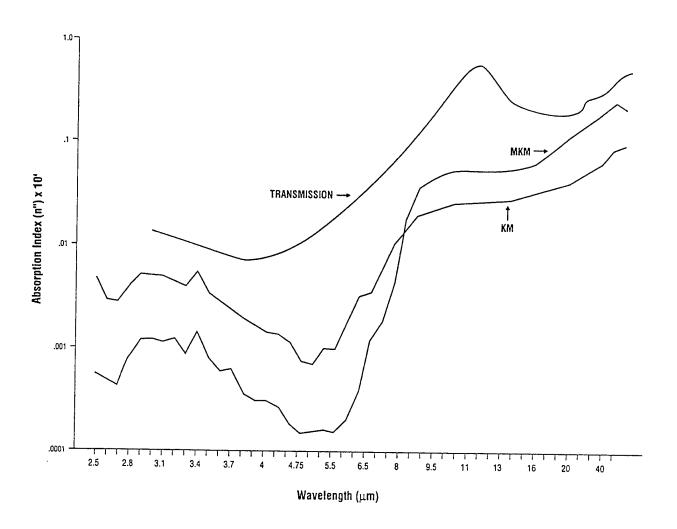
Viewgraph VII: Comparison of bulk absorption with K-M and M-K-M calculations for powder and sintered bubble glass samples of Corning CS1-64;M-K-M model gives best results.

Absorption vs. Wavelength
Sahara Dust
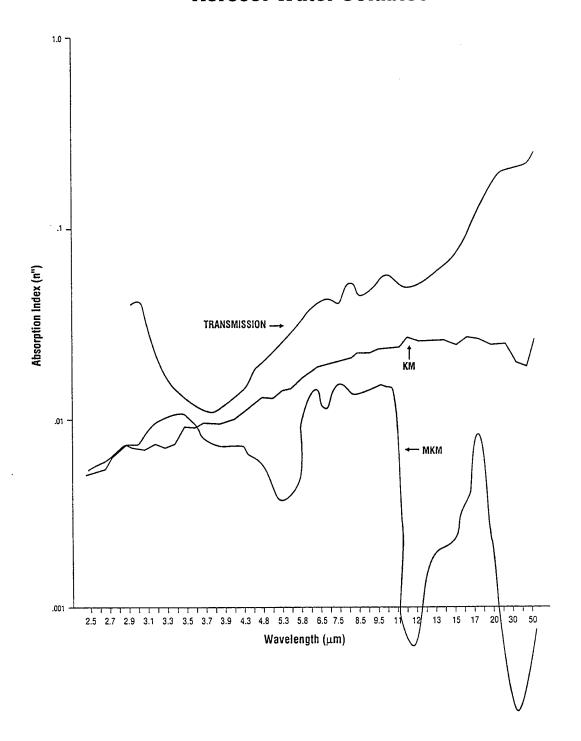
Viewgraph VIII: Optical absorption vs wavelength of Sahara dust for three models.

Absorption vs. Wavelength
Volcanic Dust

Viewgraph IX: Optical absorption vs wavelength of volcanic dust
for three models.

Absorption vs. Wavelength
Aerosol Water Solubles

Viewgraph X: Optical absorption vs wavelength of aerosol water solubles for three models.

FASE/FASCOD4: Current Status and Future Direction

H.E. Snell
Atmospheric and Environmental Research, Inc.
840 Memorial Dr.
Cambridge, MA 02139
phone: (617)-547-6207
fax: (617) 661-6479
email: snell@aer.com

G.P. Anderson, J.H. Chetwynd, and S. Miller
Geophysics Directorate, Phillips Laboratory
Hanscom AFB, MA 01731
phone: (617) 377-2335
email: ganderson@plh.af.mil

Abstract

The Optical Physics Division of the Air Force Phillips Laboratory with support from the Department of Energy (DoE) Atmospheric Radiation Measurement (ARM) Program is developing a state-of-the-art line-by-line atmospheric radiative transfer model as the successor to FASCODE (Fast Atmospheric Transmittance Code[1]). The goal of this project is to create a computationally efficient model which contains the most up-to-date physics. The new model, known as FASCODE for the Environment, or "FASE", combines the best features of FASCODE and LBLRTM (Line-by-Line Radiative Transfer Model[2]), the DoE's standard radiative transfer model. Upgrades to FASE include the addition of a solar spectrum module to compute the attenuated, line-of-sight solar radiance, improvement of the cloud and aerosol descriptors, based on changes made to MODTRAN (Moderate Resolution Transmittance Model), and the ability to incorporate the new heavy molecule absorption cross-section data found on the HITRAN96 database, which is of slightly different format from the previous HITRAN cross-section data. This paper focuses on the new heavy molecule cross-sections.

Introduction

Laboratory measurements of the absorption properties of heavy molecules were recently made by Varanasi et al.[3] (subsequently referred to as "Varanasi's cross sections") and are included on the 1996 release of the HITRAN databases[4]. The measurement errors of the new values are much lower than the old data, hence the inclusion on HITRAN-96. Because of the complexity of these molecules and the fact that individual spectral lines cannot be resolved at temperatures and pressures typical of the earth's atmosphere, the

measurements consist of relatively low spectral resolution information in the form of absorption cross-sections (i.e. without information about line strengths, positions, halfwidths, etc.). Many of these molecules have been included on previous versions of the HITRAN databases in that form, as temperature dependent cross sections rather than the traditional HITRAN format of line position, line strength, halfwidth, etc. However, the Varanasi measurements are provided as a function of pressure and temperature as opposed to the previous HITRAN format, which extrapolated the temperature-dependent values to zero pressure. To compute the optical depth for a particular (p,T) combination with the 'old' data, it was necessary to interpolate between temperatures while convolving with the appropriate Lorentz line shape for the pressure, finally combining this derived cross section with the density weighted path amounts. With the Varanasi data, one is required to interpolate and/or extrapolate between the tabulated data in order to arrive at the correct absorption coefficient. Thus in order to accommodate this new data directly it would be necessary to re-configure the FASE algorithms to bypass the convolution and perform the necessary interpolation and/or extrapolation. Further, one must develop an appropriate scheme for extrapolating the tabulated values to pressures and temperatures outside the range of the measurements.

One approach through which the Varanasi cross-sections may be utilized by the FASE algorithms is to perform a least-squares fit to the data with a series of spectral lines, solving for the line strength, halfwidth, and lower state energy[5]. The pseudo-line approach incorporates all the (p,T) combinations of data into the least-squares fit and increases the accuracy from a simple interpolation between two (p,T) values. The pseudo-line data is easily merged with the spectral data taken from HITRAN when creating the 'TAPE3' line file, and the radiative transfer calculations are performed as usual, with the model using the spectral line routines, rather than the cross-section routines, when computing the absorption of these species.

One drawback to the pseudo-line approach is that new sets of pseudo-line fits are required as more molecules are added. In the long run it would be desirable to develop a scheme to use the cross-sections given as a function of pressure and temperature. Since the problem lies in interpolating/extrapolating the absorption coefficient data to specific values of the pressure and temperature, one might use the pseudo-line approach to fill out the full matrix of required pressures and temperatures (that is, use FASE to compute the absorption coefficients for the regions not represented by the measurements). For the time being it is sufficient to investigate the implementation of the pseudo-line approach and begin to explore ways in which the actual data can be used, perhaps in conjunction with 'pseudo-data' based on calculations with the pseudo-lines.

Pseudo-line fits have been made available for FASE for a number of heavy molecules (see Table 1). However, before this method can be accepted there are some questions which must be addressed: (1) does the calculation with the pseudo-lines accurately reproduce the measured absorption coefficients? (2) how do the new values for heavy molecule absorption impact the radiance and transmittance computed by FASE? and (3) what is the timing impact of using the pseudo-lines compared to the (low spectral resolution) cross-sections? An evaluation of the first of these questions was previously presented by Snell et al.[6] for CFC-12 and will not be discussed here. The latter two questions are discussed below.

Table 1: List of gases with pseudo-lines currently available for use with FASE. Those species with cross-sections given on the HITRAN-96 database are indicated in the rightmost column.

Gas	Interval (cm^{-1})	Grid (cm^{-1})	Measurer	HITRAN-96
CF4	1265-1295	0.005	Varanasi	
CFC-12	850-950	0.01	Varanasi	X
CFC-12	1050-1200	0.01	Varanasi	X
CFC-11	770-810	0.01	Varanasi	X
CFC-11	1050-1120	0.01	Varanasi	X
CCl4	770-810	0.01	Orlando	X
CFC-22	776-850	0.00742	Varanasi	X
CFC-113	786-990	0.01	McDaniel	
SF6	925-955	0.01	Varanasi	X
HCFC-142b	870-1270	0.01	Newnham	
ClONO2	750-831	0.00964	Ballard	X
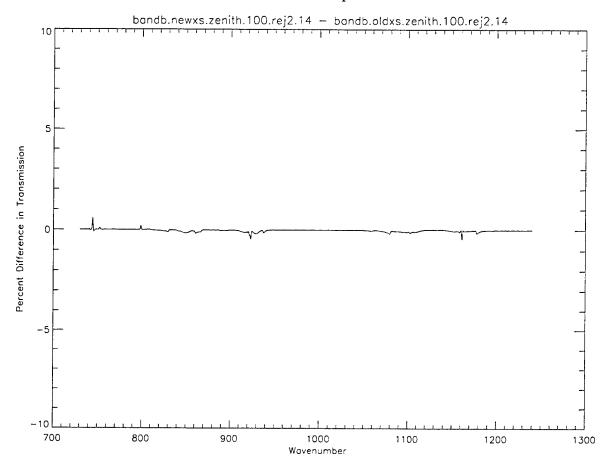
Radiance/Transmittance Tests

One feature of the new heavy molecule cross sections is that the measurements were made at higher spectral resolution and with a better signal-to-noise ratio. Thus the new values exhibit more structure and a larger cross-section at band center than the cross-sections tabulated on previous versions of the HITRAN database. While the heavy molecules constitute only a minor fraction of gases in the atmosphere, the impact of the new values on different calculations must be determined. The test scenario was conducted over the spectral region from 725 to 1245 cm^{-1}. The atmosphere consisted of a US Standard profile with the first seven molecules on the HITRAN database (those

most likely to contribute to a typical calculation) along with HNO3, and the cross-sections CFC-11 and CFC-12. The CFC profiles were consistent with those obtained from the CIRRIS-1A experiment (Bingham, 1997) and were extrapolated to the top of the atmosphere using the shape of the curve given in Brasseur and Solomon (1986).

The tests were conducted for input atmospheres with (a) no CFCs, (b) CFCs with the old cross-sections, and (c) CFCs with the new cross-sections. It was found that the new cross-sections have a negligible impact on the radiance and transmittance for zenith- and nadir-looking conditions. There are, however, noticeable differences for certain limb paths. For example, Figure 1 shows the percent difference in transmission between calculations using the old and new values for the cross-sections for a zenith-looking path from the surface to 100 km. One can see that the differences are much less than 1%. Figure 2 shows the difference in transmission with a tangent path from 100 km to 10 km to 100 km. The region around 1050 cm-1 is opaque due to ozone absorption, so these differences are strictly numerical. However, in the CFC regions (~800 - 950 cm^{-1} and ~1070-1200 cm^{-1}) there are differences of the order of 2-5% (though the differences at the center of the CFC-12 band reach 6%). A comparison of radiance values for these types of paths gives similar results. The above tests show that for certain paths the new values of the heavy-molecule absorption cross-sections give answers which differ from those given by previous versions of the measurement data. Further study is required to assess the impact of these new values in trying to fit measured atmospheric spectra.

Figure 1: Differences in transmission for a zenith path.

bandb.newxs.zenith.100.rej2.14 — bandb.oldxs.zenith.100.rej2.14
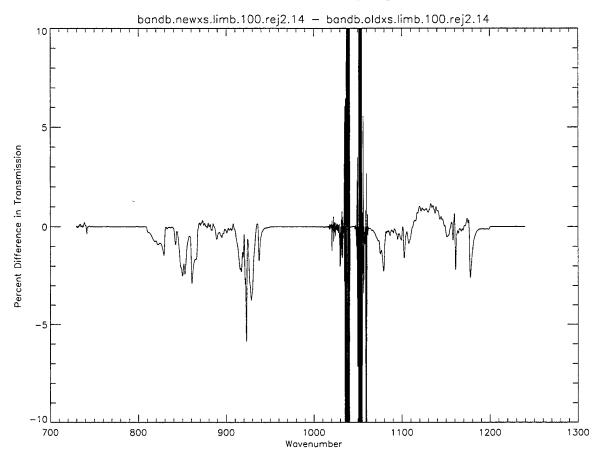
Figure 2: Differences in transmission for a 10 km tangent path.

bandb.newxs.limb.100.rej2.14 − bandb.oldxs.limb.100.rej2.14

Timing Tests

The ability to read the new cross-section data as a series of pseudo-lines is an inexpensive alternative to developing a more sophisticated interpolation/extrapolation scheme. However, the price paid is one of algorithm timing. The inclusion of pseudo-lines can add anywhere from thousands to tens of thousands of spectral lines to a given calculation. For calculations which require a large number of atmospheric layers, this can add a significant amount of time to the calculation.

A series of tests was conducted in the spectral range from 725 - 1245 cm^{-1} using the heavy molecule species F-11, F-12, and CCl4. These species were chosen because they have data in the form of 'old' cross-sections and 'new' pseudo-lines. Calculations were done for the uplooking radiance and transmittance from 0 - 40 km and 0 - 100 km with a US Standard Atmosphere (as described in the previous section). The timing results, given in Table 2, represent an average of eight individual runs for each case; the standard deviation for each case was less than 3 seconds.

143

The calculations from 100 km to the surface take longer than those from 40 km because of an increased number of atmospheric layers, and because the upper layers require higher spectral resolution than the lower layers. With the cross-sections, calculations from 100 km take approximately 3.1 times longer than those from 40 km. The difference is larger with the pseudo-lines, a factor of about 3.5, because each pseudo-line must be accurately computed at each layer. In reality, the concentration profiles of many species, the heavy molecules in particular, decrease rapidly with altitude. Using the option to zero the contribution from weak lines when they no longer contribute significantly to the overall optical depth (NOZERO=0 on input RECORD 3.1) dramatically decreases the computation time for both the pseudo-line and cross-section cases (however, care must be taken for calculations which require very high accuracy, such as remote sensing retrieval problems, where the zeroing of absorber amounts can introduce systematic errors). For the 0-100 km case shown here there is a 20% timing penalty for using the pseudo-lines instead of the cross-sections, which is small compared to the change in accuracy with this new data.

Table 2: Timing test results

Case	Old Cross-Section	New Pseudo-Line
0 - 40 km	178.96	401.11
0 - 100 km	562.93	1413.07
0 - 100 km (Zero small absorber amounts)	263.02	327.36

Conclusion

New values of cross-sections for several heavy-molecules have been included on the 1996 release of the HITRAN database in a format different from that of pervious versions. A pseudo-line approach was adopted whereby "lines" were fit to the cross-sectional curves to allow for extrapolation/interpolation to temperatures and pressures not given on HITRAN. Depending on the type of path and spectral region, the new values can produce significantly different values (~5%) for the calculated transmission. Tests have shown that the use of this approach can add a significant amount of time to the calculation. Calculation run-time can be reduced by neglecting the calculation at altitudes where the species of interest has only a small contribution to the total radiance/transmission.

References

[1]Anderson, G.P., et al., History of One Family of Atmospheric Radiative Transfer Codes, The European Symposium on Satellite Remote Sensing, Conference on Passive Infrared Remote Sensing of Clouds and Atmosphere II, 26-30 September 1994, Rome, Italy.

[2]Clough, S.A., et al., Radiative Transfer Model Development in Support of the Atmospheric Radiation Measurement (ARM) Program, Proceedings of the Second ARM Science Team Meeting, DOE Conf. 9303112, Norman, OK, 1-4 March 1993.

[3]Varanasi, P., and V. Nemtchinov, Thermal Infrared Absorption Coefficients of CFC-12 at Atmospheric Conditions, J. Quant. Spectro. Radiat. Transfer, 51, 679-687, 1994.

[4]Rothman, L.S., R.R. Gamache, A. Goldman, L.R. Brown, R.A. Toth, H.M. Pickett, R. Poynter, J.-M. Flaud, C. Camy-Peyret, A. Barbe, N. Husson, C.P. Rinsland, and M.A.H. Smith, the HITRAN Database 1986 Edition, *Applied Optics*, 26, 1987.

[5] Geoff Toon, Jet Propulsion Laboratory, Private Communication, November 1995.

[6]Snell, H.E., G.P. Anderson, J.H. Chetwynd, and S. Miller, FASCODE for the Environment (FASE), Proceedings of the 19th Annual DoD Review Conference on Atmospheric Radiance and Transmission, Hanscom AFB, June 1996. **PL-TR-97-2069, ADA328230**

FASE-Calculated Contribution Functions for MSX SPIRIT-III MWIR Bands for BTH Measurements

W. Gallery, H. E. Snell, C. Sarkisian, D. Hogan

AER, Inc.

A. Zachor

Atmospheric Radiation Consultants, Inc.

J. Winick

PL/GPOS
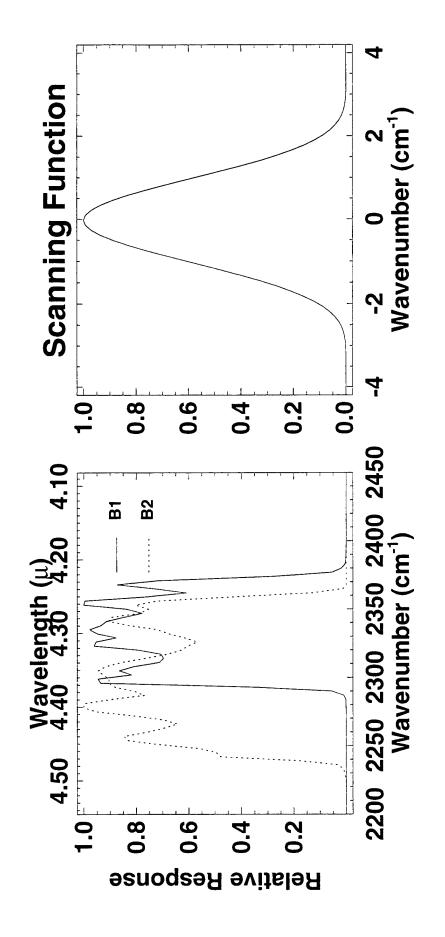
MSX SPIRIT III MWIR Measurements

- MSX: Midcourse Space Experiment
  - High Spatial Resolution (~100 μRad), High Sensitivity Imagers And Spectrometers, Far-IR To UV
  - View both the Limb and Below-the-Horizon (BTH)
- SPIRIT III
  - Cryogenically Cooled Radiometer and Interferometer Sharing Common Optics
  - Scanning Radiometer
    - 5 Bands
      - Only Filters B1 (4.21-4.36 μ) and B2 (4.24-4.46 μ) Do Not Saturate Viewing BTH
  - Interferometer
    - 6 Channels, 28 to 2.3 micrometers
    - Only Channel 2 (2.6 to 4.9 micrometers) Does Not Saturate BTH
    - High-Resolution Mode: 0.534 cm Optical Path Difference
      - Kaiser-Bessel Apodization, alpha=3.15
      - Spectral Resolution: 2.37 cm^{-1} Full Width Half Height

MSX Radiometer Filters B1 & B2 and Interferometer Scan Function

Weighting, Contribution and Sensitivity Functions Defined

- **Radiative Transfer Equation, Non-Scattering Atmosphere, No Surface Term**

$$R_\upsilon = \int_\infty^s J_\upsilon(s) \frac{dT_\upsilon(s)}{ds} ds$$

Where :

R is the outgoing radiance (will drop explicit frequency dependence for clarity)

s is the path variable (z for vertical path)

$J(s)$ is the source function: Plank Function (LTE) or Non-LTE Source Function

$T(s)$ is the transmittance from the top of the atmosphere down to s

q is a path variable, e.g. temperature or water vapor at a level

Function	
Weighting	$\dfrac{dT}{dz}$
Contribution	$J(s)\dfrac{dT}{dx}$
Sensitivity	$\dfrac{dR}{dq} = \int (\dfrac{dJ}{dq}\dfrac{dT}{ds} + J\, d(\dfrac{dT}{ds})\big/dq)ds$

FASE-Calculations

- **Temperature Profile: From CIRRIS 1A Analysis, Midlatitude Northern Hemisphere, Merged to CIRA Atmosphere Above 55 km**
  - Top of Atmosphere at 120 km, 2 km Layers
  - Water Vapor, Ozone from US Standard 76
  - Non-LTE Vibrational Populations from SHARK, Solar Zenith Angle = 50 Deg
  - Surface Term Not Included
- **Use IMRG = 13 Option: Space to Ground, Scanned Results**
- **Scanning Function: Kaiser-Bessel**
- **Nadir Angles**

Zenith Angle at Ground (deg)	Nadir Angle at MSX (deg)	Air Mass (relative)
0	0	1.0
60	49.5	2.0
75	57.9	3.8
85	60.97	10
90	61.36	37

Function Algorithms

- For Finite Layers z_i, define:

  T_i is the FASE-calculated transmittance from the top of the atmosphere down to the bottom of layer i

  R_i is the FASE-calculated radiance contribution from layers 1 to i starting at the top of the atmosphere, and
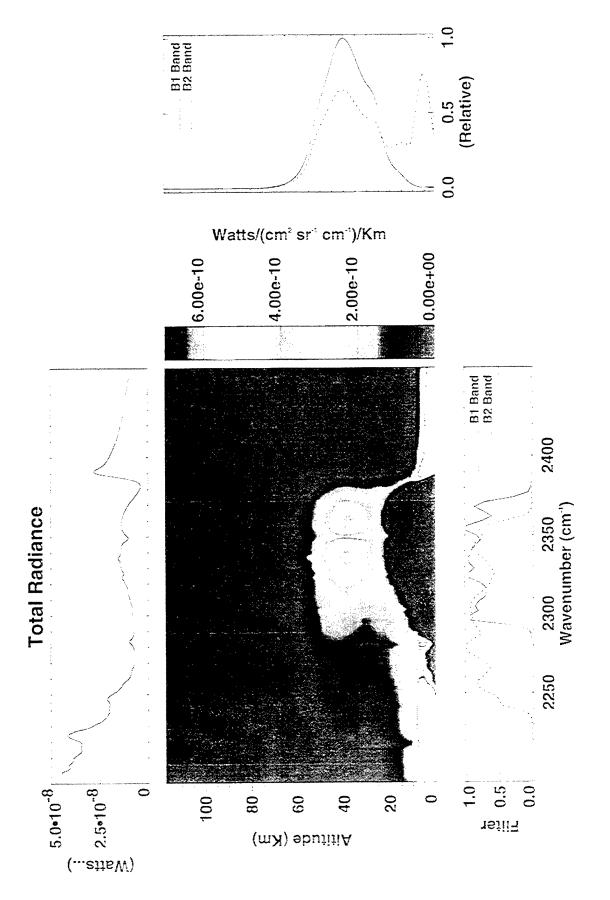
  B is the Plank function at the temperature $\Theta(z_i)$ for the layer z_i

Function Type	Algorithm
Weighting:	$\dfrac{T_i - T_{i+1}}{z_i - z_{i+1}}$
Contribution:	$\dfrac{R_{i+1} - R_i}{z_i - z_{i+1}}$ or $B(\Theta(z_i))\dfrac{T_i - T_{i+1}}{z_i - z_{i+1}}$
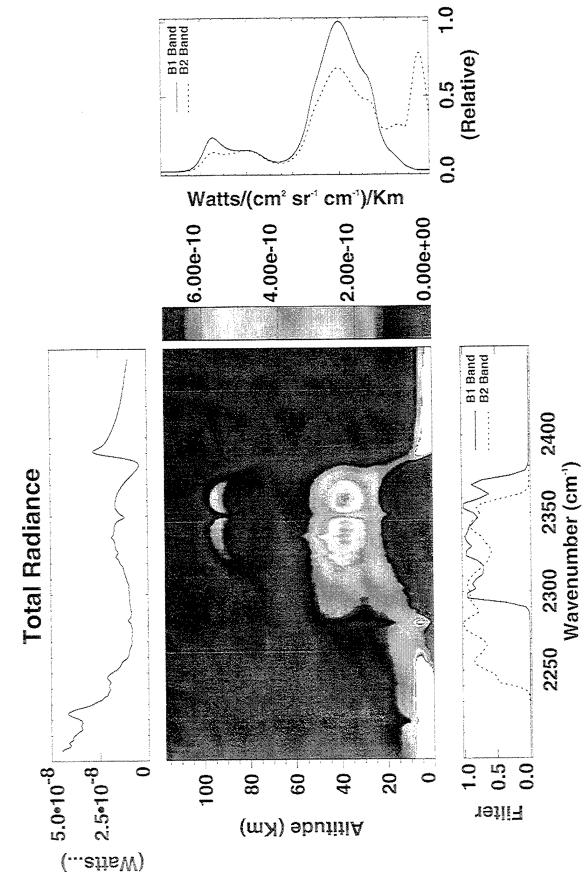
- Filtering, Finite Differences and Plotting: Used IDL®

151

LTE Contribution Function: ZenithAngle = 0

04/28/98
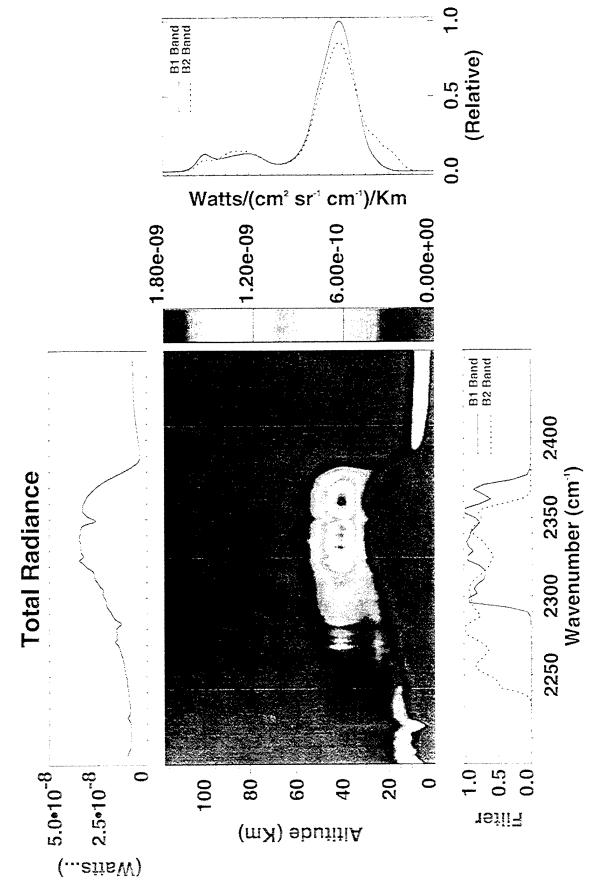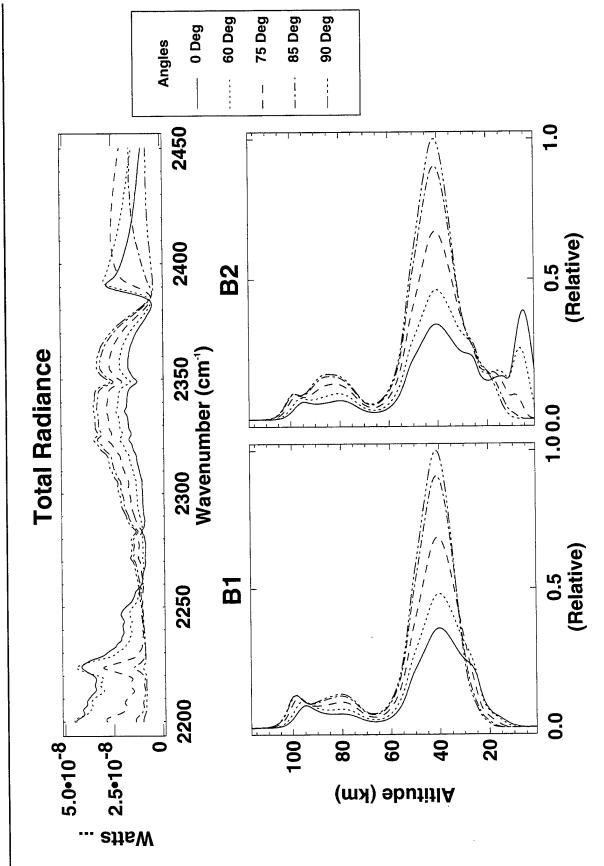
Non-LTE Contribution Function: Zenith Angle = 0 deg

04/28/98

Non-LTE Contribution Function: Zenith Angle = 90 deg

B1 and B2 Non-LTE Contribution Functions: 0 to 90 Deg

Total Radiance

Angles
0 Deg
60 Deg
75 Deg
85 Deg
90 Deg

04/28/98

10 of 10

155

Characterization of Optical Extinction Profiles Using Raman Lidar Techniques

Michael D. O'Brien and C. Russell Philbrick

Department of Electrical Engineering
Penn State University

1. Introduction

The presence of aerosol particles and cloud droplets in the atmosphere strongly affects the propagation of light through the atmosphere. These particles have an important impact on the Earth's climate and the operation of electro-optical sensors. A useful tool for measuring optical extinction due to aerosols is a Raman lidar. Raman lidars also have the capability to measure atmospheric temperature and humidity. The lidars we have at Penn State also have the capability to measure ozone in the lower troposphere. This profile can then be used to determine the extinction due to ozone absorption. The present lidar system provides extinction measurements at UV and visible wavelengths. The technique has been verified over a horizontal path with independent measurements of the particle size distribution and provides measurements with a high degree of temporal resolution.

The current lidar system employs Raman scatter from a ND:YAG laser beam from the 2nd, 3rd, and 4th harmonics at 532, 355, and 266 nm to obtain the profiles of optical extinction. The measurements have been made using the molecular nitrogen profiles at 607, 387, and 285 nm, which are the first Stokes vibrational Raman shifts from the ND:YAG laser. The rotational Raman scatter at 530 nm has also been used to obtain optical extinction profiles. This paper will begin with a description of the two Raman lidars used to acquire the data to be presented. Next, the details of our analysis will be discussed. Then, the capabilities of the system will be illustrated with several examples of data taken during two field campaigns.

2. Background

The Raman lidar technique is a powerful way of measuring a variety of atmospheric properties. At Penn State we currently have two Raman lidars, LAMP and LAPS. The LAMP system began operation in 1991 and has been used to make a variety of atmospheric measurements[1]. In their current configuration, both LAMP and LAPS are capable of measuring water vapor, temperature, ozone, and extinction profiles in the troposphere. The LAPS lidar system is a second generation version of LAMP[2]. The LAPS system has a much greater return signal, due in part to a larger receiving telescope and a more powerful laser. In addition, the system was designed as an operational prototype

with numerous automated systems. This makes its operation easier and somewhat more reliable and stable. Table 1 summarizes the specifications of the two systems.

Table 1. Specifications for the Penn State LAMP and LAPS lidar systems.

	LAMP	LAPS
Transmitter	Continuum NY-82 ND:YAG laser 20 Hz 400 mJ at 532 nm 80 mJ	Continuum 9040 ND:YAG laser 30 Hz 600 mJ at 532 nm 120 mJ at 266 nm
Receiver	0.41 m diameter telescope	0.6 m diameter telescope
Detector	7 PMT channels 528, 530 nm - Temperature 660, 607 nm - Visible Water Vapor 295, 284 nm - UV water Vapor 277, 284 nm - Ozone	7 PMT channels 528, 530 nm - Temperature 660, 607 nm - Visible Water Vapor 295, 284 nm - UV water Vapor 277, 284 nm - Ozone
Data System	100 MHz count rate 75 m range resolution	100 MHz count rate 75 m range resolution

For both of the systems, water vapor profiles are determined by taking the ratio of the vibrational Raman return from water vapor to the vibrational Raman return from molecular nitrogen. The water vapor measurements are made at both ultraviolet and visible wavelengths using the 295/284 and 660/607 ratios. The UV measurement is corrected for ozone absorption by measuring the O_2 vibrational Raman signal. The ratio of the molecular oxygen to the molecular nitrogen signal provides a Raman/DIAL measurement of the tropospheric ozone density[3]. The system uses the temperature dependence of rotational Raman scattering to obtain profiles of atmospheric temperature using the ratio of 530/528 signals[4]. These measurements provide useful background meteorological data for studying changes in optical extinction. The aerosol extinction coefficient is determined by observing departures from the expected gradient of the Raman lidar profiles. The analysis used for this method will be presented later.

The Raman lidar data can also be used to measure the optical extinction at 284, 387, 530, and 607 nm. The lidars measure the scattered light corresponding to the 1st Stokes vibrational Raman transition for molecular nitrogen to obtain a profile of atmospheric nitrogen. Any deviation in this profile from the gradient of the molecular atmosphere is due to aerosol extinction. Figure 1 shows a schematic representation of this. The figure shows the range corrected signals for a Raman shifted nitrogen channel and a corresponding elastic backscatter channel. The figure demonstrates when there is a large increase in the backscatter there is a deviation in the slope of the molecular nitrogen Raman signal. We are trying to measure the change in this slope, which is proportional to the exponential attenuation term in the Raman lidar equation. Figure 2 shows an example

of the raw photon count profiles from LAPS on 9 October 1996 while it was aboard the U.S.N.S. Sumner. The profiles rapidly increase to a maximum as the laser fully enters the field of view of the telescope at approximately 1000 m [5]. Above this altitude the profile shows an altitude region where the slope of the profile is much greater than the expected gradient for the molecular atmosphere. This increased slope is caused by an increase in the optical extinction due to scattering particles.
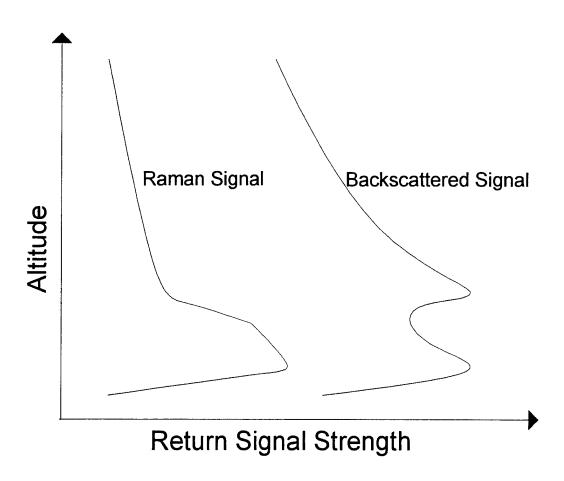
Figure 1. This figure depicts the change in the slope of the Raman signal as the lidar hits an intense scattering layer.
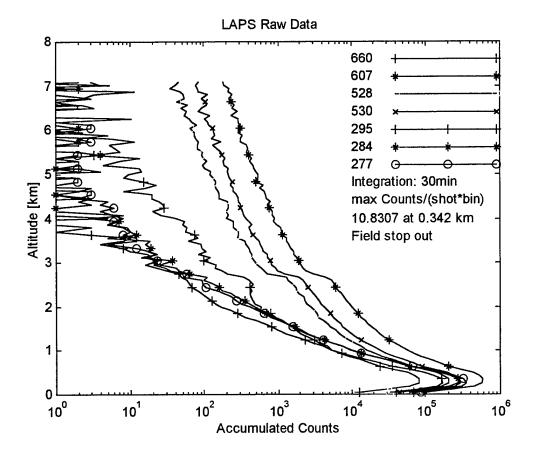
Figure 2. This figure shows a plot of the raw data from LAPS taken on 9 October 1996 at 03:16 GMT aboard the U.S.N.S. Sumner. The profiles show a region of heavy aerosol extinction.

3. Analytical Equations

It is possible to derive a relation for the extinction coefficient from the Raman lidar equation [6,7,8,9]. The Raman lidar equation is given as,

$$P(z) = \frac{\xi(z)}{z^2} N(z) \frac{\partial \sigma}{\partial \Omega} \exp\left(-\int_0^z \left(\alpha_0^{mol}(z) + \alpha_R^{mol}(z) + \alpha_0^{aer}(z) + \alpha_R^{aer}(z)\right)dz\right), \qquad (1)$$

where P(z) is the received signal power at the Raman shifted wavelength, k is an instrumental constant, $\xi(z)$ is the telescope form factor, N(z) is the molecular number density, $\partial\sigma/\partial\Omega$ is the Raman backscattering cross section, α_0^{mol} and α_R^{mol} are the molecular extinction coefficients for the transmitted and Raman scattered wavelengths, α_0^{aer} and α_R^{aer} are

159

the aerosol extinction coefficients for the transmitted wavelength and Raman scattered wavelengths, and z is the range. The aerosol extinction coefficient can be determined from (1) and is given by,

$$\alpha_R^{aer} = \frac{d}{dz}\left[\ln\frac{N_R(z)}{P_R(z)\cdot z^2}\right] - \alpha_0^{mol}(z) - \alpha_R^{mol}(z) - \alpha_0^{aer}(z) \ . \tag{2}$$

Only data above the altitude where the laser is completely in the field of view of the telescope is used in this analysis. The molecular number density and extinction coefficients are determined from a standard atmosphere and the known molecular scattering cross section. The aerosol extinction coefficient for the transmitted wavelength of 532 nm is determined from the rotational Raman signal. The received signal for the rotational Raman channels is also given by (1), and in this case the extinction coefficients of the transmitted and backscattered Raman wavelengths are assumed to be the same because they are only separated by 2 nm. The 532 nm aerosol extinction coefficient is then determined with,

$$\alpha_{532}^{aer} = \frac{d}{dz}\left[\frac{1}{2}\ln\frac{N(z)}{P_{530}(z)\cdot z^2}\right] - \alpha_{532}^{mol}(z) \ . \tag{3}$$

This value of α_{532}^{aer} is then used as the value of α_0^{aer} in (2) so that α_R^{aer} can be calculated. This procedure assumes that the optical depth is not too great and that multiple scattering can be neglected.

At UV wavelengths a rotational Raman signal is not available so only the vibrational Raman signals are used. The extinction due to ozone absorption is determined with the ozone profile measured by the lidar. The difference between the extinction coefficients between the transmitted and received wavelengths is accounted for with a power law relationship, which assumes the same wavelength dependence for scattering as was found between 532 and 607 nm. The resulting equation is given as,

$$\alpha_{284}^{aer} = \frac{\frac{d}{dz}\left[\ln\frac{N(z)}{P_{284}(z)\cdot z^2}\right] - \left(\alpha_{266}^{mol} + \alpha_{284}^{mol}\right) - (\sigma_{266}^{O_3} + \sigma_{284}^{O_3})\cdot N_{O_3}(z)}{1 + \left(\frac{284}{266}\right)^k} \ , \tag{4}$$

where $\sigma_{266}^{O_3}$ and $\sigma_{284}^{O_3}$ are the ozone absorption cross sections for the transmitted and Raman scattered wavelengths, $N_{O_3}(z)$ is the ozone density profile, and k is determined by the wavelength dependence of particle scattering.

4. Results

Over the past years our research group has gathered data with the two lidar systems under a variety of conditions and locations. The LAMP lidar was used in September 1995 to measure the particle size distributions and extinction properties of coastal aerosols in the Coastal Aerosol Scattering Experiment I (CASE I) campaign conducted at NASA's Wallops Island test facility. The lidar was operated in vertical and horizontal modes. In the vertical operating mode, the lidar measured water vapor, temperature, and ozone profiles simultaneously with other lidar and balloon sensors[10]. In the horizontal operating mode, the aerosol extinction coefficient was determined from the Raman lidar profiles and from particle size measurements made with a bistatic lidar. The bistatic lidar consists of a camera that focuses an image of the horizontal laser beam onto a linear photodiode array. This allows for the measurement of the scattering intensity from the aerosol particles at a number of angles. Data from the ratio of the cross polarization scattering phase function is inverted to determine the particle size distribution[11]. The aerosol extinction coefficient that corresponds to this distribution is then calculated. A comparison of the extinction values determined with the two techniques is given in Table 2. The two extinction coefficients agree within the experimental error for the methods.

Table 2. Comparison of aerosol extinction coefficients measured with a Raman lidar and a bistatic lidar.

Wavelength	Extinction from Raman Lidar	Extinction from Bistatic Lidar
532 nm	0.259 (km^{-1})	0.279 (km^{-1})
607 nm	0.209 (km^{-1})	0.243 (km^{-1})

During the Fall of 1996 LAPS was deployed aboard the USNS Sumner for its first field tests. The system performed quite well and provided several hundred hours of data. One example of an extinction profile from this data is shown in Figure 3. This profile of optical extinction for 532 nm was obtained on 9 October 1996. The profile shows a several layers of strong extinction. At the same time we determined the extinction coefficient at 284 nm, which is shown in Figure 4. With the LAPS lidar system we have the capability to make measurements of the extinction coefficient with high time resolution. An example of this capability is shown in Figure 5.
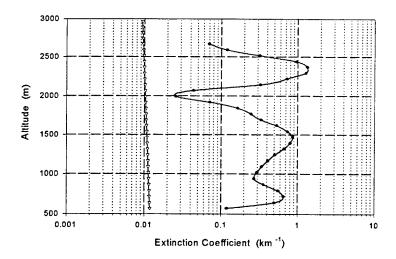
Figure 3. This Figure shows the optical extinction for 532 nm measured vertically with LAPS on 9 October 1996 at 04:16 GMT. The data was acquired with a 30 minute integration. The molecular extinction profile is shown for reference.
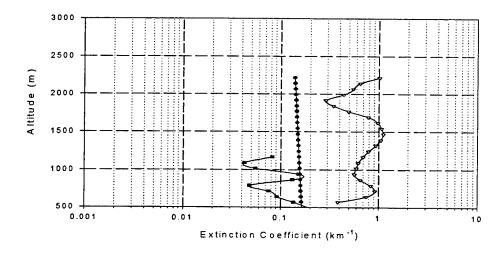
Figure 4. This Figure shows the optical extinction at 284 nm measured vertically with LAPS on 9 October 1996 at 04:16 GMT. The data was acquired with a 30 minute integration. The profiles left to right are ozone extinction, molecular extinction, and aerosol extinction.
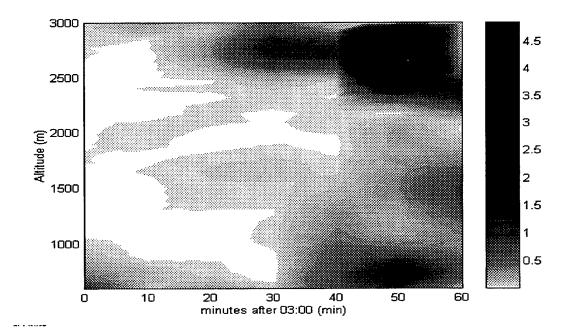
Figure 5. This Figure shows a time series of the 532 nm extinction coefficient starting at 03:00 EDT on 9 October 1996 from LAPS aboard the U.S.N.S. Sumner. The intensity scale is in km^{-1}.

4. CONCLUSIONS

The measurements presented in this paper have demonstrated the utility of the Raman lidar technique in measuring optical extinction. These measurements have been independently verified with the bistatic lidar measurements. The vertical profiles showed that this technique can be successfully employed to measure extinction coefficients in the lower troposphere for aerosols. In addition we have shown that the time resolved measurements of extinction provide a powerful way of studying aerosols in the atmosphere.

ACKNOWLEDGMENTS

Special appreciation for the support of this work goes to J. Richter and D. Jensen of NCCOSC Nrad, G. Schwemmer of NASA GSFC, and SPAWAR PMW-185. The efforts of D. B. Lysak, Jr., T. Petach, G. Pancoast, W. Smith, S. Mathur, and T. Stevens have contributed much to the success of this project.

REFERENCES

1. C. R. Philbrick, "Raman Lidar Measurements of Atmospheric Properties," *Atmospheric Propagation and Remote Sensing III*, SPIE Vol. 2222, pp. 922-931, 1994.

2. C. R. Philbrick and D. B. Lysak, "Lidar measurements of meteorological prperties and profiles of RF refractivity," *Proc. Of 1996 Battlespace Atmospherics Conference*, pp. 595-609, December 1996.

3. F. Balsiger and C. R. Philbrick, "Comparison of lidar water vapor measurements using Raman scatter at 266 nm and 532 nm," *Applications of Lidar to Current Atmospheric Topics*, SPIE Vol. 2833, pp. 231-240, 1996.

4. F. Balsiger, P. A. T. Haris, and C. R. Philbrick, "Lower tropospheric temperature measurements using a rotational Raman lidar," *Optical Instruments for Weather Forecasting*, SPIE Vol. 2832, pp. 53-60, 1996.

5. J. R. Jenness, Jr., D. B. Lysak, Jr., and C. R. Philbrick, "Design of a lidar receiver with fiber optic output," *Appl. Opt.*, Vol. 36, No. 18, pp. 4278-4284, 1997.

6. M. D. O'Brien, T. D. Stevens, and C. R. Philbrick, "Optical extinction from Raman lidar measurements," *Optical Instruments for Weather Forecasting*, SPIE Proc. Vol. 2832, pp. 45-52, 1996.

7. A. Ansmann, M. Riebesell, and C. Weitkamp, "Measurement of atmospheric aerosol extinction profiles with a Raman lidar," *Opt. Let.*, vol. 15, no. 13, pp. 746-748.

8. V. M. Mitev, I. V. Grigorov, and V. B. Simeonov, "Lidar measurement of atmospheric aerosol extinction profiles: a comparison between two techniques-Klett inversion and pure rotational Raman scattering methods," *Appl. Opt.*, vol. 31, no. 30, pp. 6469-6474, 20 October 1992.

9. R. A. Ferrare, S. H. Melfi, D. N. Whiteman, and K. D. Evans, "Raman lidar measurements of Pinatubo aerosols over southwestern Kansas during November-December 1991," *Geo. Res. Let.*, vol. 19, no. 15, pp. 1599-1602, August 3, 1992.

10. R. Harris, F. Balsiger, C. R. Philbrick, "Comparison of lidar water vapor measurements using Raman scatter at 266 nm and 532 nm," *Proc. 1996 International Geoscience and Remote Sensing Symposium*, Vol. III, pp. 1826-1829, 1996.

11. T. D. Stevens, "Bistatic Lidar Measurements of Lower Tropospheric Aerosols," Ph.D. Dissertation, Department of Electrical Engineering, Penn State University, 1996.

CIRRIS-1A limb spectral measurements on mesospheric ozone airglow

D. K. Zhou,[1] M. G. Mlynczak,[2] G. E. Bingham,[1] J. O. Wise,[3] and R. M. Nadile[3]

[1]Space Dynamics Laboratory, Utah State University, Logan, Utah
[2]Atmospheric Sciences Division, NASA Langley Research Center, Hampton, Virginia
[3]Geophysics Directorate, Phillips Laboratory, Hanscom AFB, Massachusetts

Abstract. Shuttle-based limb infrared spectral measurements on mesospheric ozone airglow were made by the Cryogenic Infrared Radiance Instrumentation for Shuttle (CIRRIS-1A) during one flight of the space shuttle *Discovery* (28 April to 6 May, 1991). A significant difference between ozone nightglow and dayglow was observed. A spectrally integrated ozone υ_3 fundamental band radiance profile was used to retrieve its excited state density which, in conjunction with the modeled ozone υ_3 vibrational temperature, was used to infer the total ozone density. The night/day ozone profiles demonstrate evidence of a non-local thermodynamic equilibrium mesospheric ozone diurnal variation.

1. Introduction

Measurements of the mesospheric ozone airglow were first made by the Cryogenic Circular-Variable Filter Spectrometer, a rocket-borne experiment [*Stair et al.*, 1974]. Later, more advanced sensors were used to observe mesospheric ozone [e.g., *Stair et al.*, 1985; *Rawlins et al.*, 1993]. Some laboratory studies have been made to improve our understanding of ozone kinetics and spectroscopy [e.g., *Menard et al.*, 1992; *Upschulte et al.*, 1994]. It is well known that ozone is produced by the highly exothermic recombination ($O+O_2+M \rightarrow O_3+M$), and mainly destroyed by the photolytic reaction ($O_3+h\nu \rightarrow O+O_2$). A few non-local thermodynamic equilibrium (non-LTE) ozone models have been developed based on the knowledge of ozone kinetics and spectroscopy [e.g., *Mlynczak and Drayson* 1990a, b; *Manuilova and Shved*, 1992; *Sharma et al.*, 1996]. Laboratory studies, model developments, and experimental measurements have sought to gain the information necessary to understand the middle atmospheric ozone behavior and its role in Earth's atmospheric environment.

This letter reports on the shuttle-based infrared spectral measurements of the Cryogenic Infrared Radiance Instrumentation for Shuttle (CIRRIS-1A) which was operated on-board the space shuttle *Discovery* (28 April to 6 May, 1991). This broadband interferometer with moderated spectral resolution (1.0 cm⁻¹) provided the data needed to analyze spectrally radiant contributions from the different gases and their emission bands; and the limb scan profile allowed the retrieval of atmospheric gas densities. Mesospheric ozone night/day measurements are reported in section 2. The retrieved ozone υ_3 excited state population and inferred total ozone abundance are presented in section 3, and the summary and remarks are given in section 4.

2. Spectral Analysis / Data Preparation

The CIRRIS-1A data presented here were collected on 29 April 1991 by a Michelson interferometer with detectors, preamplifiers, and collection optics (0.3-m telescope) cooled to near-liquid-helium temperatures. The CIRRIS-1A instrument, measurements, calibration, tangent height determination, and other details of this experiment are documented elsewhere [e.g., *Ahmadjian et al.*, 1990; *Bingham et al.*, 1997]. Four nighttime limb scan profiles and two daytime limb scan profiles were used to provide one mean profile for nighttime and one mean profile for daytime. The data collection location, solar zenith angle (SZA), and local time (LT) are listed in Table 1.

Table 1. CIRRIS-1A Limb Scan[*]

Lat.	Long.	SZA	LT
60°N	185°E	49°	1342
59°N	168°E	50°	1419
28°S	353°E	152°	0142
29°S	13°E	153°	0132
44°S	25°E	147°	2249
43°S	316°E	149°	2304

[*]Indicated near 85 km.

The samples of spectra (1010 - 1140 cm⁻¹) obtained from limb observations under nighttime and daytime conditions (near 85 km) are shown in Figures 1a and 1b, respectively. The estimated sensor noise of ~2×10⁻¹¹ (W cm⁻² sr⁻¹/cm⁻¹) near 10 μm through the mesosphere, yields a signal to noise level high enough to identify the O_3 υ_1 band emissions at tangent heights below ~90 km. The spectra are primarily generated by the emissions: (1) O_3 υ_3 and υ_1 fundamental bands and the wealth of O_3 hot bands, and (2) CO_2 (00011-10002) band mostly at daytime. The O_3 υ_3 emission band contribution was dominated in this region, with the O_3 υ_1 band and hot bands, as well as the CO_2 band making minor

but significant contributions. The shaded regions shown in Figure 1 are the Strategic High-Altitude Radiance Code (SHARC) [*Sharma et al.*, 1996] modeled spectra fit to the CIRRIS-1A data.

has a higher signal to noise ratio and the band strength is less thermally dependent (~7% from 296 K to 200 K), the spectrally integrated O_3 υ_3 radiance mean profile is chosen to invert the O_3 υ_3 excited state population which, in conjunction with the modeled vibrational temperature, is used to infer the total O_3 abundance profiles in the next section.
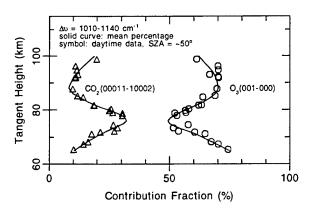
Figure 2. Daytime O_3 (001-000) and CO_2 (00011-10002) band radiance contributions to the spectral region of 1010-1140 cm^{-1}.

Figure 1. Examples of CIRRIS-1A mesospheric ozone spectra collected at (a) nighttime and (b) daytime. The spectral contributions from different bands were modeled by SHARC-3 model to derive the band radiance profiles.
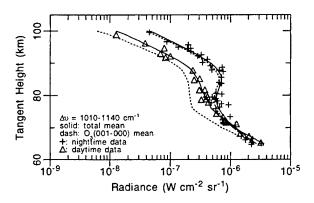
Figure 3. Nighttime and daytime CIRRIS-1A measured band radiance profiles with the mean profiles and O_3 υ_3 band radiance profiles.

SHARC modeled spectra were added band to band to fit the measurement. In the nighttime profiles, the CO_2 contribution is negligible while the O_3 υ_3 band takes ~91.5% of the total band radiance with the standard deviations of ~1.6% through tangent heights of 70 - 100 km. The same analysis was performed for the daytime profiles. The averaged contribution fractions of the CO_2 (00011-10002) band and O_3 (001-000) band were derived using two daytime profiles collected under almost the same conditions (SZA of ~50°) as shown in Figure 2. As a result, the spectrally integrated band radiance data were averaged to one mean nighttime profile and one mean daytime profile as shown in Figure 3. Because the O_3 υ_3 band radiance

3. Results

The retrieval can be processed using the line-by-line (LBL) method or the weak line (WL) approximation [e.g., *Zachor and Sharma*, 1985; *Solomon et al.*, 1986]. Before the inversion, both the LBL and WL approximation forward O_3 υ_3 band radiance calculations were made and the discrepancy between these two methods was small (< 5% at tangent heights above 70 km). Therefore the WL approximation was used in this work, $R_{001} = (1/4\pi)\Sigma\{hc\nu_{10}[O_3(001)]A_{10}\}dx$, where R_{001} is the measured O_3 υ_3 band radiance, h is the Planck's constant, c is the speed of light, ν_{10} is the frequency of the transition in wave-

number, $[O_3(001)]$ is the ozone υ_3 excited state population, A_{10} is the Einstein coefficient, and dx is the elements of limb measurement path length along the line of sight. However, the thermal correction and bandpass correction on the Einstein coefficient were made through the band strength correction (using HITRAN database [*Rothman et al.*, 1992]). Now, the $[O_3(001)]$ retrieval is an Abel-type inversion. The retrieved $[O_3(001)]$ profiles from nighttime and daytime are shown in Figure 4.
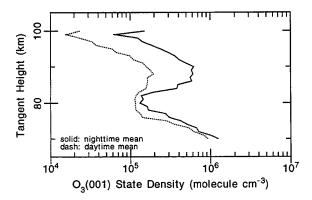
Figure 4. Retrieved ozone nighttime and daytime υ_3 excited state population associated with υ_3 radiance shown in Figure 3.

To accurately retrieve O_3 abundance depends on the knowledge of O_3 kinetics and spectroscopy which yield the ratio of the O_3 excited state to ground vibrational population (i.e., the vibrational temperature). The chemical pumping fraction of O_3 recombination, the collisional quenching rates, etc. become the critical parameters of the O_3 non-LTE model to precisely predict vibrational temperatures [*Mlynczak et al.*, 1996]. Therefore, the following results, viewed as an estimation, are based on the models using current knowledge of O_3 kinetics and spectroscopy.

Estimation of the O_3 ground state population is made utilizing two models: (1) the SHARC-3 model and (2) the Simplified Single Mode (SSM) non-LTE O_3 model [*Mlynczak and Drayson*, 1990a, b]. The model atmosphere for CIRRIS-1A observation was obtained from the 2-dimensional (2-D) photochemical model of *Garcia and Solomon* [1983, 1985]. The different model inputs (e.g., the quenching rates) largely affect the vibrational temperature calculations. For example, the temperature independent quenching rate was used in the SSM model while a Landau-Teller type temperature dependent quenching rate was used in the SHARC model. It was found that the quenching rates initially used in the SSM model were larger in comparison with recent laboratory measurements [e.g., *Menard et al.* 1992; *Upschulte et al.*, 1994]. The following results, related to the SSM model, were obtained

using the modified quenching rates (scaled down by a factor of 4).

The total inferred O_3 abundance is dependent on the model predicted vibrational temperature which is shown in Figure 5. The population ratio written as a function of the vibrational temperature is $[O_3(001)]/[O_3] = \exp(-C_2\upsilon_{10}/T_{001})$, where C_2 is the second radiation constant and T_{001} is the vibrational temperature. Using the T_{001} derived from the applications of SHARC and SSM O_3 models to 2-D modeled atmosphere, the ground state number density $[O_3]$ profile was readily inferred using the above equation which applies retrieved $[O_3(001)]$ data. The $[O_3]$ profiles resulting from the SHARC and SSM modeled T_{001} and the $[O_3(001)]$ retrieved from the measurements, including the discrepancies $[([O_3]_{SHARC} - [O_3]_{SSM}) / [O_3]_{SHARC}]$, are plotted in Figure 6.
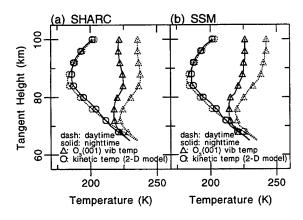
Figure 5. The 2-D photochemical model derived local kinetic temperature, and ozone υ_3 vibrational temperatures modeled by (a) SHARC-3 and (b) SSM ozone models.
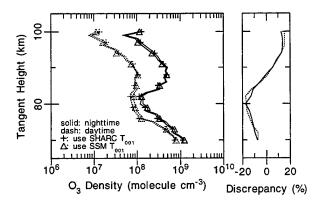
Figure 6. Inferred ozone density profiles using CIRRIS-1A O_3 υ_3 excited state population profiles in conjunction with modeled υ_3 vibrational temperatures calculated by the SHARC and SSM models. The discrepancy from the SHARC and SSM models, $([O_3]_{SHARC} - [O_3]_{SSM}) / [O_3]_{SHARC}$, was also plotted.

4. Summary / Remarks

Mesospheric O_3 infrared emission data from CIRRIS-1A shuttle-based interferometer limb measurements were analyzed. This high quality spectra data set allowed determination of the O_3 υ_3 and υ_1 fundamental bands and CO_2 band contributions. The limb profile measurement allowed the retrieval of the O_3 υ_3 excited state population used to infer the total ozone abundance which is partially based on the current knowledge of ozone formation (chemical pumping process), quenching, absorption, and other elements, as well as the modeled atmosphere. Accurate laboratory measurements of ozone kinetic parameters will be beneficial in the more precise modeling of non-LTE ozone and hence accurately retrieve mesospheric ozone measurements.

This set of data is deemed of interest because the energy loss rate through the O_3 infrared radiation (860 - 1160 cm^{-1}) can be retrieved; the energy absorption gain rate through the O_3 υ_3 band, the chemical potential energy deposition rate, and the solar energy deposition rate through the O_3 Hartley band can be evaluated based on the ozone density taken from CIRRIS-1A measurements. A more complete communication which addresses some of these issues is in preparation.

References

Ahmadjian, M., R. M. Nadile, J. O. Wise, and B. Bartschi, CIRRIS 1A space shuttle experiment, *J. Spacecr.*, *27*, 669-674, 1990.

Bingham, G. E., D. K. Zhou, B. Y. Bartschi, G. P. Anderson, D. R. Smith, J. H. Chetwynd, and R. M. Nadile, Cryogenic Infrared Radiance Instrumentation for Shuttle (CIRRIS 1A) Earth limb spectral measurements, calibration, and atmospheric O_3, HNO_3, CFC-12, and CFC-11 profile retrieval, *J. Geophys. Res.*, *102*, 3547-3558, 1997.

Garcia, R. R., and S. Solomon, A numerical model of the zonally averaged dynamical and chemical structure of the middle atmosphere, *J. Geophys. Res.*, *88*, 1379-1400, 1983.

Garcia, R. R., and S. Solomon, The effect of gravity waves on the atmosphere and low thermosphere, *J. Geophys. Res.*, *90*, 3850-3868, 1985.

Manuilova, R. O., and G. M. Shved, The 4.8 and 9.6 μm O_3 band emissions in the middle atmosphere, *J. Atmos. Terr. Phys.*, *54*, 1149-1168, 1992.

Menard, J., L. Doyennette, and F. Menard-Bourcin, Vibrational relaxation of ozone in O_3-O_2 and O_3-N_2 gas mixtures from infrared double-resonance measurements in the 200 to 300 K temperature range, *J. Chem. Phys.*, *96*, 5773-5780, 1992.

Mlynczak, M. G., and S. R. Drayson, Calculation of infrared limb emission by ozone in the terrestrial middle atmosphere 1. Source function, *J. Geophys. Res.*, *95*, 16,487-16,511, 1990a.

Mlynczak, M. G., and S. R. Drayson, Calculation of infrared limb emission by ozone in the terrestrial middle atmosphere 2. Emission calculations, *J. Geophys. Res.*, *95*, 16,513-16,521, 1990b.

Mlynczak, M. G., D. K. Zhou, and J. M. Russell, III, Kinetic and spectroscopic requirements for the SABER experiment on the TIMED mission (abstract), *Eos Trans. AGU*, *77(46)*, Fall Meet. Suppl., F546, 1996.

Rawlins, W. T., A. M. Woodward, and D. R. Smith, Aeronomy of infrared ozone fluorescence measured during an aurora by the SPIRIT 1 rocket-borne interferometer, *J. Geophys. Res.*, *98*, 3677-3691, 1993

Rothman, L. S., et al., The HITRAN molecular database: Editions of 1991 and 1992, *J. Quant. Spectrosc. Radiat. Transfer*, *48*, 469-507, 1992.

Sharma, R. D., J. H. Gruninger, R. L. Sundberg, L. S. Bernstein, D. C. Robertson, J. H. Brown, S. M. Adler-Golden, J. W. Duff, M. W. Mathew, and R. J. Healey, Users' manual for SHARC-3, strategic high-altitude radiance code, *PL-TR-96-2104*, Geophys. Dir., Phillips Lab., Hanscom Air Force Base, Mass., 1996.

Solomon, S., J. T. Kiehl, B. J. Kerridge, E. E. Remsberg, and J. M. Russell III, Evidence for nonlocal thermodynamic equilibrium in the υ_3 mode of mesospheric ozone, *J. Geophys. Res.*, *91.*, 9865-9876, 1986.

Stair, A. T., Jr., J. C. Ulwick, D. J. Baker, C. L. Wyatt, and K. D. Baker, Altitude profiles of infrared radiance of O_3 (9.6 μm) and CO_2 (15 μm), *Geophys. Res. Lett.*, *1*, 117-118, 1974.

Stair, A. T., Jr., R. Sharma, R. M. Nadile, D. J. Baker, and W. F. Grieder, Observations of limb radiance with cryogenic spectral infrared rocket experiment (SPIRE), *J. Geophys. Res.*, *90.*, 9763-9775, 1985.

Upschulte, B. L., B. D. Green, W. A. M. Blumberg, and S. J. Lipson, Vibrational relaxation and radiative rates of ozone, *J. Phys. Chem.*, *98*, 2328-2336, 1994.

Zachor, A. S., and R. D. Sharma, Retrieval of non-LTE vertical structure from a spectrally resolved IR limb radiance profiles, in *Advances in remote sensing retrieval method*, edited by Deepak, A., H. E. Fleming, and M. T. Chahine, pp. 119-132, A. Deepak, Hampton, Virginia, 1985.

Limb and below-the-horizon spectra measured by the MSX SPIRIT III interferometer; comparison to SAMM template spectra

Alexander S. Zachor
Atmospheric Radiation Consultants, Inc.

R. R. O'Neil, H. A. B. Gardiner and J. J. Gibson
Phillips Laboratory, Geophysics Directorate

W. O. Gallery
AER, Inc.
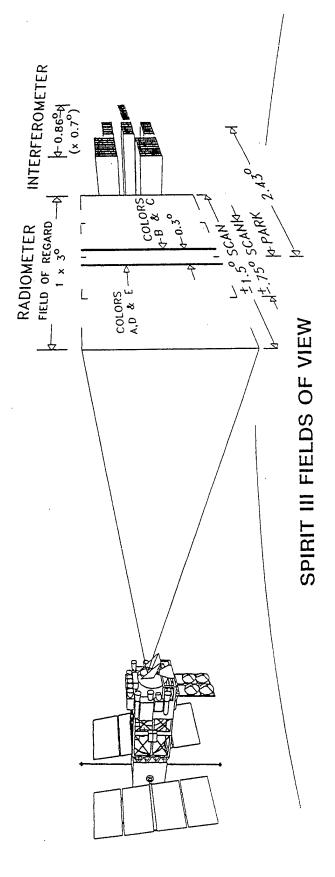
OUTLINE
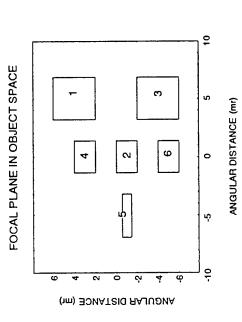
- MIDCOURSE SPACE EXPERIMENT (MSX) -- THE SPIRIT III SENSORS

- THE SPIRIT III INTERFEROMETER ABOARD MSX

- AUTOMATED PROCESSING OF THE INTERFEROMETER DATA:
  Production of data spectra and "indicator" histories
  Construction of predictive "template" spectra

- SAMPLES OF ACQUIRED SPECTRA
  From a DC37 Above-The-Horizon (ATH = limb-view) experiment
  From an EL09 Below-The-Horizon (BTH) experiment

- USE OF "INDICATORS" DERIVED FROM THE SPECTRAL DATA
  Indicator for stratospheric ozone depletion
  MWIR indicators for quantifying BTH background clutter

170

MIDCOURSE SPACE EXPERIMENT (MSX)

- a BMDO Program
- supports ballistic missile defense objectives,
  also science objectives in remote sensing and astronomy
- SPIRIT III is the primary sensor on the MSX satellite
  - is a radiometer with five bands, high spatial resolution (90 μr)
  - is an interferometer spectrometer with six channels, having
    1.2 to 4 mr spatial resolution and 2, 4 or 20 cm⁻¹ spectral resolution
  - launched 24 April 96, cryogen exhausted 22 February 97

SPIRIT III FIELDS OF VIEW

171

THE INTERFEROMETER'S SIX CHANNELS

FOCAL PLANE IN OBJECT SPACE

Channel	Spectral range (μm)	Vertical resolution[1]		Tangent height range[2] (km)
		(mr)	(km)	
5	10.5-13	1.17	4.0	8-90
2	2.6-4.9	1.85	6.3	0 (or nadir) to 70
3	5.8-8.9	3.7	12.5	30-90
1	17-28	3.7	12.5	55-120
4 (Open)[3]	3-28	1.85	6.3	60-160
6 (Prewhitened)[4]	3-26	1.85	6.3	45-130

[1] For tangent heights near 60 km
[2] Lower value corresponds to saturation (max S/N), upper one to to max[spectral S/N], (based on preflight engineering data)
[3] "Open" = "no filter"
[4] "Prewhitened" = notch attenuation (10^{-3}) over the 15 μm CO_2 band

AUTOMATED PROCESSING

OF THE INTERFEROMETER EARTHLIMB (EL) DATA

Data ingest, reduction and analysis
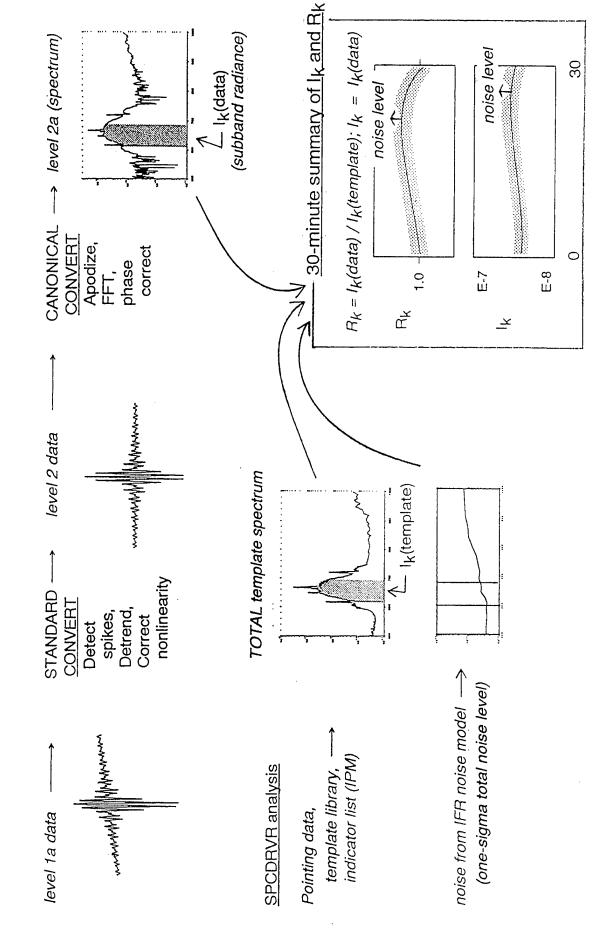
Raw data + processing Script → **STANDARD Convert** → corrected i'grams (level 2)

→ **CANONICAL Convert** → *calibrated spectra* (level 2a)

→ **automated analysis (SPCDRVR)** →

STORED PRODUCTS:

<u>SPECTRA</u>
a) **measured**
b) **templates**
   (model predictions)
c) total noise level

<u>INDICATORS</u>
e.g., **subband radiances**
(integrated spectral radiances),
ratios of these to template
   subband radiances

<u>INTERFEROGRAMS</u>
   (level 2)

OVERVIEW OF AUTOMATED ANALYSIS AND INTERACTIVE GRAPHICAL REVIEW

level 1a data → *level 2 data* → *level 2a (spectrum)*

STANDARD → CANONICAL →
CONVERT   CONVERT
Detect   Apodize,
spikes,   FFT,
Detrend,   phase
Correct   correct
nonlinearity

I_k(data)
(subband radiance)

SPCDRVR analysis

Pointing data,
template library, →
indicator list (IPM)

TOTAL template spectrum

I_k(template)

noise from IFR noise model →
(one-sigma total noise level)

30-minute summary of I_k and R_k

$R_k = I_k$(data) / I_k(template); $I_K = I_k$(data)

noise level

R_k 1.0

noise level

I_k E-7

          E-8

          0   30

174

CONSTRUCTION OF TEMPLATE SPECTRA

Template spectra include

1) atmospheric/Earth emissions
2) Non-Rejected Earth Spectral Radiance (NRESR) = off-axis light
3) zodiacal light

Atmospheric/Earth emissions (1) are based on the SAMM code
for average, tropical, cloud-free conditions, and for

a) Above-The-Horizon (ATH) viewing for DAY,
   (every 2 km in tangent height, 0-300 km)

b) ATH/NIGHT, (every 2 km in tangent height, 0-300 km)

c) Below-The-Horizon (BTH) for DAY vs. nadir angle

d) BTH/NIGHT vs. nadir angle

CONSTRUCTION OF TEMPLATE SPECTRA (continued)
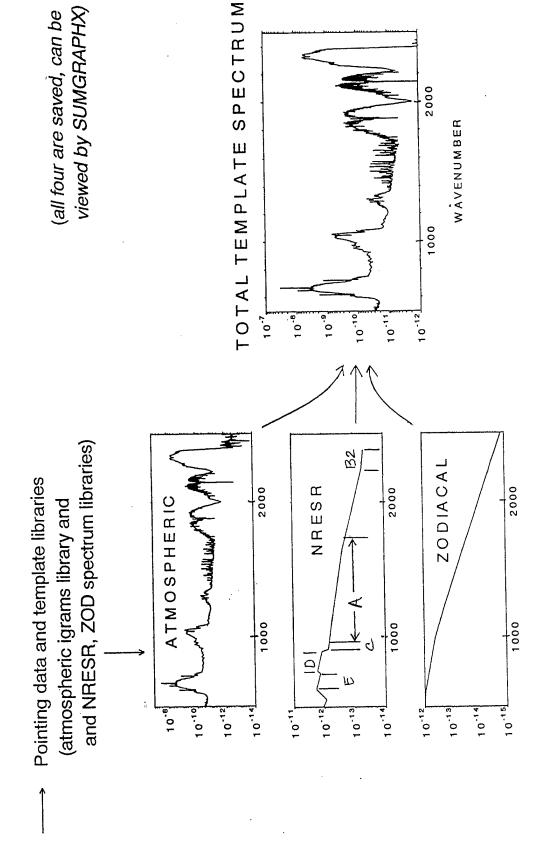
The four SAMM libraries (a-d) are

- averaged in tangent height (ATH) or nadir angle (BTH) to represent the finite spatial resolution of each interferometer channel.

- re-binned to wavenumber intervals of the FFT data reduction

- converted to interferograms that can be processed the same as the data i'grams
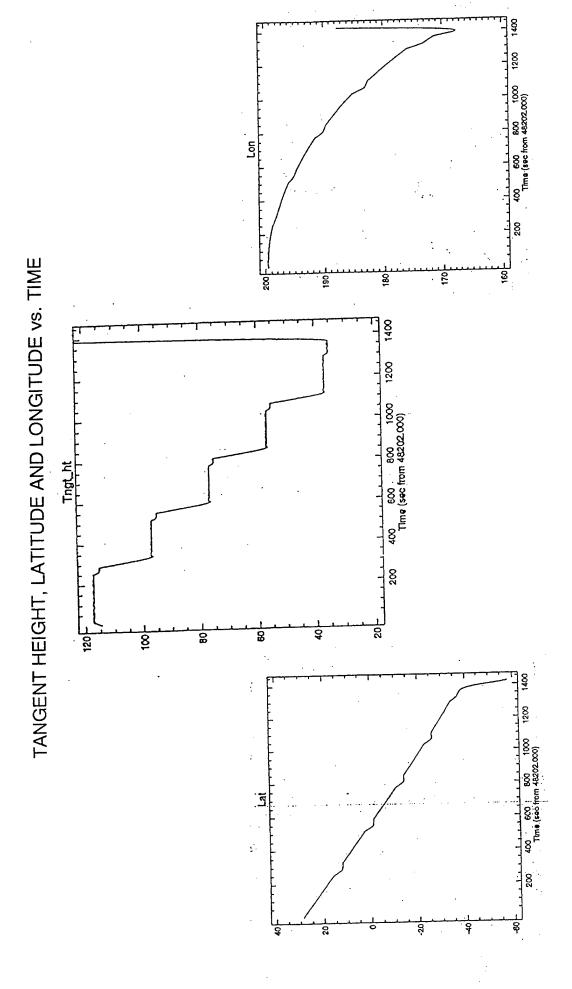
The atmospheric/Earth component of the template spectrum is "recovered" in the automated analysis from the *interferogram template library.*

It has the same spatial resolution, spectral resolution and instrument spectral line shape as the data spectra.
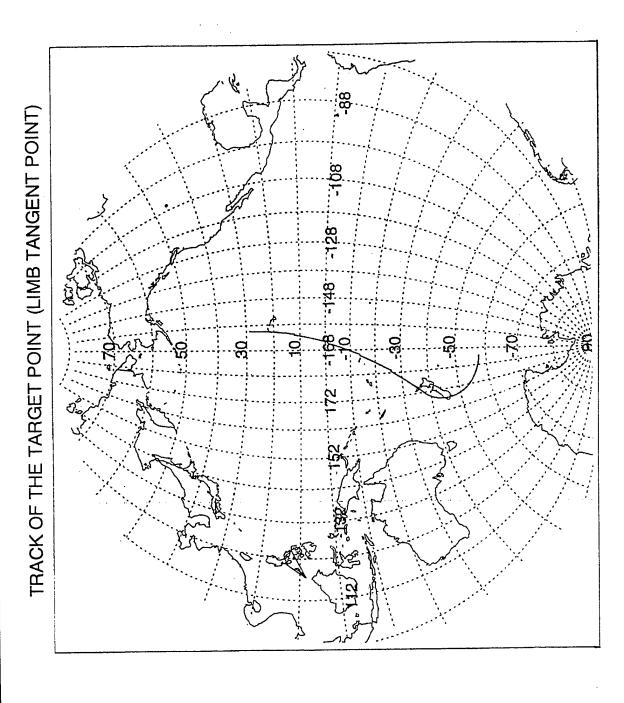
TEMPLATE SPECTRA CONSTRUCTED IN THE AUTOMATED ANALYSIS

→ Pointing data and template libraries
  (atmospheric igrams library and
  and NRESR, ZOD spectrum libraries)

*(all four are saved, can be
viewed by SUMGRAPHX)*

177

TANGENT HEIGHT, LATITUDE AND LONGITUDE vs. TIME
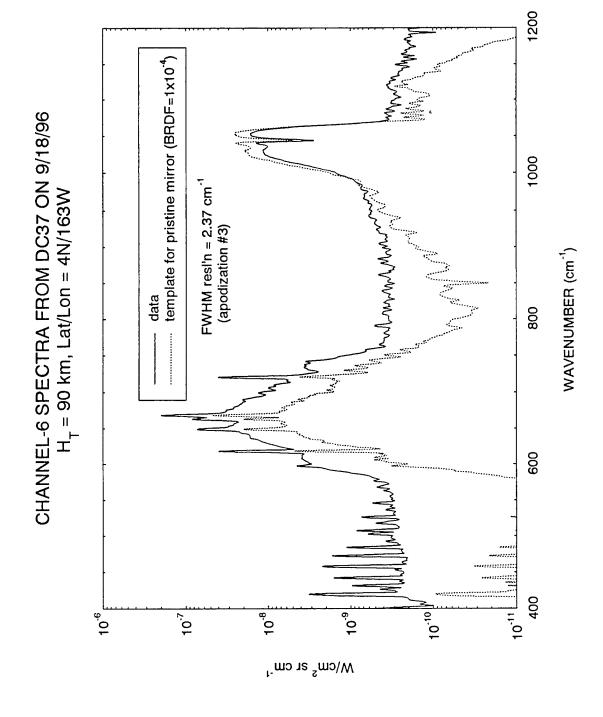
DCATT EXPERIMENT DC370100005 ON 18 SEPTEMBER 1996
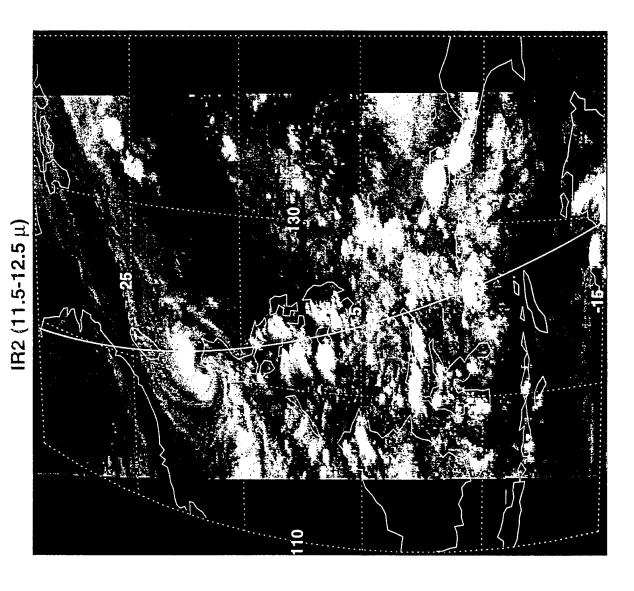
TRACK OF THE TARGET POINT (LIMB TANGENT POINT)

CHANNEL-6 SPECTRA FROM DC37 ON 9/18/96
H_T = 90 km, Lat/Lon = 4N/163W

data
template for pristine mirror (BRDF=1×10^{-4})

FWHM resl'n = 2.37 cm^{-1}
(apodization #3)

WAVENUMBER (cm^{-1})

W/cm^2 sr cm^{-1}

CHANNEL-6 SPECTRA FROM DC37 ON 9/18/96
H_T = 90 km, Lat/Lon = 4N/163W

data
template (BRDF=8x10^{-3})

FWHM resl'n = 2.37 cm^{-1}
(apodization #3)

W/cm^2 sr cm^{-1}

WAVENUMBER (cm^{-1})

CHANNEL-1 SPECTRA FROM DC37 ON 9/18/96
H_T = 80.6 km, Lat/Lon = 7S/168W

Legend:
— data
···· template (BRDF=8x10^{-3})

FWHM resl'n = 2.07 cm^{-1}
(apodization #2)

X-axis: WAVENUMBER (cm^{-1})
Y-axis: W/cm^2 sr cm^{-1}

EARTHLIMB EXPERIMENT EL090200050 ON 18 OCTOBER 1996

GMS-5: 8:32 on October 18, 1996

IR2 (11.5-12.5 μ)

Thu May 29 12:29:00 1997

SPECTRAL DATA BASE ACQUIRED IN EL0902000050

- NADIR ANGLE NEARLY CONSTANT = 55.5 DEGREES

- ALL DATA IS FROM CHANNEL 2, WHICH COVERS 2.6-4.9 μm
  - ONLY CHANNEL NOT SATURATED FOR BTH VIEW

- SPIRIT III RADIOMETER NOT IN OPERATION

- 2200 CHANNEL-2 INTERFEROGRAMS OBTAINED BETWEEN ~40° S. AND ~40° N.

- INTERFEROGRAMS OBTAINED IN "SHORT-STROKE" MODE
  - MAXIMUM ALONG-TRACK SAMPLING, BUT
    LOWEST SPECTRAL RESOLUTION

- I'GRAMS PROCESSED TO SPECTRA USING KAISER-BESSEL APODIZATION:
  - OBTAINED 20 cm^{-1} FWHM SPECTRAL RESOLUTION $\cong$ 0.037 μm AT 4.3 μm
  - FIRST SIDELOBE IS 2.2 x 10^{-4} (10^{-3} RELATIVE TO SINC FUNCTION)
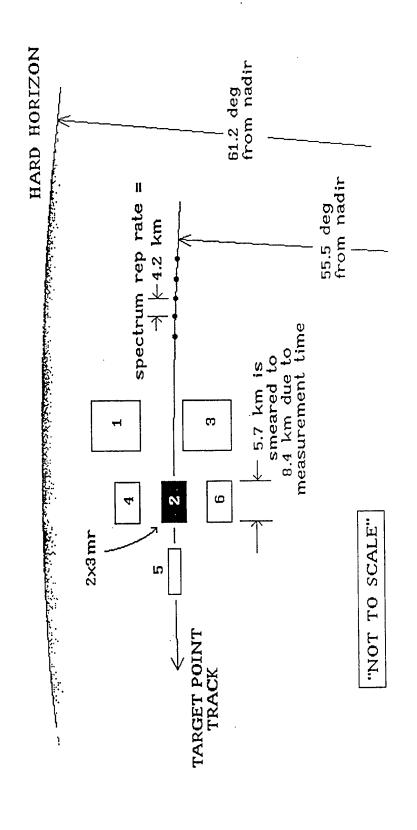
SPATIAL RESOLUTION AND SAMPLING RATE

HARD HORIZON

61.2 deg
from nadir

55.5 deg
from nadir

spectrum rep rate =
|← 4.2 km

1

3

4

2

6

5

2×3 mr

5.7 km is
smeared to
8.4 km due to
measurement time

TARGET POINT
TRACK

"NOT TO SCALE"

this page intentionally blank

FIVE SPECTRA NEAR 12° SOUTH (CLOUD-FREE REGION)
AND THE B1, B2 NORMALIZED FILTER SPECTRAL TRANSMITTANCES

FILTER TRANSMITTANCE

WAVELENGTH (μm)

W/cm² sr μm

186

EIGHT SPECTRA NEAR THE EQUATOR (ITCZ BROKEN CLOUDS)
AND THE B1, B2 NORMALIZED FILTER SPECTRAL TRANSMITTANCES
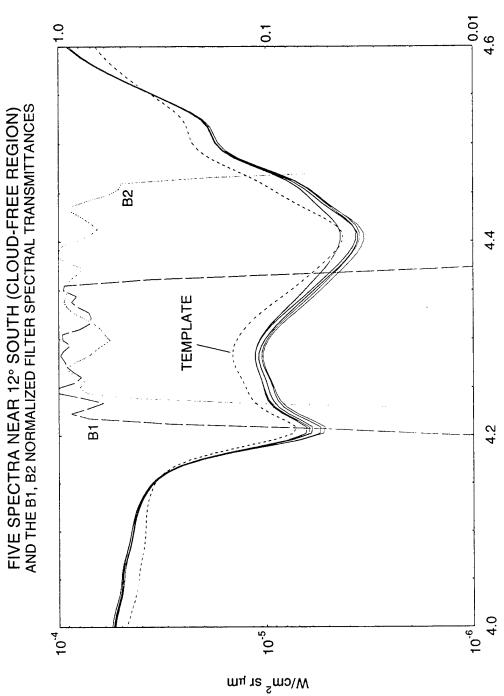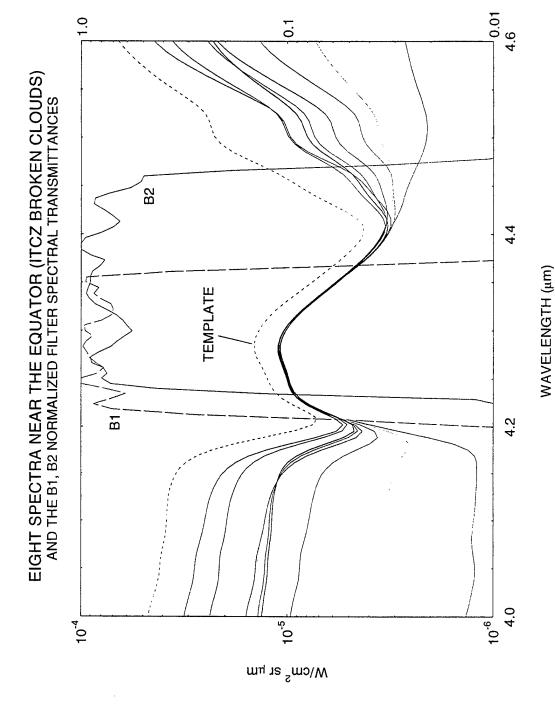
EXAMPLES OF THE USE OF "INDICATOR" HISTORIES

- ## *USE OF BAND RADIANCE (I$_k$ type) INDICATORS*

$$I_k(t) \equiv \int_{\lambda k1}^{\lambda k2} I_\lambda (measured \ @ \ time \ t) \, d\lambda \quad = \quad \text{"subband-k" radiance history}$$

Cumulatively sum the radiance histories I$_k$(t) for successive (contiguous) subbands to find the "red" cutoff that minimizes sensitivity to background clutter for a candidate MWIR midcourse detection band

- ## *USE OF RATIO TYPE (R$_k$ type) INDICATOR*

Indicator AG-056-5 is for recognizing ozone depletion.
Its value is the ratio
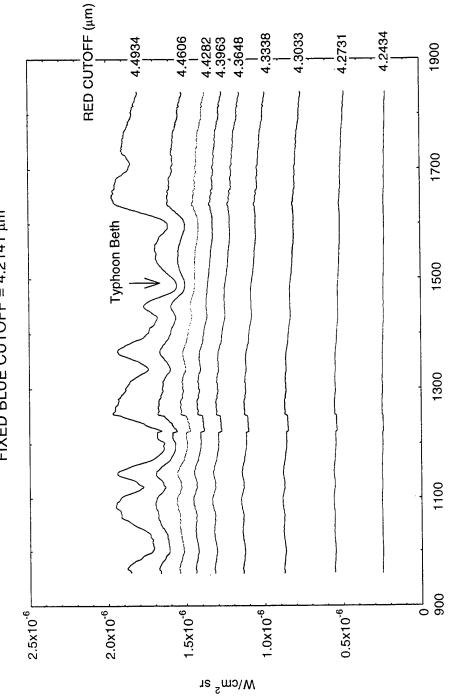
$$R \equiv \int_{12.7 \, \mu m}^{12.9 \, \mu m} I_\lambda (measured) \, d\lambda \ \bigg/ \ \int_{12.7 \, \mu m}^{12.9 \, \mu m} I_\lambda (template) \, d\lambda$$

which is computed versus tangent height (vs. time in EL19 experiments).
R vs. H$_\tau$ is compared to a threshold value that indicates O3 depletion.

RADIANCE HISTORIES AFTER 30-POINT WINDOW SMOOTH
FIXED BLUE CUTOFF = 4.2141 μm

RED CUTOFF (μm)

4.4934
4.4606
4.4282
4.3963
4.3648
4.3338
4.3033
4.2731
4.2434

Typhoon Beth

W/cm² sr

2.5x10⁻⁶
2.0x10⁻⁶
1.5x10⁻⁶
1.0x10⁻⁶
0.5x10⁻⁶
0

900   1100   1300   1500   1700   1900
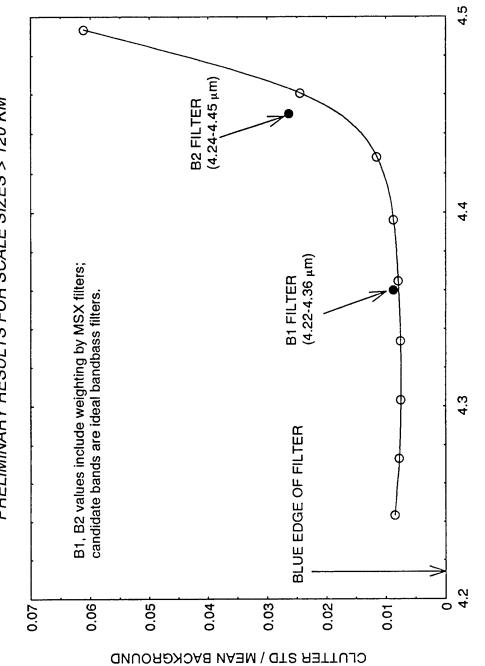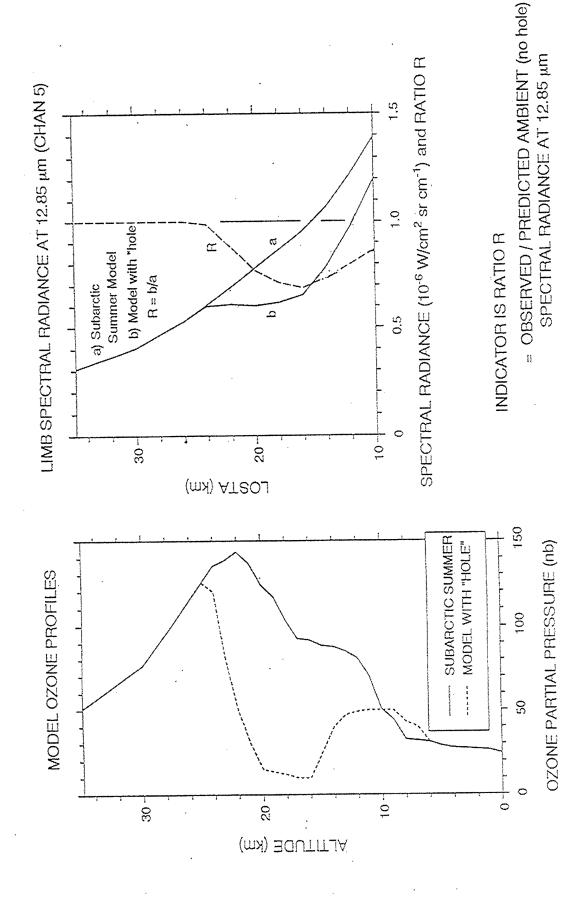
SPECTRUM NUMBER

PERFORMANCE OF CANDIDATE DETECTION/SURVEILLANCE FILTERS
PRELIMINARY RESULTS FOR SCALE SIZES > 120 KM

B1, B2 values include weighting by MSX filters; candidate bands are ideal bandbass filters.

B2 FILTER (4.24-4.45 μm)

B1 FILTER (4.22-4.36 μm)

BLUE EDGE OF FILTER

CLUTTER STD / MEAN BACKGROUND

RED EDGE OF FILTER (μm)

AN INDICATOR FOR OZONE DEPLETION ("OZONE HOLE")

LIMB SPECTRAL RADIANCE AT 12.85 µm (CHAN 5)

a) Subarctic Summer Model
b) Model with "hole"
R = b/a

R

a

b

LOSTA (km)

30

20

10

SPECTRAL RADIANCE (10⁻⁶ W/cm² sr cm⁻¹) and RATIO R

0   0.5   1.0   1.5

INDICATOR IS RATIO R

= OBSERVED / PREDICTED AMBIENT (no hole)
SPECTRAL RADIANCE AT 12.85 µm

MODEL OZONE PROFILES

SUBARCTIC SUMMER
MODEL WITH "HOLE"

ALTITUDE (km)

30

20

10

OZONE PARTIAL PRESSURE (nb)

0   50   100   150

Pure Rotation Emissions From Mesospheric OH Observed Using the SPIRIT III Interferometer

P S Armstrong[2], S J Lipson[1], R R O'Neil[1], H A Gardiner[1], A Zachor[3], M Kendra[4], J J Gibson[1], J A Dodd[2], D L Vititoe[1], W A M Blumberg[1], K Farnham[4], and T Woolston[5]

[1]Phillips Laboratory Geophysics Directorate, Hanscom Air Force Base, MA

[2]Stewart Radiance Laboratory, Bedford, MA

[3]ARC, Inc., Acton, MA

[4]Radex Inc., Bedford, MA

[5]Utah State University, Logan, UT
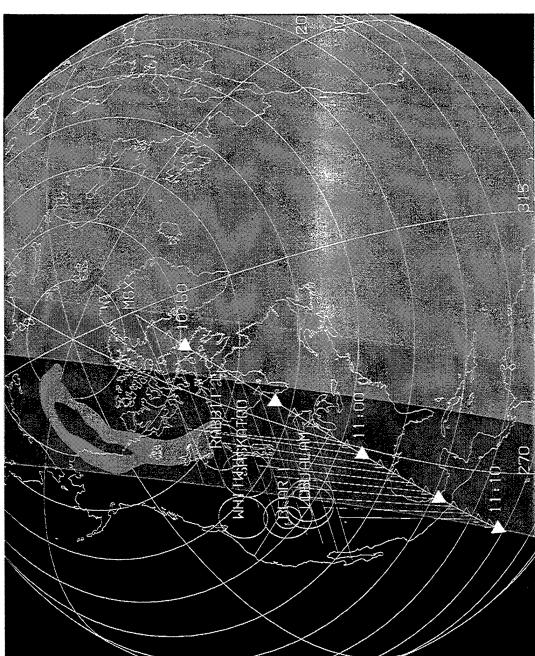
The 20th Annual Review Conference of Atmospheric Transmission Models

11 June 1997

Phillips Laboratory, Geophysics Directorate, Hanscom AFB, MA

MSX Earthlimb Measurement: October 8, 1996
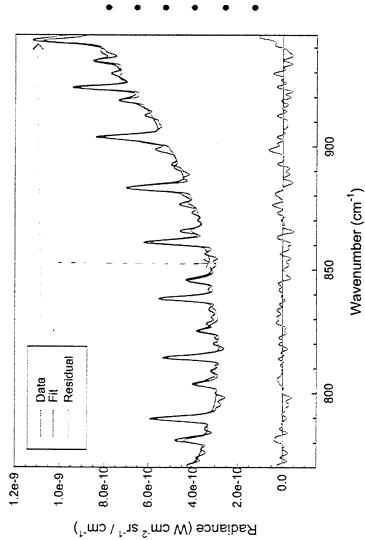
OH Pure Rotation Emissions

- Radiance results from *very high* rotational excitation (2 eV)
- $\Delta v=0$, $\Delta N=-1$ transitions from OH($v=0-3$, $N=24-31$)
- Nighttime data: SZA 114°
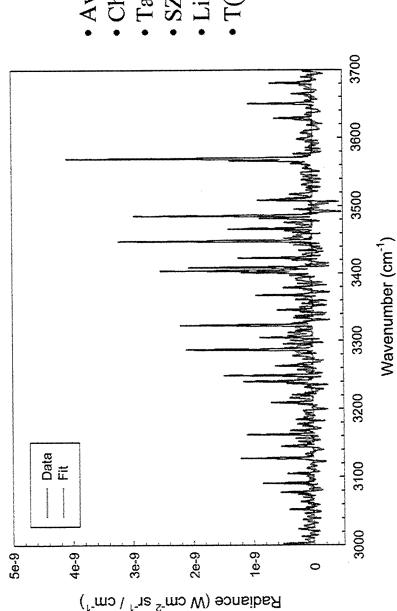
- Average of 10 spectra
- Channel 5 data
- Tangent height 84.9 km
- Linewidth 1.8 cm^{-1}
- Effective T(rotation) 8000 K
- Empirical baseline fit

Plot legend: Data, Fit, Residual

Y-axis: Radiance (W cm^{-2} sr^{-1} / cm^{-1}), 0.0, 2.0e-10, 4.0e-10, 6.0e-10, 8.0e-10, 1.0e-9, 1.2e-9

X-axis: Wavenumber (cm^{-1}), 800, 850, 900

OH Fundamental Band Emissions

- Radiance from rotationally thermal states of $OH(X\,^2\Pi)$
- Observed $\Delta v = -1$ transitions originating from $v = 1\text{-}9$
- Fitting $v > 6$ requires modeling additional molecular emitters
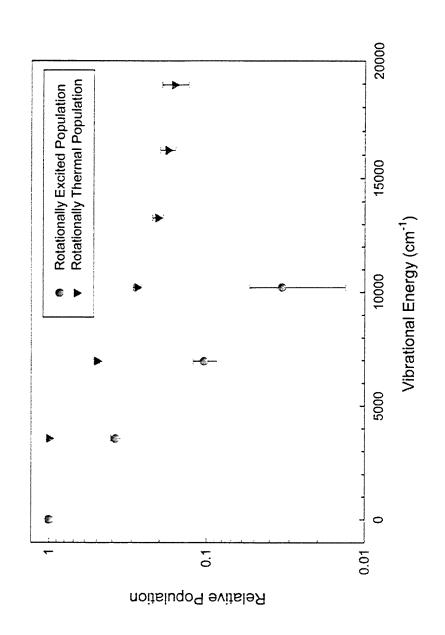
- Average of 6 spectra
- Channel 2 data
- Tangent height 85.3 km
- SZA 122°
- Linewidth 1.9 cm^{-1}
- T(rotation)= 205 ± 11 K

Radiance (W cm^{-2} sr^{-1} / cm^{-1})

Wavenumber (cm^{-1})

Data
Fit

OH Vibrational Distributions

- Determined from synthetic spectral fitting

- Normalized to lowest vibrational level observed
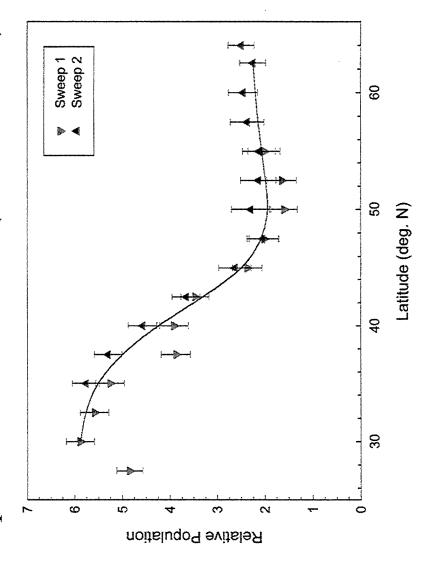
Latitude Dependence: Rotationally Excited Population

- Two consecutive, overlapping sweeps
- Duration of about 10 minutes each
- Population shown for OH(v=0, N=24-31)
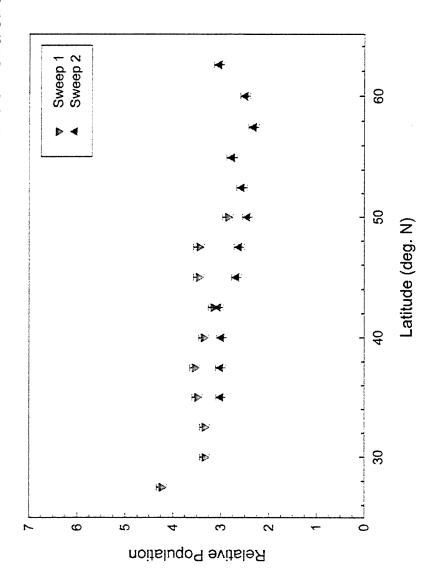
Latitude Dependence:
Rotationally Thermal Population

- Population shown for OH(v=1, N≈1-5)
- Less variation than observed for high-N states
- Geometric and kinetic effects to be considered

Summary

- **MSX OH spectra: what's new**
  - Simultaneous high-resolution measurements of high-N pure rotation emissions and low-N fundamental bands
  - Continuous coverage of over 30 degrees of latitude
  - Coordinated ground measurements
  - Extends previous observations

- **Determination of OH populations**
  - Synthetic spectral fitting
  - OH vibrational and rotational distributions
  - Strong latitude dependence of the high-N population
  - Implications for odd oxygen chemistry models

MSX: Overview of the 15 uM CO_2 Limb Emission Measurements

J O Wise, R R O'Neil, H Gardiner, J R Winick, and R H Picard
(Geophysics Directorate, Phillips Laboratory)

P P Wintersteiner (Arcon Corp, Waltham Mass)

U B Makhlouf (Stewart Radiance Lab, Bedford, Mass)

M Kendra (Radex Corp, Bedford, Mass)

Band D Data

- Filter Bandpass: 13.5 – 15.9 microns
- Focal Plane Arrays: 4 columns x 192 pixels each
- Detector Size: 90 microrad
- Full Latitudinal Coverage
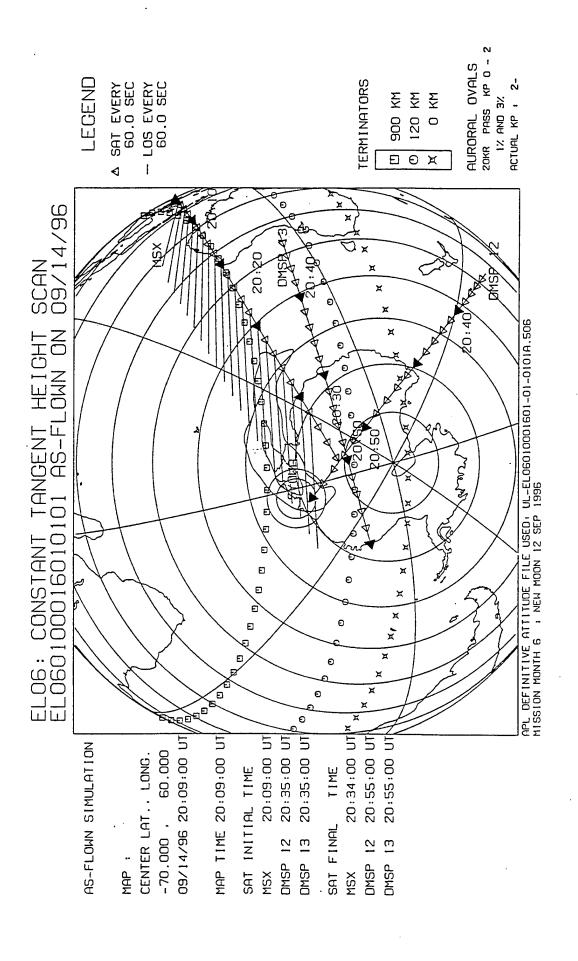
High Latitude (Auroral) Scenes

- There is evidence of latitudinal structure, with increased radiance above 110 km with increasing latitude.

- Band B (4.3 um CO_2) indicates presence of aurora.

- 15 um CO_2 in lower thermosphere is due to thermal excitation of CO_2 by atomic oxygen.

- Depletions in 15 um at ~105 km appear to correspond with the 4.3 um enhancements - may be due to depletions in atomic oxygen concentration [*Hecht et al.*, 1991, *Hays et al.*, 1973]. The downward flow of atomic oxygen is enhanced during particle and Joule heating events.
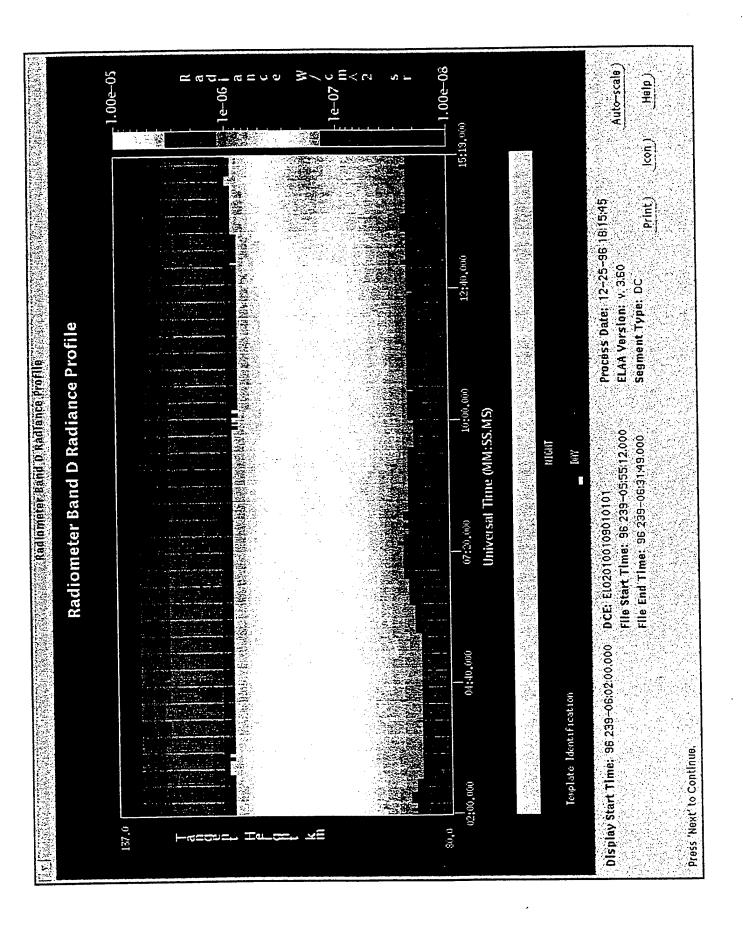
Low to Mid-Latitude Scenes
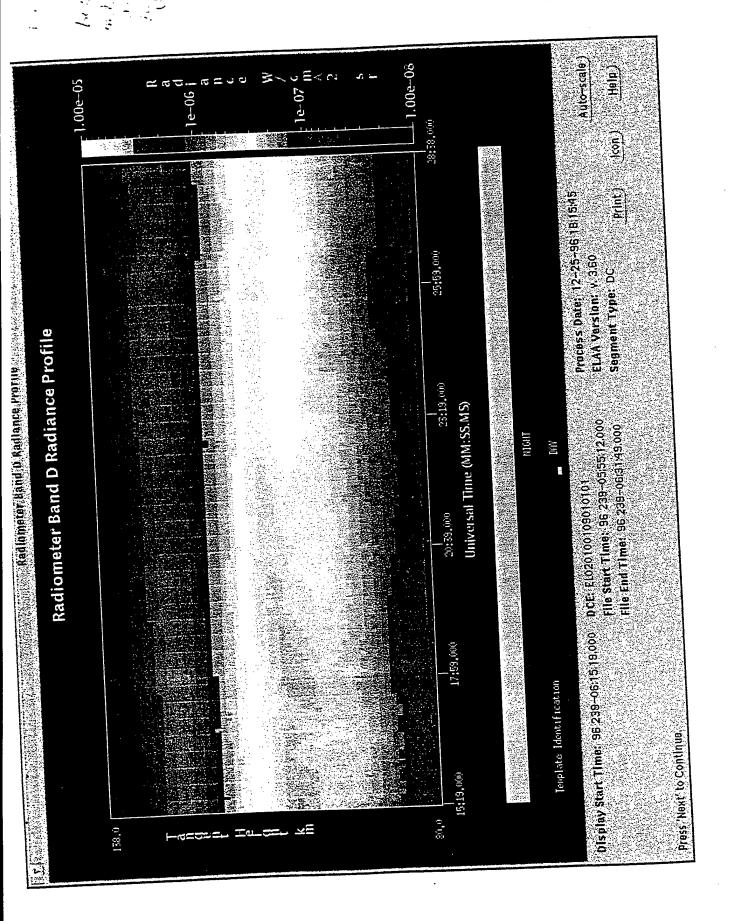
- Emissions are much more benign than the high latitude scenes, but there is evidence of dynamic activity around 105 km which is related to variations in atomic oxygen, CO_2, and temperature.

- Enhancement in emission near the equator.

EL06: CONSTANT TANGENT HEIGHT SCAN
EL06010001601010101 AS-FLOWN ON 09/14/96

LEGEND

△ SAT EVERY 60.0 SEC
— LOS EVERY 60.0 SEC

TERMINATORS

⊞ 900 KM
⊖ 120 KM
✕ 0 KM

AURORAL OVALS
20KR PASS KP 0 - 2
1% AND 3%
ACTUAL KP : 2-

AS-FLOWN SIMULATION

MAP :
CENTER LAT., LONG.
-70.000 , 60.000
09/14/96 20:09:00 UT

MAP TIME 20:09:00 UT

SAT INITIAL TIME
MSX   20:09:00 UT
DMSP 12   20:35:00 UT
DMSP 13   20:35:00 UT

SAT FINAL TIME
MSX   20:34:00 UT
DMSP 12   20:55:00 UT
DMSP 13   20:55:00 UT

APL DEFINITIVE ATTITUDE FILE USED: UL-EL06010001601-01-0101A.506
MISSION MONTH 6 ; NEW MOON 12 SEP 1996

PLH/GPD/RADEX
12/31/96

204

Conclusions

- MSX Spirit III Band D (15 um) data is unique because:

  - The vertical array of detectors allows for simultaneous coverage of about 60 kms in altitude vs time to generate a 2-Dimensional image.

  - Narrow band (13.5-15.9um) superior to that of CIRRIS (8-17um) since it can reject ozone (v3) below 100 km. This will help quantify the CO_2 cooling rates.

  - Can be examined simultaneous with other SPIRIT III radiometer bands such as 9.6 um O_3 and 4.3 um CO_2.

- 15 um data indicate:

  - Enhancements in 4.3 um CO_2 during aurorae are coincident with depletions in 15 um CO_2. This is probably due to depletions in O during geomagnetic activity.

205

Radiometer Band D Radiance Profile

Radiometer Band D Radiance Profile

Radiometer Band B Radiance Profile

Universal Time (MM:SS.MS)

Template Identification

Display Start Time: 96-239-06:02:00.000 **DCE:** E102010109010101 **Process Date:** 12-24-96 17:41:00
File Start Time: 96-239-05:55:12.000 **ELAA Version:** v.3.60
File End Time: 96-239-06:31:49.000 **Segment Type:** DC

Print   con   Auto-scale   Help

Press 'Next' to Continue.

208

Radiometer Band B Radiance Profile

Press 'Next' to Continue.

MSX: Middle–Atmospheric Structure in 4.3 μm Emission Data. I. Observations
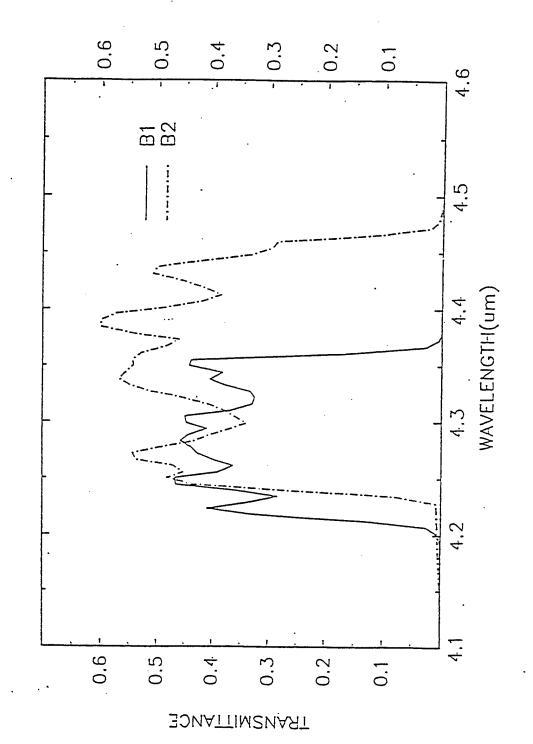
R. H. Picard, R. O'Neil, H. Gardiner, J. Gibson, E. M. Dewan, J. R. Winick, J. Brown, G. P. Anderson, Phillips Lab / Geophysics, Bedford, Mass.

E. R. Hegblom, N. A. Grossbard, E. Richards, Boston College ISR, Chestnut Hill, Mass.

U. B. Makhlouf, Stewart Radiance Lab, Bedford, Mass.

Abstract

Much MSX radiometer data from the 4.3-mm spectral region dominated by CO_2 n_3-band emission features shows evidence of significant structure arising in the cloud-free atmosphere. This occurs in both below-the-horizon (BTH) and above-the-horizon (ATH) data-gathering modes. In particular, wavelike structures are seen for the first time in this band in the MSX 4.3-mm BTH data taken at large nadir angles near 57°. Such data taken on the night of 17 August 1996 near 11 UT over the Indian subcontinent and Tibet are analyzed in more detail. The radiometer array covers 1° in angle, with individual elements covering 80 m in nadir view and roughly 200 m at 57° nadir angle. The structures are observed in both the narrow B1 band imagery (4.22- 4.36 mm), which is confined to the heart of the strongest n_3 band, and the wide B2 band imagery (4.24-4.45 mm), which has extended response on the long-wave side encompassing hot and isotopic bands. Both filters have very steep edges resulting in high out-of-band rejection. Clouds are ruled out because the structure is very different in form than cloud structure, which is seen in nadir views, and because the radiance weighting functions for both bands peak near 40 km and are very narrow, at least for the B1 band. The wavelike structures appear to have scales of 30 km with a maximum fractional radiance modulation of 2.2%, independent of band. Pronounced BTH wavelike structures were also observed in a later staring data collection over Central Florida. Here waves were observed for the whole duration of the data collection with nadir angles varying between 41° and 60°. The most likely explanation of the structure is that it is caused by atmospheric gravity waves.

211

OCLI FILTERS WITH DSI BEAM SPLITTERS,BLOCKERS

212

MSX Structure – Problem & Approach
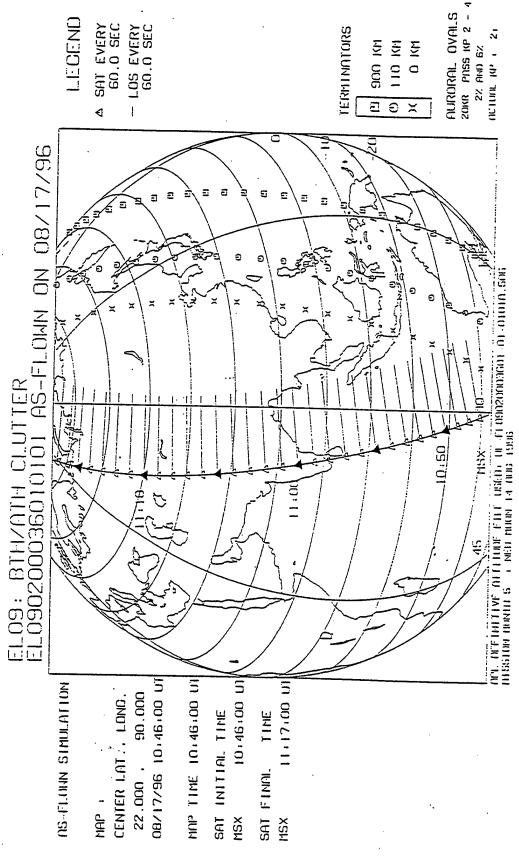
- Survey MSX 4.3-μm database BTH / ATH (below- / above-the-horizon) for evidence of structure

- Emphasize BTH data in 4.3-μm Bands B1 & B2:
  - B1: narrow (4.22–4.36 μm)– heart of CO_2 ν_3 band
  - B2: wide (4.24–4.45 μm)– includes hot, isotopic bands

- Find morphologies of 4.3-μm structure fall into two different classes, one associated with clouds & the other distinctly different

- Second class of structures must originate at higher altitude ($\geq$ 40 km) due to the nature of radiative transfer in 4.3-μm CO_2 ν_3 bands

- Higher-altitude structure is consistent with origin in internal gravity waves (GW)

213
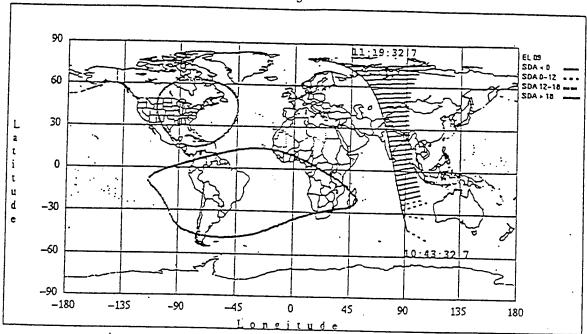
MSX Structure - Observations

DATE	EXPERIMENT†	UT DAY/HR:MIN	OBSERVATION
• 25 May 96	EL18	146/08:06	High Cloud
• 17 Aug 96	EL09	230/11:03	Wavelike
• 10 Sep 96	EL18	254/09:27	Wavelike
• 2 Oct 96	EL09	276/21:02	Wavelike
• 13 Nov 96	EL09	318/10:32	Wavelike

†Experiments: EL09 - ATH / BTH Clutter

EL18 - BTH Clutter

EL09: BTH/ATH CLUTTER
EL0902000360101 AS-FLOWN ON 08/17/96

AS-FLOWN SIMULATION

MAP :
CENTER LAT., LONG.
22.000 , 90.000
08/17/96 10:46:00 UT

MAP TIME 10:46:00 UT

SAT INITIAL TIME
MSX   10:46:00 UT

SAT FINAL TIME
MSX   11:17:00 UT

LEGEND

△   SAT EVERY
     60.0 SEC

—   LOS EVERY
     60.0 SEC

TERMINATORS

☐   900 KM
⊙   110 KM
✕   0 KM

AURORAL OVALS
20KR PASS KP 2 - 4
2% AND 6%
ACTUAL KP = 2:

10:50
11:00
11:10
45

EL09   17 August 1996

EL18 25 May 1996   (part 3)
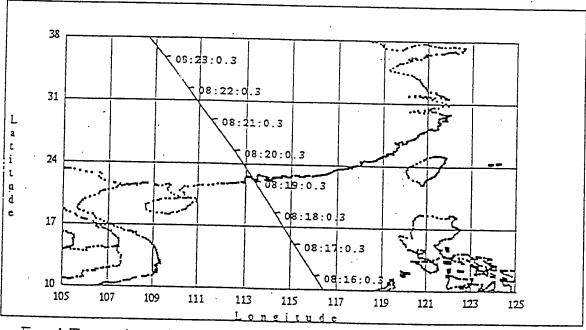
Figure 1. The ground trace of the MSX spacecraft and the target point at 1 minute intervals. The upper figure is for the 17 August 1996 EL09 (nadir angle 57.5 deg.) data collection event. In the lower figure the satellite ground trace and the target point trace are nearly coincident for the 25 May 1996 EL18 (nadir angle 1.5 deg.) measurement.

216
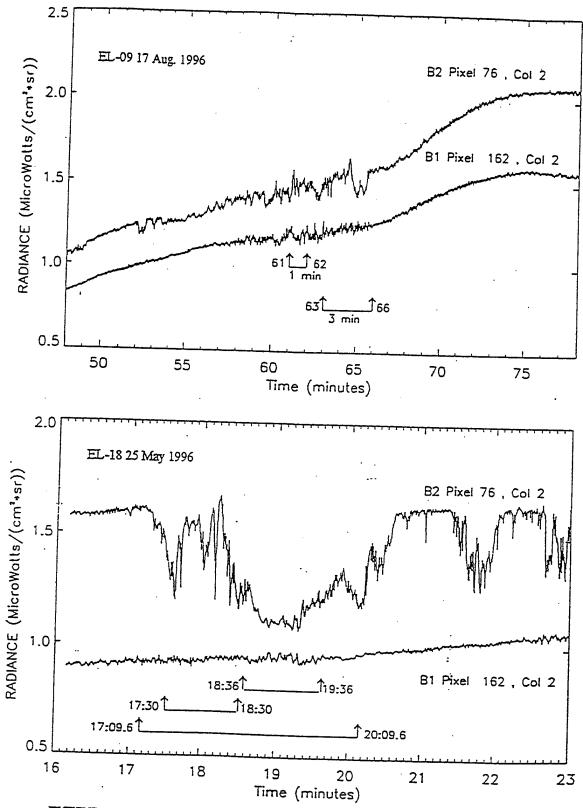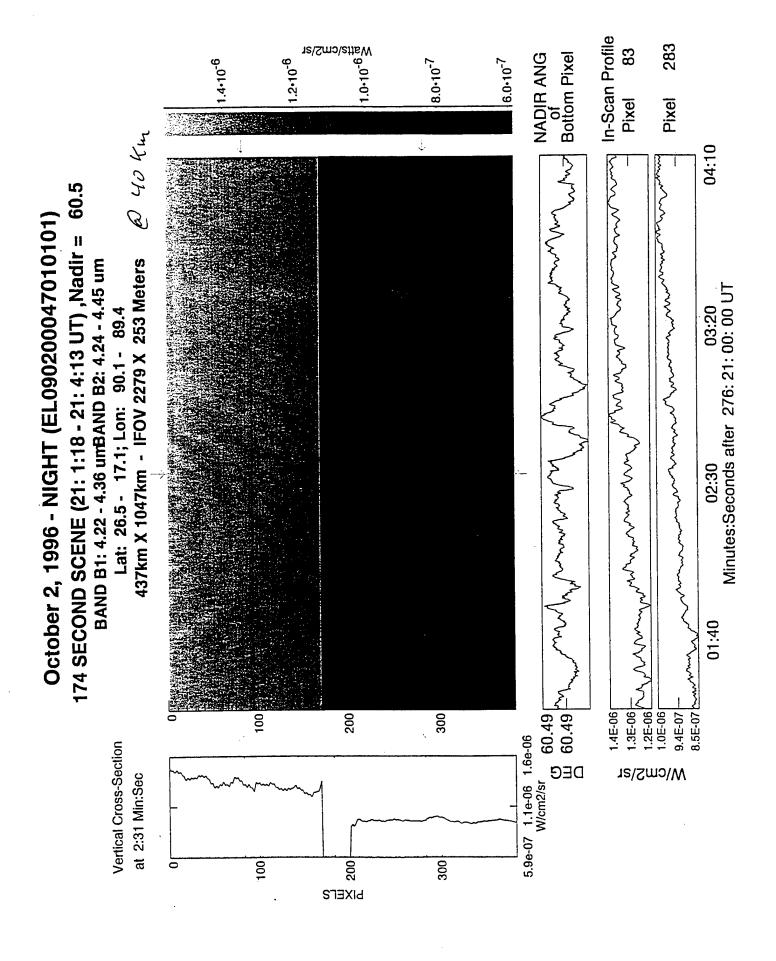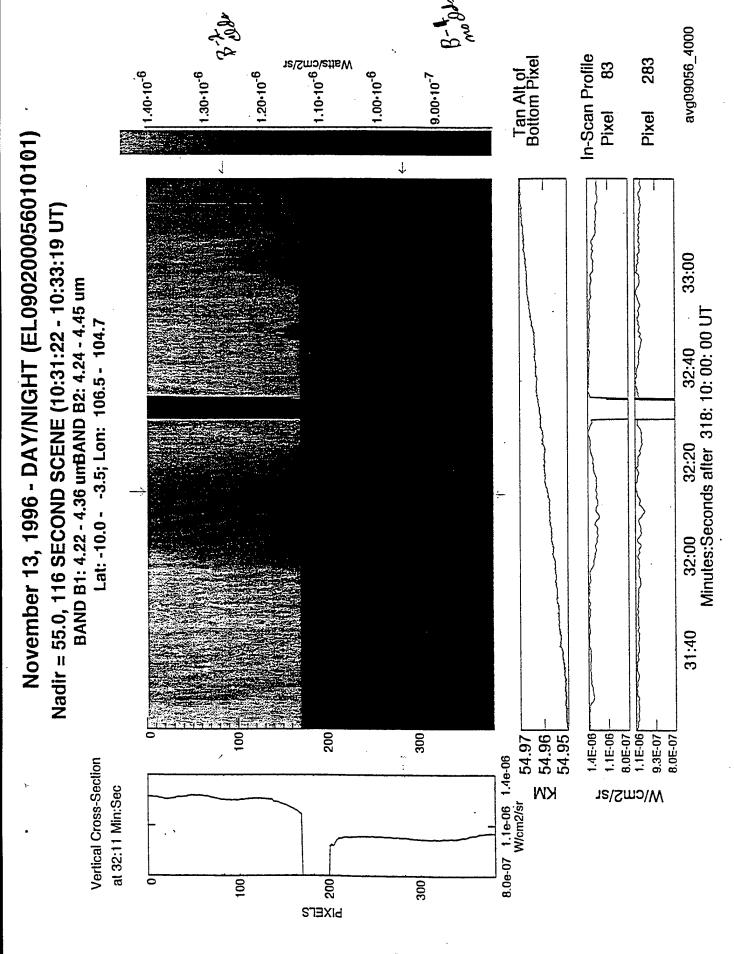
FIGURE 2. BTH B1 and B2 radiometer data for a single pixel in each band. The upper figure is for the 17 August 1996 EL-09 (nadir angle 57.5 deg.) measurement and the lower figure shows the 25 May 1996 EL-18 (nadir angle 1.5 deg.) data.

October 2, 1996 - NIGHT (EL090200047010101)

174 SECOND SCENE (21: 1:18 - 21: 4:13 UT) ,Nadir = 60.5

BAND B1: 4.22 - 4.36 um BAND B2: 4.24 - 4.45 um

Lat: 26.5 - 17.1; Lon: 90.1 - 89.4

437km X 1047km - IFOV 2279 X 253 Meters

@ 40 Km

Vertical Cross-Section at 2:31 Min:Sec

NADIR ANG of Bottom Pixel

In-Scan Profile

Pixel 83

Pixel 283

Minutes:Seconds after 276: 21: 00: 00 UT

November 13, 1996 - DAY/NIGHT (EL09020005601010101)

Nadir = 55.0, 116 SECOND SCENE (10:31:22 - 10:33:19 UT)
BAND B1: 4.22 - 4.36 umBAND B2: 4.24 - 4.45 um
Lat: -10.0 - -3.5; Lon: 106.5 - 104.7

avg09056_4000

219

MSX Structure - 4.3-μm Radiative Transfer

- 4.3-μm CO_2 ν_3 bands are severely self-absorbed in BTH (downlooking) and ATH (limb) lines-of-sight

- Above ~45 km in the daytime (~65 km at night) there are deviations from LTE (local thermodynamic equilibrium)

- Use non-LTE codes to calculate atmospheric radiance and its distribution with altitude (weighting function)

   - SAMM (SHARC And MODTRAN Merged)

   - ARC (Atmospheric Radiance Code)

LTE and Non-LTE Radiative Transfer

- **LTE**
  - Source function in equation of transfer Planckian, determined solely by temperature T

- **Non-LTE**
  - Processes (non-LTE):
    - energy transfer from/to $N_2(v)$ to/from CO_2 v_3 vibrational mode
    - radiative excitation of CO_2 v_3
    - radiative loss of CO_2 v_3
    - Integrate optically thick/thin 4.3-μm CO_2 v_3 lines over line-of-sight
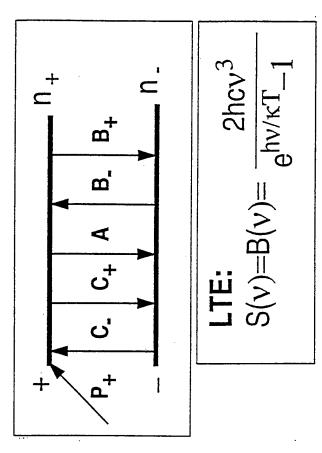
221

The LTE and Non-LTE Radiative Transfer Problem

- Solve coupled equations for monochromatic specific intensity of radiation and species / level population densities

  - Equation of transfer:

  $$\frac{dI(\nu)}{d\tau_\nu} = S(\nu) - I(\nu)$$

  - Source function:

  $$S = \frac{\frac{n'}{n''}A}{B_+ - \frac{n'}{n''}B_-}$$

  - Rate equation:

  $$\frac{dn_+}{dt} = P_+ + (C_- + B_- \bar{J})n_- - (C_+ + A + B_+ \bar{J})n_+$$

  $\bar{J}$ = integrated mean intensity = average of I(ν) over absorption line and over solid angle

LTE:
$$S(\nu) = B(\nu) = \frac{2hc\nu^3}{e^{h\nu/\kappa T} - 1}$$

SAMM (SHARC And MODTRAN Merged)

- Narrow band model (2 cm^{-1}) IR radiative-transfer code

  - Ground to 300 km

  - Lower atmosphere: MODTRAN

  - Upper atmosphere: SHARC

- Includes non-LTE effects, refraction, molecular and aerosol single / multiple scattering, single-scatter solar radiance

- Path averages by Curtis-Godson approximation

ARC (Atmospheric Radiance Code)

- First-principles non-LTE (non-local thermodynamic equilibrium) model

- Solve equation of transfer coupled to rate equations for level populations

- Line-by-line method for radiative transfer

- Calculate excited-state population or vibrational temperature T_{vib}, including radiative and collisional excitation/loss $\dfrac{N_+}{N_-} = \dfrac{g_+}{g_-} \bullet \exp\left(\dfrac{E_+ - E_-}{k_B T_{vib}}\right)$

- Calculate line-of-sight radiance spectra including opacity effects

Production & Loss Processes - $CO_2(\nu_3)$

-Radiative (4.3 μm)

$$CO_2(\nu'_1\nu'_2\nu'_3) \underset{B\bar{J}}{\overset{A}{\Leftrightarrow}} CO_2(\nu'_1\nu'_2\nu''_3) + h\nu$$

(solar and earthshine pumped; strong diurnal variation)

-Collisional (V-T)

$$CO_2(\nu'_1\nu'_2\nu'_3) + M \underset{k}{\overset{k}{\Leftrightarrow}} CO_2(\nu'_1\nu'_2\nu''_3) + M$$

(M=N$_2$, O$_2$, O)

-Vibrational transfer (V-V)

$$CO_2(\nu'_1\nu'_2\nu'_3) + N_2 \underset{k_v'}{\overset{k_v}{\Leftrightarrow}} CO_2(\nu'_1\nu'_2(\nu'_3-1)) + N_2(\nu=1)$$

$\Delta E = 19.2$ cm^{-1}; $k_v = 5.0 \times 10^{-13}(300/T)^{0.5}$

Production & Loss Processes - $N_2(v)$

-Collisional (V-T)

$N_2(v=1) + M <\text{--}> N_2(v=0) + M, \quad k_0$

-Vibrational transfer (V-V)

$N_2(v=1) <\text{--}> CO_2(v_3)$

$N_2(v=1) + O_2(v=0) \text{--}> N_2(v=0) + O_2(v=1)$
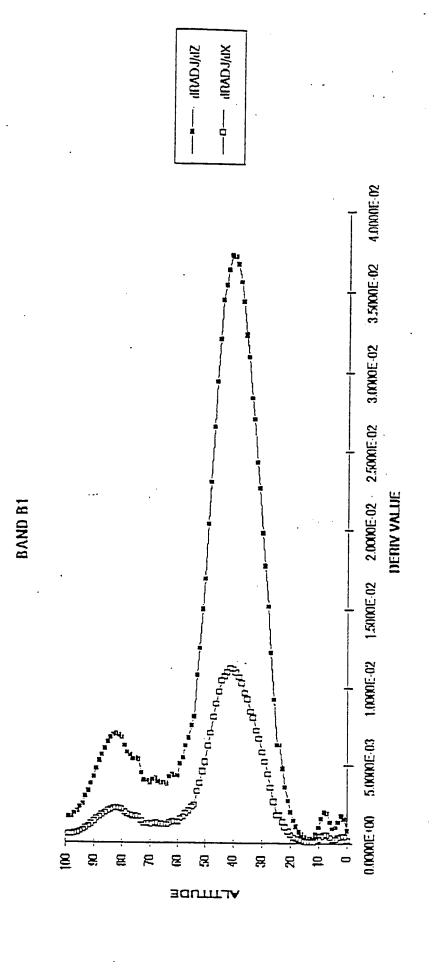
MSX Structure – Weighting Functions

- Weighting function W[s(r)] = relative contribution of element along BTH line-of-sight to radiance at sensor
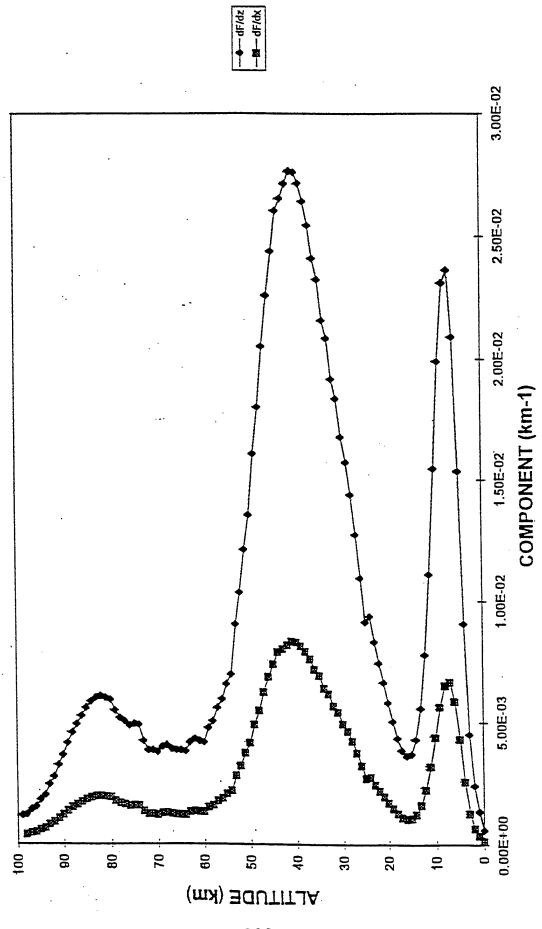
- $W[s(r)] = dI[s(r)]/ds(r)$, where $I[s(r)] = \mathcal{N}^{-1}\left(\int_0^{\tau[s\{r\}]} S(\tau')e^{-\tau'}\,d\tau'\right)$

  and $\tau[s\{r\}] = \int_0^{s\{r\}} \sigma(s')n_-(s')\,ds'$

- For typical model atmosphere,

  - W peaks near 40 km for bands B1 and B2
  - B2 weighting function has second tropospheric peak
  - Both have weaker non-LTE contribution from 80 km due to solar fluorescence

- Peak altitude independent of nadir angle θ, but as θ

  - W narrows
  - tropospheric peak disappears
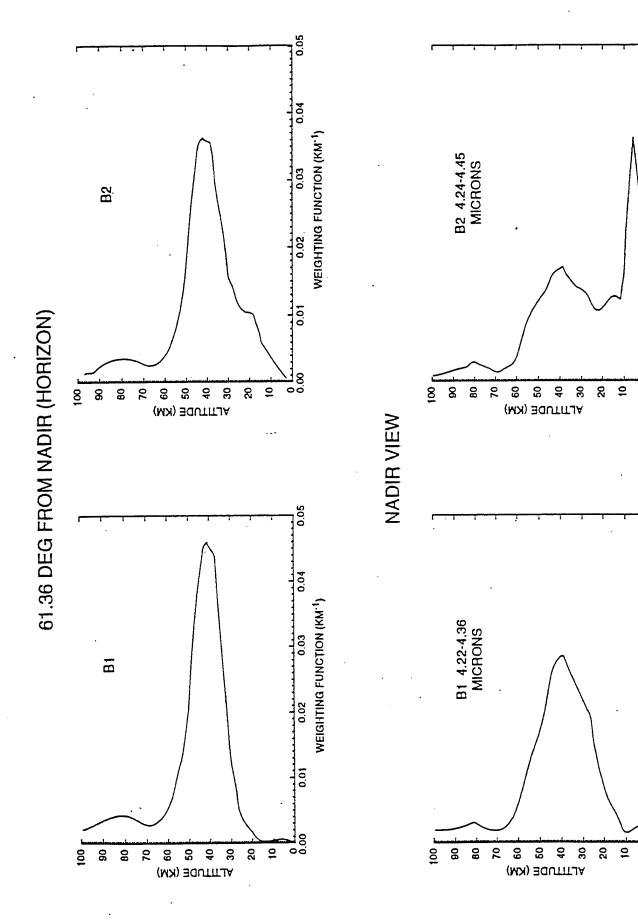
227

BAND B1

228

B2 WEIGHTING FUNCTIONS

61.36 DEG FROM NADIR (HORIZON)

B1

B2

NADIR VIEW

B1 4.22-4.36 MICRONS

B2 4.24-4.45 MICRONS

230

61.36 DEG FROM NADIR (HORIZON)

B2   4.24 ~ 4.45 MICRONS

B1   4.22 ~ 4.36 MICRONS

NADIR VIEW

B2

B1

231
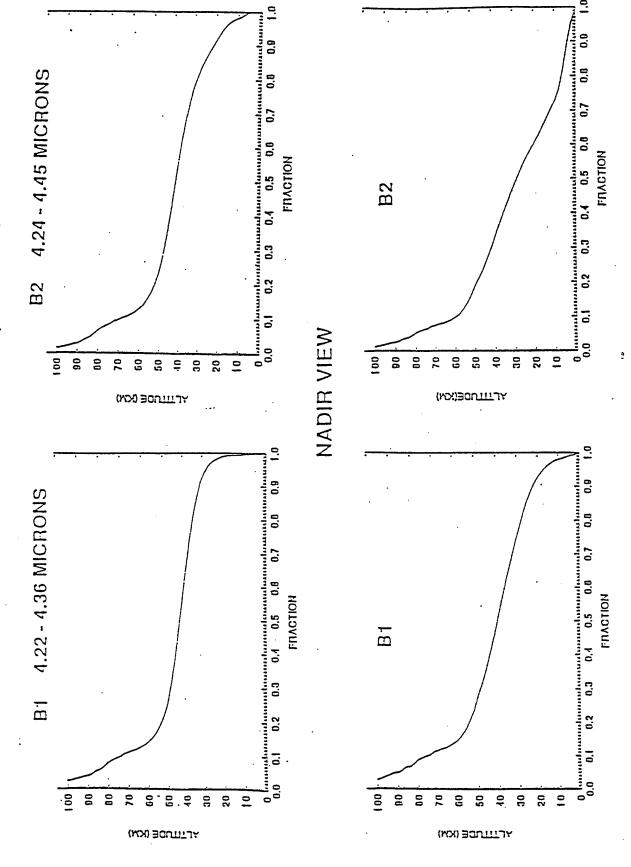
MSX Structure - Radiance Power Spectra (PSDs)

- Saturated-cascade theory of gravity-wave (GW) saturation predicts temperature PSDs dependence on horizontal wavenumber k_x satisfies

$$\Psi_{\Delta T}(k_x) = A\, k_x^{-\frac{5}{3}}$$

- Path integration effects result in extra power -1 in radiance PSD (Gruninger & Brown, 1995)

- Thus would expect

$$\Psi_{\Delta I}(k_x) = A\, k_x^{-\frac{8}{3}}$$

- In-scan PSDs confirm this prediction

232

RADIANCE POWER SPECTRUM

THIS IS PLOT NUMBER 16   THIS IS PLOT TYPE 54   B1   12are_b_E1.09.02.00036.01_1 - Date: August 17, 1996 - DAY

THIS IS FILE MATHSX2 RUN ON DATE 17-Apr-97 DEC IN CR SCAN= 5   2 ST PT=1 2 Tan Alt (Limb) or Nadir Angle (E1.09, E1.10) of Boresight: 57.00 Deg

ALTITUDE OF OBSERVER= 9.00E102 ORIGINAL AVE,S.D= 1.21E-06   5.62E-00   Offtrack: 270.000 Deg

NUMBER OF POINTS ANALYIZED CROSS SCAN AND IN SCAN =89 9504   Column 1: Seconds after 230:10:00:00

REMOVE POLYNOMIAL OF ORDER=2 USE MEDIAN FILTER OF LENGTH=10   Columns 2 - 3: Latitude, Longitude (Deg) of Boresight

FIT PSD FOR SLOPE BETWEEN FREQENCIES F SMALL-0.070 0.070 F LARGE=0.300 0.300   Columns 4 - 5: Tan Alt (Km)/Nadir Angle (Deg) of pixel 1, pixel 38'

TO FIND SLOPE FROM PERIODOGRAM USE LENGTH FFT'S (CROSS SCAN,IN SCAN)=64 1024   Temporarily zeroed out

NUMBER OF AR COEF FOR ANAL IN ,CROSS=20 80   AVERAGE OF SCENE=-3.43E-09 ROOT MEAN SQUARE= 1.81E-00

ASSUMED LENGTH D1,D2,IN SCAN(KM)= 5.93E101 5.59E101 3.96E103

NUMBER   SECONDS
1   3.7500E103

FINDINGS:

① $\ln$-$\ln$ slope $\approx -8/3$ (Antegral-scale correlation length)

② $L_c \approx 37$ km   ($\frac{1}{e}$ correlation length)

③ $L_c(\frac{1}{e}) \approx 32$ km

Data Length = 658.93 sec
≈ 3963. km

$\delta x \approx 0.417$ km

$f_{sur} \approx 0.00025$ km^{-1}

$f_{Ny} \approx 1.2$ km^{-1}

Aug 17, 1996, Nadir : 57°
Time starts from 230:10:00:00

Data Treatment:

① 2nd order polynomial trend removed from original data. Polynomial bounds are all in-scan data (64 cross-scan pixels)

② Averages subtracted from in-scan data for each pixel.

PSD Method:
See y-axis caption.

B1

BAND

$-\frac{5}{3}$

AVERAGE IN SCAN SURG L2

WAVENUMBER(1./KM)

VALUES FOR PSD

RADIANCE POWER SPECTRUM M

THIS IS PLOT NUMBER 10   THIS IS PLOT TYPE 54
THIS IS FILE MATHSX2 RUN ON DATE 18-Apr-97 DEC IN CR SCAN= 5   2 ST FT=1 2 Tan Alt (Limb) or Nadir Angle (EL09, EL18) of Boresight: 57.00 Deg
ALTITUDE OF OBSERVER= 9.00E102 ORIGINAL AVE,S.D= 1.57E-06   8.55E-08 Offtrack: 270.000 Deg
NUMBER OF POINTS ANALYIZED CROSS SCAN AND IN SCAN =84 9504   Column 1: Seconds after 230:10:00:00
REMOVE POLYNOMIAL OF ORDER=2 USE MEDIAN FILTER OF LENGTH=10   Columns 2 - 3: Latitude, Longitude (Deg) of Boresight
FIT PSD FOR SLOPE BETWEEN FREQENCIES F SMALL=0.070 0.070 F LARGE=0.300 0.300 Columns 4 - 5; Tan Alt (Km)/Nadir Angle (Deg) of pixel 1, pixel 30.
TO FIND SLOPE FROM PERIODOGRAM USE LENGTH FFT'S (CROSS SCAN,IN SCAN)=64   1024   Temporarily zeroed out
NUMBER OF AR COEF FOR ANAL IN ,CROSS=20 80   AVERAGE OF SCENE=-5.56E-09 ROOT MEAN SQUARE= 3.70E-08
ASSUMED LENGTH B1,B2,IN SCAN(KM)= 5.93E101 5.59E101 3.96E103

12are_b_El.09.02.00036.01.1.1 - Date: August 17, 1996 - DAY

NUMBER SECONDS
1   3.7500E+03

B_2 BAND (IN-SCAN)

$L_c \approx 90$ Km

B_2 "Sees" lower into the atmosphere

Note that the PSD spectral index $\approx -\frac{8}{3}$ at high freq.

but $\approx -\frac{5}{3}$ at low freq.

Conjecture: ① Terrain or Cloud features radiating gives $\alpha \sim -\frac{5}{3}$ ^ spectrum

② Low flying structure correl... from lower altitudes & High flying structure correl... from high altitudes.

Alternative: ① Cloud/Terrain Non-stationarity messes up the PSD.

WAVENUMBER(1./KM)   VALUES FOR PSD

AVERAGE IN SCAN 3ORG L2
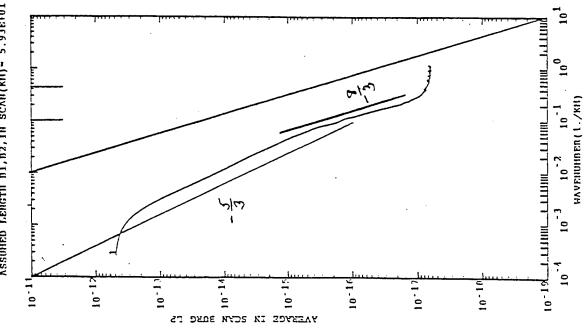
Conclusions

- MSX ATH and BTH data show evidence of a variety of types of structure

- In BTH data, structure is often due to clouds

- CO_2 4.3-μm emission in the MSX B bands enables one to distinguish another class of structures which
  - have distinctly different morphology
  - appear to originate from near 40 km altitude

- This structure has wavelike properties

- Radiative-transfer calculations allow the possibility that it is due to atmospheric gravity waves (GW)

- Radiance power spectra consistent with GW structure

MODTRAN SW AND VNIR SPECTRAL RADIANCES AND FLUXES

A. Berk, L.S. Bernstein, P.K. Acharya,
D.C. Robertson and S.Adler-Golden
Spectral Sciences, Inc. (SSI), Burlington, MA

G.P. Anderson and J.H. Chetwynd
Geophysics Directorate, Phillips Laboratory, Hanscom AFB, MA

H. E. Snell
Atmospheric and Environmental Research Inc. (AER), Cambridge, MA

J. J. Vail
Mei Technology Corp., Lexington, MA

Presented At
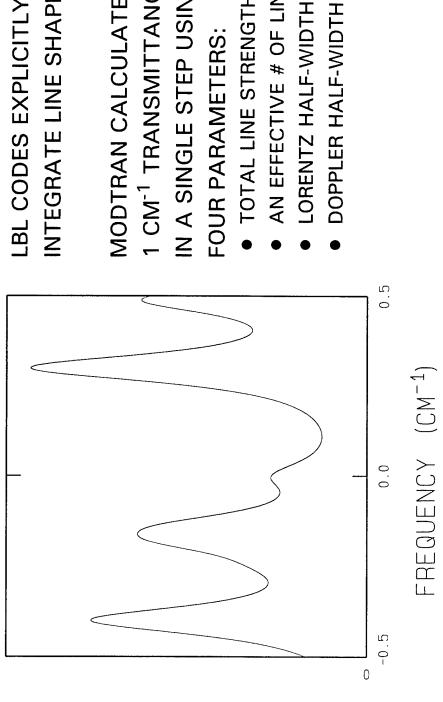
20th Annual Review Conference on Atmospheric Radiation Models
AF Phillips Laboratory, Hanscom AFB

10-12 June 1997

MODTRAN FEATURES

- SPECTRAL TRANSMITTANCES, RADIANCES, FLUXES & COOLING RATES FROM 0 TO 50,000 CM^{-1} ($>0.2\mu m$)

- 2 CM^{-1} RESOLUTION FROM 1 CM^{-1} BAND MODEL

- MODEL OR USER-DEFINED PROFILES

- SPECTRAL VARYING SURFACE ALBEDOS

- 26 MOLECULAR RADIATORS

- VARIABLE ICE AND WATER CLOUDS

- LOCAL THERMODYNAMIC EQUILIBRIUM

- SOLAR AND THERMAL MULTIPLE SCATTERING

- 10 TO 1000 TIMES FASTER THAN LBL MODELS

BAND MODEL APPROACH
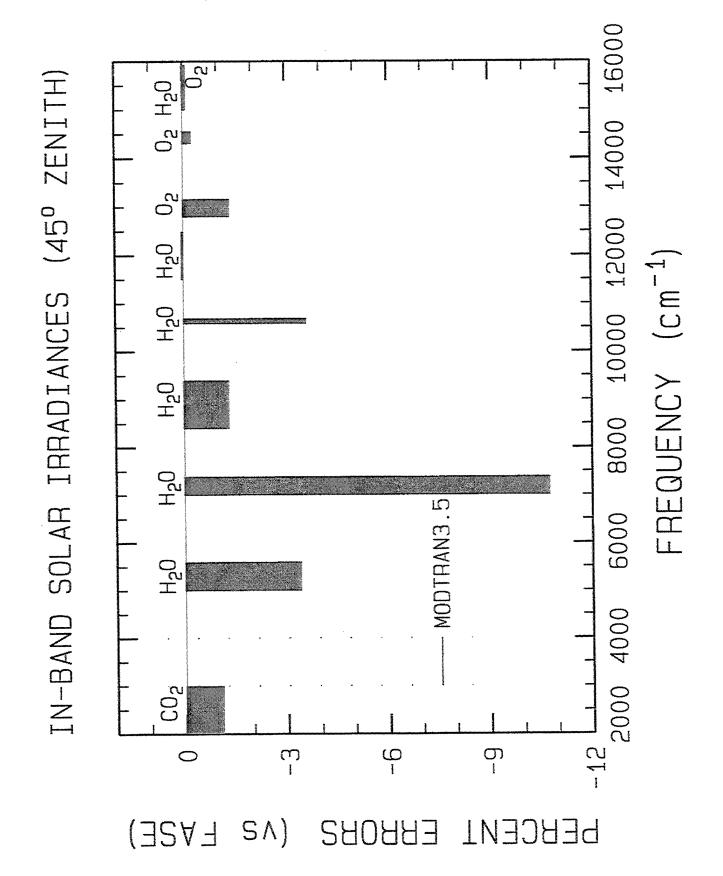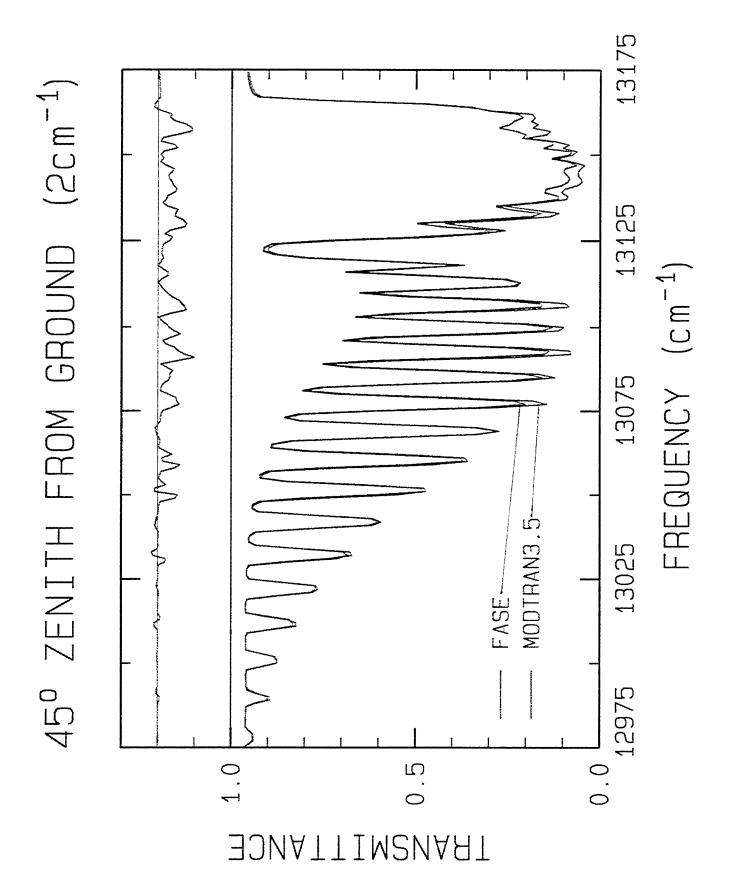
LBL CODES EXPLICITLY
INTEGRATE LINE SHAPES
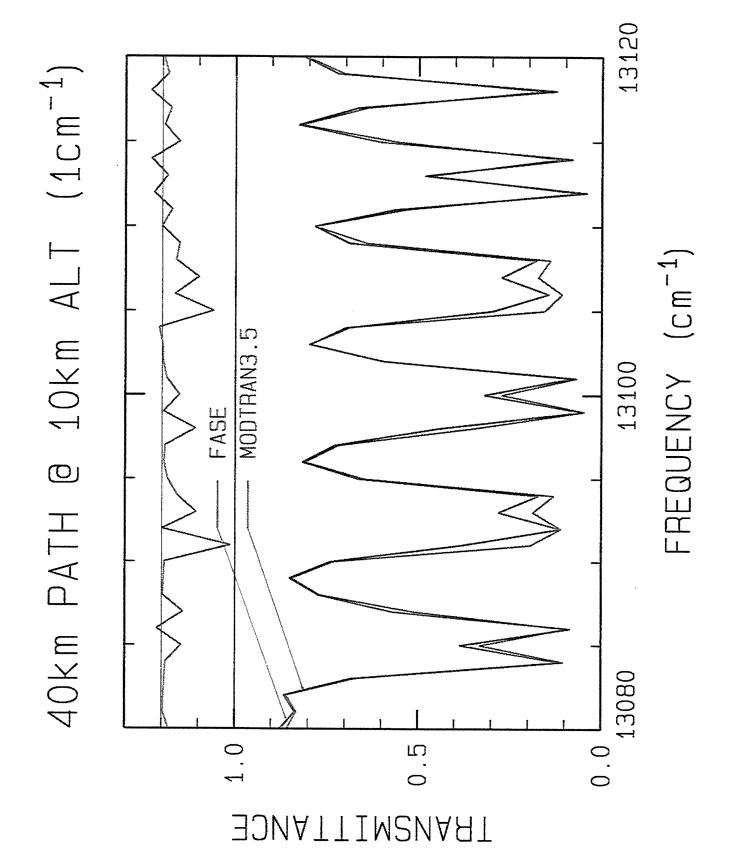
MODTRAN CALCULATES
1 CM^{-1} TRANSMITTANCES
IN A SINGLE STEP USING
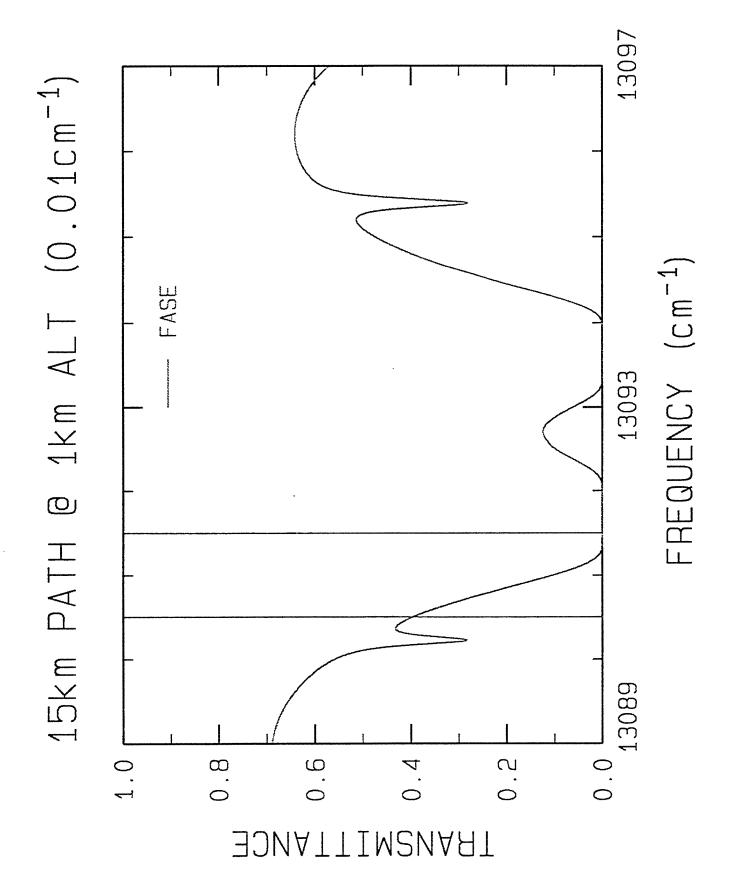
FOUR PARAMETERS:
- TOTAL LINE STRENGTH
- AN EFFECTIVE # OF LINES
- LORENTZ HALF-WIDTH
- DOPPLER HALF-WIDTH

FREQUENCY (CM^{-1})

ABSORPTIVITY

238

IN-BAND SOLAR IRRADIANCES (45° ZENITH)

45° ZENITH FROM GROUND (2cm⁻¹)

240

40km PATH @ 10km ALT (1cm^{-1})

FASE

MODTRAN3.5

15km PATH @ 1km ALT (0.01cm^{-1})

— FASE

FREQUENCY (cm^{-1})

TRASMITTANCE

242

40km PATH @ 10km ALT (1cm⁻¹)

FASE
MODTRAN3.5
MODTRAN3.5 with ¹/₄ cm⁻¹ tails

TRANSMITTANCE

FREQUENCY (cm⁻¹)

13080   13100   13120

243

15km PATH @ 1km ALT (1cm^{-1})

TRANSMITTANCE

FREQUENCY (cm^{-1})

FASE

MODTRAN3.5

MODTRAN3.5 with $^1\!/_4$ cm^{-1} tails

244

45° ZENITH FROM GROUND (2cm⁻¹)

FASE
MODTRAN3.5
MOD3.5 (¹/₄ cm⁻¹ tails)

IN-BAND SOLAR IRRADIANCES (45° ZENITH)

10 KM ALT : 50 KM RNG : 2 NM RES

TRANSMITTANCE

WAVELENGTH (NM)

MODTRAN – FASE
MODTRAN
FASE

CURRENT MODELS

- MODTRAN3.5 - IN PUBLIC RELEASE

  <u>10.9 MINUTES</u>*

- MODTRAN4 - INCLUDES CK ALGORITHM

  32 k'S PER CM^{-1}

  IMPROVED FLUXES

  SPECTRAL AND IN-BAND COOLING RATES

  <u>105 MINUTES</u>*
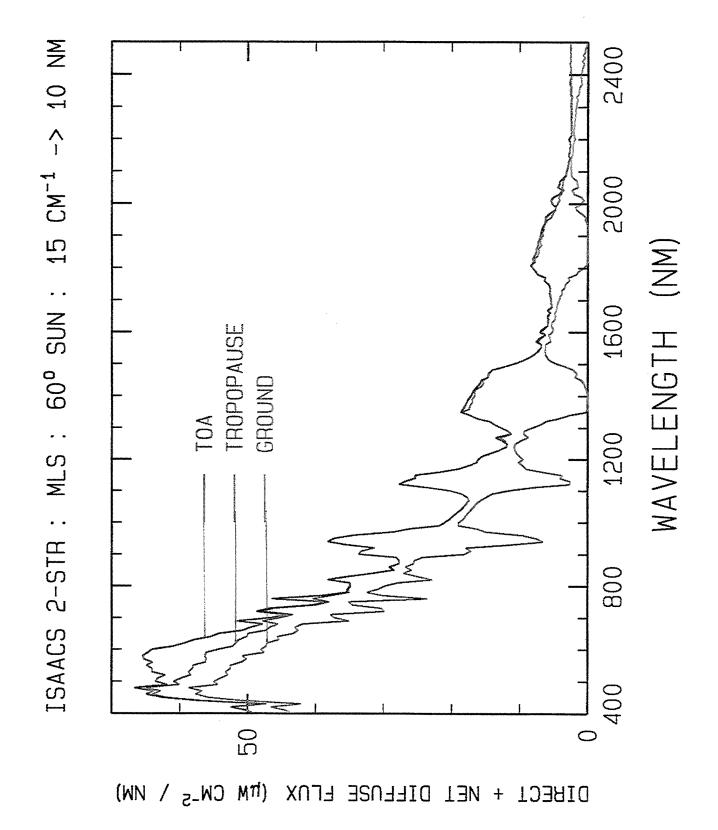
- HYPERMOD - TAILORED FOR SW HYPERSPECTRAL

  15 CM^{-1} BAND MODEL: $\Delta\lambda = 9.375$nm @ 2500nm

  $\Delta\lambda = 0.240$nm @ 400nm
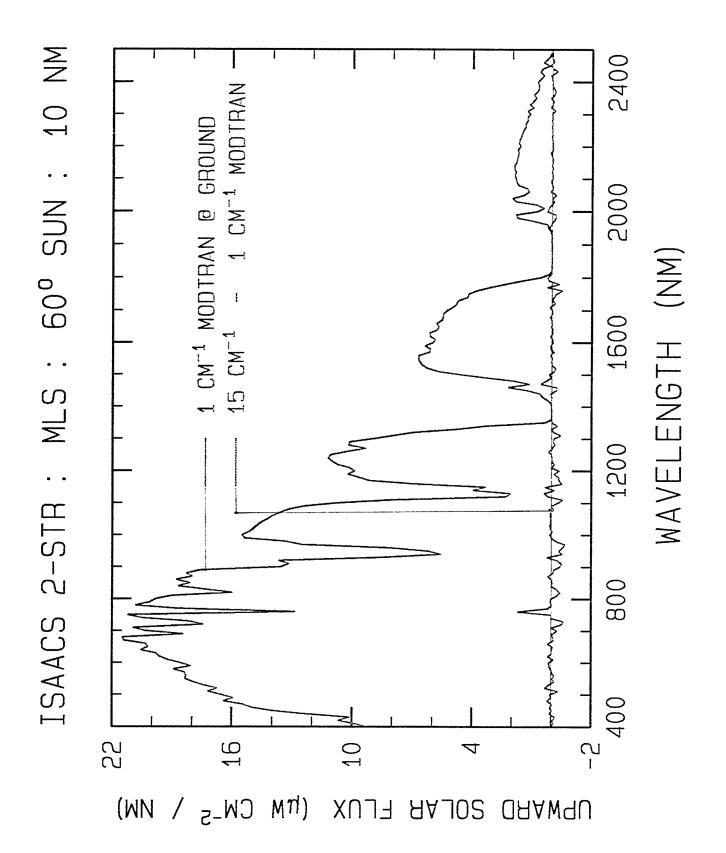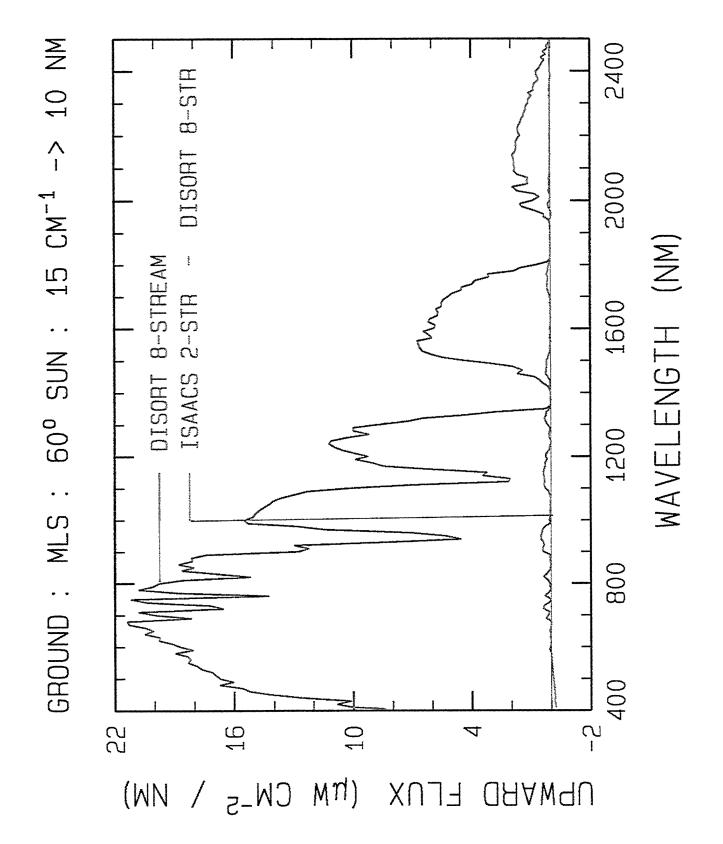
  17 k'S PER CM^{-1}
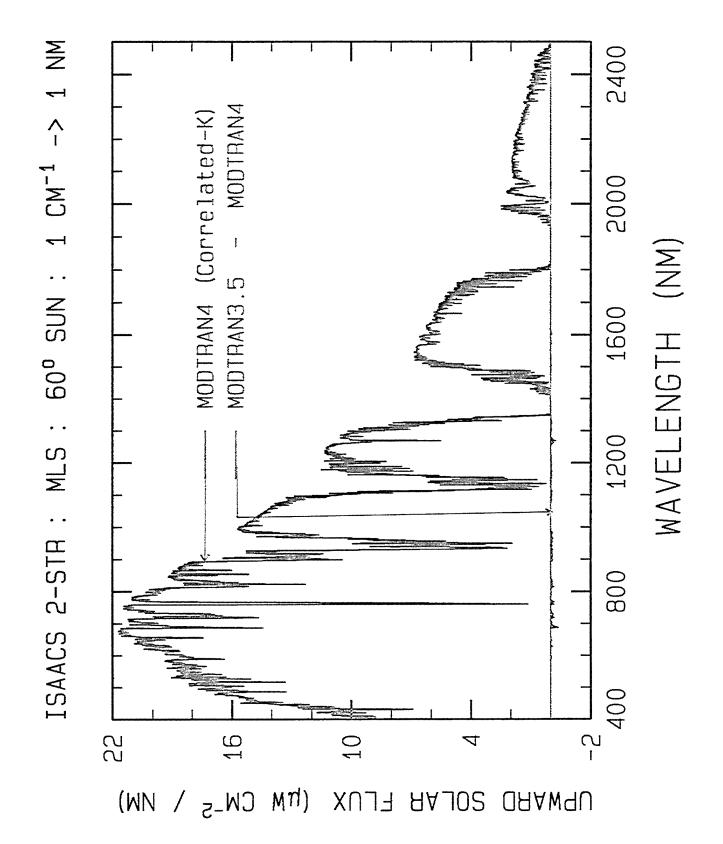
  <u>4.5 MINUTES</u>* (388 MINUTES WITH 8-STREAM DISORT)

* 0.4 TO 2.5 μm SPECTRAL FLUXES AT 75 ALTITUDES ON A 99 MHz MACHINE.

ISAACS 2-STR : MLS : 60° SUN : 15 CM⁻¹ → 10 NM

TOA
TROPOPAUSE
GROUND

WAVELENGTH (NM)

DIRECT + NET DIFFUSE FLUX (μW CM^{-2} / NM)

ISAACS 2-STR : MLS : 60° SUN : 10 NM

1 CM⁻¹ MODTRAN @ GROUND

15 CM⁻¹ – 1 CM⁻¹ MODTRAN

UPWARD SOLAR FLUX (μW CM⁻² / NM)

WAVELENGTH (NM)

250

GROUND : MLS : 60° SUN : 15 CM^{-1} -> 10 NM

DISORT 8-STREAM ———— DISORT 8-STR
ISAACS 2-STR ————— DISORT 8-STR

UPWARD FLUX (μW CM^{-2} / NM)

WAVELENGTH (NM)

251

ISAACS 2-STR : MLS : 60° SUN : 1 CM⁻¹ -> 1 NM

MODTRAN4 (Correlated-K)
MODTRAN3.5 - MODTRAN4

UPWARD SOLAR FLUX (μW CM^{-2} / NM)

WAVELENGTH (NM)

252

CONCLUSIONS

- A RECENT UPGRADE TO THE MODTRAN MODEL LOWERS ABSORPTION BRINGING PREDICTIONS INTO MUCH BETTER AGREEMENT WITH FASE.

  TO BE RELEASED BEFORE 30 JUNE 1997

- MODTRAN3.5 AND MODTRAN4 (CK) FLUXES AGREE UNDER CLEAR SKY CONDITIONS.

- MODTRAN4 IS REQUIRED FOR ACCURATE PREDICTION OF MULTIPLE SCATTERING / FLUXES IN THE PRESENCE OF CLOUDS.

ABSTRACT

RECENT UPGRADES TO MODTRAN - NEW SOLAR IRRADIANCE AND
INSTRUMENT SCANNING FUNCTIONS

20th Annual Air Force Transmission Meeting
Phillips Laboratory/GPO
Hanscom AFB, MA 01731

P. K. Acharya, A. Berk, L. Bernstein and D. Robertson
Spectral Sciences, Inc.
99 S. Bedford Street, Suite No. 7
Burlington, MA 01803

G. Anderson and J. Chetwynd
Phillips Laboratory/GPO
Hanscom AFB, MA 01731

H. E. Snell
Atmospheric and Environmental Research, Inc.
Cambridge, MA

J. Vail
Mei technologies, Lexington, MA

Recent upgrades are intended to make MODTRAN a more
accurate, convenient and versatile atmospheric modeling tool.
The current default solar irradiance database due to Kurucz
was corrected in the 310-340 nm region using measured data.
Several other data sets are also made available to the user.
The user can also use his/her own data residing in a file.
Examination confirms that the corrected Kurucz data is still
the best overall among all currently available data sets.
MODTRAN can now be run using frequency inputs which are in
wavenumber, nm or micron. Additionally, there is now the
capability of obtaining radiance and transmittance which are
convolved with an appropriate instrument scanning function.
Several choices of scanning functions are available including
an user-defined option. This upgrade is helpful to users who
would like to model satellite data which are gathered as a
function of wavelength and have undergone instrument
degradation. All upgrades are accomplished while maintaining
strict compatibility of TAPE5 with earlier versions of the
code. Work is currently in progress to incorporate NOVAM
(Navy Oceanic Vertical Aerosol Models) into MODTRAN.

RECENT UPGRADES TO MODTRAN - NEW SOLAR IRRADIANCES AND INSTRUMENT SCANNING FUNCTIONS

P. K. ACHARYA, A. BERK AND L. B. BERNSTEIN
Spectral Sciences, Inc., Burlington, MA

G.P. ANDERSON AND J.H. CHETWYND
Phillips Laboratory/GPOS, Hanscom AFB, MA

H.E. SNELL
Atmospheric and Environmental Research, Inc., Cambridge. MA

J. VAIL
Mei Technologies, Lexington, MA

THE 20TH ANNUAL DOD CONFERENCE ON ATMOSPHERIC TRANSMISSION MODELS (10-12 JUNE, 1997)

MOTIVATION

- MODTRAN REQUIRES ACCURATE TOA SOLAR IRRADIANCE (I_0)

- CURRENTLY CALCULATIONS DUE TO KURUCZ ARE USED

  - EXTENSIVE LBL CALCULATIONS BASED ON SOLAR TEMPERATURE PROFILE, SOLAR ABUNDANCES AND VOIGT LINE PROFILE
  - STANDS UP WELL AGAINST MEASUREMENTS

- NEW MEASUREMENTS ARE AVAILABLE INCLUDING THOSE AT TOA

  - MEASUREMENTS AT KITT-PEAK (USED BY THE GOME COMMUNITY)
  - TOA SOLAR UV MEASUREMENTS (ATLAS SSBUV)
  - TOA MEASUREMENTS BY FRENCH SCIENTISTS (SOLSPEC)

- NEED TO ACCOMMODATE USER-SUPPLIED I_0
  - HAS APPLICATIONS, FOR EXAMPLE, IN O_3 RETRIEVAL

NEW CHOICES OF BUILT-IN I_0 FILES

- CARD 1A, COLUMNS 61-80, TRIGGERS CHOICE OF I_0

- FOUR BUILTIN SOLAR I_0 FILES

  - NEWKUR.DAT (CORRECTED KURUCZ); INPUT 1 OR BLANK
  - OLDKUR.DAT (KURUCZ); INPUT 2
  - CHKUR.DAT (KITT-PEAK, COURTESY OF K. CHANCE); INPUT 3
  - CEBCHKUR.DAT (ATLAS SSBUV, COURTESY OF R. CEBULA); INPUT 4
  - THKUR.DAT (SOLSPEC, COURTESY OF G. THUILLIER); INPUT 5

- CORRECTED KURUCZ IS DEFAULT (BLANKS IN COLS 61-80)

- ALL ARE FROM 50-50000 CM^{-1}; NON-KURUCZ HAVE MULTIPLE SOURCES
  - IRRADIANCES IN (W/CM^2)/CM^{-1} VERSUS CM^{-1}

- USER-SUPPLIED DATA CAN BE USED (FILENAME IN COLS 61-80)

STRUCTURE OF USER-SUPPLIED I_0 FILE

• FILE CONTENT

FREQUENCY UNIT DESIGNATOR	IRRADIANCE UNIT DESIGNATOR
FREQUENCY 1	IRRADIANCE 1
FREQUENCY 2	IRRADIANCE 2

...

• UNIT DESIGNATORS

1	FREQUENCY IN CM^{-1}	I_0 IN (W/CM^2)/CM^{-1}
2	FREQUENCY IN NM	I_0 IN (PHOTONS/S)/CM^2
3	FREQUENCY IN MM	I_0 IN (MILLIWATTS/M^2)/NM OR
		(W/M^2)/μM (NUMERICALLY IDENTICAL)

• I_0 AT INTEGRAL CM^{-1}, ARE OBTAINED BY INTEGRATION/INTERPOLATION

• PADDED BY DATA FROM DEFAULT BUILTIN FILE

UPPER ATMOSPHERIC (SHUTTLE EXPT) DATA
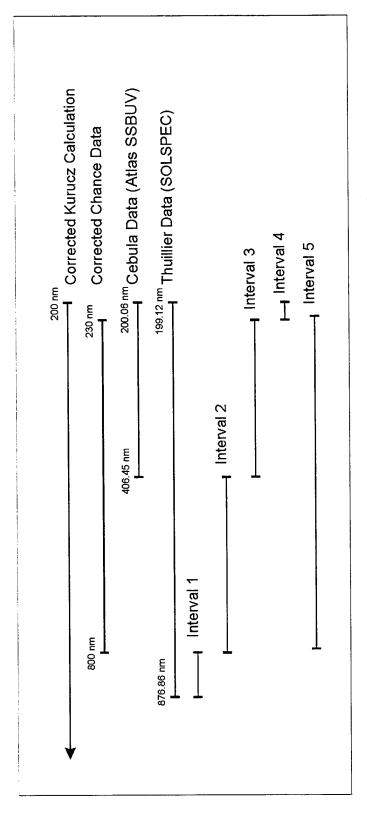
- ATLAS SSBUV DATA; 200.06-406.45 NM (49985-24603 CM^{-1})

  - STEP SIZE 0.152-0.136 NM
  - UNCERTAINTY IN $\lambda \pm 0.026$ NM
  - 2σ UNCERTAINTY 6% AT 200 NM, 2.8% AT 250 NM AND 2.6% 300-400 NM

- SSBUV WAS AUGMENTED BY KITT-PEAK DATA AND KURUCZ

- SOLSPEC INSTRUMENT; 199.12-876.86 NM (11404-50221 CM^{-1})

  - STEP SIZE 0.36-0.9 NM

- SOLSPEC SET WAS BY AUGMENTED BY KURUCZ CALCULATION

- ATLAS SSBUV IS TAKEN TO BE THE BENCHMARK FOR THIS TASK

KITT-PEAK MEASUREMENTS DATA

- TWO SETS OF MEASUREMENTS MERGED (230-800 NM)

  - CALIBRATION IS ± 0.002 NM, STEP SIZE IS 0.01

- DATA WAS NOT CORRECTED FOR O_2 ATMOSPHERIC BAND LINES

  - REPLACED O_2 LINES BY KURUCZ'S

- SOME ATMOSPHERIC EFFECTS STILL REMAIN

  - AROUND 720 NM ATMOSPHERIC H_2 MAY BE A PROBLEM

  - AROUND 320-330 NM THERE IS ALSO SOME PROBLEM

INTEGRATED BANDPASS RADIANCES (w/m^2)
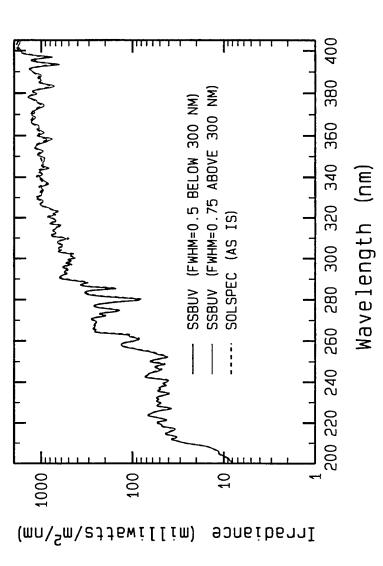
	877-800 nm	800-406 nm	406-230 nm	230-200 nm	800-230 nm
	Interval 1	Interval 2	Interval 3	Interval 4	Interval 5
KR 80		647	122	0.95	768
CH		645	118		764
CB			121	1.02	
TH 82		654	124	1.02	778

(KR = corrected Kurucz, CH = corrected Chance, CB = SSBUV, TH = SOLSPEC)
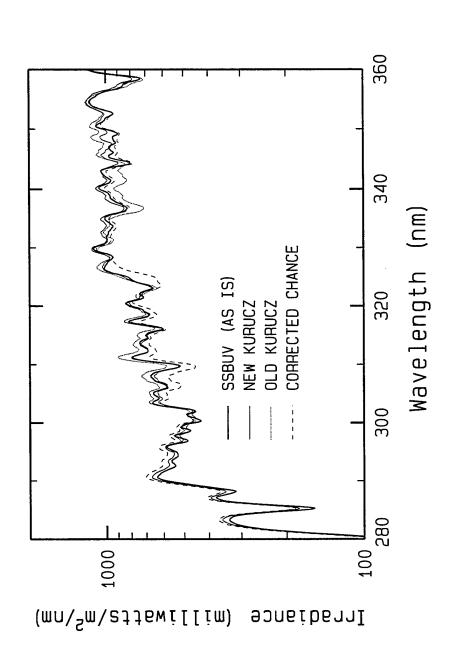
UPPER ATMOSPHERIC DATA COMPARED
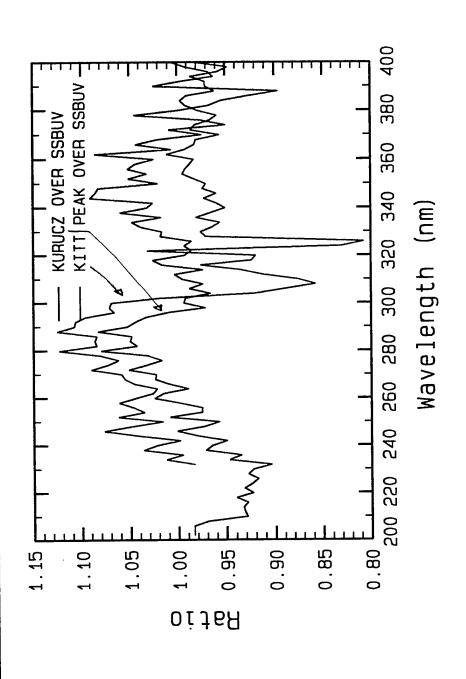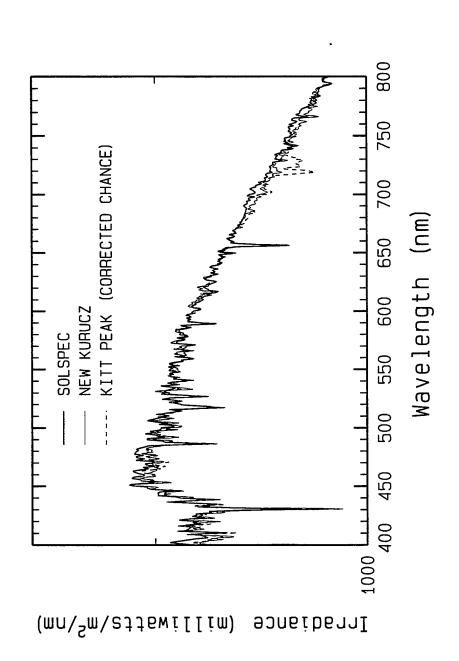
- SSBUV AND SOLSPEC COMPARED AT "COMMON" RESOLUTION
- MAXIMUM DIFFERENCE IS 11% AT 263 NM
- AGREEMENT IS BETTER AT SHORTER WAVELENGTHS

KITT-PEAK AND CORRECTED KURUCZ (310-340 NM)
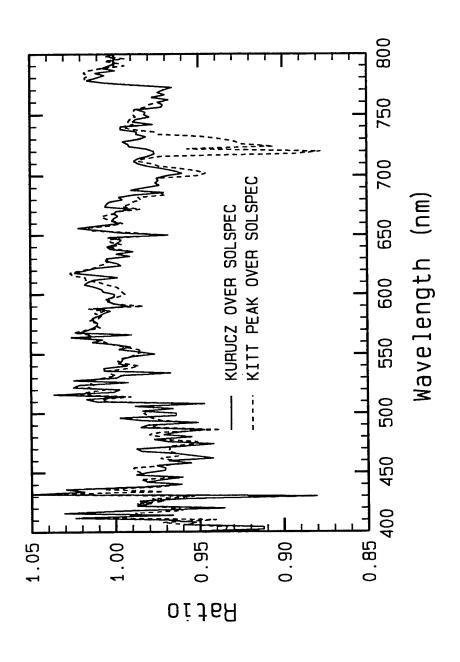
KITT-PEAK AND CORRECTED KURUCZ (200-400 NM)

KITT-PEAK AND CORRECTED KURUCZ (400-800 NM)

KITT-PEAK AND CORRECTED KURUCZ (200-400 NM)

GENERALIZED UNITS FOR CARD 4 INPUTS

CARD 4: V1, V2, DV, FWHM, YFLAG, XFALG, DLIMIT, FLAGS
FORMAT(4F10.0, 2A1, A8, A4)

- FREQUENCY INPUTS CAN NOW BE IN μM, NM AND CM^{-1}

- UNIT IS INDICATED BY FLAGS(1:1) WHICH IS W, M, N OR BLANK

- DEFAULT (FLAGS(1:1) IS BLANK) IS CM^{-1}

- OLD TAPE5's WORK JUST FINE WITH THE NEW CODE

INSTRUMENT SCANNING FUNCTION

- CHOICE IS INDICATED BY FLAGS(2:2)

  1 TRIANGULAR   2 SQUARE   3 GAUSSIAN
  4 SINC   5 $SINC^2$ 6 HAMMING
  7 USER-SUPPLIED

- DEFAULT (BLANK) IS TRIANGULAR; OLD TAPE5's ARE FINE

- FLAGS(3:3) INDICATES IF FWHM IS RELATIVE
  - RELATIVE % FWHM CAN HELP MODEL, E.G., CVFs

- CAN ONLY DEGRADE TOTAL TRANS AND RAD TO SAVE TIME
  - MUST SET FLAGS(4:4) TO BLANK

- IF FWHM IS TOO FINE ERROR MSG IS PRINTED AT THE OUTSET

268

SUMMARY OF MODTRAN UPGRADES

- SEVERAL CHOICES OF SOLAR I_0 DATA IS AVAILABLE

- THE KURUCZ SPECTRUM (CORRECTED IN 310-340 NM)
  IS STILL THE BEST (*DEFAULT*)

- USER-DEFINED I_0 FILE WITH FLEXIBLE UNITS CAN BE INPUT

- CARD 4 INPUTS CAN BE IN μM, NM OR CM^{-1}

- SEVERAL SCANNING FUNCTIONS (INCLUDING USER-DEFINED
  FUNCTION) ARE NOW AVAILABLE

NEW OUPUTFILES

- PLOTOUT.SCN AND TAPE7.SCN

SOLAR ULTRAVIOLET IRRADIANCE AND ITS VARIATION

Giuliana de Toma, Gary J. Rottman, Thomas N. Woods

Laboratory for Atmospheric and Space Physics, University of Colorado, Boulder, CO, USA

Abstract

Solar ultraviolet irradiance, especially at wavelengths below 300 nm, is strongly absorbed by the Earth's middle atmosphere, where is the dominant source of energy. Knowledge of the amount of solar energy deposited in the atmosphere and its variation with time is important for atmospheric studies. The Solar Stellar Irradiance Comparison Experiment, SOLSTICE, on the UARS satellite makes daily observations of solar spectral irradiance in the wavelength region from 119 to 420 nm. SOLTICE observations, started in October 1991 and have continued since that time. They cover the entire declining phase of solar cycle 22 from solar maximum to solar minimum providing information on solar ultraviolet variability over both short- and long-time scales. In this paper, the SOLSTICE irradiance measurements are reviewed with particular emphasis on variability. For the period 1991-1996, we report a variation of about a factor of two at Lyα, a variation of about 5% near 200 nm, gradually decreasing to less than 1% near 300 nm.

1 Introduction

The solar irradiance in the spectral interval 120-420 nm is of particular interest not only for studying the Sun and its magnetic activity but also for its effects on the terrestrial environment (Lean, 1991; Rottman et al., 1996). This wavelength region, which covers the far ultraviolet (FUV) up to the visible, originates in different levels of the solar atmosphere (Foukal, 1990). The solar emission at wavelengths short of 150 nm, has its origin in the outer layers of the solar atmosphere: the chromosphere and transition region. These are hotter, less-dense regions where the magnetic fields of the Sun play an important role. Consequently, radiation emitted from these layers is strongly influenced by solar magnetic activity and shows significant variability with the solar activity cycle. Longer wavelengths originate in lower levels of the solar atmosphere: radiation emitted around 160 nm comes from the temperature minimum region and even longer wavelengths have origin in the photosphere. Above the Al I ionization edge at 208 nm almost all the solar emission is from the lower photosphere with the exception of the strong absorption lines of Mg II at 280 nm and of Ca II at 393 and 397 nm, both formed in the chromosphere. Unlike the chromospheric emission, the solar photospheric radiation shows much less variability related to the magnetic activity of the Sun (Foukal, 1990; Lean, 1991).

An example of the solar FUV spectrum measured by SOLSTICE is shown in Figure 1. We note that the spectrum below 160 nm is characterized by emission lines (some of them not completely resolved at SOLSTICE resolution) superposed on a relatively weak continuum. This shorter wavelength region is dominated by the the H I Lyα line at 121.57 nm, which is the strongest line in the entire UV region. At longer wavelengths, where radiation is mainly photospheric, the solar spectrum changes appearance and there are fewer and fewer lines in emission. Above 200 nm the spectrum is characterized by many absorption lines in the underlying continuum. The intensity of the solar emission is also a function of wavelength, and increases by several orders of magnitude from the H I Lyα to the visible. The ultraviolet region is only a small fraction of the total radiative output of the Sun: solar irradiance below 420 nm contributes about 10% to the total solar irradiance, and the ultraviolet region below 300 nm, which is about 15 Watt/m^2, contributes only 1%. Yet, because the largest amplitude variations of the Sun's output occur at ultraviolet and radio wavelengths the region between 120 and 300 nm contributes to a large fraction of total solar variability.

Solar ultraviolet radiation is very important because of its influence on Earth's environment, and solar radiation measurements are required for many geophysical studies and for climate models. Different

wavelengths affect different regions of the atmosphere. Solar emission at wavelengths between 300 and 420 nm reachs the ground only moderately attenuated by the Earth's atmosphere. In contrast, the spectral region 120–300 nm is almost totally absorbed in the stratosphere and mesosphere where it is responsible for radiative heating and photodissociation of important atmospheric constituents (O_2, O_3, H_2O, NO_2, etc.) (Brasseur and Solomon, 1986). Changes in solar ultraviolet irradiance can therefore result in changes in the temperature structure and composition of the middle atmosphere from 20 to 80 km (Brasseur, 1993; London, 1994). For example, the ozone distribution is strongly influenced by the solar ultraviolet radiation both directly (O_3 photodissociation) and indirectly (O_2 and H_2O photodissociation). Changes in total ozone caused by solar variations are comparable to the ozone depletion caused by the chlorofluorocarbons (CFCs). The solar influence can enhance or partially cancel this anthropogenic effect (Chandra, 1991; Hood and McCormack, 1992). Less clear, but not less important, is the effect of solar variability for the wavelength region above 300 nm. This spectral region varies less than 1% during the solar cycle and total solar irradiance varies only 0.1% (Wilson, 1991). This small solar effect seems too small to play an important role on the climate change, yet several geophysical records seem to show a solar signature in the past climate of the Earth (Lean, 1994 and references therein).

Measurements of the solar ultraviolet irradiance and its variability are thus necessary to separate the effects of solar variability on the Earth's middle atmosphere (and possibly the troposphere) from changes induced by other natural phenomena or by anthropogenic activity. This separation has been difficult in the past because accurate solar measurements were not available. Measurements of ultraviolet radiation must be performed from space which makes the measurements particularly difficult due to the limited lifetime of space missions and also to the degradation of instruments with time. Until recently, no space instrument had measured the ultraviolet irradiance and its variation in time with high accuracy. The Upper Atmosphere Research Satellite (UARS) carries two ultraviolet solar spectrometers and is the first satellite that can monitor the UV solar irradiance with high precision and accuracy. UARS was launched in September 1991, near the maximum of solar cycle 22, and it is still operating normally. It now provides 6 years of reliable, continuous solar irradiance observations from solar maximum to solar minimum conditions. In this paper, the solar measurements from one of the two UARS solar instruments, the Solar Stellar Irradiance Comparison Experiment (SOLSTICE), are presented (Section 2), and solar variability as a function of wavelength over both short– and long–time scales is reviewed for the wavelength range 120–300 nm (Section 3). Monitoring of the solar ultraviolet radiation will continue with a second generation SOLSTICE instrument for the NASA Earth Observing System (EOS) with a launch in the year 2002. This instrument will achieve higher accuracy for the wavelength region 300–420 nm and will extend the measurements to the visible and near infrared regions (Section 4).

2 SOLSTICE Solar Observations

The SOLSTICE instrument on the UARS satellite is a 3–channel ultraviolet spectrometer which performs full–disk solar irradiance observations in the spectral region 119–420 nm with a resolution varying from 0.15 to 0.3 nm (Rottman et al., 1993; Woods et al., 1993, 1996). SOLSTICE observations started in October 1991, about a month after UARS launch, and have continued regularly to the present time with only a few gaps (only 7% of the data are missing). Solar spectra are measured about 15 times a day during the daytime portion of each orbit, and reported as a daily average with a 1–nm resolution. A list of the major ultraviolet emission lines, and the Mg II index of chromospheric activity are also provided daily. The data in irradiance units and corrected to one astronomical unit can be obtained by anonymous FTP from "ftp://daac.gsfc.nasa.gov/data/uars/solstice/".

The primary science objective of SOLSTICE is to measure the ultraviolet irradiance with high absolute accuracy over long periods of time. This has been achieved through an extensive pre–flight calibration (Woods et al., 1993) and the in–flight capability to track calibration changes (Rottman et al., 1993). To monitor changes in instrumental sensitivity, a group of bright stars, very stable at UV wavelengths, are observed on a daily basis during the nighttime portion of each orbit. Using these stars as a calibration reference, it is then possible to correct for instrumental effects and determine the long–term solar variability
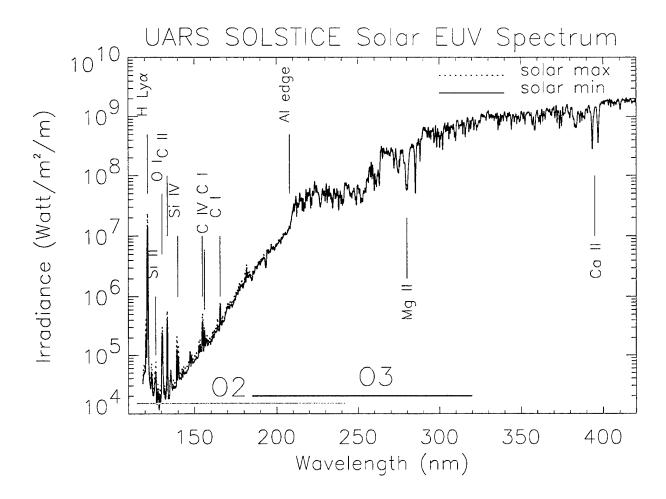
271

Figure 1: Two solar FUV spectra from SOLSTICE are shown for solar maximum and solar minimum conditions. The spectra are obtained averaging SOLSTICE daily measurements over three solar rotations, during the periods: 30 Dec. 1991 – 19 Mar. 1992 and 17 Feb. 1996 – 7 May 1996. Several of the major solar lines are identified. The spectral ranges which can induce dissociation of molecular oxygen and ozone, the two major absorbers of ultraviolet radiation, are also shown.

with 1-2% relative accuracy.

SOLSTICE measurements have been validated by the observations of the second solar instrument on UARS, the Solar Ultraviolet Spectral Irradiance Monitor (SUSIM), which covers the same wavelength range (Brueckner, 1993). The measurements of the two instruments are consistent and agree within their $2-\sigma$ calibration uncertainty of about 10% (Woods et al., 1996).

An example of SOLSTICE solar observations is presented in Figure 1, where spectra for solar maximum and solar minimum conditions are shown. These spectra are the average over 81-day (three solar rotations) during the winter of 1992, representing solar maximum for solar cycle 22, and during the spring of 1996, corresponding to the recent solar minimum. The data at solar minimum are still preliminary values because the correction for instrument degradation is not yet final. New SOLSTICE data with all the corrections included will be publicly available in early 1998.

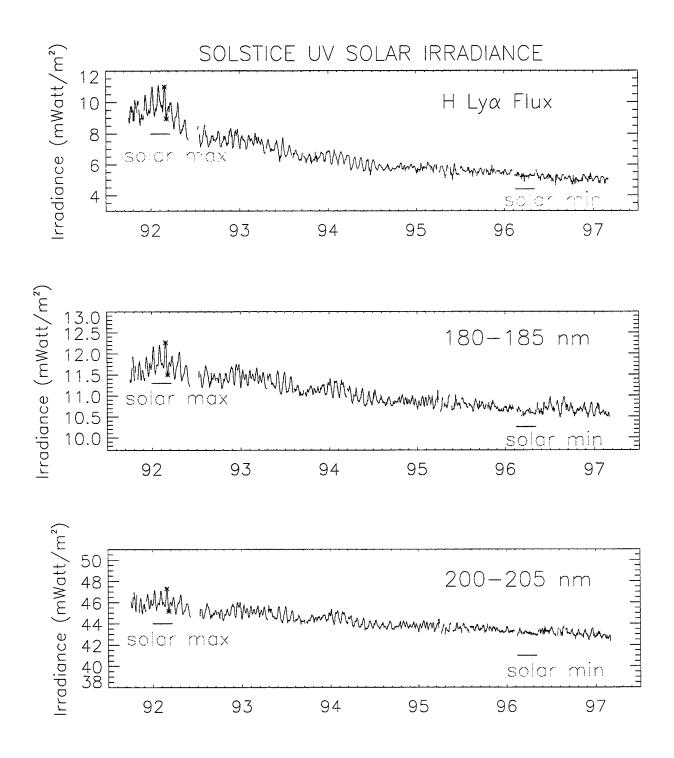Figure 2: Solar irradiance as a function of time in three wavelength regions important for the terrestrial atmosphere. Solar variability decreases at longer wavelengths: for the period 1992–1996 we observe a change of about a factor of two at the H I Lyα, 14% in the band 180–185 nm, and 8% in the band 200–205 nm (notice that the y–axis for the center and bottom plots are chosen to have the plots are on the same relative scale)
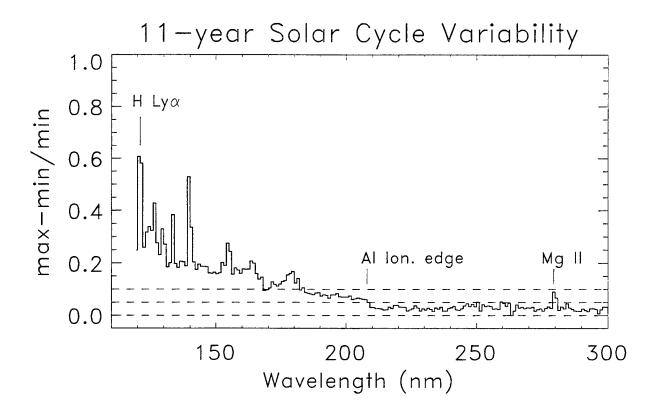
273

Figure 3: Solar variability associated with the 11–year solar activity cycle as a function of wavelength. Data at solar minimum are still preliminary.

3   Solar UV Variability

In Figure 2 the solar irradiance observed in three important wavelength regions is shown as a function of time. The Sun exhibits variability over several time scales, from minutes to years, but the most obvious variations in these time series are the slow change in the average intensity related to the 11–year activity cycle of the Sun, and the 27–day modulation of this variation induced by the rotation of the Sun through the appearance and disappearance of active regions on the solar disk.

In the top panel of Figure 2 the H I Lyα line is shown. This emission line is very important because of its high intensity and because of its influence on the mesosphere where it dissociates O_2 as well as CH_4 and H_2O with consequent ozone destruction. The H I Lyα line has origin in the upper chromosphere and is quite sensitive to solar magnetic activity. We notice a change of almost a factor of two in its intensity from solar maximum to solar minimum. The central and bottom panels of Figure 2 show the time series for the spectral regions 180–185 and 200–205 nm respectively. These emissions correspond to the Schumann–Runge bands and Herzberg continuum of molecular oxygen and also influence ozone densities. In contrast to H I Lyα, radiation at these wavelengths originates in lower and cooler regions of the solar atmosphere. Variability is still significant, but quite smaller than for the H I Lyα.

3.1   Solar Cycle Variability

Solar cycle variability is associated with the evolution of the solar magnetic fields during a period of approximately 11 years from solar maximum to solar minimum. At solar maximum several active
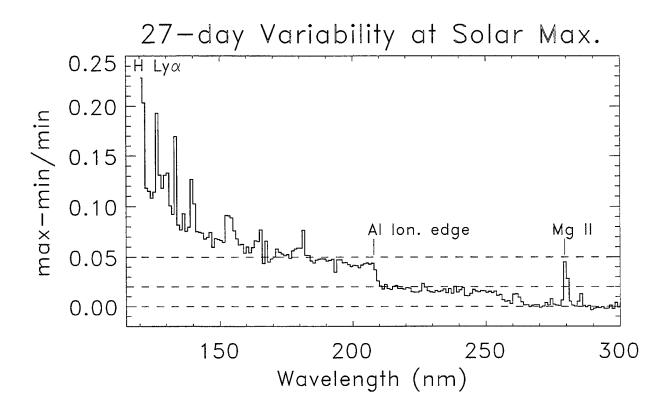
274

Figure 4: Solar variability associated with the 27–day rotational modulation as a function of wavelength for winter 1992, during solar maximum activity.

regions, which are regions of emergence of magnetic fluxes, are present on the surface of the Sun, while at solar minimum the solar surface appears relatively uniform and "quite". At ultraviolet wavelengths, dark sunspots are not very important and radiation is enhanced at solar maximum by the presence of bright active regions (plages) surrounding the sunspots.

To estimate solar variability over the 11–year solar cycle, we have used the average spectra for the winter of 1992 and spring of 1996 shown in Figure 1. Their ratio in 1–nm bin intervals is plotted in Figure 3. Solar maximum was reached in 1989–1991, but the winter of 1992 was a period of very high solar activity and well represents solar maximum conditions. The data in spring of 1996 correspond to the recent solar minimum. These latter SOLSTICE measurements are still preliminary so the results shown here must be considered only a first estimate for variability during solar cycle 22. Nevertheless, we can call attention to several interesting aspects of solar variability seen in Figure 3. Solar variability is considerably larger at the shorter wavelengths (especially in correspondence of the emission lines) and decreases at the longer wavelengths as we move from hotter to cooler emission regions of the solar atmosphere. The H I Lyα varies 70% or more, the wavelength region around 170 nm varies about 10%, and the region at 200 nm about 5–6%. Then variability decreases sharply above the Al I ionization edge at 208 nm, with the exception of the Mg II emission at 280 nm, which is of chromospheric origin. For wavelengths longer than 300 nm the solar variability is less than 1% and is beyond the accuracy limit of the SOLSTICE instrument.

3.2 Rotational Modulation

The amplitude of the 27–day modulation caused by the Sun's rotation changes throughout the solar cycle. If we examine Figure 2 we notice episodes of activity which indicate the emergence of new bright

active regions. These regions dominate for several rotations (typically 4 to 8 rotations) and then wane. At solar maximum, when the Sun is very active, the amplitude of the 27–day modulation is generally larger, and then gradually decreases with decreasing solar activity. This change from maximum to minimum is not strictly monotonic, as the appearance of new active complexes can cause a new pulse of activity; for example in early 1994. At solar minimum, when the Sun is very quite, we have times when the rotational modulation is almost absent; an example is the spring of 1996, when it is very difficult to identify the rotational signal in the data.

To study the 27–day modulation as a function of wavelength, we have chosen a solar rotation near maximum solar activity, when rotational modulation is quite large. We ratio two SOLSTICE solar spectra taken on February 27 and March 6, 1992. These days are identified by asterisks in Figure 2 and correspond to the peak and the valley of a solar rotation period. The ratio of peak to valley in 1–nm bin intervals are shown in Figure 4. This plot has many similarities with Figure 3. Variations are larger at the shorter wavelengths and decrease at the longer wavelengths which originate in the photosphere. Again we notice the enhancement in variability of the chromospheric Mg II line and the drop associated with the Al I edge. As we move toward visible wavelengths (not shown here) the effect of sunspots starts to appear, and we sometimes observe a slight decrease in intensity associated with their passage across the solar disk instead of an increase associated with plages.

4   Conclusions and Future Missions

Variations in the ultraviolet irradiance can significantly affect the energy balance, photochemistry and dynamics of the middle atmosphere between 20 and 80 km. Therefore, knowledge of the magnitude and variability of solar output is important to understand the solar influence on the Earth's atmosphere, and to separate solar effects from other natural and anthropogenic forcing.

SOLSTICE measurements from the UARS satellite now provide a 6–year set of ultraviolet irradiance data with better accuracy and precision than previous measurements. The careful pre–flight calibration of the SOLSTICE instrument and the validation of SOLSTICE measurements with SUSIM measurements have allowed us to establish the value of solar ultraviolet irradiance with higher photometric accuracy, especially at the shorter wavelengths. Moreover, the length of the UARS mission which now covers the entire declining phase of solar cycle 22, provides new information about solar ultraviolet variability. Because of the SOLSTICE in–flight calibration technique it is now possible to establish solar UV variability over long–time scales with an accuracy of 1–2%, and with an even higher accuracy over short–term scales of the order of a solar rotation.

This 1–2% accuracy limit is appropriate for the shorter ultraviolet wavelengths where solar emission is highly variable, but can only set an upper limit for the photospheric emission at wavelengths longer than 300 nm, where variability is typically less than 1%. In the visible and infrared regions, solar variability is known to be small, but very little is known about the spectral distribution of variations since only the total solar irradiance variation has been recorded. Because this portion of the solar radiation reaches the Earth's surface and affects directly the troposphere, its long–term variation can influence the Earth's climate. Accurate measurements are therefore important to establish the solar contribution to climate change. At this purpose, a new improved version of SOLSTICE, SOLSTICE II, will be flown in the year 2002 as part of the EOS Mission. SOLSTICE II will continue to monitor the ultraviolet region between 120–300 nm using a grating spectrometer similar to the current SOLSTICE. In addition, an electrical substitution radiometer and prism spectrometer will cover the visible and near infrared region up to $2.0\mu m$ with a relative accuracy of 0.01%. New solar measurements will also be available in the near future at the shorter ultraviolet wavelengths. The Solar EUV Experiment (SEE), on the TIMED mission planned for the year 2000, will carry two solar instruments which will make daily solar measurements from 0.1 to 200 nm. They will provide new information on the spectral region very important for the upper atmosphere above 80 km whose long–term variability is still poorly known.

References

Brasseur G., and S. Solomon, *Aeronomy of the middle atmosphere: chemistry and physics of the stratosphere and mesosphere*, Kluwer Academic Publishers, 1986.

Brasseur, G., The response of the middle atmosphere to long-term and short-term solar variability: a two-dimensional model, *J. Geophys. Res.*, **98**, 23079, 1993.

Brueckner, G. E., K. L. Eldow, L. E. Floyd, J. L. Lean, and M. E. VanHoosier, The Solar Ultraviolet Spectral Irradiance Monitor (SUSIM) experiment on board the Upper Atmosphere Research Satellite (UARS), *J. Geophys. Res.*, **98**, 10695, 1993.

Chandra, S., The solar UV related changes in total ozone from a solar rotation to a solar cycle, *Geophys. Research. Lett.*, **18**, 837, 1991.

Foukal, P., *Solar astrophysics*, New York, Wiley, 1990.

Hood, L. L., J. P. McCormack, Components of interannual ozone change based on Nimbus 7 TOMS data, *Geophys. Research. Lett.*, **19**, 2309, 1992.

Lean, J., Variations in the Sun's radiative output, *Rev. of Geophys.*, **29**, 505, 1991.

Lean, J., Solar Forcing of Global Change in the *The Solar Engine and its Influence on Terrestrial Atmosphere and Climate*, E. N. Ribes editor, Springer–Verlag, 1994.

London, J., Observed solar UV irradiance variations of importance to middle atmosphere energetics and photochemistry, *Adv. Space Res.*, **14**, 9, 933, 1994.

Rottman, G. J., T. N. Woods, and T. P. Sparn, Solar–Stellar Irradiance Comparison Experiments 1, 1. Instrument design and operation, *J. Geophys. Res.*, **98**, 10667, 1993.

Rottman, G. J., Cebula R. P., Gillot D., and Simon P., Solar Ultraviolet Irradiance, 120 to 300 nm in the *Proceedings of the SOLARS22 Workshop*, Sacramento Peak, June 1996.

Wilson, R. C., The Sun's luminosity over a complete solar cycle, *Nature*, **351**, 42, 1991.

Woods, T. N., G. J. Rottman, and G. J. Ucker, Solar–Stellar Irradiance Comparison Experiments 1, 2. Instrument calibration, *J. Geophys. Res.*, **98**, 10679, 1993.

Woods, T. N., R. T. Wrigley, G. J. Rottman, and R. R. E. Haring, Scattered light properties of diffraction gratings, *Appl. Opt.*, **33**, 4273, 1994.

Woods, T. N., et al., Validation of the UARS solar ultraviolet irradiances: Comparison with ATLAS 1 and 2 measurements, *J. Geophys. Res.*, **101**, 9541, 1996.

Preliminary results of comparing
RSS measurements with MODTRAN

Lee Harrison, Qilong Min, and Joe Michalsky
Atmospheric Sciences Research Center
State University of New York at Albany
251 Fuller Road
Albany, New York 12203

Abstract

The Rotating Shadowband Spectroradiometer (RSS) is a new instrument that provides spectral direct, diffuse, and total horizontal irradiances with a 512 CCD-array over the wavelength range from 350 nm to 1075 nm. We compare the measured spectra from the RSS to that taken by a collocated MFRSR, and MODTRAN-3.5 calculations. The measurements from both instruments (RSS and MFRSR) agree within 2%. The model calculated direct-horizontal irradiances show very good agreement with the measurements. However, the model substantially overpredicts the diffuse-horizontal if the standard "rural aerosol" model is applied. If instead we use MODTRAN's "urban aerosol" properties for the asymmetric factor and single scattering albedo, the discrepancy can be eliminated. The spectral signatures of discrepancy suggest that the scattering treatment of the diffuse irradiance and uncertainties about aerosol microphysics may be the reasons for "clear-sky anomaly".

Introduction

The two prototype RSS instruments were operated at the H_2O Intensive Operation Period held at the Southern Great Plains (SGP) field site of the Atmospheric Radiation Measurement (ARM) Program, September 1996. Both instruments operated continuously without failure for the campaign. Each instrument was calibrated at least once per day to assess instrument stability under field conditions. The instruments were stable and reproducible to approximately 0.3% in irradiance (the limit of stability of our calibrating standard) over the experiment period, with no statistically significant trend. For the RSS, the external dimensions of the fore-optic diffuser and associated shadowband mechanism are identical in scale and operation to that of the Multi-filter Rotating Shadowband Radiometer (MFRSR) [Harrison et al., 1995]. However the internal geometry of the fore-optic is substantially different, and instead feeds a prism spectrograph with a 512 element linear CCD-array detector [Harrison et al., 1996].

We will compare the clear-sky data to that taken by a collocated MFRSR and model calculations using MODTRAN-3.5 [Berk et al., 1989] during H_2O IOP at SGP site. After the IOP campaign with a new windowless CCD array device, the instrument's out-of-band rejection has been improved. We further compare the improved measurements observed at ASRC with the MODTRAN calculations.

Comparison with MODTRAN and MFRSR

The modeled spectra were produced using MODTRAN 3.5: a recent release that includes a discrete-ordinates scattering code (DISORT) [Stamnes, 1988], so that scattering atmospheres can be treated. All calculations were done using 16 ordinates. Spectra were computed at much higher spectral resolution, and then convolved with an estimate of the RSS slit-function to produce the results shown here. The standard fall mid-latitude H_2O column was used without modification; in this particular case, September 22, 1996, shown in Figure (1), it was close to the real atmospheric state. Calculations were done for two aerosol models: MODTRAN's standard "urban" and "rural." In both cases the visibility was set to 54 km: a value that produced best agreement in the direct-horizontal. (Equivalent to using the direct-beam measurement to determine the optical depth.)
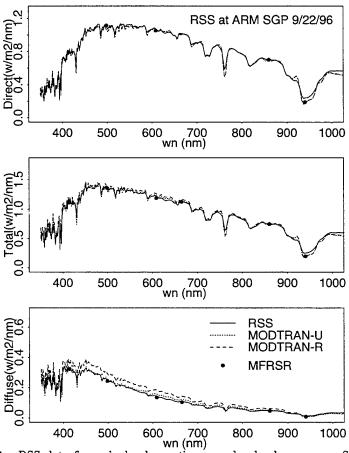

Figure 1 RSS data for a single observation near local solar noon on Sept. 22, 1996 at SGP, together with data from a collocated MFRSR and results modeled using MODTRAN 3.5.

In the top panel of Figure (1) (the direct-horizontal) we can see that agreement is exceptional, for all wavelengths less than 900 nm. At wavelengths greater than 900 nm the RSS shows an irradiance greater than that seen by the MFRSR at 940 nm, or than MODTRAN predicts. For wavelengths beyond 1 μm the slope is aphysical. The RSS data from SGP are affected at these longest wavelengths by inadequate out-of-band rejection. This problem is due to reflections associated with the window in front of CCD array (Modifications made to the instrument after the field campaign have eliminated this artifact, and arguably we can recover accurate data from the
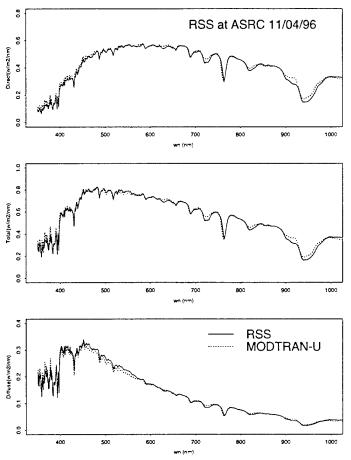
279

Figure 2 RSS data for a single observation near local solar noon on Nov. 4, 1996 at ASRC, and results modeled using MODTRAN 3.5.

campaign via deconvolution). However, for the moment we should simply ignore RSS data taken during this campaign at wavelengths > 900 nm.

The second two panels show that if the standard "rural aerosol" model is applied it then over-predicts the total-horizontal shortwave irradiance by roughly 8%. This result is reminiscent of current discussions about a "shortwave anomaly" based on broadband shortwave data and models [Wild et al., 1995; Kato et al., 1996]. They see comparable agreement of direct-beam irradiance between measurements (active cavity radiometer) and models, and model overprediction of diffuse broadband irradiance compared to pyranometer measurements. The situation is difficult to untangle solely with broadband data both because without spectral signatures it has been difficult to ascribe the mechanism, and calibration uncertainties associated with the pyranometers (and hence the accuracy of derived direct/diffuse ratios) are difficult to rule out.

The third panel demonstrates that the discrepancy seen between the prediction assuming a rural aerosol and the observations clearly has an aerosol-like signature. Further, the discrepancy can be eliminated by choosing the "urban aerosol" model that decreases the assumed single-scattering albedo and asymmetry factor. At the moment the microphysical optical properties of the aerosol over the SGP site are not observed, and so the question of whether the assumption of an "urban aerosol" is plausible remains moot. The issue awaits further collection of data (where we may see a range of aerosol properties), and hopefully aerosol optical measurements aloft.

280

Figure (2) shows the comparison of MODTRAN calculation with an terrestrial spectrum taken with RSS at ASRC (in Albany NY) after the windowless CCD array device was substituted. The long wavelength data are now accurate.

In this case the data were taken at ASRC on Nov 4, 1995, and again the default standard seasonal atmosphere (for H_2O) and urban aerosol model were assumed. In this case the atmosphere clearly had a greater water column than model, but otherwise agreement is excellent throughout the spectrum, except for the A-band of O2 . The likely cause of this discrepancy is a mild underestimate of the width of the instrument-function used to convolve the spectrum, or the overestimate of O2 absorption coefficients in MODTRAN3.5.

Conclusion

We compare the data to that taken by a collocated MFRSR and model calculations using MODTRAN-3.5. Agreement is generally excellent (better than 2%, an optimistic assessment of our calibrator's absolute uncertainty). The modeled diffuse irradiance is substantially too large for the two clear days of the IOP in comparison to the observed results unless MODTRAN's "urban aerosol" properties for the single-scattering albedo and phase function are used. If the "rural aerosol model" is used then the total surface irradiance predicted by the model is about 8% too large. The broad spectral behavior of this potential discrepancy, and it's presence only in the diffuse component, clearly identifies it as associated with scattering processes, not trace gas absorption. The spectral signatures of discrepancy suggest that the scattering treatment of the diffuse irradiance and uncertainties about aerosol microphysics may be the reasons for "clear-sky anomaly". In the absence of more data, and hopefully in-situ measurements of single-scattering albedo and asymmetry parameter, the question of whether there is a "clear sky anomaly" remains moot.

References

Berk, A., L. S. Bernstein, and D. C. Robertson, *MODTRAN: a moderateresolution model for LOWTRAN7*, Report AFGL-TR-89-0122 (Air Force Geophysics Laboratory), Hanscom, AFB, Ma, 1989.
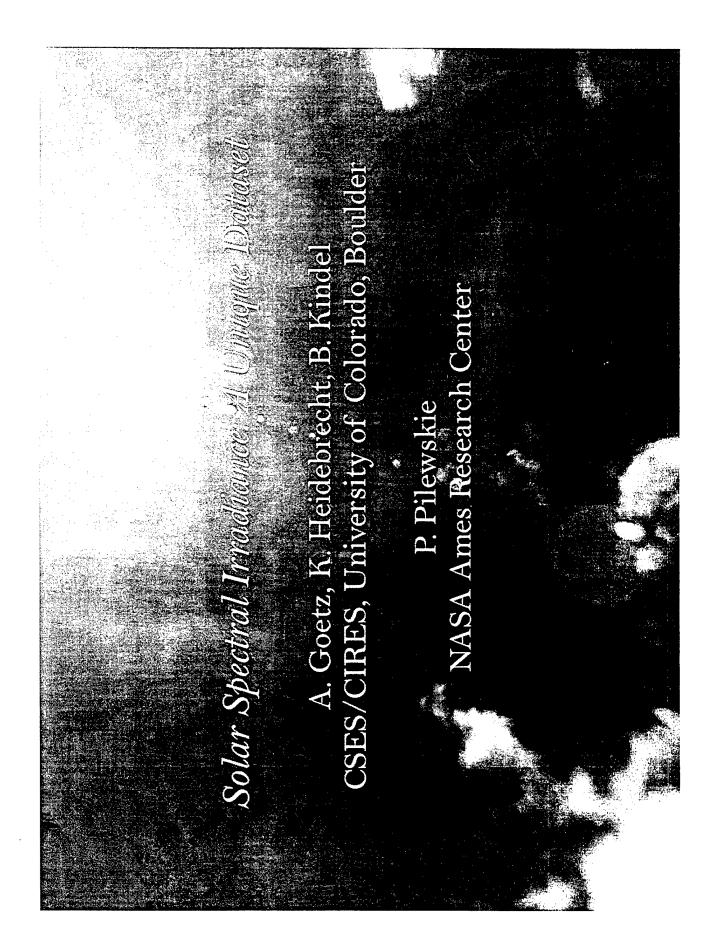
Harrison, L. C., J. J. Michalsky, and J. Berndt, Automated multi-filter rotation shadowband radiometer: an instrument for optical depth and radiation measurements, *Appl. Optics, 33*, 5188, 1994.
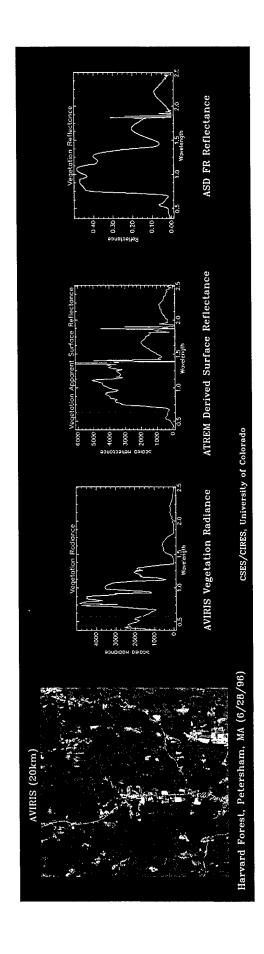
Harrison, L. C., J. Berndt, M. Beaharnois, B. Berkheiser III J. Michalsky, and Q. Min, Rotating Shadowband Spectroradiometry at SGP, RSS-Report, on solsun1.asrc.cestm.albany.edu: *pub/RSS_Report.pdf*, 1996.

Kato, S., T.P. Ackerman, C.N. Long, E. Clothiaux, and J. Mather, A comparison between clear-sky short-wave flux calculations and observations during ARESE. Abstracts of Sixth Atmospheric Radiation Measurement Science Team Meeting, 39, 1996.

Stamnes, K, S.-C. Tsay, W. Wiscombe, and K. Jayaweera, Numerically stable algorithm for discrete-ordinate-method radiative transfer in multiple scattering and emitting media, *Appl. Optics, 27*, 2502, 1988.

Wild, M., A. Ohmura, and H. Gilgen, Validation of general circulation model radiative fluxes using surface observations. J. Clim., 8, 1309, 1995.

Solar Spectral Irradiance: A Unique Dataset

A. Goetz, K. Heidebrecht, B. Kindel
CSES/CIRES, University of Colorado, Boulder

P. Pilewskie
NASA Ames Research Center

AVIRIS (20km)

Vegetation Radiance

AVIRIS Vegetation Radiance

Vegetation Apparent Surface Reflectance

ATREM Derived Surface Reflectance

Vegetation Reflectance

ASD FR Reflectance

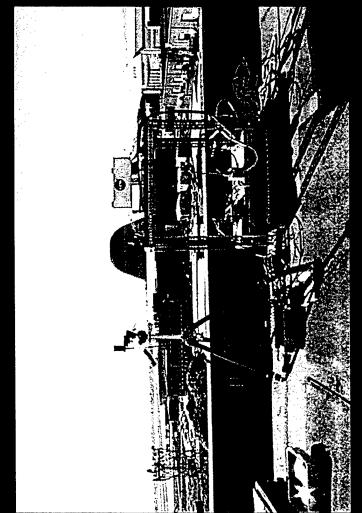Harvard Forest, Petersham, MA (6/28/96)

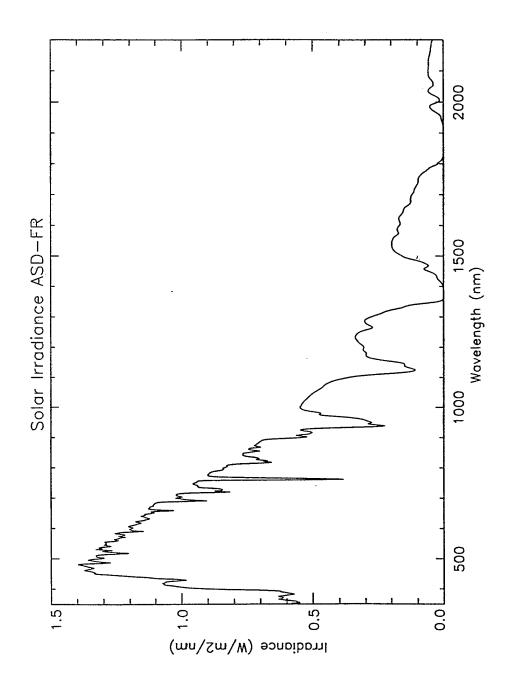CSES/CIRES, University of Colorado
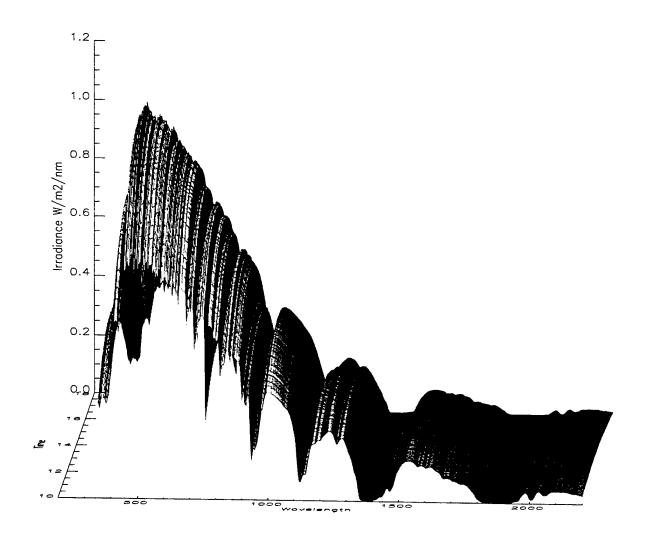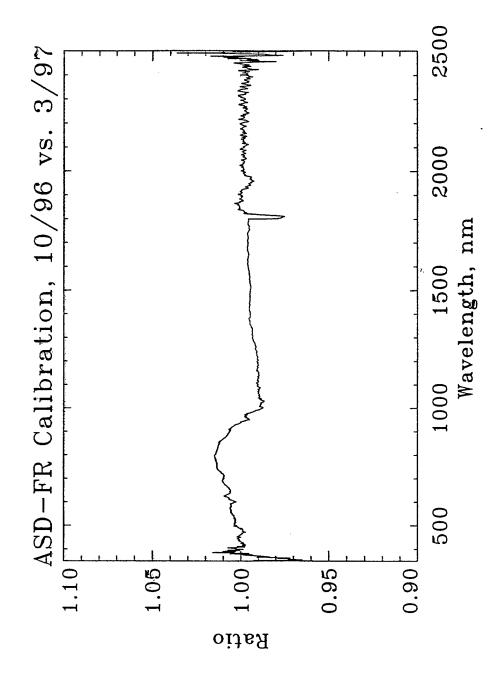
ASD-FR Spectroradiometer

Spectral Range
350-2500 nm

Spectral Resolution
3-4 nm VNIR
10-12 nm SWIR
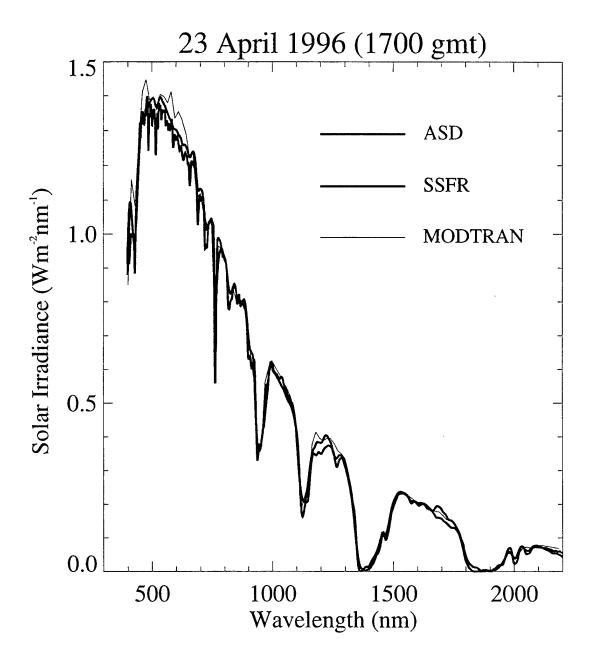
Spectral Sampling
1.4 nm VNIR
2.2 nm SWIR
Resampled to 1 nm

Solar Irradiance ASD-FR

Irradiance (W/m2/nm)

Wavelength (nm)

ASD–FR Calibration, 10/96 vs. 3/97

287

23 April 1996 (1700 gmt)

Harvard Forest, MA

ASD
— — Modtran

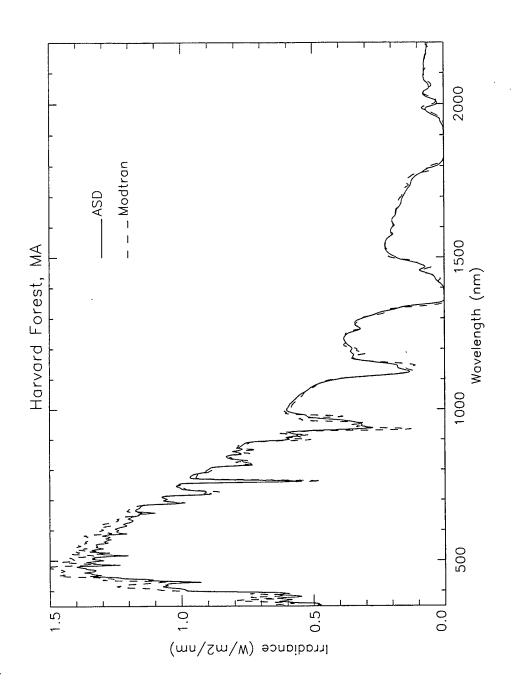Irradiance (W/m2/nm)

Wavelength (nm)

Further work

- Continue measurements during Summer-Fall 1997.

- Atmospheric parameterization (principal components analysis).

- Calibration study (absolute):
  - cross calibration experiment with NASA Ames, Los Alamos, JPL, NASA Goddard.
  - cosine response characterization.

- Improved MODTRAN modeling:
  - optical depth (10 channel sun photometer).
  - radiosonde data.

- Side by side comparison with broadband instruments.

- DOE CART site.

Conclusions

- The ASD-FR is a stable instrument capable of measuring surface solar irradiance at resolutions which can provide additional information on the important constituents of the atmosphere.

- A large surface solar spectral irradiance dataset exists for Boulder, CO, under a variety of atmospheric conditions. These data will be made generally available when calibration issues are resolved.

- Preliminary results show good agreement with the MODTRAN model.

Pages 292-304 intentionally blank
text of talk not available

This page intentionally blank

MWIR ATMOSPHERIC CORRECTION ALGORITHM

H.K. Burke, J.W. Snow, K.E. Rhoades, J.P. Kerekes, M.P. Jordan and C.A. Upham

MIT Lincoln Laboratory

20th Annual DoD Atmospheric Radiance and Transmission Meeting

10-12 June 1997

MIT Lincoln Laboratory

Remote Sensing Applications
(3-5 μm)

- **Missile Warning and Tracking**
  - Effective radiation from "hot" objects
  - Absorption bands

- **Atmospheric and Earth Background Sensing**
  - Distinct surface and cloud radiative properties
  - Window bands

- **Signature Sources**
  - Thermal emission
  - Solar reflection
  - Major atmospheric absorbers
    - water vapor, CO_2, aerosols, clouds

MIT Lincoln Laboratory

MWIR Atmospheric Correction Experiments

Objective:

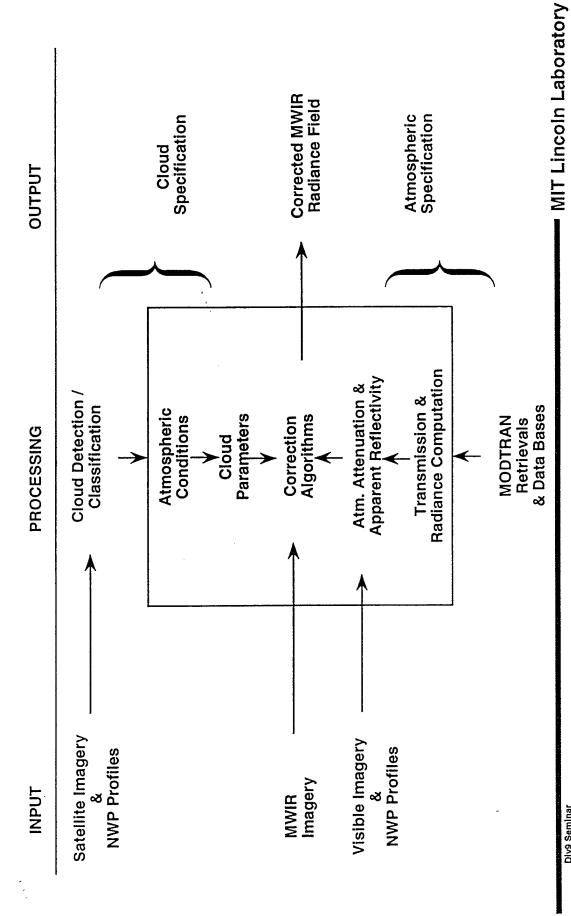- Enhance utility of space-based MWIR-only observations of earth's surface

Approach:

- Synergistic algorithm

  - Physics-based technique with improved models

  - Utilizes operational environmental data

  - Includes new cloud analysis methodology

Architecture of the MWIR Data Correction Technique

INPUT	PROCESSING	OUTPUT

Satellite Imagery & NWP Profiles → Cloud Detection / Classification

Atmospheric Conditions → Cloud Parameters → Correction Algorithms

Cloud Specification

Corrected MWIR Radiance Field

Atmospheric Specification

MWIR Imagery

Visible Imagery & NWP Profiles

Atm. Attenuation & Apparent Reflectivity

Transmission & Radiance Computation

MODTRAN Retrievals & Data Bases

Correction Algorithm

$$B_s = \frac{Rsat - (1 - \varepsilon_s)\tau \; Bsky - Batm}{\varepsilon_s \tau}$$

$$T_r = Planck^{-1}(B_s)$$

WHERE   Rsat (Night) = SATELLITE MEASURED SPECTRAL RADIANCE

Rsat (Day)   = MEASURED RADIANCE - SOLAR COMPONENTS
(atmospheric scattering & ground reflection)

T_r =   SURFACE TEMPERATURE
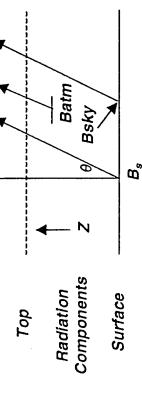
ε_s =   SURFACE EMISSIVITY

B_s =   CORRECTED SURFACE SPECTRAL RADIANCE

τ =   GROUND - TO - SPACE TRANSMITTANCE
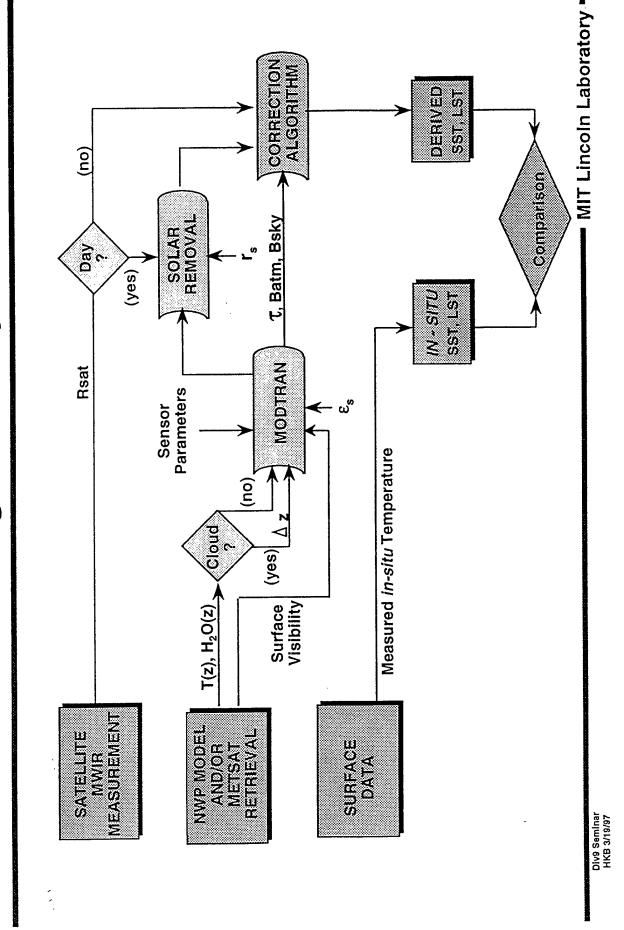
Bsky = DOWNWARD SKY SPECTRAL RADIANCE

Batm = UPWARD ATMOSPHERIC PATH RADIANCE

Top

Radiation Components

Z

θ

Batm

Bsky

B_s

Surface

Data Processing and Analysis Procedure
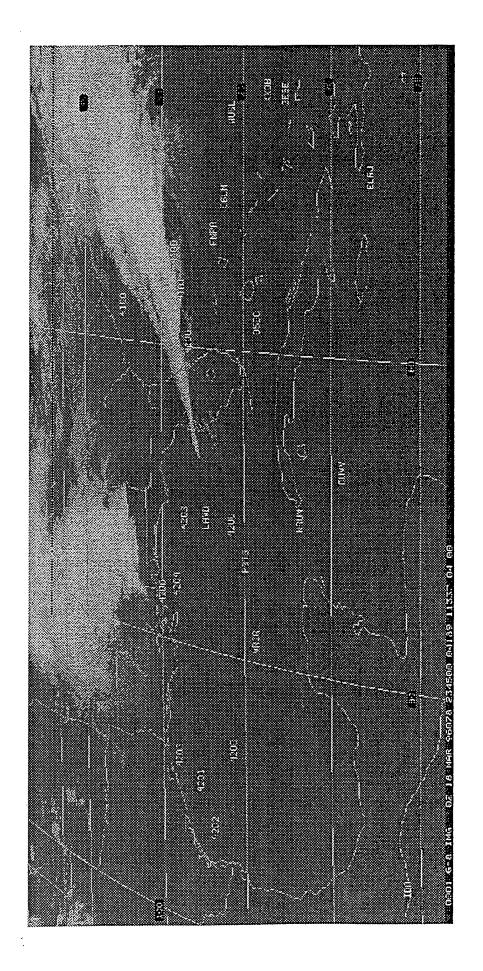
GOES-8 MWIR Imagery (with Buoy Locations)
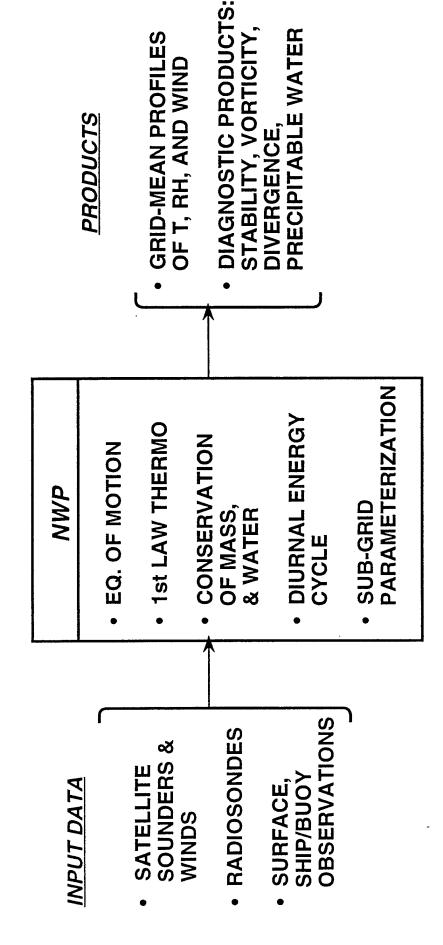
Numerical Weather Prediction (NWP)
- Overview -

INPUT DATA

- SATELLITE SOUNDERS & WINDS
- RADIOSONDES
- SURFACE, SHIP/BUOY OBSERVATIONS

NWP

- EQ. OF MOTION
- 1st LAW THERMO
- CONSERVATION OF MASS, & WATER
- DIURNAL ENERGY CYCLE
- SUB-GRID PARAMETERIZATION

PRODUCTS

- GRID-MEAN PROFILES OF T, RH, AND WIND
- DIAGNOSTIC PRODUCTS: STABILITY, VORTICITY, DIVERGENCE, PRECIPITABLE WATER
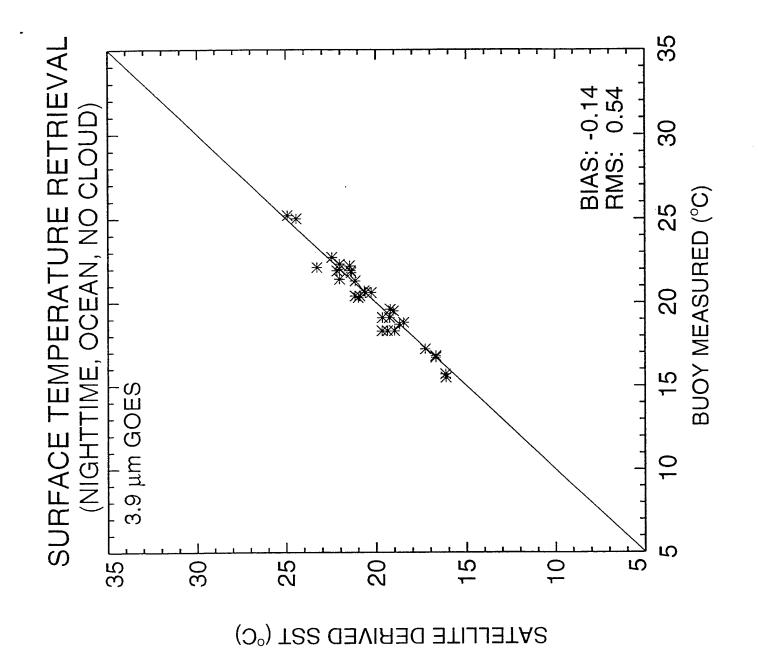
MODTRAN

- **MODTRAN is an integrated computer code used for the prediction of**

  - Atmospheric transmittance

  - Atmospheric background radiance

  - Multiple scattered solar/ thermal radiance

- **MOTRAN provides thermal structure of six model atmospheres**

  - User may input their own atmospheric data

- **Components of atmosphere include profiles of**

  - Temperature, pressure

  - Density and mixing ratios for H_2O, CO_2, O_3, CH_4, SO_2, etc.
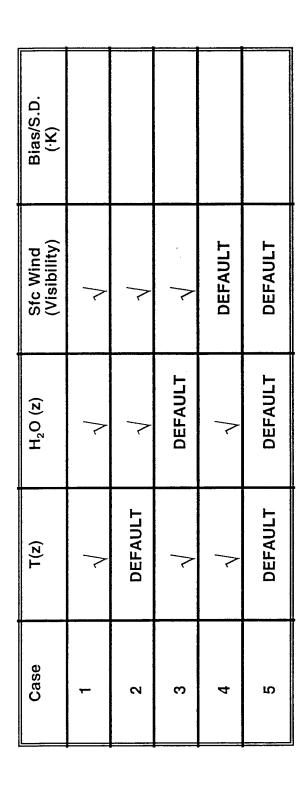
SURFACE TEMPERATURE RETRIEVAL
(NIGHTTIME, OCEAN, NO CLOUD)

3.9 µm GOES

BIAS: -0.14
RMS: 0.54

BUOY MEASURED (°C)

SATELLITE DERIVED SST (°C)

Sensitivity Analysis

- Environmental Parameter Sensitivities

- MWIR vs LWIR

Environmental Parameter Sensitivities
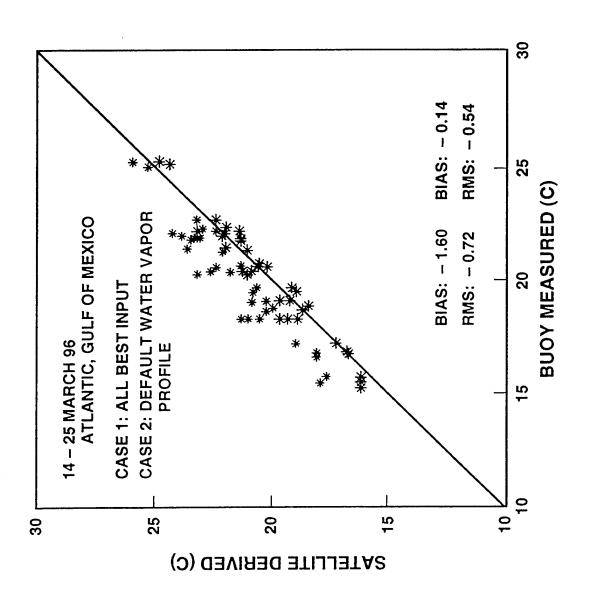
Case	T(z)	H_2O (z)	Sfc Wind (Visibility)	Bias/S.D. (°K)
1	√	√	√	
2	DEFAULT	√	√	
3	√	DEFAULT	√	
4	√	√	DEFAULT	
5	DEFAULT	DEFAULT	DEFAULT	

√ : INPUT WITH BEST INFORMATION AVAILABLE

DEFAULT 2, 3 : U.S. STANDARD ATMOSPHERE

DEFAULT 4 : MARITIME STANDARD

SATELLITE DERIVED SEA SURFACE TEMPERATURE (MWIR) vs BUOY MEASUREMENTS
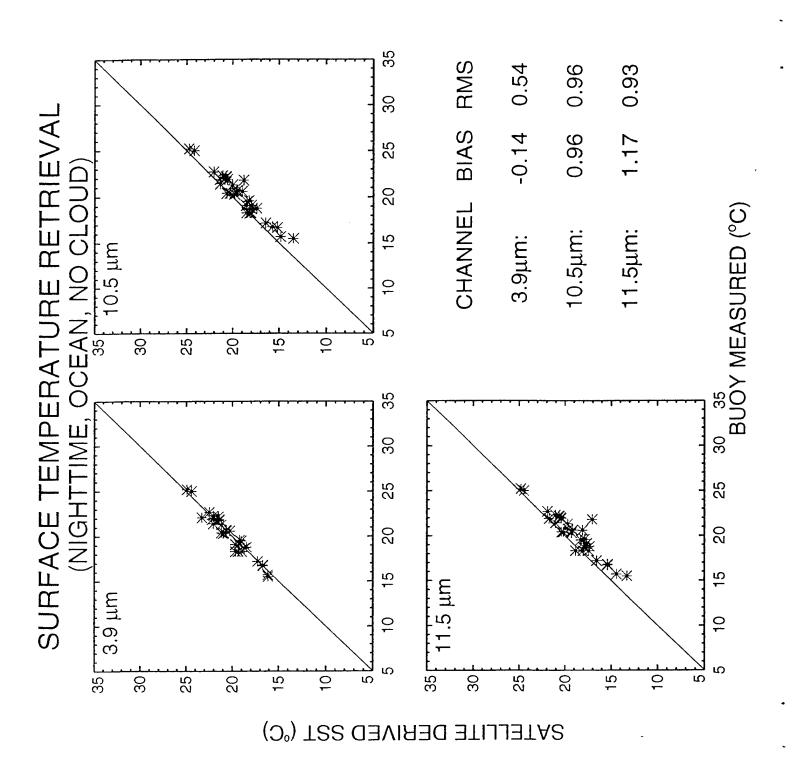
14 – 25 MARCH 96
ATLANTIC, GULF OF MEXICO

CASE 1: ALL BEST INPUT
CASE 2: DEFAULT WATER VAPOR PROFILE

BIAS: – 1.60   BIAS: – 0.14
RMS: – 0.72   RMS: – 0.54

Environmental Parameter Sensitivities

Case	T(z)	H_2O (z)	Sfc Wind (Visibility)	Bias/S.D. (·K)
1	√	√	√	-0.14/ 0.54
2	DEFAULT	√	√	-1.82/ 0.57
3	√	DEFAULT	√	-1.60/ 0.72
4	√	√	DEFAULT	-1.38/ 0.57
5	DEFAULT	DEFAULT	DEFAULT	-1.85/ 0.40

√ : INPUT WITH BEST INFORMATION AVAILABLE

DEFAULT 2, 3 : U.S. STANDARD ATMOSPHERE

DEFAULT 4 : MARITIME STANDARD

MIT Lincoln Laboratory

SURFACE TEMPERATURE RETRIEVAL
(NIGHTTIME, OCEAN, NO CLOUD)

3.9 μm

10.5 μm

11.5 μm

CHANNEL	BIAS	RMS
3.9μm:	-0.14	0.54
10.5μm:	0.96	0.96
11.5μm:	1.17	0.93

SATELLITE DERIVED SST (°C)

BUOY MEASURED (°C)

Sensitivity Analysis Results

- **Environmental parameter sensitivities**

  - Correct representation of state-of-atmosphere is essential for accurate surface retrieval

  - Operational NWP products provide sufficient input

- **MWIR vs LWIR**

  - In MWIR, water vapor absorption coefficient is ~100 times less than in LWIR

  - Given same input, MWIR results less sensitive to water vapor uncertainties

SURFACE TEMPERATURE RETRIEVAL
(NIGHTTIME, LAND, NO CLOUD)

3.9 μm GOES

BIAS: 0.16
RMS: 1.50

SURFACE STATION MEASURED (°C)

SATELLITE DERIVED LST (°C)

Tangible Benefits and Lessons Learned

Tangible Benefits:

- Experience gained in MWIR utilization

- Quality improvement to operational surface temperature models

Lessons Learned:

- NWP (e.g., Eta) output information useful characterization of atmospheric state

- MODTRAN model versatile and powerful atmospheric correction

MWIR Atmospheric Correction Algorithm

Summary

- New and innovative retrieval algorithm for surface radiance successfully developed and demonstrated

  - Approach utilizes existing "operational" products and state-of-science model

  - Various test cases (night/day, ocean/land)

- Significant results of MWIR atmospheric correction experiments

  - Improved accuracy of surface temp retrieval

    SST retrieval bias 0.1K, RMS 0.5K

324

Use of MODTRAN Software in Performance and Analysis Capability for Earth Observation Systems (PACEOS™) Simulation Software[*]
*© 1997 Lockheed Martin Corporation   All Rights Reserved

Steve Marusa, Rafael A. Rivera

Lockheed Martin Missiles and Space
230 Mall Blvd., King of Prussia, PA 19403

and

Keith D. Hutchison, William Uplinger

Lockheed Martin Missiles and Space
1111 Lockheed Martin Way
Sunnyvale, Ca. 94089

ABSTRACT

The Performance and Analysis Capability for Earth Observation Systems (PACEOS™) computer simulation software was developed as an engineering tool by Lockheed Martin to assist in the evaluation of concepts and designs for space-based remote sensing systems. This development took place over the past ten years. PACEOS™ models the entire remote sensing process from the radiation source to the information extracted by the user. The simulation is divided into 10 primary sections: Input Scene, Scene Generation, Sensor Performance, On-board Processing, Data Compression, Downlink, De-Compression, Ground Processing, Metrics, and Analysis. PACEOS™ simulates the performance of earth and atmospheric remote sensing, surveillance, and early warning systems and is primarily used for concept definition and evaluation of hardware/software performance to evaluate the effects of sensor, platform, and processing parameters on the quality and accuracy of the information provided to the ultimate users.

This paper discusses the uses of the MODTRAN software in the Scene Generation module of PACEOS™. The MODTRAN software is used to calculate radiances and transmissions that are applied to the input scene as needed by the PACEOS™ software for electro-optical systems. PACEOS™ sets up and runs MODTRAN and extracts the parameters needed to generate the scene. The PACEOS™ user has the option to calculating radiances as a function of albedo, emissivity, or temperature from an input image or from an image comprised of material characteristics. Options to vary atmospheric profiles, sensor zenith angle, and sun/moon position are available, as well as the ability to insert cloud layers over the surface scene. RADTRAN is used in a similar way for microwave scene generation.

Keywords: PACEOS™, scene generation, cloud layering, material mode, non-homogeneous atmospheres, cloud, bandpass modification

1. OVERALL PACEOS™ PROCESS

PACEOS™ is used to assess the performance of current and proposed electro-optical (EO) sensor systems by modeling the effects of: 1) scene phenomenology and propagation to the sensor, 2) sensors, detectors, and platforms, 3) on-board processing, 4) downlink, 5) ground processing and analysis, and 6) end user product generation. The overall PACEOS™ functions are illustrated in Figure 1.1. PACEOS™ is primarily used to generate data from which hardware and software trades can be made based on their effect on user information requirements. Interfaces to various data bases and external codes are provided to assist in the assessment of the performance of current and proposed UV, visible, IR, and microwave systems for surface and atmospheric remote sensing, early warning, and surveillance.

The PACEOS™ software can be run interactively or in various batch modes. PACEOS™ is designed to be user-friendly in the interactive mode with a large variety of pull-down and pop-up menus on a Sun or DEC Alpha workstation. The user is first presented with the overall menu shown in Figure 1.2, from which any portion or an entire set of the software can be run. With each primary section chosen, the user can select the desired level of simulation detail, which determines the options available in the remaining menus. If the user is less familiar with a given portion of the simulation, a level with less detail can be chosen and defaults used for some of the less critical choices. If the user is familiar with a given portion, a more detailed level can be chosen with more control over the simulation parameters. A discussion of the overall simulation was presented in a 1994 SPIE paper, "Geometric Mapping
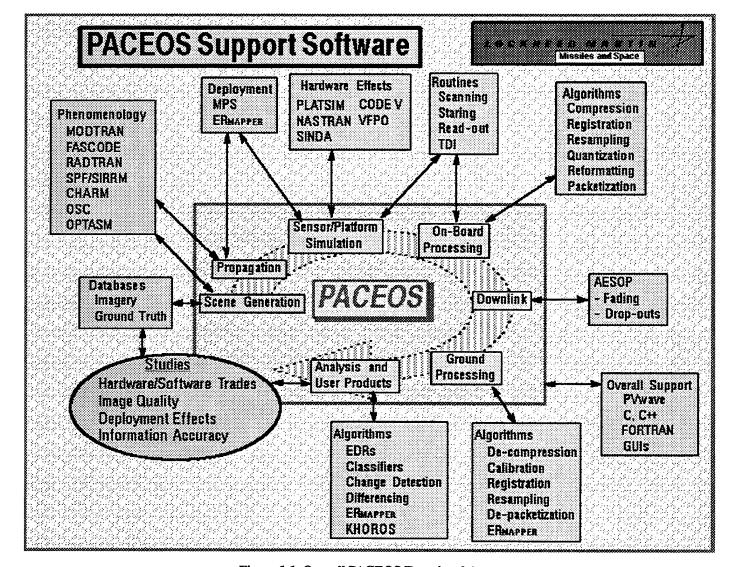
Figure 1.1 Overall PACEOS Functional Areas

in an Advanced Remote Sensing Simulator"[1]. Other details on PACEOS™ scene generation were discussed in a 1995 SPIE paper, "Input Scene Generation for System Performance Evaluation"[2].

2. INPUT SCENE SELECTION

The PACEOS™ process begins with the selection of an input scene from data bases containing different scene categories. A large variety of satellite and airborne single or multi-band scenes are available to choose from, as well as scenes made up of materials from either a materials classification code, Environmental Data Record (EDR) algorithms or manually generated scenes. Various routines are available to apply geometric corrections to the scene. Other routines allow the user to modify the intensity of pixels within the scene to represent different albedos or emissivities and to add targets and test patterns to the scenes. Other input scenes have be generated for space or limb viewing and complete simulations have been made for airborne as well as space-based systems.

MODTRAN software is used to calculate the emitted and scattered radiance for scenes propagated through an atmosphere. PA-CEOS™ sets up most of the needed MODTRAN parameters based on the conditions to be simulated and gives the user the opportunity to view and modify the inputs if desired. No changes internal to MODTRAN have been made; however, a large amount of software written in C, UNIX and PVwave has been generated to setup the input files and to extract the calculated temperatures and wavelengths. MODFIL is used to apply spectral filters to the MODTRAN-calculated radiances and transmissions. The remainder of this paper discusses the setup and running of MODTRAN and the use of its outputs in generating input scenes. This methodology is described by showing two examples, one for a material-based earth surface input scene and one for an earth limb-viewing scene from space.
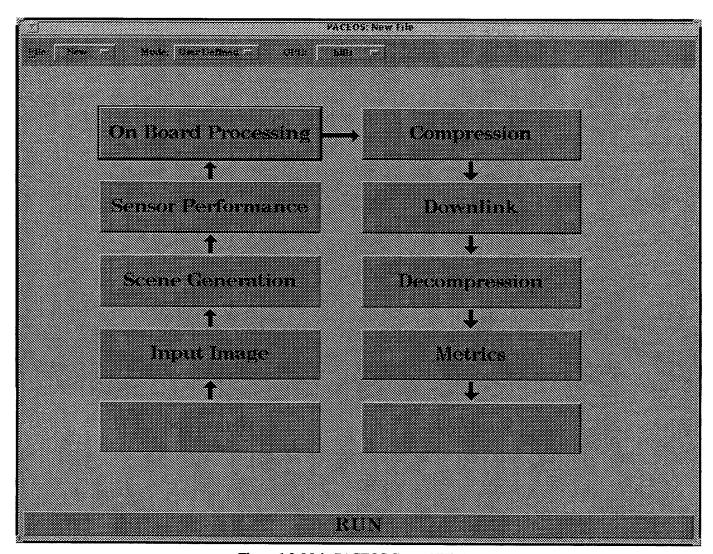
Figure 1.2 Main PACEOS Control Window

3. MATERIAL BASED INPUT SCENE GENERATION

In this example, the radiance distribution of a 512x512 pixel input scene generated using three surface materials with varying surface temperature will be propagated through a non–homogeneous atmosphere with low and high altitude cloud layers using the spectral response of AVHRR band 4 centered at approximately 10.8 μm. The sensor zenith angle and the solar azimuth and elevation angles will also be varied across the scene. The initial input scene used for this run is shown in Figure 3.1.

3.1 BAND FILE SELECTION AND CONTENT

Most of the sensor and platform related parameters used by PACEOS™ are contained in "band" files. These files are generated prior to or during the running of PACEOS™, a separate file is generated for each band of each sensor. For the simulation results shown in this paper, band 4 of the AVHRR sensor was chosen. Parameters in this file include values that define the beginning and ending wavenumbers and the resolution of the MODTRAN run, the viewing geometry, and the system's spectral response as a function of wavelength for MODFIL. These values are used along with default values to generate the interactive input window shown in Figure 3.2.

Any of the values presented in this window can be changed by the user prior to or during the simulation. In this case, MODFIL will be run; therefore, the bandpass specified for the MODTRAN run is wide enough to accommodate all the wavelengths defined in the MODFIL input file. All of the MODTRAN options for atmospheric, haze, and dust models can be selected from this window.
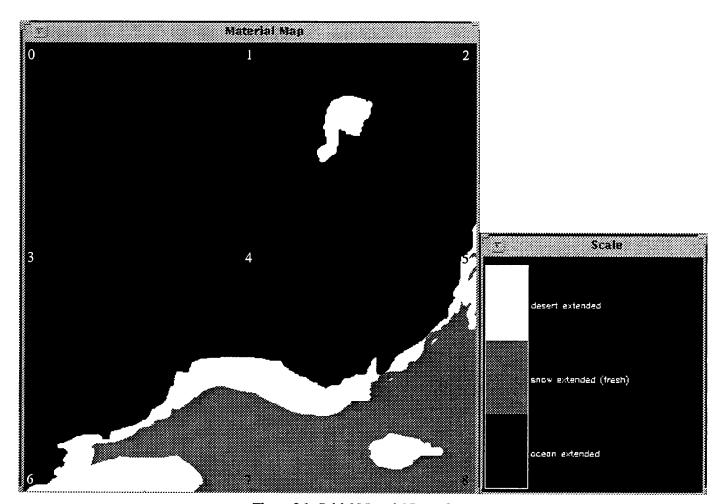
327

Figure 3.1. Initial Material Input Scene

If a user-defined atmospheric model is chosen, PACEOS™ will present other windows through which the user can build the desired profile. Choosing to vary temperature across the scene results in the amplitude of the scene being scaled between two temperature values (which are defined later in the run) and the setup of the MODTRAN input file to run cases at the two temperature values. The option to force MODTRAN to run was installed to allow the user to skip the running of MODTRAN if a identical run was done previously and the output files saved. The parameters illustrated in Figure 3.2 result in MODTRAN being run at 1 cm^{-1} resolution from 833 to 1030 cm^{-1}.

3.2 MATERIAL MODE OPERATION

When an input scene consisting of several materials is chosen, PACEOS™ sets up to run MODTRAN sequentially for each material. The individual material output scenes are merged into a single complete image. In this mode of operation, it is necessary to have each material in the scene identified with the appropriate index value for that material in the MODTRAN reference background (refbkg) file. It is also necessary for the refbkg file to have reflectance values for all the materials in the scene across the bandpass being simulated.

The selected input scene, shown in Figure 3.1, is comprised of three materials: ocean, desert, and snow. The refbkg file was extended to include values for these materials at high spectral resolution across the band being simulated, 10.8 μm for this run, and the materials were assigned numerical values that correspond to the material index values in the modified refbkg file.

3.3 NON-HOMOGENEOUS ATMOSPHERE

The non-homogeneous atmosphere mode is chosen in PACEOS™ to allow variations in the atmospheric profile, viewing angles, and sun/moon position across the scene. Nine points are selected for profile specification: one in each corner of the scene, one in the center of the scene, and one midway down and across the edges of the scene as illustrated by the numbers overlaying the scene

Figure 3.2 Fully Editable MODTRAN Parameters Window

in Figure 3.1. The surface temperature, *tbound*, was varied for each material as shown in Table 3.1. The values that were varied for each of the grid points at which the conditions are specified are shown in Table 3.2.

Table 3.1. Specified Surface Temperature (K) for Materials

Material	Point 0	Point 1	Point 2	Point 3	Point 4	Point 5	Point 6	Point 7	Point 8
Ocean	280	280	278	274	273	272	271	271	270
Snow	270	270	270	271	270	270	270	269	268
Desert	279	279	279	273	273	273	270	269	270

Table 3.2. Parameters Varied at Atmospheric Profile Grid Points

Grid Point	Atmospheric Model	Haze Model	Dust Model	Sun/Moon El, Az (degrees)	Sensor Zenith Angle (degrees)
0	6 – US Standard	4 – Maritime	8 – Extreme	1/2 Moon 30, 180	180
1	6 – US Standard	4 – Maritime	3 – High/Fresh	Sun 70, 180	160
2	6 – US Standard	2 – Rural, 5 km vis	3 – High/Fresh	Sun 90, 180	140
3	3 – Midlat Winter	2 – Rural, 5 km vis	5 – Moderate	1/2 Moon 10, 180	180
4	3 – Midlat Winter	1 – Rural, 23 km vis	5 – Moderate	Sun 60, 180	160
5	3 – Midlat Winter	1 – Rural, 23 km vis	5 – Moderate	Sun 80, 180	140
6	5 – Subarctic Winter	None	None	Sun 0, 180	180
7	5 – Subarctic Winter	None	None	Sun 20, 180	160
8	5 – Subarctic Winter	None	None	Sun 40, 180	140

3.4 SCENE RADIANCE CALCULATES

No cloud layers were added during this run. The resultant radiance distribution is shown in Figure 3.3. The effects of the surface temperatures and atmospheric models used can be seen vertically across the scene with higher radiances toward the top. The effect of the haze can be seen by comparing the lower left corner to the center right region with the snow and desert materials. In the lower left corner with no haze, it is easier to see the differences in radiances than in the center right where the rural haze with 23 km visibility was added.

Generation of this image required many individual MODTRAN runs. There is no limit, other than the time required to setup and run the simulation, and the number of atmospheric grid points that can be specified.

4.0 CLOUD LAYERING OPTION

An input scene with a low and high altitude cloud layer was simulated for band 1 of AVHRR centered at 0.87 μm. This simulation was run with the same non-homogenous atmospheric conditions as the 10.8 μm scene. A stratus cloud layer and a 0.15 km cirrus cloud layer at a base height of 12 km were added to the scene. The spatial distribution of each cloud layer was specified by previously generated maps which were scaled by PACEOS™ to match the input scene size.

4.1 VARIATION OF CLOUD RADIANCES AND TRANSMISSIONS

Various algorithms were developed for PACEOS™ to generate realistic cloud radiances and transmission distributions and to overlay them on the surface scene. The process involves generating a map using fractal routines that represents the type of spatial distribution desired. Several of these maps have been generated and are accessed from PACEOS™ for both low and high altitude cloud layers. MODTRAN is setup to generate radiances and transmissions with and without the clouds present and interpolates between the values based on the weighting obtained from the cloud distribution maps specified for each run.

Calculations are made for various altitude layers in the atmosphere. The first layer calculated is from the surface scene to the top of the first cloud layer. In this case, the surface was specified to an altitude of 0 km for all atmospheric grid points and the top of the lower altitude cloud layer, the stratus clouds, was specified to an altitude of 1 km. Since this run was done in the material mode, the radiance distribution for each material was calculated separately, and the sections were merged together to form the radiance distribution at the top of the cloud layer. The results of these calculations are illustrated in Figure 4.1. Many additional MODTRAN and MODFIL runs were made to generate the radiance distribution at the top of this altitude layer.

The cloud distribution chosen for this layer has large sections with no clouds present. In these regions the surface can be seen. The effect of the moon illumination can be seen in the very low minimum radiance and in the upper left side of the image where the clouds over the ocean are very dark.
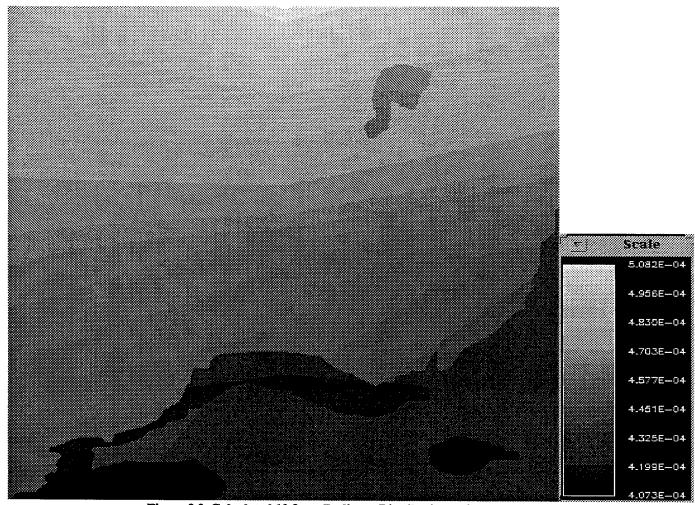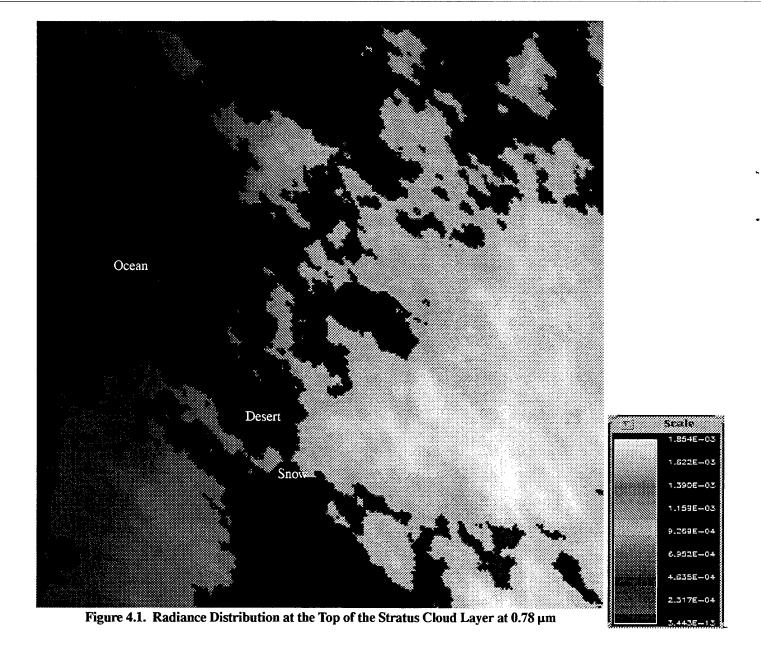
Figure 3.3. Calculated 10.8 μm Radiance Distribution at Sensor Aperture

Figure 4.1. Radiance Distribution at the Top of the Stratus Cloud Layer at 0.78 μm

The second layer calculated is from the top of the stratus cloud layer to the top of the cirrus layer. In this case, separate runs for each material are not needed since the radiance at the top of the lowest layer is calculated with all the effects of the materials accounted for. The radiance distribution at the top of this layer is not shown separately. Instead the radiance distribution at the sensor aperture is presented in Figure 4.2. This distribution includes the remainder of the atmospheric path radiance and transmission effects.
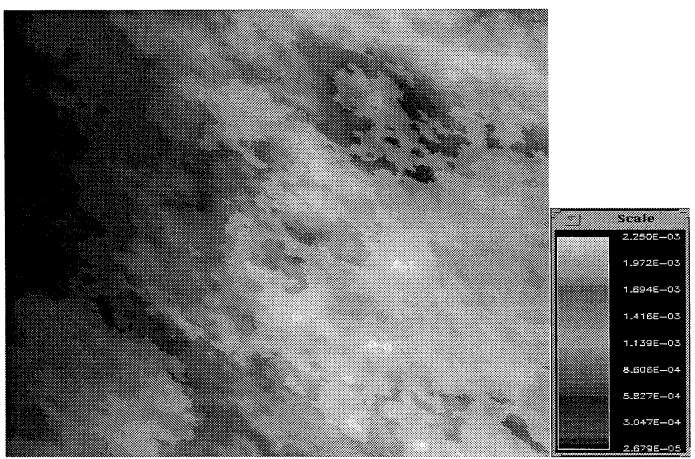
Figure 4.2. Radiance Distribution for 0.87 μm Scene at Sensor Aperture

Due to its thinness the cirrus cloud layer is partially transparent, and the underlying stratus and surface features are visible across the scene.

5. EARTH LIMB SCENE GENERATION

Generation of limb scenes by PACEOS™ require some differences in the setup and running of MODTRAN. The scene illustrated here is calculated using the non-homogeneous mode to select grid points at which the MODTRAN atmospheric conditions and illumination and viewing geometries are specified. A 5x5 set of grid points is specified and setup to run at five tangent heights with five horizontal variations across the scene, with the line-of-sight passing through the entire atmosphere from space to space. Radiances calculated for each grid point are interpolated to form a 512x512 pixel image representing the radiance at the sensor aperture.

The five tangent heights used were 1, 5, 10, 20, and 40 km. Horizontal variations are simulated by choosing the Subarctic Winter atmospheric model for the right side of the image and the Tropical atmospheric model for the left side of the image. The three profiles specified between these two are the Subarctic Summer, Mid Latitude Winter, and Mid Latitude Summer. This simulation is run at 11 μm. Changing the illumination location is not required since at this wavelength the majority of the radiance is from the surface and atmospheric emittance and the effects of the solar scattering are minimal. No clouds are added to this scene. The calculated radiance at the sensor aperture is shown in Figure 5.1.
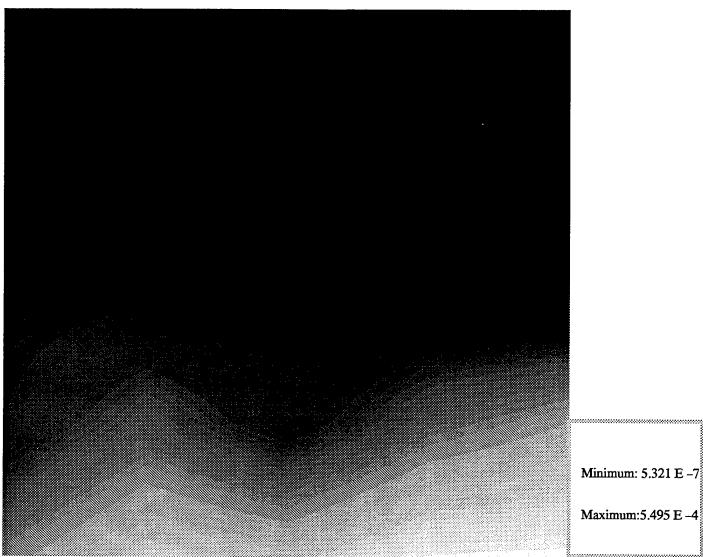
Minimum: 5.321 E –7

Maximum: 5.495 E –4

Figure 5.1. Simulated 11 μm Limb Scene

6. SUMMARY AND PLANNED FUTURE DEVELOPMENTS

This paper illustrates some aspects of one of the modules in the PACEOS™ software. MODTRAN is used to calculate radiances and transmission for electro-optical system performance assessment. As illustrated by the scene generation process shown in this paper, a wide variety of scenes can be generated using the Scene Generation module of PACEOS™. An example of using PACEOS™ to generate simulated data for a 1.6 μm band and illustrations of additional information that could be extracted if a 1.6 μm band were added to AVHRR is being prepared for publication. The simulation runs rather quickly; and the generation of all the scenes presented here took less than a day to setup and run.

The accuracy of the scenes generated by PACEOS™ have been evaluated by simulation of operational systems such as LANDSAT and TIROS and by extracting scene parameters with EDR algorithms such as Sea Surface Temperature and comparing them to the known inputs. Scenes simulated using MODTRAN in conjunction with PACEOS™ have been found to be of sufficient accuracy to evaluate the effects of modifications to various remote sensing system and sub-system elements. The use of the PACEOS™ simulation software within Lockheed Martin and in support of other organizations is increasing as the modelling capability of the software is further developed.

PACEOS™ was used in conjunction with MODTRAN3 for these calculations. Currently, MODTRAN3.5 version 1.2 is being interfaced to PACEOS™ and will replace MODTRAN3. In addition, new interfaces and input/output options are planned for PACEOS™ so that MODTRAN calculations can be made and scenes generated for other applications with more fidelity and accuracy. Other

334

planned upgrades to the Scene Generation portion of PACEOS™ include: modeling of cloud shadowing; more efficient means to simulate hyper-spectral systems; more efficient means to account for surface elevation effects; and the use of bi-directional reflectances for the materials.

9. REFERENCES

1. W. Beauchamp, S. Marusa, R. Gupta, B. Hoffman, "Geometric Mapping in a Advanced Remote Sensing Simulator", Applications of Digital Image Processing XVII, Andrew G. Tescher, pp. 430 – 439, SPIE Vol. 2298, San Diego, CA, 1994.

2. Steve Marusa, Steve Caputi, John Lehman, "Input Scene Generation for System Performance Evaluation", Targets and Backgrounds: Characterization and Representation, Wendell R. Watkins, pp. 42 – 52, SPIE Vol. 2469, Orlando, FA, 1995

PENN STATE
1855

Analysis of Visible Transmissometer Data in the Coastal Surf Zone

by

Mike Zugger and C. Russell Philbrick
Department of Electrical Engineering

for

Abstract

Introduction. A visible transmissometer was designed and constructed at Penn State by the authors. During April 1997, this instrument was used to take transmittance data at the Scripps Institution of Oceanography, as part of the Navy's Electro-Optical Propagation Assessment in the Coastal Environment (EOPACE) program. The goal of EOPACE is to improve the understanding of surf-generated aerosols and of electro-optical propagation in coastal regions.

Hardware. A feedback-controlled constant current source drives a halogen bulb, which serves as the white light source (approximated by a 3000K black body). The light is then mechanically chopped and filtered to eliminate near-IR, and is collimated by the source telescope. A receiving telescope collects some of the light at the far end of the optical path, focusing it through a second IR blocking filter onto a blue-enhanced silicon detector. The received signal is then amplified by the receiver and extracted from DC and noise by the lock-in amplifier. The lock-in uses a reference signal from the chopper to perform this extraction, so a coax cable runs from the source to the receiver. The lock-in then digitizes the signal and transmits it to the computer via RS-232 serial interface. The computer processes and stores the data (2 samples per second) using LabView software.

System layout. The diagram shows the locations of the source and receiver units during the intensive operating period (IOP). The 264m optical path included the entire surf zone. Note that the elevations shown are approximate maximum distances above the ocean surface (based on mean lower low tide), and the distances were less during most of the IOP.
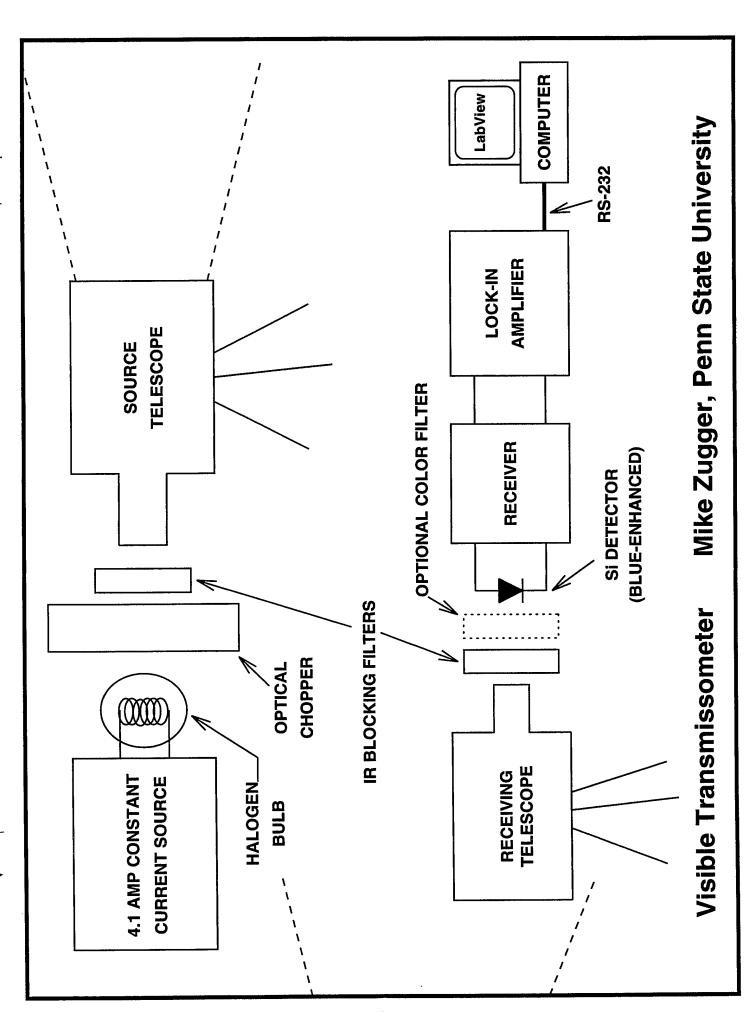
Data analysis. The next viewgraph is an example of the raw data obtained from the instrument. This graph shows the data taken on April 7 between 1:36am and midnight. The vertical axis is the signal level in volts, and the horizontal axis is arbitrary data point number (0 to 163,000). Note that there are many "dropouts" in the data; these were caused by interference picked up by the 350m coax cable. By taking the maximum of ten consecutive points (5 seconds), then averaging twelve consecutive maxima, most of the dropouts were eliminated.
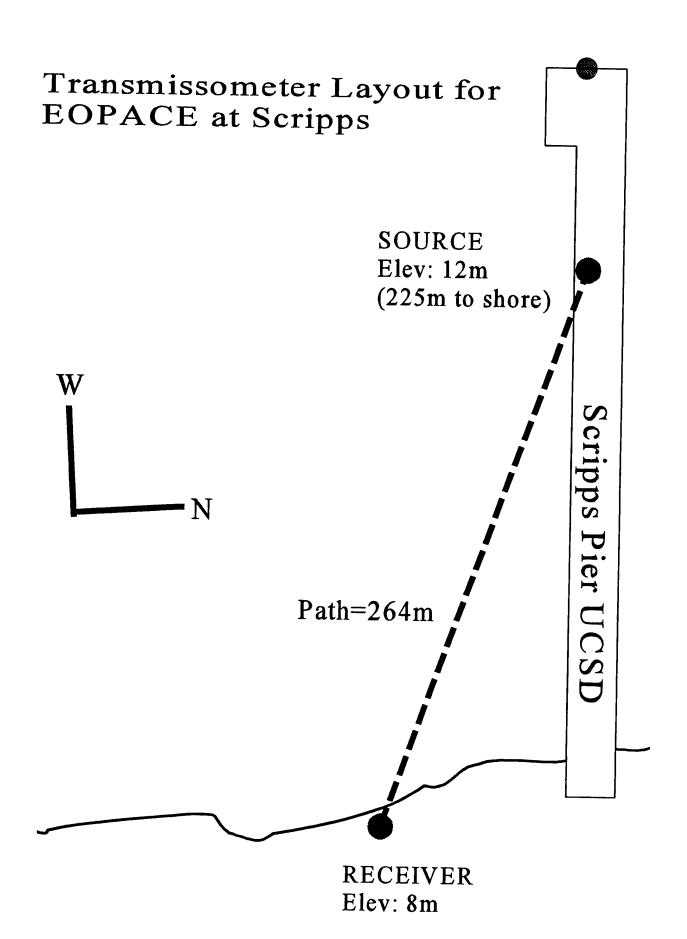
A wide variety of meteorological data during the IOP was provided by Scripps and NRad, including air, sea surface, and bottom temperatures, relative humidity, wind speed and direction, wave height and period, tides, and barometric pressure. Data from a vertical array of temperature sensors was also available from another Penn State experiment. These parameters were compared with the transmittance data in an attempt to find a correlation. The best correlation found was with wind speed and direction. On April 7 and 8, a moderately strong west wind (10-15 knots) was present during much of the daylight hours, and correlates with the times of low transmittance. On April 5, data collection began at about 2pm, and transmittance remained roughly constant through the remainder of the day. On this day, the wind speed was only about 7 to 8 knots. It is
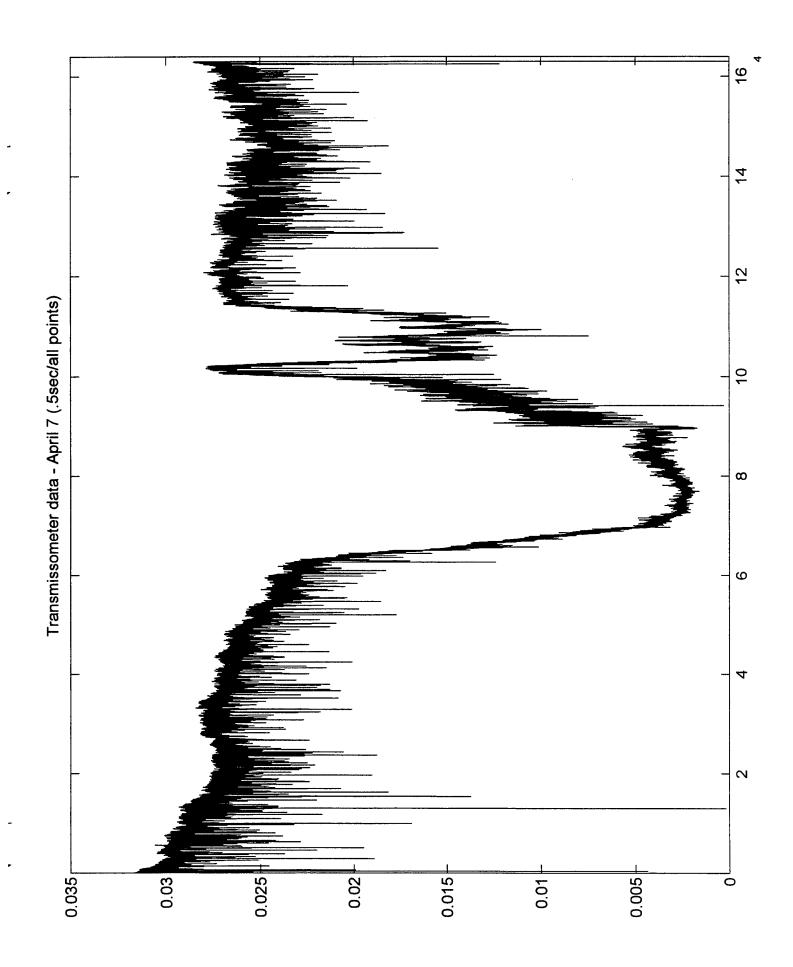
theorized that the west wind is either bringing in aerosols from the open ocean, or affecting the surf plumes in such a way as to reduce transmittance.

Preliminary modeling (MODTRAN). The predicted transmission versus wavelength curves for the 264km path were plotted using four standard MODTRAN aerosol models: Rural 23km Visibility, Rural 5km Visibility, Maritime 23km Visibility, and Navy Maritime 23km Visibility. Next, the combined spectral responses of the detector and the two IR-block filters were entered into the filter function associated with MODTRAN. The "Filter Function Input" viewgraph shows the resulting wavelength weighting curve. The black body input was set to 3000K for the halogen bulb. Finally, the filter function was applied to the four models, yielding predicted transmittances of 82.9%, 95.9%, 95.7%, and 98.4%, respectively. Returning to the data, when the voltage-to-transmittance conversion is applied, it is seen that the measured transmittance for the 57 hours of data falls predominantly at about 65% and about 7%.

Future work. Additional transmittance data and improved understanding of surf plumes will be required in order to better understand and predict surf zone transmittance. Comparison of data from this visible transmissometer with the NRad infrared transmissometer (also operated during this EOPACE IOP) may also provide some insights.

SOURCE
TELESCOPE

4.1 AMP CONSTANT
CURRENT SOURCE

HALOGEN
BULB

OPTICAL
CHOPPER

IR BLOCKING FILTERS

RECEIVING
TELESCOPE

OPTIONAL COLOR FILTER

Si DETECTOR
(BLUE-ENHANCED)

RECEIVER

LOCK-IN
AMPLIFIER

RS-232

COMPUTER

LabView

Visible Transmissometer   Mike Zugger, Penn State University

Transmissometer Layout for EOPACE at Scripps

W

N

SOURCE
Elev: 12m
(225m to shore)

Scripps Pier UCSD

Path=264m

RECEIVER
Elev: 8m

Transmissometer data - April 7 (.5sec/all points)

Meteorological Data Available

Scripps

- Air Temperature
- Relative Humidity
- Wind Speed & Direction
- Bottom Water Temp
- Wave Height & Period
- Barometric Pressure
- Radiation (PAR)
- Tides
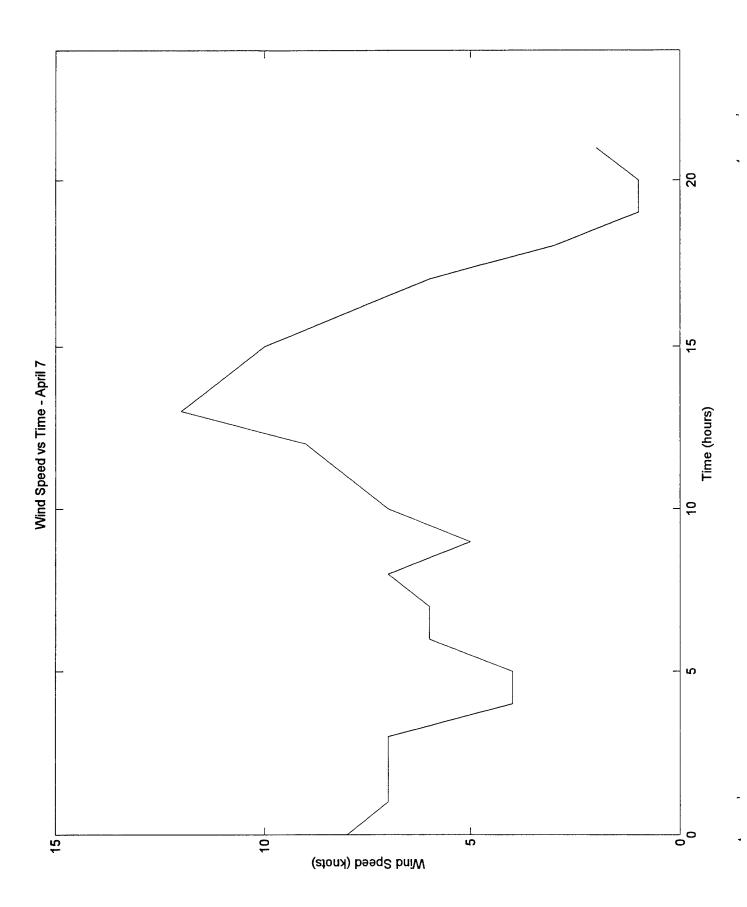
NRad
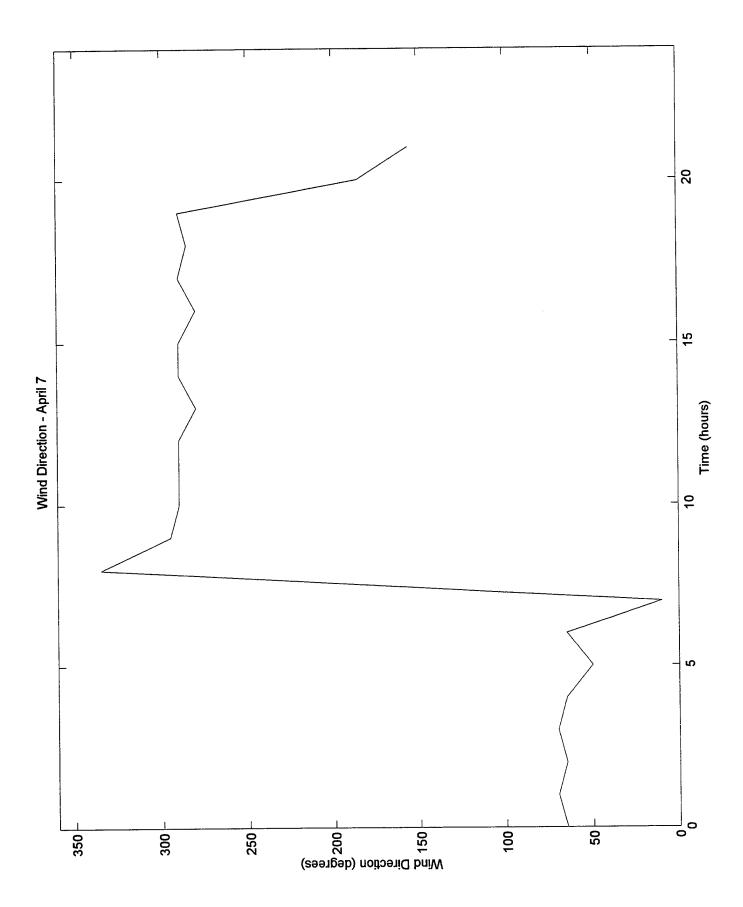
- Air Temperature
- Relative Humidity
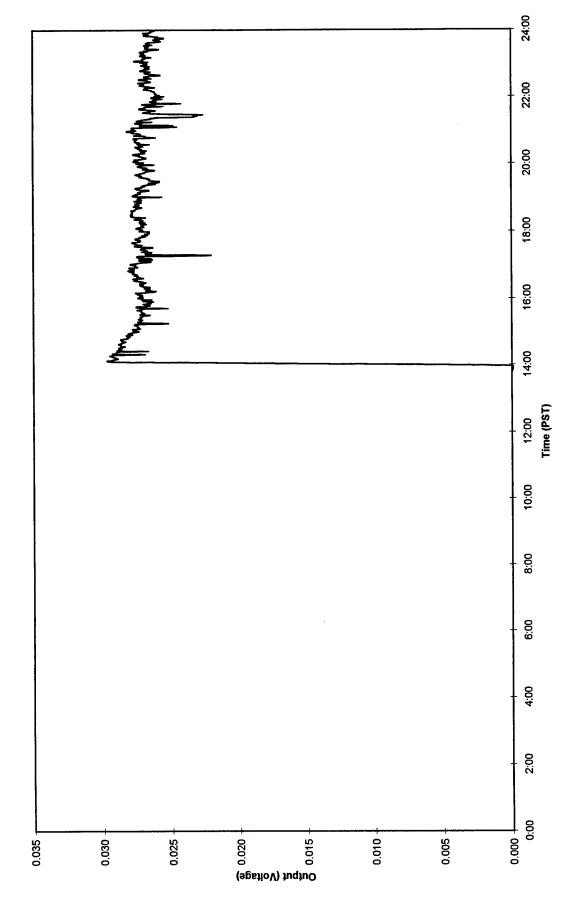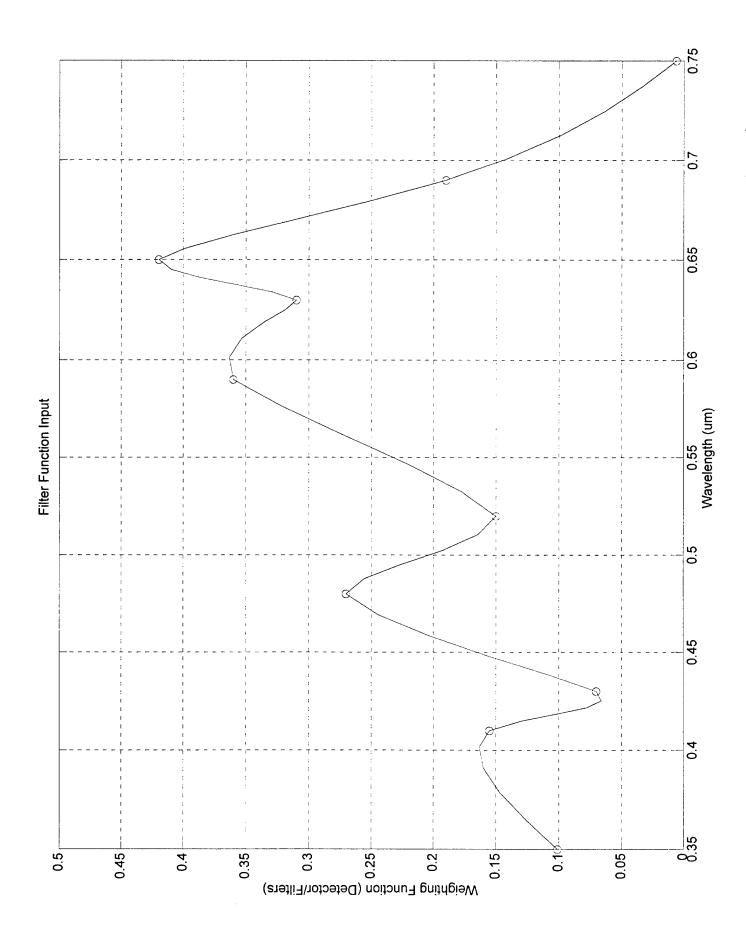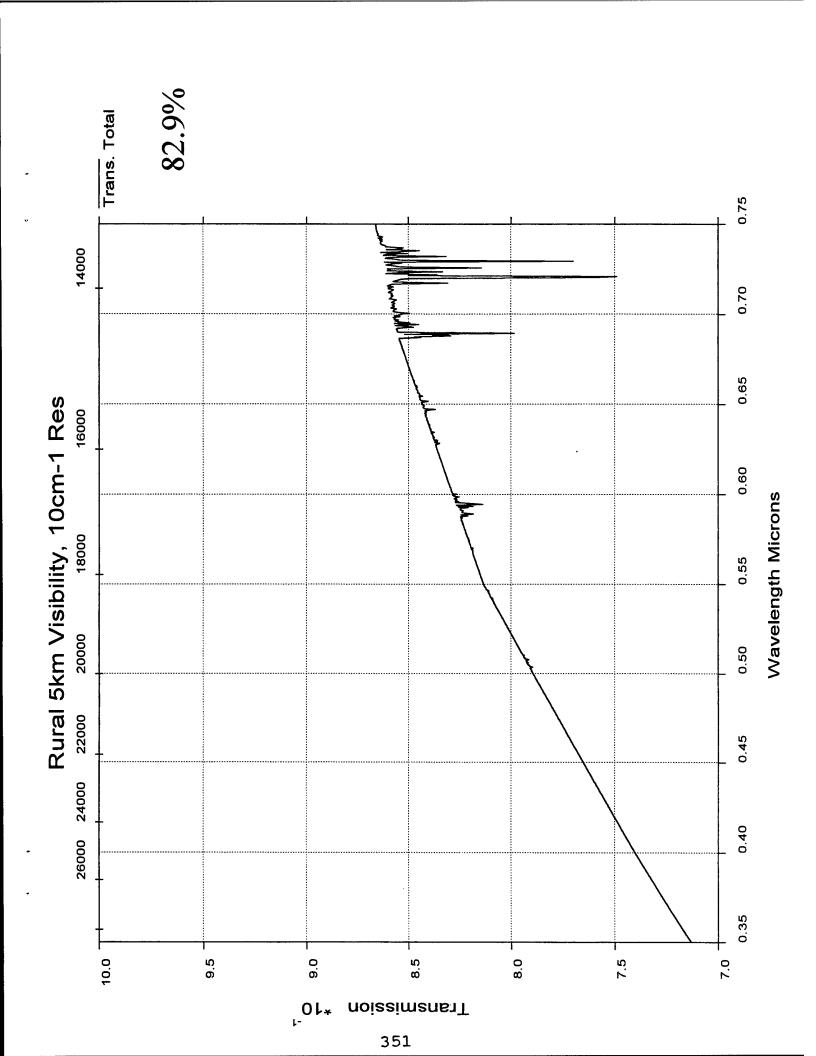- Wind Speed
- Sea Surface Temp
- Wave Height
- Condensation Nuclei

Transmissometer Data - April 7 (1 min average / 5 sec max)
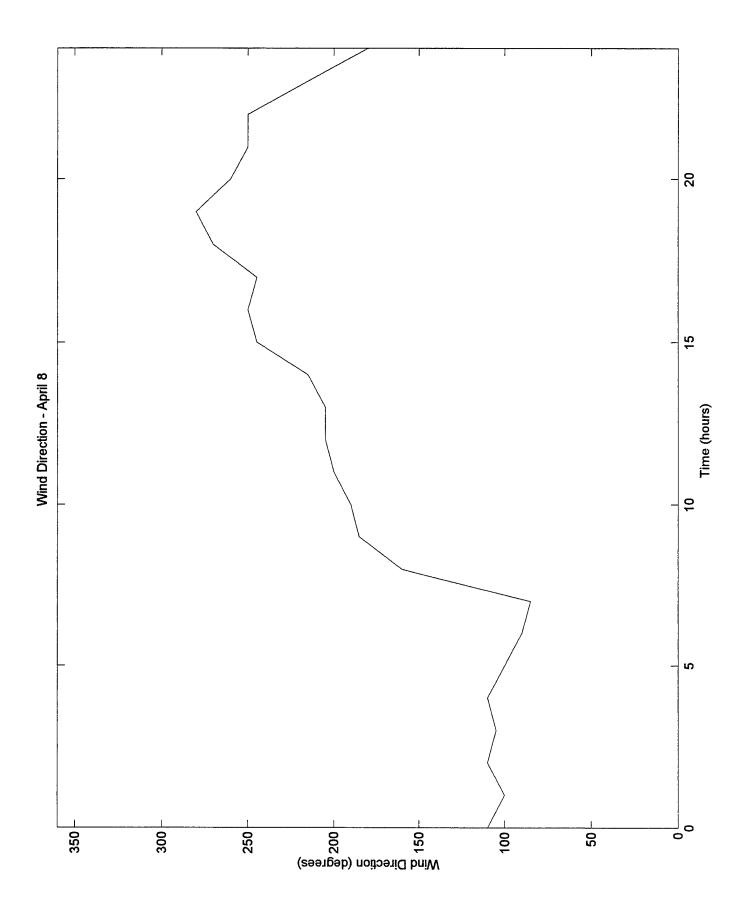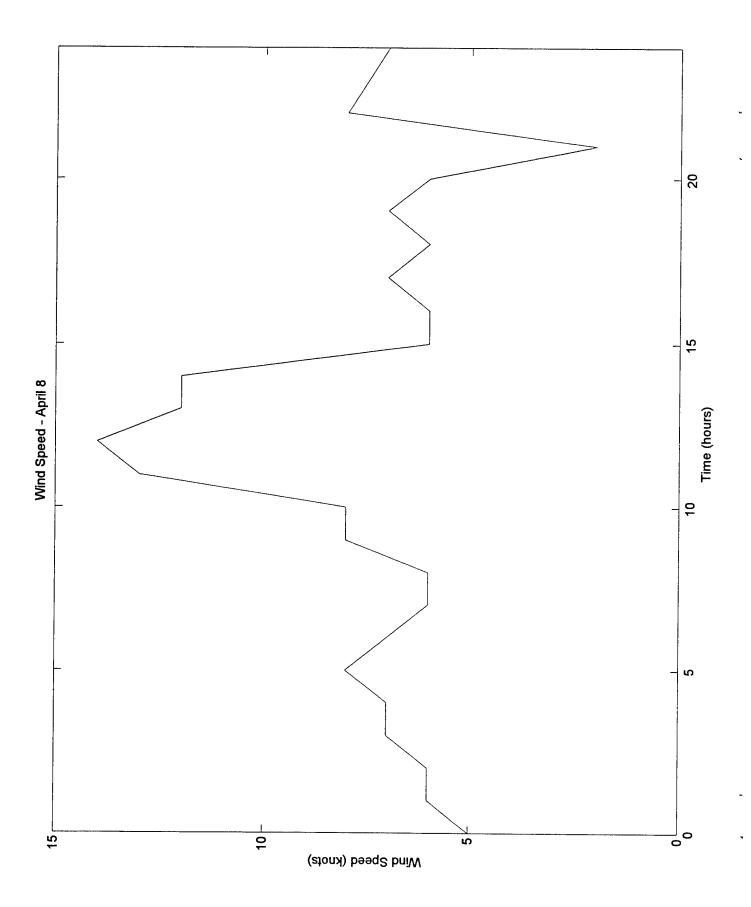
Time (PST)

Output (Volts)

Wind Speed vs Time - April 7

Wind Speed (knots)

Time (hours)

Wind Direction - April 7

Wind Direction (degrees)

Time (hours)
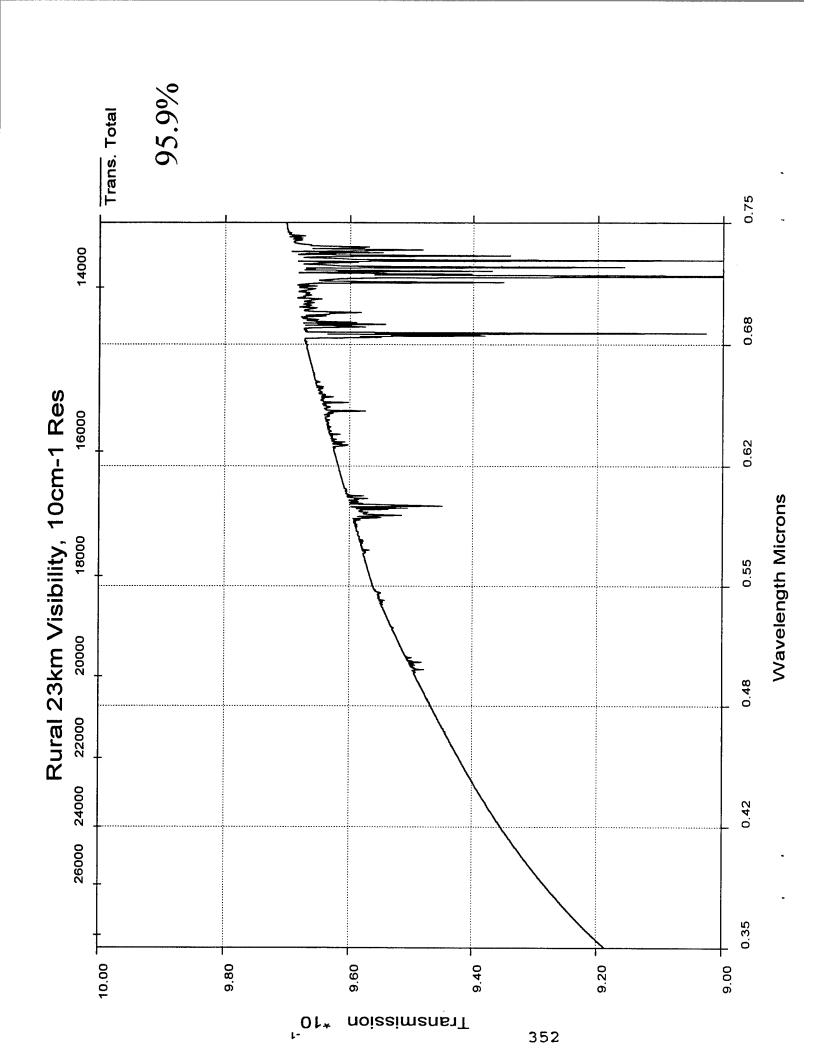
345

Transmissometer Data - April 8 (1 min average / 5 sec max)

346

Wind Direction - April 8

Wind Direction (degrees)

Time (hours)

Wind Speed - April 8

Wind Speed (knots)

Time (hours)

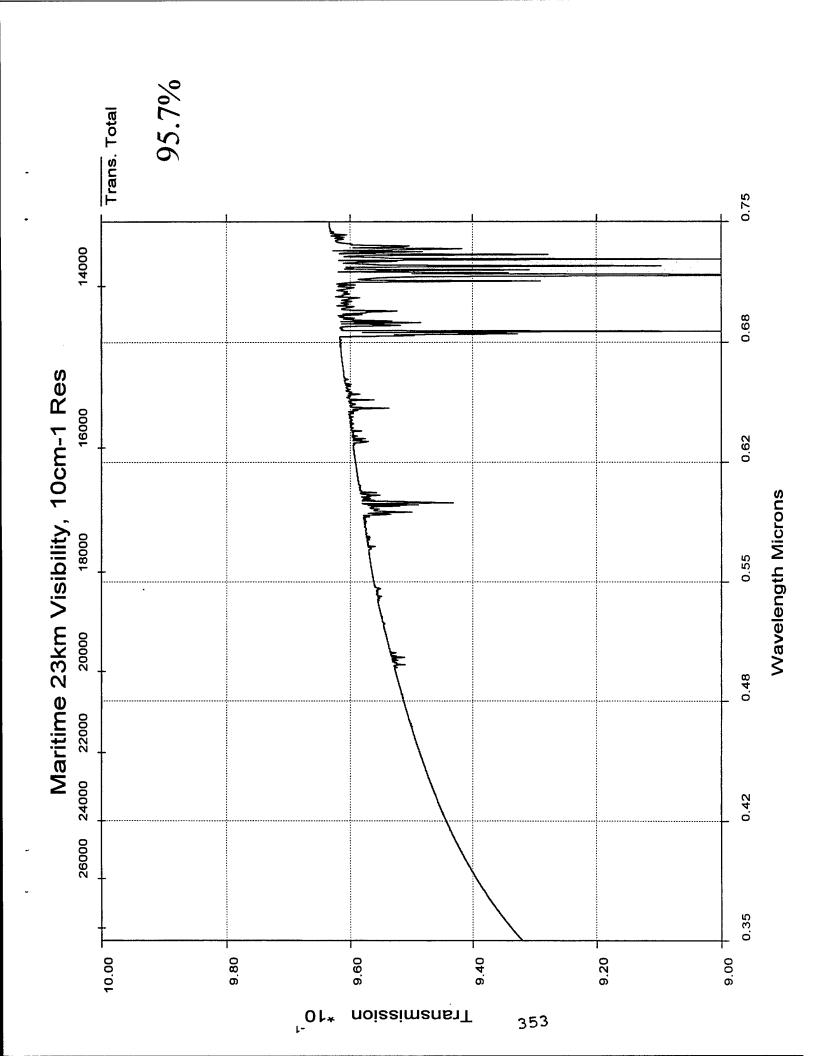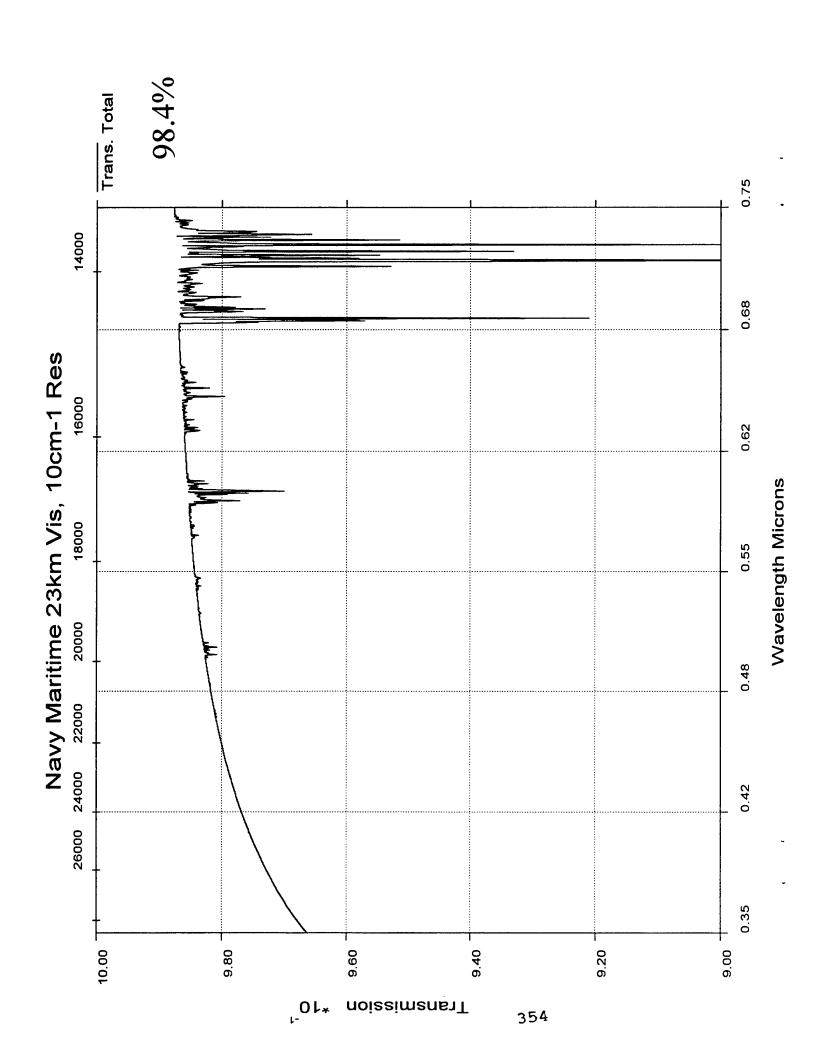Transmissometer Data - April 5 (1 min average / 5 sec max)

349

Filter Function Input

Wavelength (um)

Weighting Function (Detector/Filters)

Rural 5km Visibility, 10cm-1 Res

Trans. Total

82.9%

Wavelength Microns

Transmission *10⁻¹

Rural 23km Visibility, 10cm-1 Res

Trans. Total

95.9%

Wavelength Microns

Transmission *10⁻¹

352

Maritime 23km Visibility, 10cm-1 Res

Trans. Total

95.7%

Wavelength Microns

Transmission *10⁻¹

353

Navy Maritime 23km Vis, 10cm-1 Res

Trans. Total

98.4%

Wavelength Microns

Transmission *10⁻¹

354

Predicted Transmittances for Standard Models

Rural 5km Visibility   82.9%

Rural 23km Visibility   95.9%

Maritime 23km Visibility   95.7%
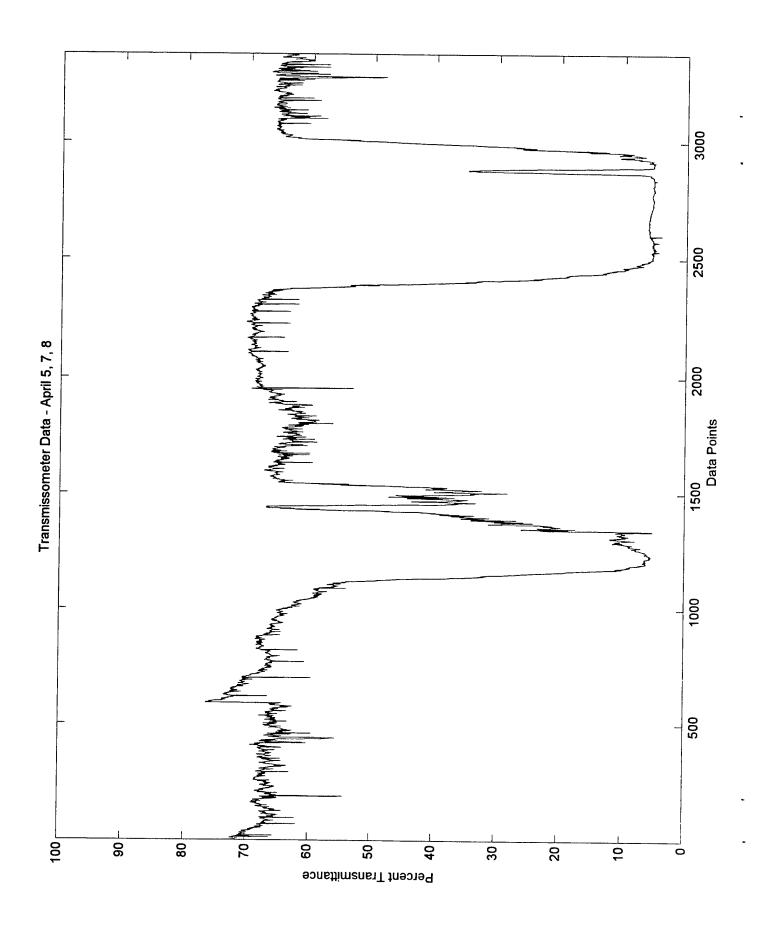
Navy Maritime 23km Visibility   98.4%

Transmissometer Data - April 5, 7, 8

Percent Transmittance

Data Points

Conclusions

- Transmissometer data correlates with wind

- Standard aerosol models predict higher transmission – model surf plume effects

Future Work

- Verify calibration
- Hardware enhancements
- Comparison with NRad IR transmissometer
- Meteo data correlation
- Custom aerosol modeling

Contributors

Penn State

Bill Durbin

Dr. Franz Balsinger

Glenn Pancoast

Dr. Dan Lysak

Mike Patterson

NCCOSC

Carl Zeisse

Christophe Bas

Tom Petach

Bob Smith

Steve Esposito

Anil Nunduri

Temporal and Spatial Characteristics of Surf zone Plumes[1]

Christophe F. Bas[2] and C. Russell Philbrick[3]
The Pennsylvania State University
Electrical Engineering Department
University Park, PA 16802

Abstract

One of the goals of the investigation, Electro-Optical Propagation Assessment in the Coastal Environment (EOPACE), is to enhance our understanding of the impact that surf generated aerosols have on the propagation of optical radiation through coastal regions. A bi-static LIDAR system uses a fan beam to illuminate the atmospheric region above the surf which permits measurements of both the vertical and horizontal extent of aerosol plume structures. The scattered radiation is imaged by two sensitive CCD cameras and a digital imaging camera, the latter being available only for the most recent test. Three measurement phases of the experiment program have provided data on the surf generated coastal plumes at two locations and under a range of different meteorological conditions. General spatial and temporal characteristics of these "coastal plumes", are described in this report.

1. Introduction

Judging from the interest in scientific investigations such as MAPTIP [1], VOCAR [2], and EOPACE [3], the coastal environments are of considerable importance. The attraction of the EOPACE program is its focus on the propagation of electromagnetic waves at optical frequencies in the coastal environment.

Toward this study, ARL/PSU (Applied Research Laboratory of The Pennsylvania State University) has provided measurement support using three instruments: (1) a LIDAR, (2) a transmissometer [4], and (3) a temperature mast (included in the April 1997 experiment). The ARL/PSU lidar has obtained data at the two Californian experimental sites: (1) the Scripps Institution of Oceanography (SIO, La Jolla) in 1996 and 1997 and (2) Moss Landing (Monterey) in 1996. Upon the first visit to the SIO (22 January to 5 February 1996), tall vertical structures were revealed by the bi-static LIDAR (Figure 1). These plumes provided a visual depiction of the scatters which decrease transmission. Hence, both the composition and characteristics of these plumes are of interest.

Figure 1: Typical plumes observed over the surf zone at La Jolla, CA, when illuminated by a vertical Argon-ion laser sheet. The picture was taken on 2 February 1996, at 7:15 PM with a low-noise CCD camera. The exposure time was 10 seconds.

---

2. Experimental set-up

Figure 2 shows the set-up of the third experiment which, like the first one, was conducted at the SIO (31 March 31 to 11 April 11 1997). The unconventional bi-static LIDAR used a cylindrical lens to transform the incident Argon-ion (514.5 nm) CW laser beam into a vertical laser sheet. The receivers were low-noise high-resolution (16 bits) CCD cameras and one digital video camera. The former allows long integration times to retrieve distribution of the scatterers [5] and the latter to reveal the dynamics of the plumes. The temperature mast was located on the pier in the middle of the surf zone and provided more details about the processes just above the interface. Simultaneously, the SIO kept a record of the meteorological conditions from a weather station at the end of the pier. The distance over which the waves continuously break has been observed to be typically between 200 and 100 meters from the beach end of the 300 meter long pier.
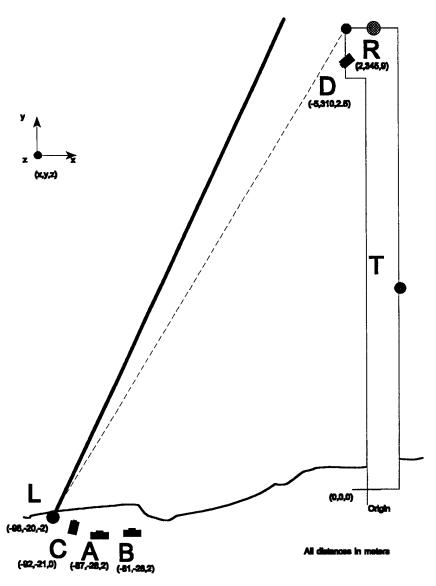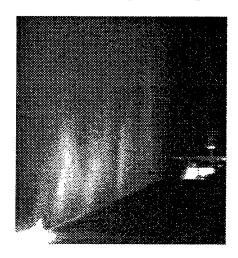

Figure 2: Experimental set-up at La Jolla, CA. L refers to the location of the source for the laser fan (emitter), A and B refer to those of the CCD cameras, C and D refer to those of the digital video camera, T refers to the one of the temperature mast, and R is a fixed reference point of known location which appears in every image.

361

3. The Coastal Atmospheric Boundary Layer

Considerable effort is currently underway to model the dynamics of coastal environments [6]. Those focusing on the first few tens of meters above the surf zone may validate their models using the ARL/PSU images. Figure 3 shows a sample of a cropped image from one of the CCD cameras and its corresponding projection along the pier. By keeping track of the location of the plumes and their heights under similar atmospheric conditions, one can plot the distribution of those heights versus the distance from the origin of the pier. Figure 4 displays such a plot obtained during the night of 2 April 1997, night during which a
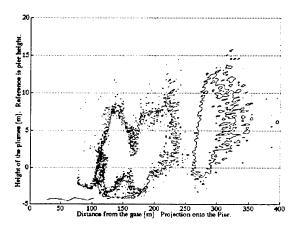

Figure 3: The left-hand side image shows a truncated image captured by the CCD camera positioned at A (see the map of Figure 2) on 2 April 1997, at 11:43 PM. Exposure time was 10 seconds. The structure in the background is that of the weather station at the end of the pier and the bright dot on its top is R, the reference point. The projection of this image onto a vertical plane which is parallel to the pier is shown on the right-hand side plot. The intensity contour chosen to define a plume was set to 3315 digital counts.
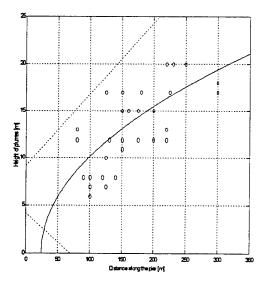

Figure 4: Plume height versus distance from the origin of the pier during the night of 2 April 1997. The tilted dashed lines trace the aperture of the laser fan. The solid line corresponds to a least-square fit of the data points (circles) with the following function:
Height = Const$\sqrt{\text{Distance} - \text{Origin}}$.

slight offshore wind was present. As the air mass advected from land glides over the warmer surf-zone, a Thermal Internal Boundary Layer (TIBL) develops [7]. Several equations exist to model a TIBL, but most of them can be parameterized as:

$$\text{Height} = \text{Const}\sqrt{\text{Distance} - \text{Origin}} \qquad (1)$$

where the value of *Const* depends on the environmental conditions. The offshore wind acts as a sink for the net flux of particles emanated from the breaking waves. These conditions typically existed from late evening to early morning during the experimental phase (Figure 5a). When the temperature difference between water and land was small, the wind decreased in intensity and the density of the scatterers is approximately symmetrically distributed over the surf zone. Figure 1 shows such a case where the plumes are standing vertically. This particular situation occurred during transitional periods corresponding to a shift in direction of the mean wind (from offshore to onshore and vice-versa) and are depicted in Figures 5b and 5d.

When land temperature is greater than water temperature, onshore wind results. With it comes an TIBL, but located at the land and water intersection. Documentation of a possible internal boundary layer generated by the change of surface roughness between the open-ocean and the surf zone has yet to be satisfactorily supported. One reason is due to the geometry of the bi-static lidar whose vision of the plumes in their full height is impossible close to the transmitter (see dashed lines in Fig. 4). We suspect that an TIBL exists over the entire ocean surface, but that it is only discernible when the aerosol from the surf provides a tracer which can be observed from the laser illumination. The distinctive feature which is believed to form the TIBL is the temperature gradient in the first several meters above the surface, which is governed by the air/sea temperature difference. If this hypothesis is true, then the same kind of plume characteristics will be present during high sea states or when the aerosols are produced in the wake of a
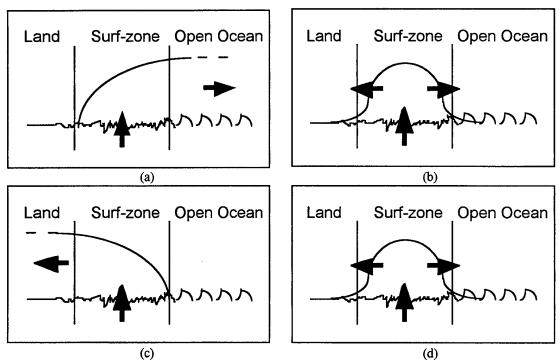

Figure 5: Cyclic temporal changes over the surf zone. (a) Over night (surface temperature of water is greater than the one over land), (b) early morning after sun rise (surface temperature of water and land are approximately equal), (c) later into the morning (surface temperature of water is smaller than the one over land), and (d) early into the night (surface temperature of water and land are approximately equal).

Table 1: Summary of the mean meteorological conditions and resulting plume heights over the surf zone during the three IOPs.

Location	SIO (I)	Moss Landing	SIO (II)
$T_{Sea}-T_{air}$ [C]	3.3	1.7	2
Wind speed [m/s]	3.1	1	1.2
Av. plume height [m]	25	10	11

ship in the presence of air/sea temperature difference. Favorable conditions for the development of the coastal TIBL were between late morning and early evening (Fig. 5c). This time frame renders the observations of the plumes even more challenging because of the presence of the extremely large optical background signal during daytime.

Table 1 reviews the mean meteorological conditions in which all three experimental phases were conducted [8]. Departures from those mean values (all else being equal) reveal interesting features. First, when the wind increases, the plume height decreases. Second, when the temperature difference between the sea and air decreases, so does the plume height. This last effect agrees with Equation 1 for which Raynor et al. and Venkatram [7] have parameterized the proportion constant as follows:

$$\text{Const} \propto |T_{Land} - T_{Water}|^{\frac{1}{2}} / \text{Wind} \qquad (2)$$

We have observed that the tallest plumes occurred with calm winds and large temperature gradients.

We have argued that the plumes scale with the depth of an internal boundary layer. This gives us a better idea of the atmospheric conditions which will likely entrain the scatterers, provided that the wave activity produces them in sufficient quantity to render the plumes visible. A reliable source of ejected and spayed droplets, i.e., scatterers, are the breaking waves. Because not all breaking waves produce the same amount of aerosols, two of their categories are of interest: plungers and spillers. As waves turn into plunging breakers, trapped pockets of air entrained below the water surface eject many aerosols (i.e., water droplets) as the bursting air bubbles reach the surface. Spilling breakers are more gentle, surface bursting bubbles remain mainly at the surface. Under similar atmospheric conditions, plunging breakers produced more scattering[4] than spilling ones.

Hence, three variables seem to be appropriate to predict the height of the plumes: wind speed, temperature difference, and breaker type.

4. Temperature Mast

One way to assess whether atmospheric stability influences the height reached by the plumes is to measure the thermal vertical structure of the region above the surf zone. This aim motivated the installation of the mast, equipped with 7 thermistors, in the middle of the surf zone (Fig. 2). Figure 6 sketches the mast and provides the height for each sensor relative to the pier level. Once the data gathered, another analysis has been undertaken because of the necessity to refine and enhance some of the data sets required to estimate the Richardson number over the surf zone. Again, it is necessary to note that the height of the plumes is affected by the intensity level chosen to define a "plume". This number depends on the intensity of the scattering by the plumes and the exposure time to capture them.

Relative comparison between the environmental characteristics and the mean height of the plumes consists of the computation of (1) the mean temperature and the standard deviation of the mean temperature over all the sensors at each point in time (this is equivalent to assuming that each sensor sees one realization of the same random variable) and (2) the time-average for both the mean and the standard

---

[4] We imported the images into MATLAB where the function contour delimited the plumes. The subjective part of the analysis was to define the intensity levels corresponding to what we defined as being "plumes". Once a number had been selected (for a given exposure), it became a reference for the other cases.
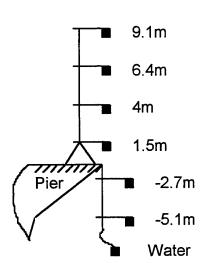
Figure 6: The temperature mast was located in the the middle of the surf zone where it captured several profiles. Heights are referenced to the pier. Water level was approximately -10 meters.
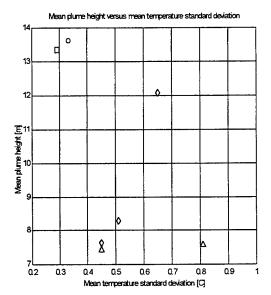
Figure 7: Mean height of the plumes for 2-10 April, 1997, as a function of temperature standard deviation. With a 10 sec exposure, squares refer to a 3315 contour-level and triangles to one of 4200. With a 30 sec exposure, diamonds refer to a 4200 contour-level and circles refer to one of 3500.

deviation of the mean temperature (which is equivalent to invoking ergodicity to expand the total number of realizations). Table 2 summarizes the results of this processing. Figure 7 plots the plume height versus the standard deviation of the mean temperature for this third experiment.

Before formulating hasty conclusions on the problem at hand, it is essential to realize that Table 2 allows comparison within the same group only. More work is required to compare results between different groups.

First, both the diamonds and the triangles reveal that the taller the plumes the higher the standard deviation of temperature. Second, the mean temperature results from a complicated process which takes

Table 2: Summary of the results from the processing of the plume heights and the data taken on the mast of temperature sensors.

Day/Month/ Year	Time (PST)	Symbol (Fig. 7)	Mean plume height [m]	Mean tempe- rature [C]	Mean temperature std. deviation [C]
2 April 97	23:35-23:38	square	13.3	11.0	0.29
2 April 97	23:54-00:00	circle	13.6	10.9	0.33
7 April 97	19:50-19:55	diamond	7.6	16.7	0.45
7 April 97	21:43-21:50	diamond	8.3	16.1	0.51
9 April 97	00:20-00:26[5]	diamond	12.1	16.9	0.65
9 April 97	01:04[6]	triangle	7.6	17.0	0.81
9 April 97	20:21-20:24	triangle	7.4	16.5	0.45

---

[5] The plumes were analyzed over this time, but the closest set of temperature data was taken on 8 April from 23:54 to midnight. The meteorological and oceanographic conditions were stationary from one time segment to the next.

[6] The plumes were analyzed at this time, but the closest set of temperature data was taken from 01:19 to 01:25. The meteorological and oceanographic conditions were stationary from one time segment to the next.

into account both the air and the droplets inside the plumes. The temperature sensors located upwind and outside the surf zone give an actual air temperature (relatively free of surf-zone generated droplets) considerably lower than the mean temperature measured by the sensors on the mast (by 2 degrees Celsius). The only other potential thermal source is the water itself whose "bottom" temperature (defined by the SIO as being 3.5 meters below the mean lower low water level) remains around 17 degrees Celsius. Hence, the measured temperature results from a mixture of air and water droplets, the latter of which interacts with the thermal sensors through the processes of deposition and evaporation. This result confirms that the content of the plumes is sea water in nature. Contamination of temperature sensors by water has been reported by Friehe [9] who has noticed the spiky signature of the measurements.

An increase in the temperature fluctuations requires that there is "enough" time for some of the water to evaporate and that there is a significant amount of water coming suddenly into contact with the thermistors. The physical processes which promote this behavior need to be further analyzed.

Out of curiosity, the analysis of the plume heights for a different intensity level has been investigated. Once this level set to 4200 (the same as for the triangles and diamonds), neither the circle nor the square of Figure 7 resolve plumes. Notice that their standard deviations are the smallest of all the data points.

Therefore, we conclude that there is a strong correlation between the mean standard deviation of temperature and the mean plume height. However, the mean temperature is not a constant indicator of the plume height.

5. Conclusion

Our study shows that an internal boundary layer provides a means of estimating the height of the surf zone plumes. The physics behind such a boundary seems to include wind speed, buoyancy forcing, and, possibly, changes in surface roughness. The study of boundary layers is rendered difficult by the nesting[7] of boundary layers over the surf zone.

The meteorological conditions seem to prepare the atmosphere to accept any aerosols to form plumes, but the major contributor of aerosols is the surf zone itself via its breaking waves which eject significant amounts of water droplets. The brightest and tallest plumes are observed in the presence of larger temperature difference between air and water, minimum wind, and plunging breakers. Further studies of the effect of turbulence is necessary to determine whether it promotes tall plumes or shreds them. Our next step is to simulate those effects using Large Eddy Simulations [10] and compare the outputs of the model to our experimental data.

---

[7] If one accounts for all the phenomena generating their own boundary layer, one faces an infinite number of intricate boundary layers, some developing, others blending in, but several boundary layers coexist, especially over the surf zone.

References

1. Gathman, S. G., and Jensen , D. R., "Maptip (Marine aerosol properties and thermal imager performance): Aerosol Characteristics in a Coastal Region", Naval Command, Control and Ocean Surveillance Center, San Diego, CA. RDT and E Div., NTIS ID No.: AD-A300 255,Aug 1995.
2. Paulus, R. A., "VOCAR: An Experiment in Variability of Coastal Atmospheric Refractivity", Naval Command, Control and Ocean Surveillance Center, San Diego, CA. RDT and E Div., NTIS ID No.: AD-A289 202, Oct 1994.
3. For a description of the EOPACE program: K. M. Littfin and D. R. Jensen, "An Overview of EOPACE (Electrooptical Propagation Assessment in Coastal Environments), Including In Situ and Remote Sensing Techniques", AGARD Conference Proceedings 582, Toulouse, France, pp. 10-1 to 10-8, October 1996.
4. Zugger, M. E., and Philbrick, C. R., "Analysis of Visible Transmissometer Data from the Coastal Surf Zone", Proceedings of the 20th Annual Conference on Atmospheric Transmission Models, 10-12 June 1995, Phillips Laboratory, Hanscom AFB, June 1997.
5. T. D. Stevens and C. R. Philbrick, "A Bistatic Lidar Receiver to Observe Lower Tropospheric Aerosol Properties", Proceedings of the 18th Annual Conference on Atmospheric Transmission Models, 6-8 June 1995, Phillips Laboratory, pp. 242-247, Hanscom AFB, April 1996. PL-TR-96-2080, ADA307971
6. R. A. Allard, L. Hsu, J. Smith, and M. D. Earle, "Surf zone Modeling", Proceedings of the Naval Postgraduate School, Monterey, CA, 1997.
7. M. Stunder and S. Sethuraman, "A Comparative Evaluation of the Coastal Internal Boundary-Layer Height Equations", Boundary Layer Meteorology, 32, pp. 177-204, 1985.
8. R.E. Kiser and K.L. Davidson, "The generation and Characterization of Surf Zone Aerosols and Their Impact on Naval Electro-Optical Systems", Proceedings of the Naval Postgraduate School, Monterey, CA, 1997.. For further analysis of the correlation between meteorological factors and plumes heights, see: R. E. Kiser, "The Generation and Characterization of Surf Zone Aerosols and Their Impact on Naval Electro-Optical Systems", MS Thesis, Naval Postgraduate School, Monterey, CA, December, 1996.
9. Friehe, C. A., "Fine-Scale Measurements of Velocity, Temperature, and Humidity in the Atmospheric Boundary Layer", in Probing the Atmospheric Boundary Layer, Ed. D. H. Lenschow, American Meteorological Society, Boston, Massachusetts, 1986.
10. L. J. Peltier and J. C. Wyngaard, "Structure-Function parameters in the Convective Boundary Layer from Large Eddy Simulation", J. Atm. Sci., 52, 3641-3659, 1995.

Use of HYPEX Atmospheric and Sensor Simulation Models for Image Data Evaluation

Sally J. Westmoreland and Frederick C. Mertz

Photon Research Associates, Inc.
5720 Oberlin Drive
San Diego, CA 92121

Dr. William M. Cornette

National Imagery and Mapping Agency (SA)
4600 Sangamore Road, MS D–33
Bethesda, MD 20816 –5003

OUTLINE

- **HYPEX Overview for atmospheric modeling and analysis**

- **Applications:**

  Compare results from different atmospheric models

  Evaluate atmospheric parameters and refine inputs

  Compare measured image data with modeled spectra

- **Examples**

  1. ARES, Key West, Florida

  2. HYDICE, Desert scene
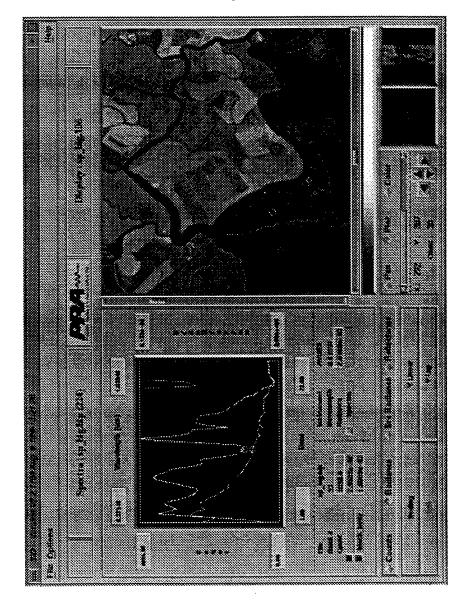
  3. AVIRIS, Rangeland in Lander, Wyoming

HYPEX Objectives

Photon Research Associates, Inc.

Integrate all Elements of:

- Hyperspectral data handling
- Atmospheric and sensor response modeling
- Hyperspectral data analysis and visualization

Provide Environment for:

- Comparison and reconciliation of measured and modeled data
- Extension of modeled data for applications to broader problems
- Evaluation of atmospheric models and characterization

PRA
Photon Research Associates, Inc.

Atmospheric and Sensor Response Modeling

- ## Atmospheric Characterization

  Complete radiative environment generated by MOSART Radiative Transfer Code

  Accepts model atmospheres or actual observations as inputs

  Multiple geometries and surface altitudes

- ## Sensor Spectral Response

  Modeled as square or gaussian using band centers, e.g, HYDICE and AVIRIS

  Actual sensor response functions, e.g, ARES, Landsat TM

  New sensor response functions are easily added, e.g, Kestrel and Lewis (HSI and LEISA)
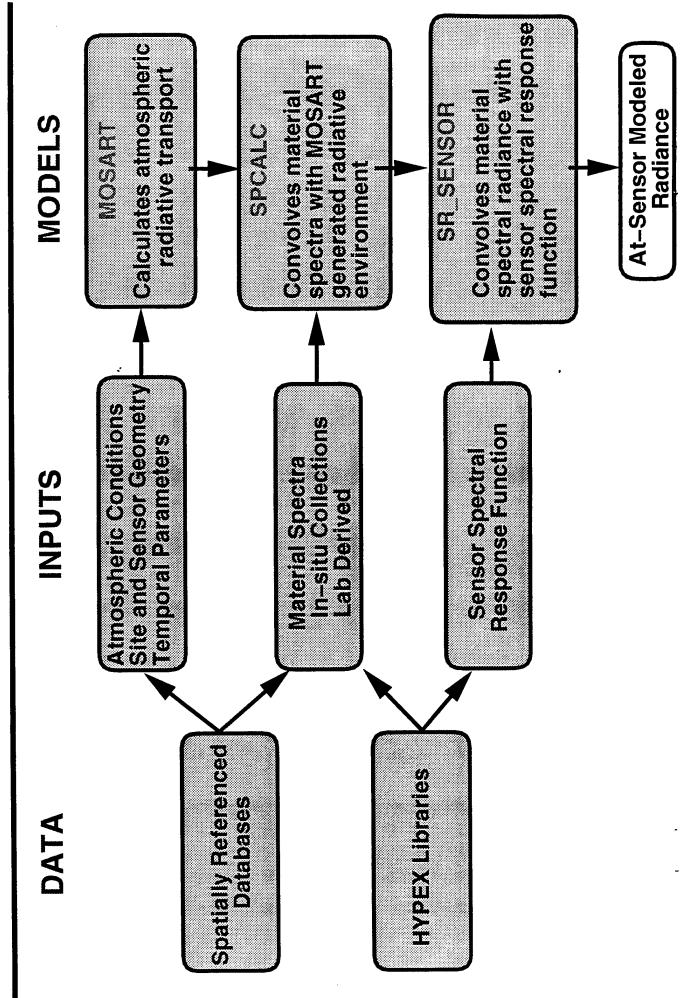
- ## Material Spectra

  Library of surface materials and clouds

  Spectal radiance calculator convolves material spectra with radiative environment and sensor spectral response function to simulate at-sensor radiance or reflectance
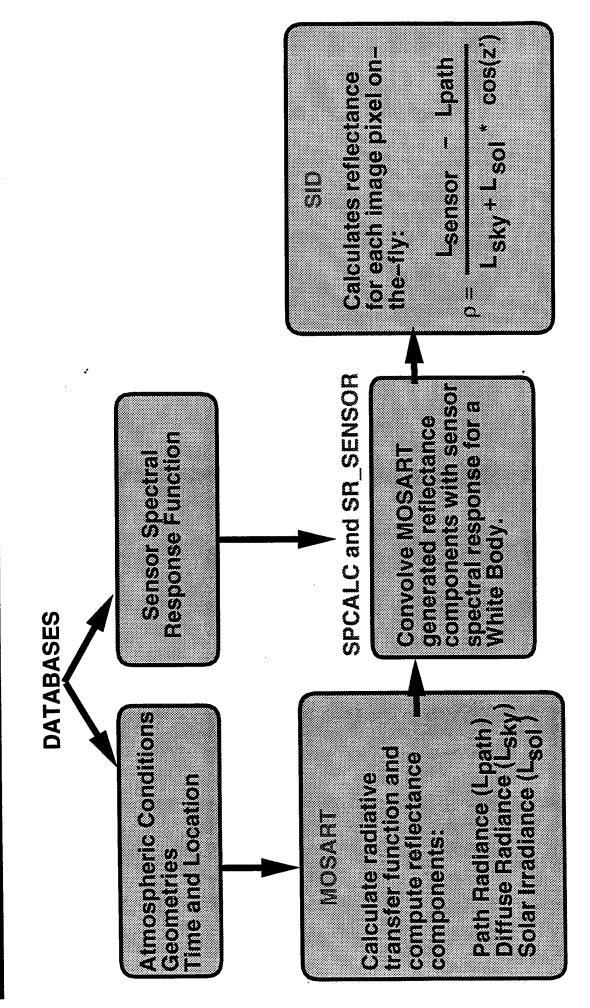
HYPEX Spectral Modeling

PRA
Photon Research Associates, Inc.

DATA   **INPUTS**   **MODELS**

Spatially Referenced Databases

HYPEX Libraries

Atmospheric Conditions Site and Sensor Geometry Temporal Parameters

Material Spectra In-situ Collections Lab Derived

Sensor Spectral Response Function

MOSART
Calculates atmospheric radiative transport

SPCALC
Convolves material spectra with MOSART generated radiative environment

SR_SENSOR
Convolves material spectral radiance with sensor spectral response function

At-Sensor Modeled Radiance

PRA
Photon Research Associates, Inc.

HYPEX Atmospheric Correction

DATABASES

Sensor Spectral Response Function

Atmospheric Conditions Geometries Time and Location

MOSART

Calculate radiative transfer function and compute reflectance components:

Path Radiance (L_{path})
Diffuse Radiance (L_{sky})
Solar Irradiance (L_{sol})

SPCALC and SR_SENSOR

Convolve MOSART generated reflectance components with sensor spectral response for a White Body.

SID

Calculates reflectance for each image pixel on-the-fly:

$$\rho = \frac{L_{sensor} - L_{path}}{L_{sky} + L_{sol} * \cos(z')}$$

ARES Measured/ Modeled Data Comparisons

Project Objective:

Use ARES spectrometer and radiometer data for validation of CLDSIM model results
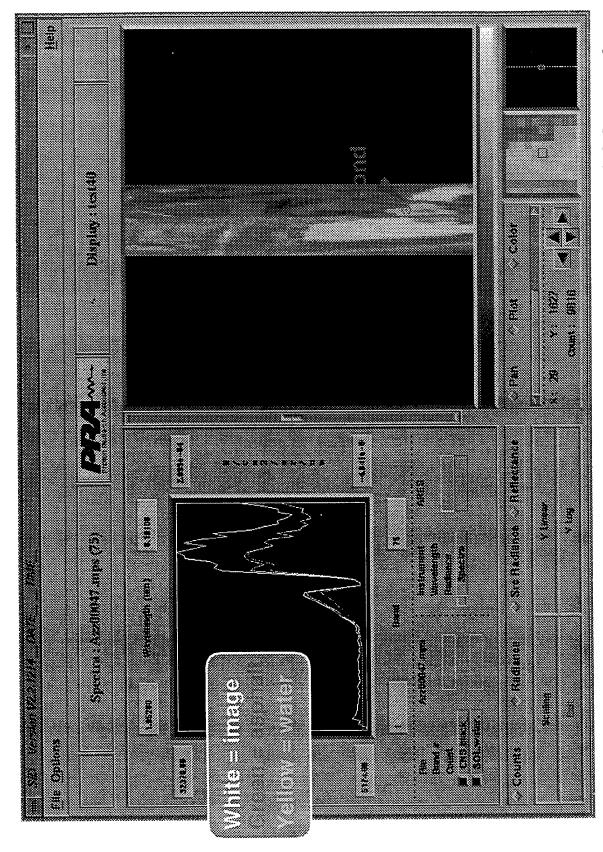
Data:

- Collected near Key West, Florida on 29 Feb 1996

- ARES instrument, 75 bands, 1.93 –> 6.1 microns

- Coincident collection of cloud, ground, and atmospheric "truth"
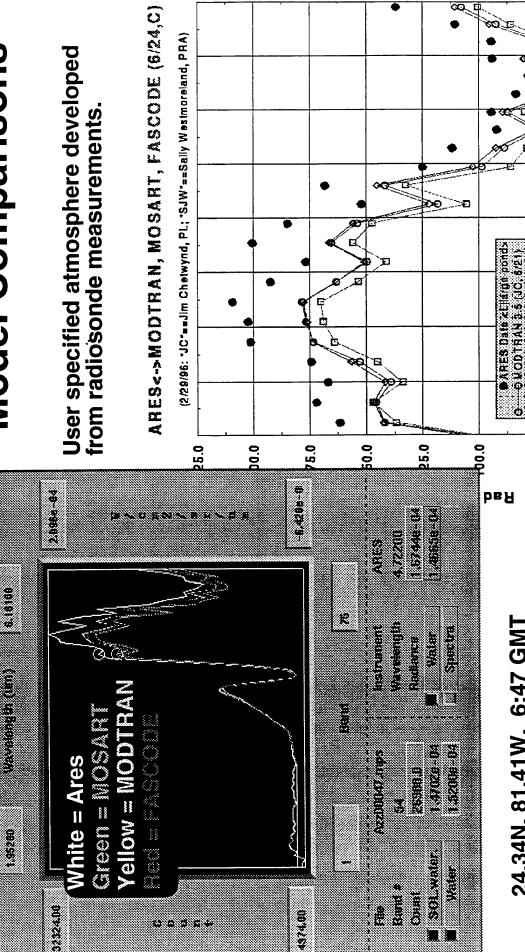
ARES – Initial Measured vs Modeled Data Comparison

PRA
Photon Research Associates, Inc.

24.34N, 81.41W, 6:47 GMT, 29 Feb 1996, Tropical Winter Model Atmosphere

MOSART – MODTRAN – FASCODE

PRA Photon Research Associates, Inc.

Model Comparisons

User specified atmosphere developed from radiosonde measurements.

ARES<->MODTRAN, MOSART, FASCODE (6/24,C)

(2/29/96: "JC"==Jim Chetwynd, PL; "SJW"==Sally Westmoreland, PRA)

White = Ares
Green = MOSART
Yellow = MODTRAN
Red = FASCODE

24.34N, 81.41W, 6:47 GMT
29 Feb 1996

Mon Jun 24 11:27:00 1996

Adjustment of Temperature Profile

PRA
Photon Research Associates, Inc.
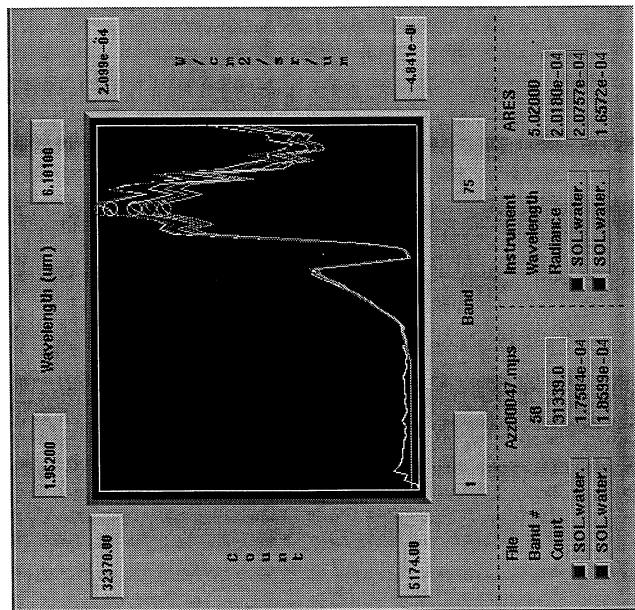
User-defined atmosphere profile developed from radiosonde measurements, with adjustments to temp/altitude profile:

White = Ares data

Red = +8 degrees

24.34N, 81.41W
6:47 GMT
29 Feb 1996
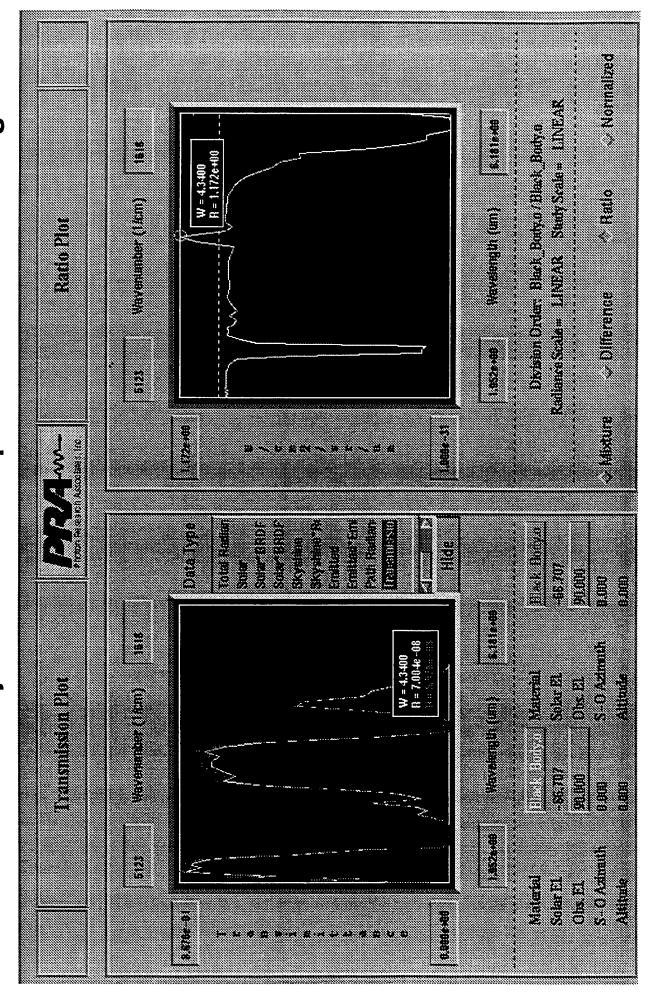
Transmission Differences
Adjustment of Temperature Profile + 8 degrees

PRA
Photon Research Associates, Inc.

PRA
Photon Research Associates, Inc.

Measured/Modeled Data Comparisons
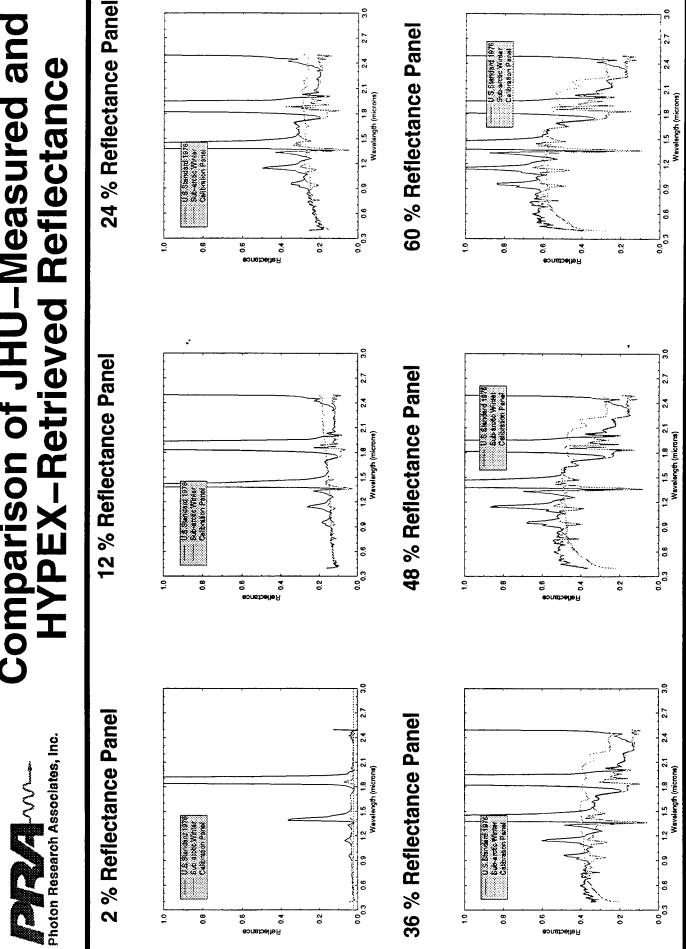
- **Concurrent hyperspectral and ground radiometry data collections**

- **Ground measurements taken from soils and reflectance "truth" panels**

- **Modeled at–sensor radiance/reflectance:**

  MOSART based – atmospheric state from model atmospheres

  Sensor spectral response modeled as Gaussian

Comparison of JHU–Measured and HYPEX–Retrieved Reflectance

Photon Research Associates, Inc.

2 % Reflectance Panel

12 % Reflectance Panel

24 % Reflectance Panel

36 % Reflectance Panel

48 % Reflectance Panel

60 % Reflectance Panel
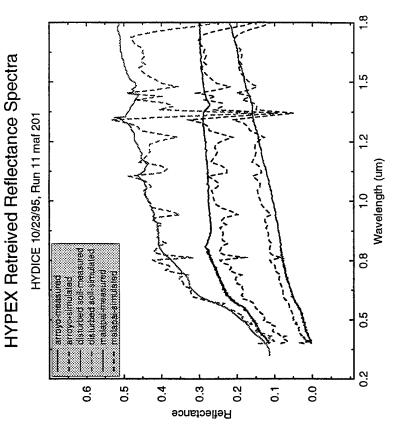
HYPEX Modeled Signatures: Terrain Materials

PRA
Photon Research Associates, Inc.

Measured and Modeled Reflectance

HYPEX Retrieved Reflectance Spectra

HYDICE 10/23/95, Run 11 maf 201

Legend:
- arroyo-measured
- arroyo-simulated
- disturbed soil-measured
- disturbed soil-simulated
- malapai-measured
- malapai-simulated

Reflectance vs Wavelength (um)
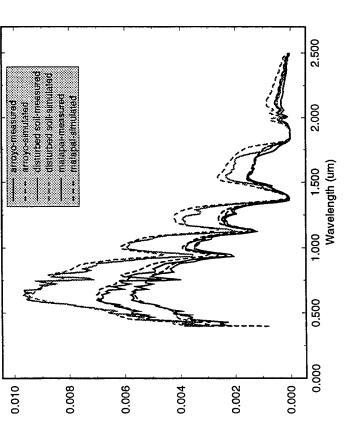
Measured and Modeled Radiance

HYPEX and HYDICE Radiance Comparison

HYDICE 10/23/95, Run 20 maf 04

Legend:
- arroyo-measured
- arroyo-simulated
- disturbed soil-measured
- disturbed soil-simulated
- malapai-measured
- malapai-simulated

Spectral Radiance (W/cm^2/sr/um) vs Wavelength (um)

PRA
Photon Research Associates, Inc.

Comparison of AVIRIS Reflectances

Project Objective:
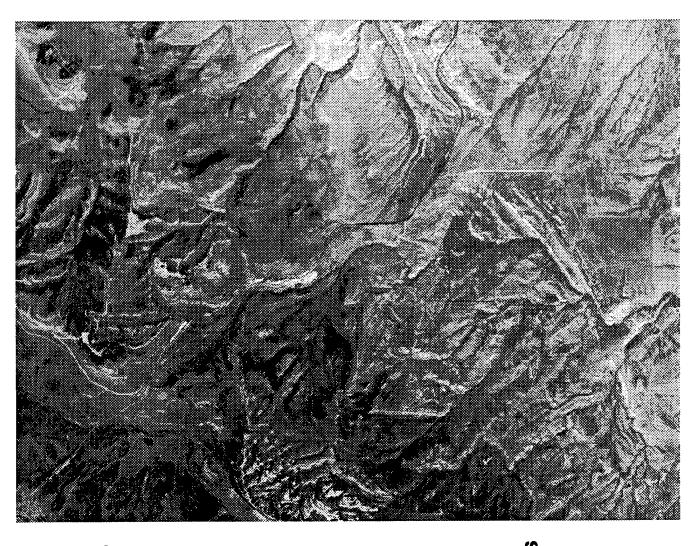
Data were collected as part of a cooperative investigation to evaluate image data for improved rangeland monitoring and management

Data:

AVIRIS, 224 bands, .4 –> 2.5 microns

Raw and ATREM Corrected Images
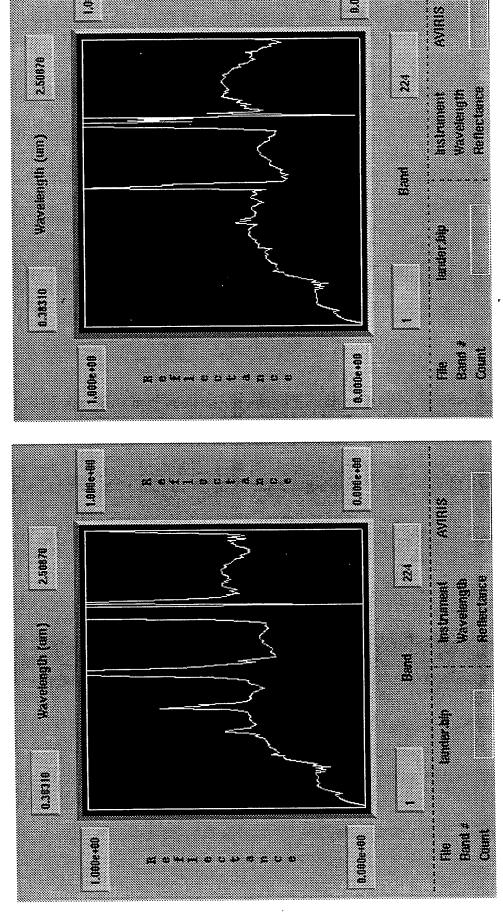
Collected near Lander, Wyoming 25 July 1995

Model Atmosphere Comparisons

Photon Research Associates, Inc.

HYPEX Derived Reflectances

US Standard 1976

Midlatitude Summer
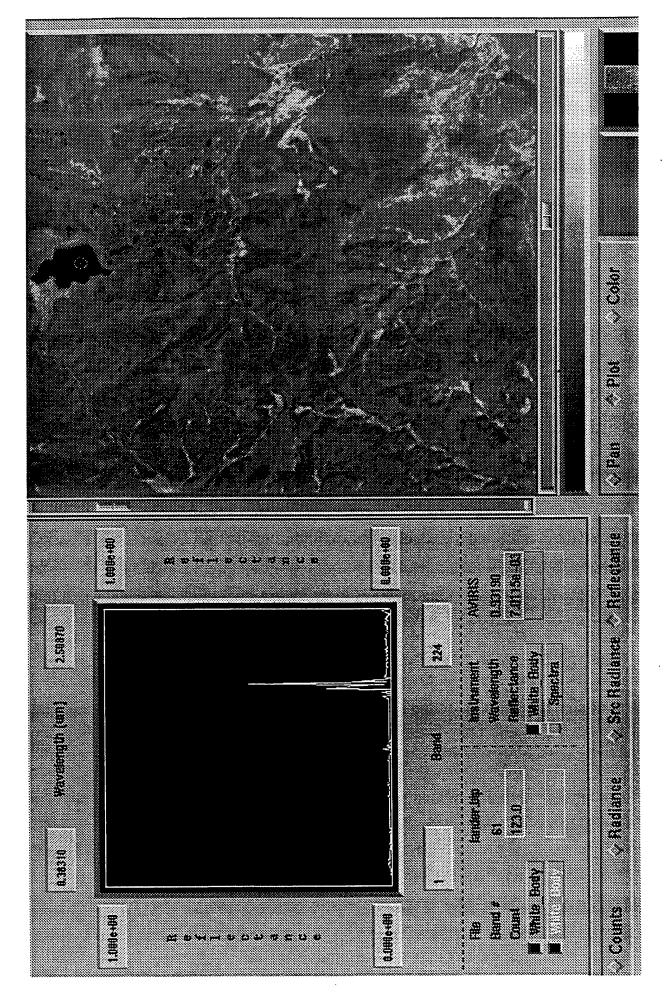
42.84N, 100.83W, 17:47 GMT, 50 km visibility, surface altitude at 2.1 km

383

HYPEX Derived Reflectances

PRA Photon Research Associates, Inc.
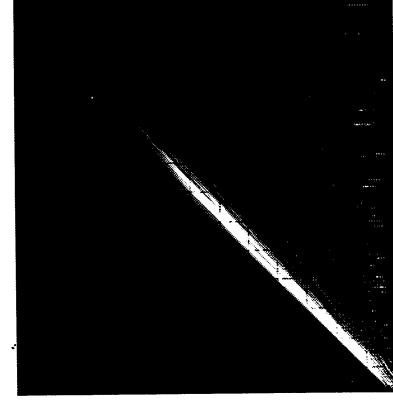
ATREM – HYPEX Derived Reflectances

PRA
Photon Research Associates, Inc.
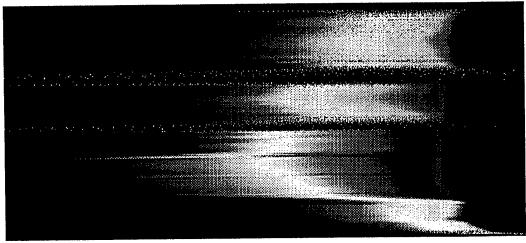
Reflectance Histograms

HYPEX

ATREM

Wavelength ------>

Wavelength ------>

R e f l e c t a n c e

Image Cube Scatterplot
All Bands

A t r e m

HYPEX
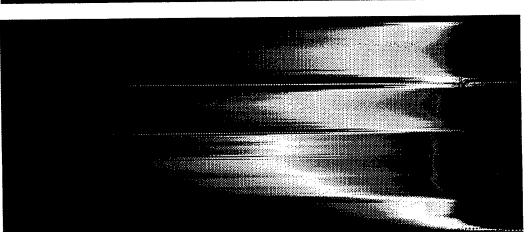
Frequency is represented by color intensity in both plots

PRA ~~~
Photon Research Associates, Inc.

Conclusions

- **Flexible tools:**

  Combines visualization with quantitative analyses

  Perform parametric studies

- **Generally good results from corrections applied**

- **Additional application areas:**

  Post launch sensor performance

  Simulated responses for sensor design

MICROWAVE TRANSMISSION
IN LIQUID WATER CLOUDS:
UNCERTAINTIES AT LOW TEMPERATURES

ALAN E. LIPTON, MICHAEL K. GRIFFIN

OPTICAL EFFECTS DIVISION
GEOPHYSICS DIRECTORATE
AIR FORCE RESEARCH LABORATORY

AND ALAN G. LING

RADEX, INC.
BEDFORD, MASSACHUSETTS

OUTLINE

* MICROWAVE ATTENUATION MODELS
* TEMPERATURE AND FREQUENCY DEPENDENCES
* CLOUD vs. TOTAL ATTENUATION
* EFFECT OF ATTENUATION UNCERTAINTY ON
    - SATELLITE BRIGHTNESS TEMPERATURES
    - LIQUID WATER CONTENT RETRIEVALS

MICROWAVE ATTENUATION MODELS
FOR CLOUD LIQUID WATER

USE RAYLEIGH ABSORPTION APPROXIMATION

CLOUD DROPLETS ARE SMALL, RELATIVE TO
WAVELENGTH OF RADIATION

ATTENUATION DEPENDS ON LIQUID WATER CONTENT,
NOT ON DROPLET SIZE DISTRIBUTION

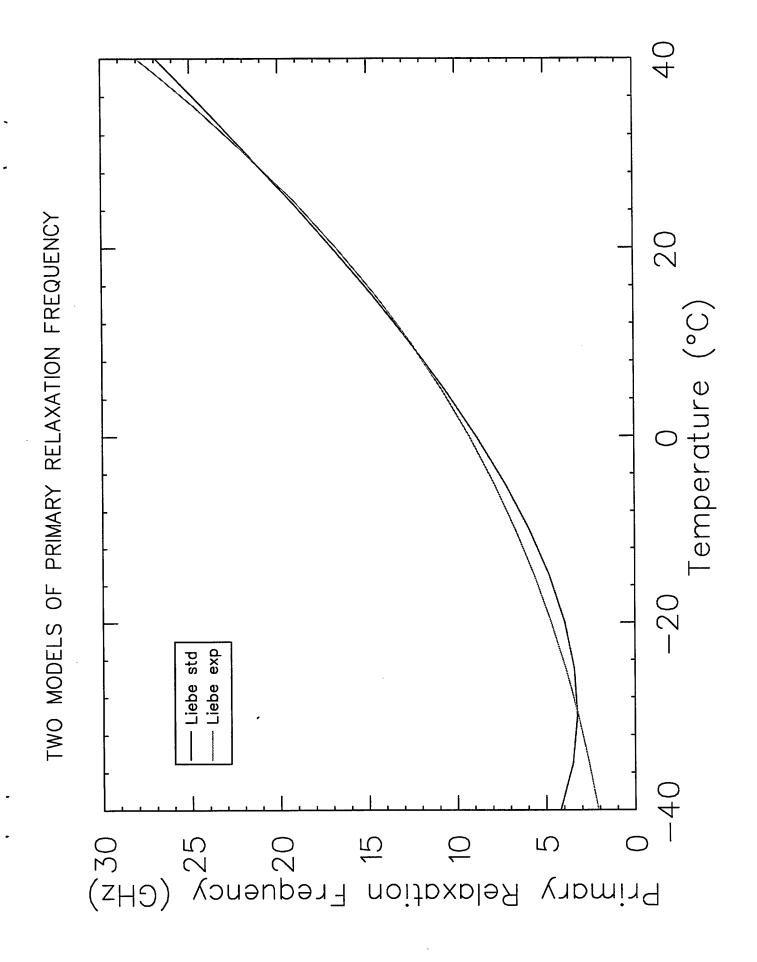DIELECTRIC CONSTANT OF WATER IS REQUIRED

RAY (1972) MODEL

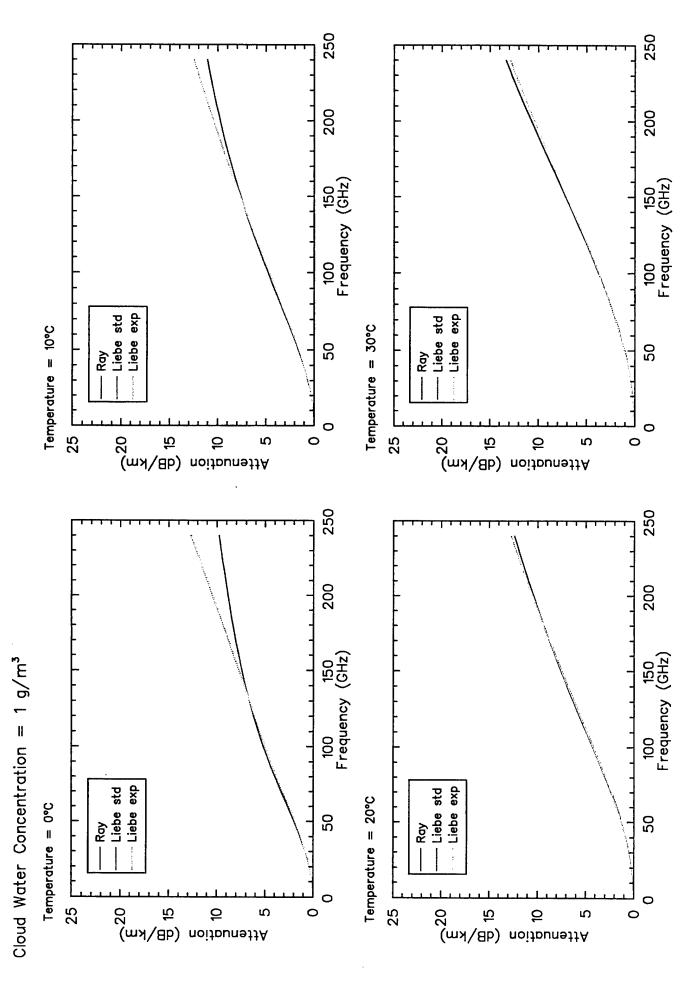— WIDELY USED STANDARD (INCL. RADTRAN, FASE)

LIEBE, HUFFORD, AND MANABE (1991) MODEL

— TWO RELAXATION TERMS
"DOUBLE DEBYE" METHOD

— TWO OPTIONS FOR TEMPERATURE DEPENDENCE
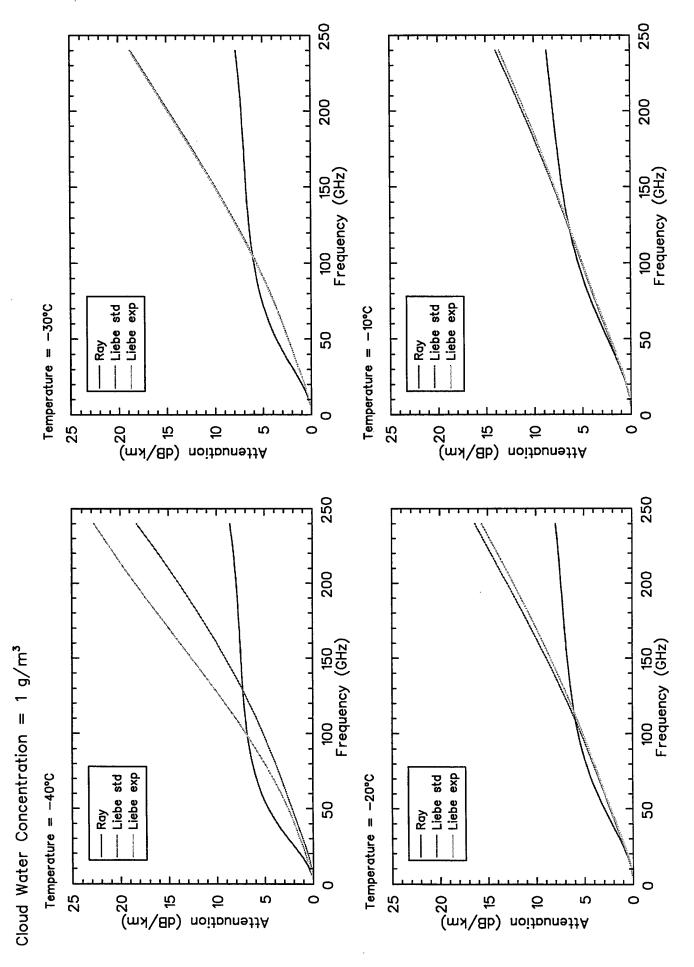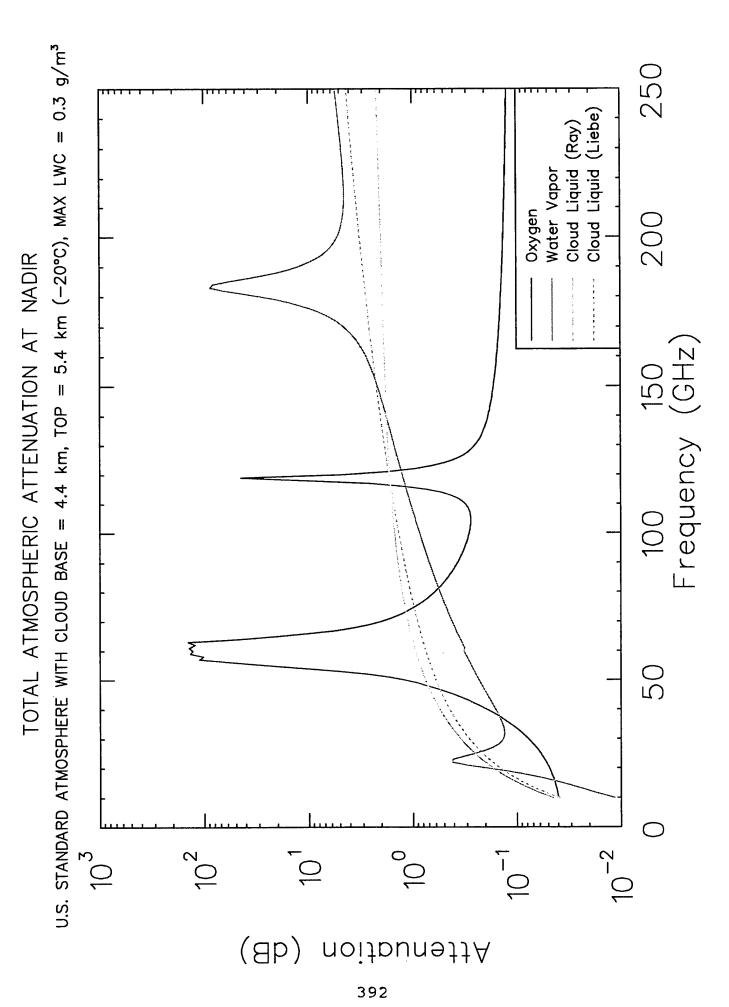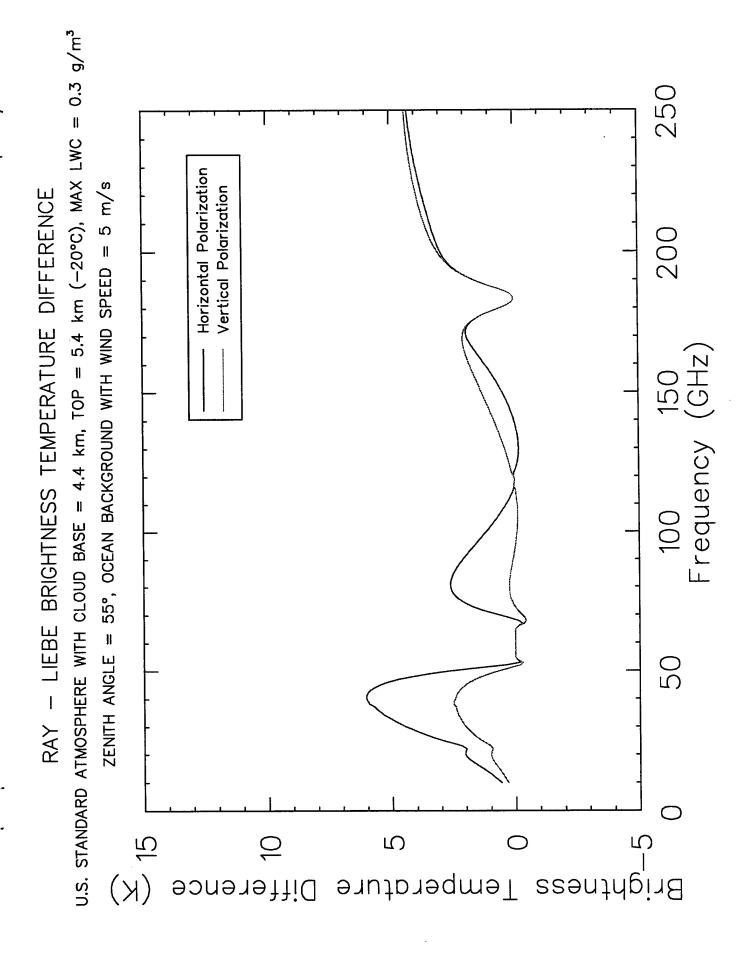OF FIRST RELAXATION FREQUENCY

NO DATA BELOW 0 °C!

TWO MODELS OF PRIMARY RELAXATION FREQUENCY

Primary Relaxation Frequency (GHz) vs Temperature (°C)

Liebe std
Liebe exp

ATTENUATION BY CLOUD LIQUID WATER

Cloud Water Concentration = 1 g/m³

ATTENUATION BY CLOUD LIQUID WATER

Cloud Water Concentration = 1 g/m³

TOTAL ATMOSPHERIC ATTENUATION AT NADIR

U.S. STANDARD ATMOSPHERE WITH CLOUD BASE = 4.4 km, TOP = 5.4 km (−20°C), MAX LWC = 0.3 g/m³

Legend:
- Oxygen
- Water Vapor
- Cloud Liquid (Ray)
- Cloud Liquid (Liebe)

X-axis: Frequency (GHz)
Y-axis: Attenuation (dB)

RAY — LIEBE BRIGHTNESS TEMPERATURE DIFFERENCE

U.S. STANDARD ATMOSPHERE WITH CLOUD BASE = 4.4 km, TOP = 5.4 km (−20°C), MAX LWC = 0.3 g/m³

ZENITH ANGLE = 55°, OCEAN BACKGROUND WITH WIND SPEED = 5 m/s

- Horizontal Polarization
- Vertical Polarization

RAY – LIEBE BRIGHTNESS TEMPERATURE DIFFERENCE

U.S. STANDARD ATMOSPHERE WITH CLOUD BASE = 5.9 km, TOP = 6.9 km (−30°C), MAX LWC = 0.3 g/m³

ZENITH ANGLE = 55°, OCEAN BACKGROUND WITH WIND SPEED = 5 m/s

Horizontal Polarization
Vertical Polarization

CLOUD LIQUID WATER RETRIEVALS FROM SIMULATED SSM/I DATA

ALISHOUSE ET AL. (1990) REGRESSION FORMULA

U.S. STANDARD ATMOSPHERE WITH CLOUD

CONCLUSIONS

THERE ARE LARGE UNCERTAINTIES IN MICROWAVE
ATTENUATION BY LIQUID WATER AT LOW TEMPERATURES
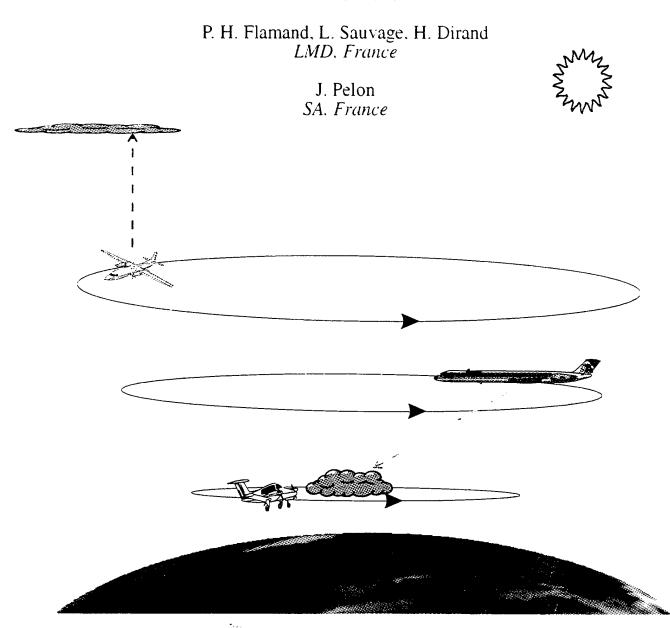
THESE UNCERTAINTIES IMPLY SIGNIFICANT ERRORS
IN SATELLITE-RETRIEVED CLOUD PROPERTIES

LABORATORY AND MODELING RESEARCH IS NEEDED
TO REDUCE THE UNCERTAINTIES

ECRIN 96

(Etude du Champ Radiatif Infrarouge des Nuages)

P. Simoneau, C. Malherbe. A. Boischot, G. Durand. B.Rosier. A. Delannoy
ONERA. France

P. H. Flamand, L. Sauvage. H. Dirand
LMD. France

J. Pelon
SA. France

ECRIN 96

Objectives

1/ Code validation :
　　　　　　　　- NUALUM
　　　　　　　　- MONET

2/ Radiance fluctuations on water clouds

3/ Microphysic data base

4/ Cirrus radiance measurements

5/ Restitution of atmospheric radiatives fluxes

3

ONERA

Measurement strategy

	ARAT/Fokker-27	Caravelle 116	Merlin IV
Ceiling altitude Cruising airspeed Endurance	5500 m 80-100 m s-1 3h-4 hours	6000 m 200-300 Knt 5 hours	7 000 m 100-130 m s-1 4-5 hours
Instrumentation	- backscatter lidar LEANDRE-1 - pyranometers, pyrgeometers, Barnes PRT-5 - in situ probes	- IR spectrometer - IR imager	- pyranometers, pyrgeometers, Barnes PRT-5 - in situ probes - microphysics probes

choice of the 3 aircraft

ECRIN 96

Measurement strategy

- Satellite information : AVHRR, SPOT
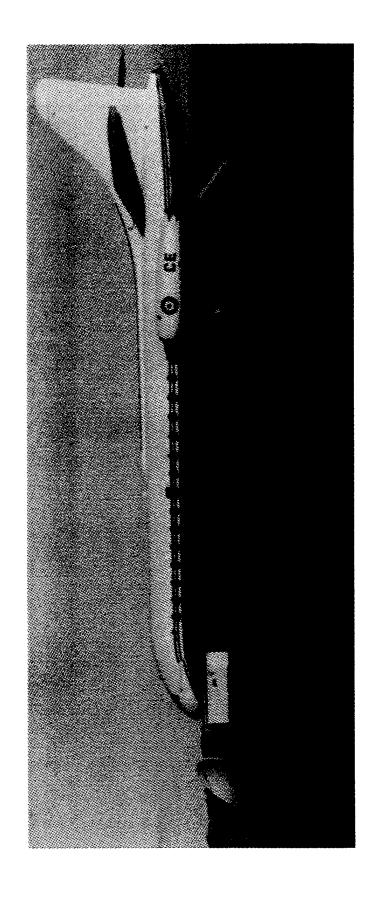
- Radiosounding

Radiance measurements :

➜ spectrometer, IR imageur

In Situ measurements :

➜ LWC/T/U probes, FSSP, ...

Cirrus occurence, aerosols :

➜ Lidar

6
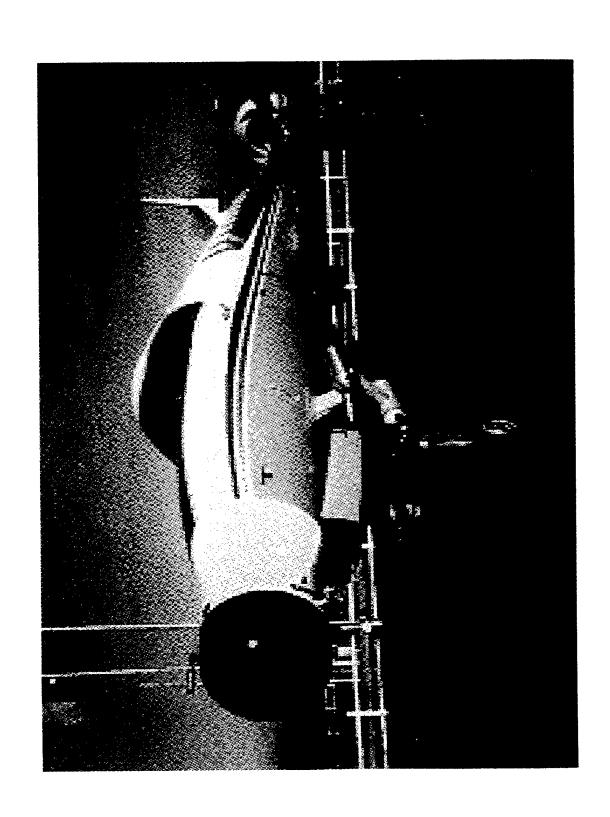
ONERA

Caravelle 116 for Radiance measurements

47

Caravelle 116

Cloud and atmospheric parameters	Instrument	Carrier
- CVF spectrometer - spectral range 1.5 - 5.3 µm - spectral resolution $\Delta\lambda/\lambda = 2\%$ - liquid nitrogen cooled - fov = 3 mrd - 10 spectra/s	Spectrometer SICAP	Caravelle
- PtSi camera - waveband 3-5µm - fov ≈ 1.5 → 14 ° (depending lens focal length) - 25 images/s	Imager CIRAP	Caravelle

Merlin 4 for in situ measurements

9

MERLIN 4
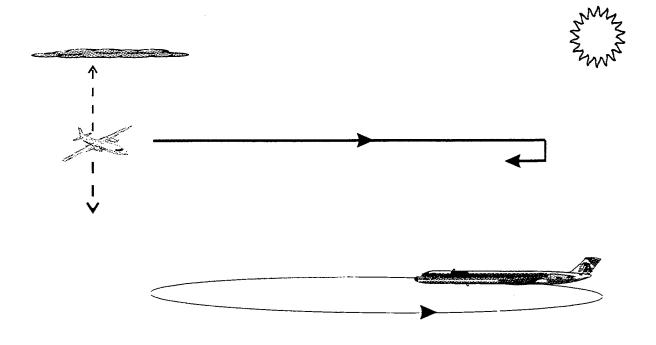
Cloud and atmospheric parameters	Instrument	Carrier
- down- ($F_{\downarrow sw}$) and upward shortwave ($F_{\uparrow sw}$) fluxes	Pyranometer	Merlin IV
- down- ($F_{\downarrow lw}$) and upward longwave ($F_{\uparrow lw}$) fluxes	Pyrgeometer	
- thermodynamic : temperature (T), pressure (p), and humidity (q) profiles	In-situ probes	Merlin IV
- microphysics : liquid water content (LWC), particles size, concentration	FSSP	

ARAT

Fokker 27 - IGN - CNES - CNRS - Météo France

F-BYAO

ARAT

Mesures radiatives vers le haut et vers le bas
Pyranomètre visible et IR
Photomètres UV

Perche instrumentée (5m)
Pressions statique et différentielle
Vitesse de l'air u,v,w
Accélérations x,y,z
Températures (haute et basse fréquence, intra-nuageuse)
Humidité (haute et basse fréquence, eau liquide nuageuse)

Fenêtres de visée vers le bas

Avion de recherche et de mesure

Avion de recherche et de mesure

ONERA

ARAT

Cloud and atmospheric parameters	Instrument	Carrier
- cloud base and height, geometrical thickness ΔH, - optical depth at 0.53 μm (δ_{VIS}), - vertical structure of extinction (α) and backscatter (β) coefficients at 0.53 μm, - scattering phase function $p(\pi)$ or backscatter to extinction ratio (k), $p(\theta) = 4\pi k$ - ice/water discrimination, vertical structure of linear depolarization ratio (Δ)	Backscatter Lidar LEANDRE-1	ARAT
- down- ($F_{\downarrow sw}$) and upward shortwave ($F_{\uparrow sw}$) fluxes - down- ($F_{\downarrow lw}$) and upward longwave ($F_{\uparrow lw}$) fluxes - down- and upward emissivity (ϵ), infrared optical depth (δ_{IR})	Pyranometer Pyrgeometer PRT-5	

ECRIN 96
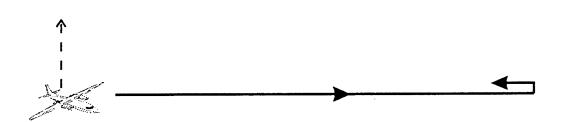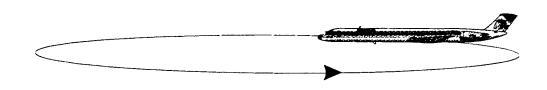
Measurement strategy for low altitude clouds   13

ECRIN 96
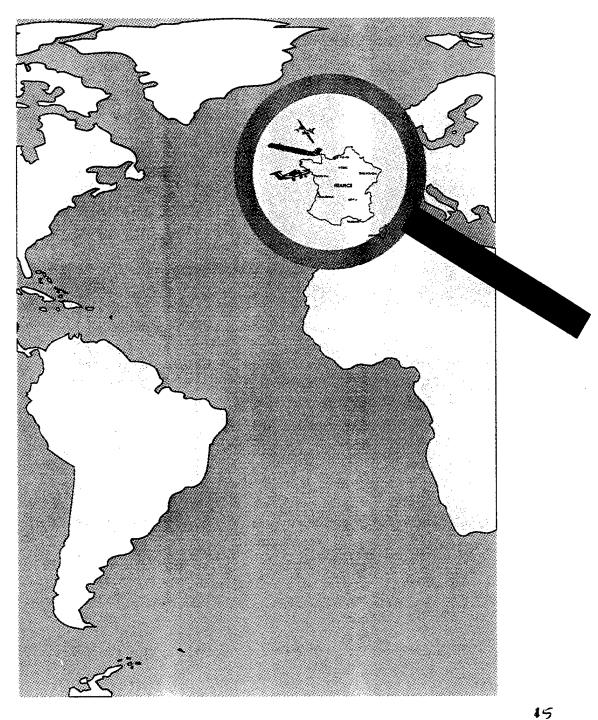
Measurement strategy for cirrus clouds

14

ECRIN 96

15
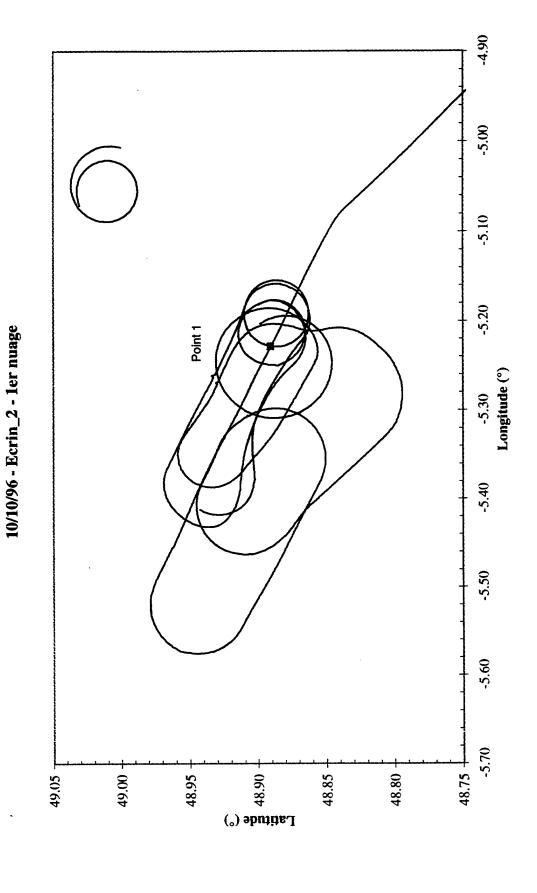
The experiment took place in Brittany near Brest
(West coast of France)

ONERA

Date in October 1996	Mission #	Take-off Duration	Objectives
9	1	3.5 hours	low clouds
10	2	3.6 hours	low clouds
11	3	2.3 hours	cirrus
14	4	2.4 hours	edges
15	5	2.6 hours	SPOT
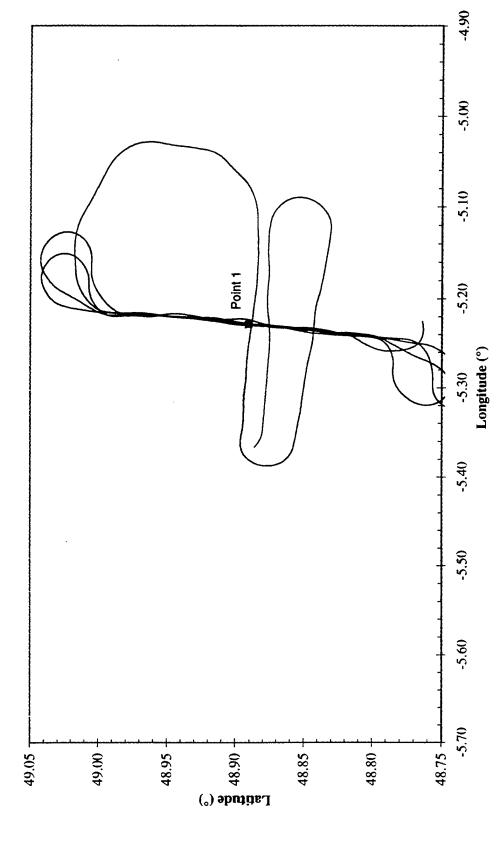
Trajectoire Totale Caravelle
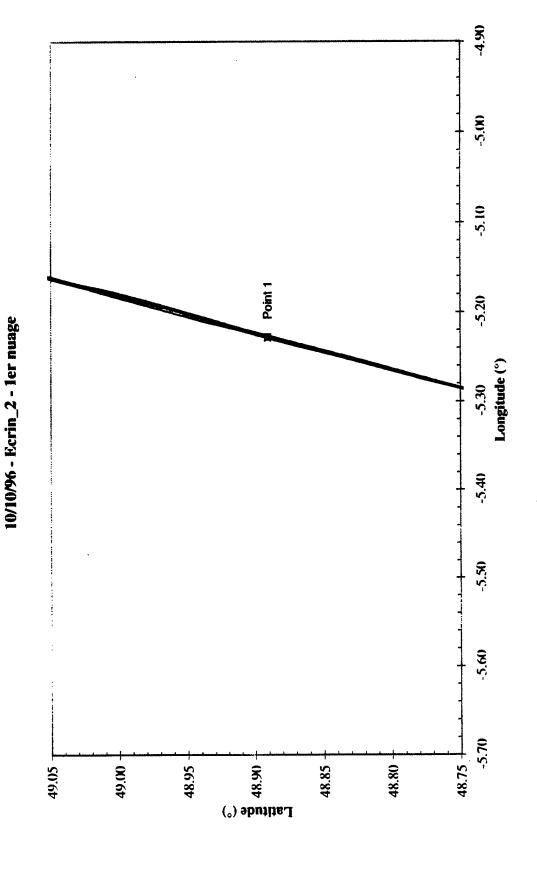
10/10/96 - Ecrin_2 - 1er nuage

Point 1

Longitude (°)

Latitude (°)

Page 1

E2_V101.xls

i7

Trajectoire Merlin

10/10/96 - Ecrin_2 - 1er nuage

Point 1

Longitude (°)

Latitude (°)

Page 1

E2_V101.xls

412

Trajectoire ARAT

10/10/96 - Ecrin_2 - 1er nuage

Longitude (°)

Latitude (°)

Point 1

Page 1

E2_V101.xls

413

19

AVHRR image during the 2nd mission

414

20

Luminances Intégrées (2)

E2. Nuage n°2. Visée -5°.

Direction de visée

Luminance Intégrée (W/m²/sr)

Direction solaire
Bande 1.5 - 2.5µm
Bande 2.5 - 4.3µm
Bande 4.3 - 5.5µm

SICAP   results

Graphique

Heure :   13:00:16.075

Status :   Désignation

Numéro(s): 2250 - (Réf : 2774 à 2786)

Spectres SICAP

Page 1
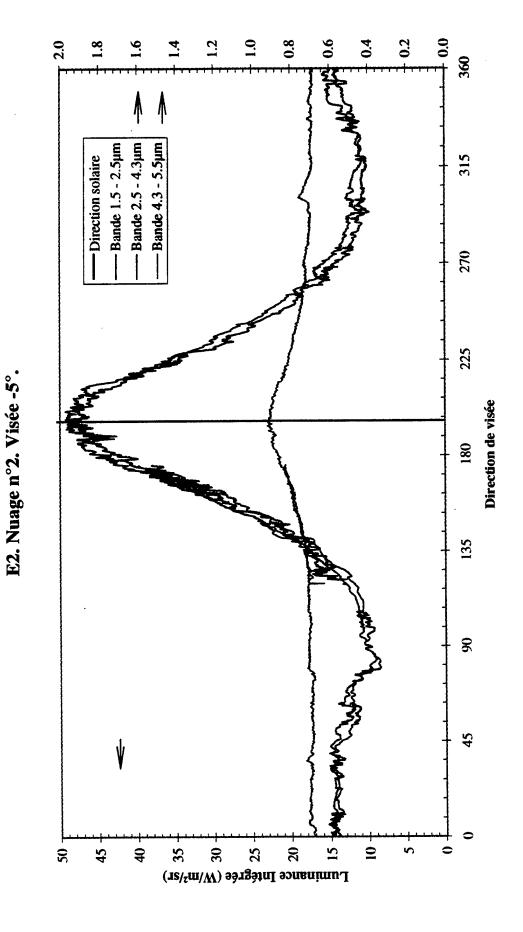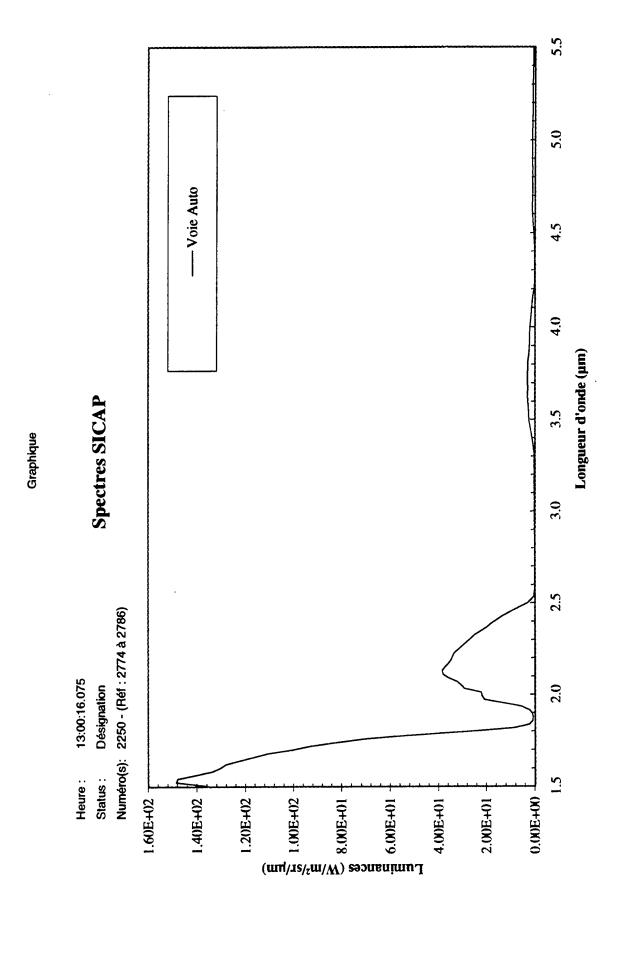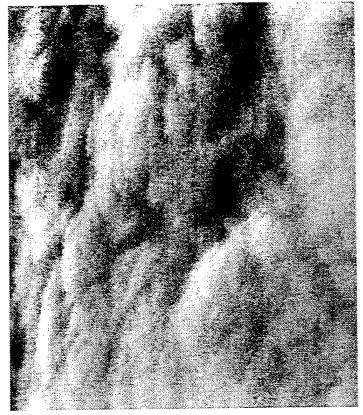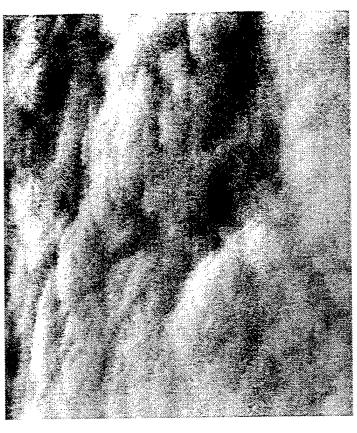
Nuage_2_Visée-05.xls

ONERA

Nuage 2 - visée à -30° - 13:18:22 TU

Nuage 2 - visée à -5° - 13:00:28 TU

ECRIN 96 - Vol E2

CIRAP results

417

23

Lwc

	Lwc
	0.551
	0.496
	0.441
	0.386
	0.331
	0.275
•	0.220
•	0.165
•	0.110
•	0.055
•	0.000

longitude

latitude

Lwc along the Merlin 4's trajectory

24

Comptes FSSP de 44600 a 44720
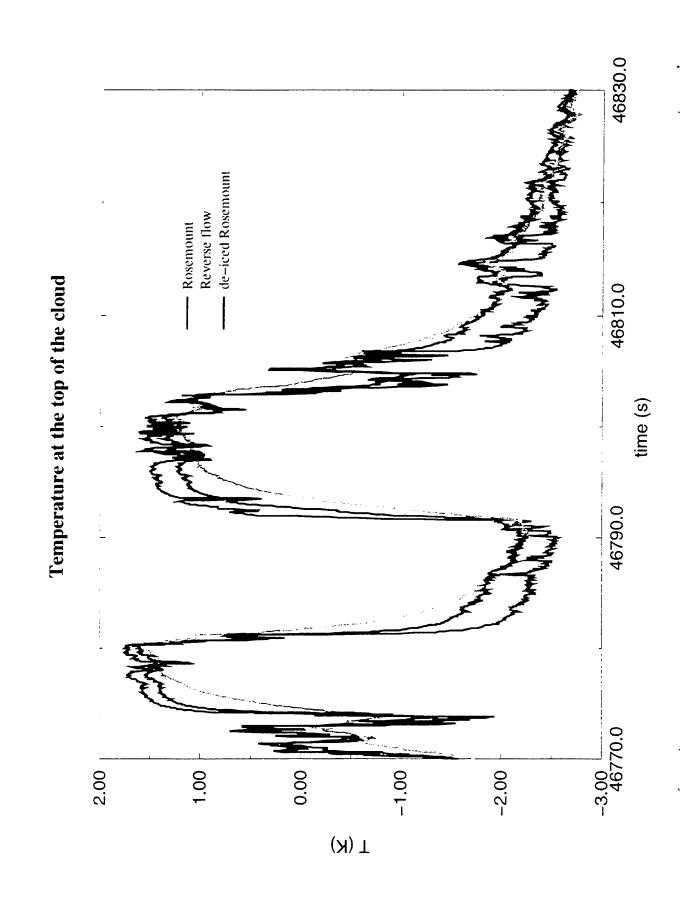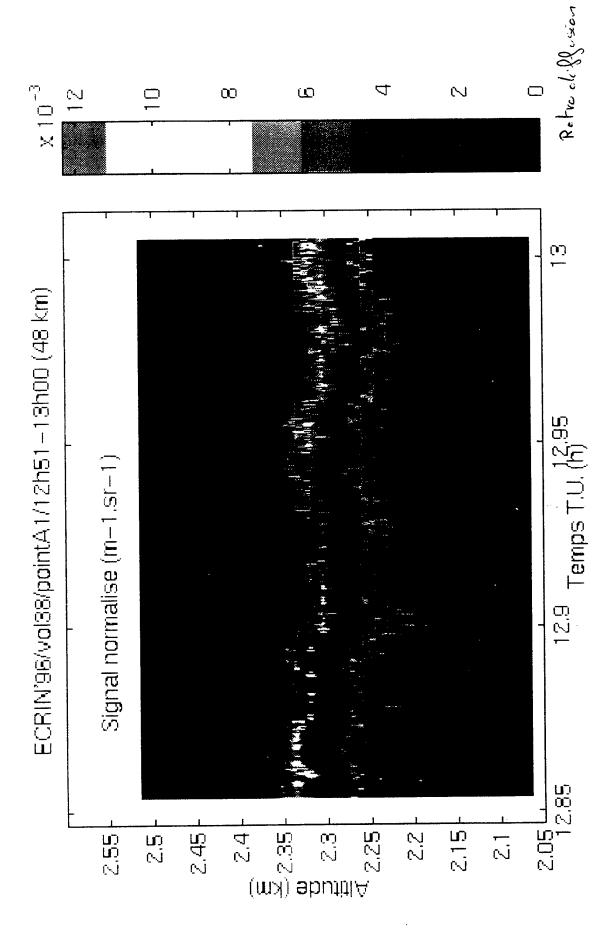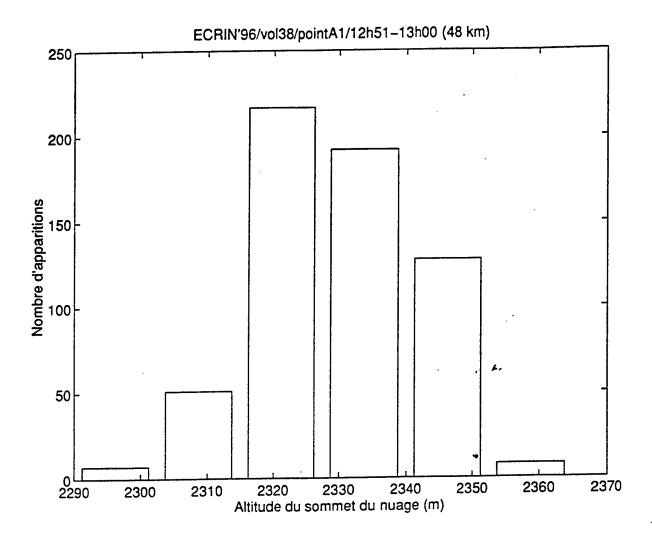
FSSP spectrum for a saw tooth
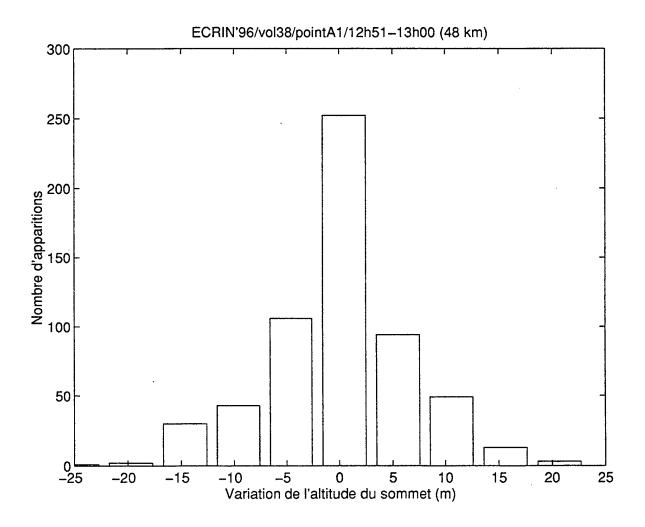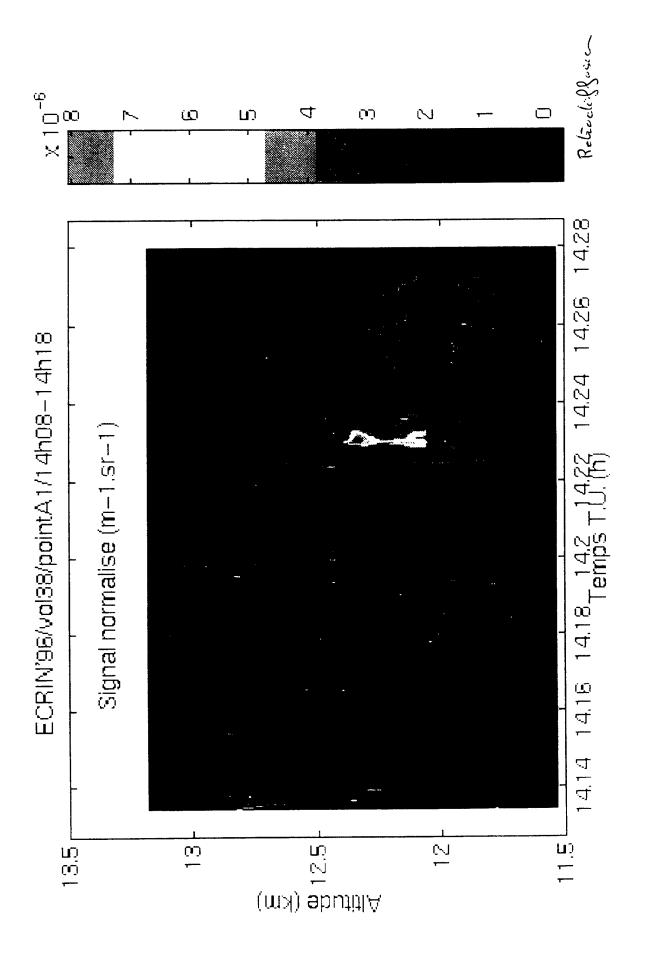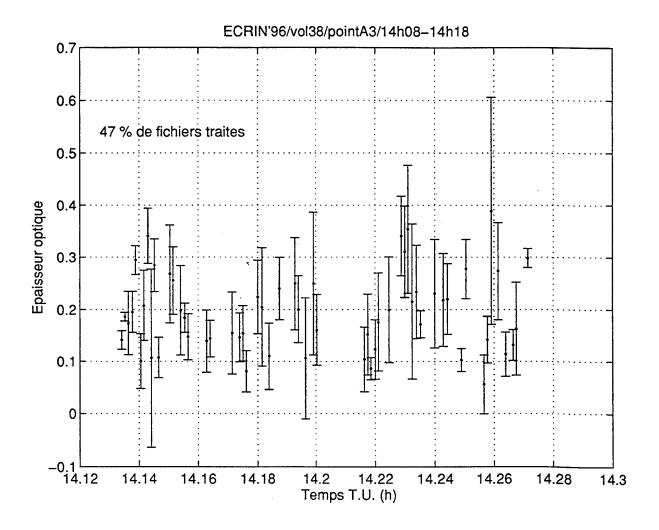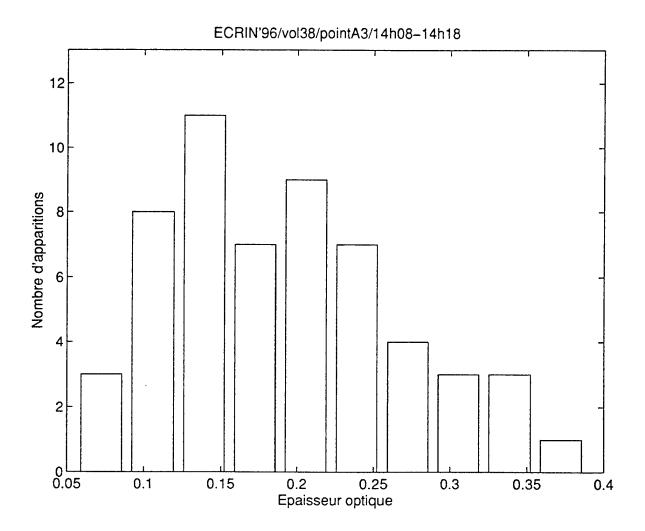
Temperature at the top of the cloud

Rosemount
Reverse flow
de-iced Rosemount

time (s)

T (K)

420

ECRIN'96/vol38/pointA1/12h51–13h00 (48 km)

Signal normalise (m−1.sr−1)

x 10⁻³

Retrodiffusion

Altitude (km)

Temps T.U. (h)

Lidar measurements on a Sc

ECRIN'96/vol38/pointA1/12h51–13h00 (48 km)

Lidar results

ECRIN'96/vol38/pointA1/12h51–13h00 (48 km)

Lidar results

ECRIN'96/vol38/pointA1/14h08-14h18

Signal normalise (m-1.sr-1)

Altitude (km)

Temps T.U. (h)

Reflectivité ???

$\times 10^{-6}$

Lidar measurements on a Cirrus cloud

ECRIN'96/vol38/pointA3/14h08–14h18

Lidar results

ECRIN'96/vol38/pointA3/14h08–14h18

Lidar results

ECRIN 96

Scientific developments

- code validations (1D, 3D)

- 3D cartography

- comparison Lidar/In Situ

- comparison in situ measurements/AVHRR informations (altimetry, microphysic)

- fluxes restitution

publication (BAMS)

ECRIN 96

Conclusion

3 flights with measurements on Scu :
   - radiance (spectra, images)
   - in situ microphysic
   - lidar information (cirrus, boundary layer)
   - AVHRR images
   - radiosounding

1 flight with measurements on CIRRUS :
   - radiance (spectra, images)
   - lidar information (k_{ext})
   - AVHRR images
   - radiosounding

1 flight with SPOT appointment :
   - presence of ice

Measurements of land and sea radiance

3

A lot of data and a lot of WORK !!

ONERA

ECRIN 96

Acknowledgments

☞ J. Deschamp, G. Grégoire, J.F. Mermet, M. Labrousse, P. Laroche

ONERA

☞ CEV' s pilots and crew

☞ M. Charpentier, B. Bernard, M. Laurens, M. P. Lefebvre, W. Maurel, J.L. Brenguier and al

MétéoFrance

☞ C. Tardieu, G. François, J. C. Lostec, C. Allet and al.

INSU / IGN

Transmissive cloud cases

H.K. Burke, J.W. Snow, K.E. Rhoades,

J.P. Kerekes, M.P. Jordan and C.A. Upham

MIT Lincoln Laboratory

20th Annual DoD Atmospheric Radiance
and Transmission Meeting

10-12 June 1997

Methodology for Cloud Determination Based on Humidity and Temperature Profiles

- **Semi-empirical approach to determine presence of cloud**
  - Threshold relative humidity (RH) for cloud generation
  - Departure of actual (RH_a) from clear atmosphere value (RH_c)

- **Low and middle tropospheric cloud top located**
  - At level where (RH_a - RH_c) first falls below 10%

- **High cirrus detection based on Clausius-Clapeyron equation**
  - Saturation vapor pressure (e_s) over ice as function of temperature (T)

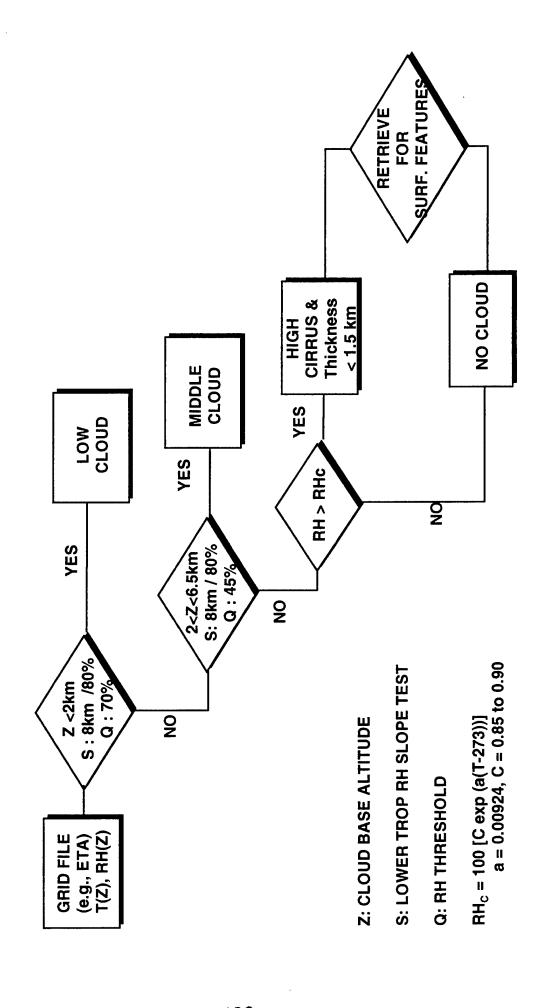$$(1/e_s) \, (de_s/dT) = L_{iv} / (R_v \, T^2)$$

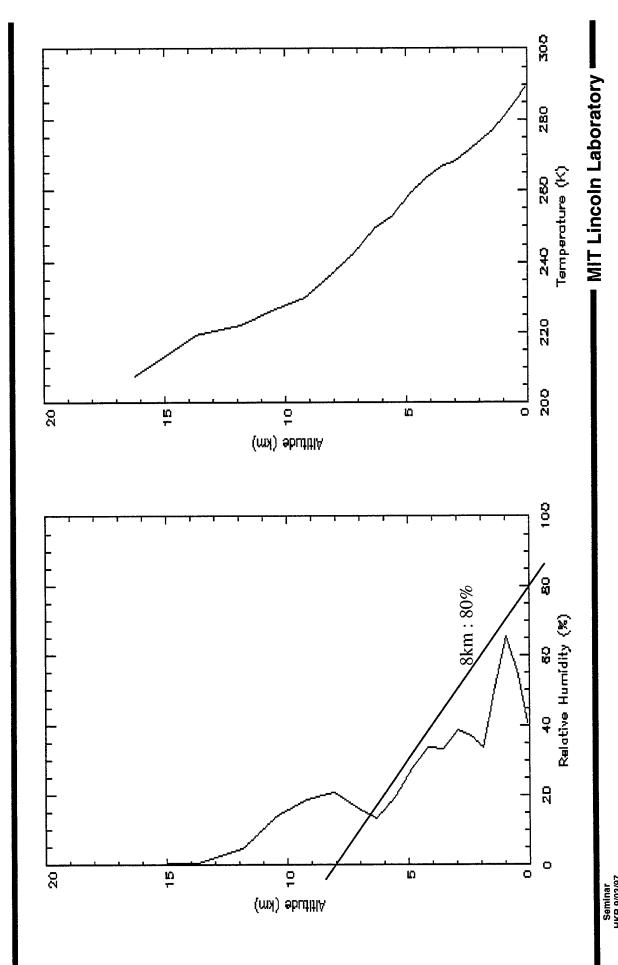L_{iv}: Latent heat of sublimation 2834 J/gm, R_v: 0.4615 J/ gm-K

Tests for
Opaque Cloud/Transmissive Cloud/ No Cloud

```
GRID FILE
(e.g., ETA)
T(Z), RH(Z)
```
        │
        ▼
      ⟨ Z <2km
        S : 8km /80%
        Q : 70% ⟩ ──YES──▶ [LOW CLOUD]
        │
        NO
        ▼
      ⟨ 2<Z<6.5km
        S: 8km / 80%
        Q : 45% ⟩ ──YES──▶ [MIDDLE CLOUD]
        │
        NO
        ▼
      ⟨ RH > RHc ⟩ ──YES──▶ [HIGH CIRRUS & Thickness <1.5 km]
        │   │
        NO   ▼
        │   ⟨ RETRIEVE FOR SURF. FEATURES ⟩
        ▼
   [NO CLOUD]

Z: CLOUD BASE ALTITUDE

S: LOWER TROP RH SLOPE TEST

Q: RH THRESHOLD

$RH_C = 100 \, [C \exp (a(T-273))]$
$a = 0.00924, C = 0.85 \text{ to } 0.90$
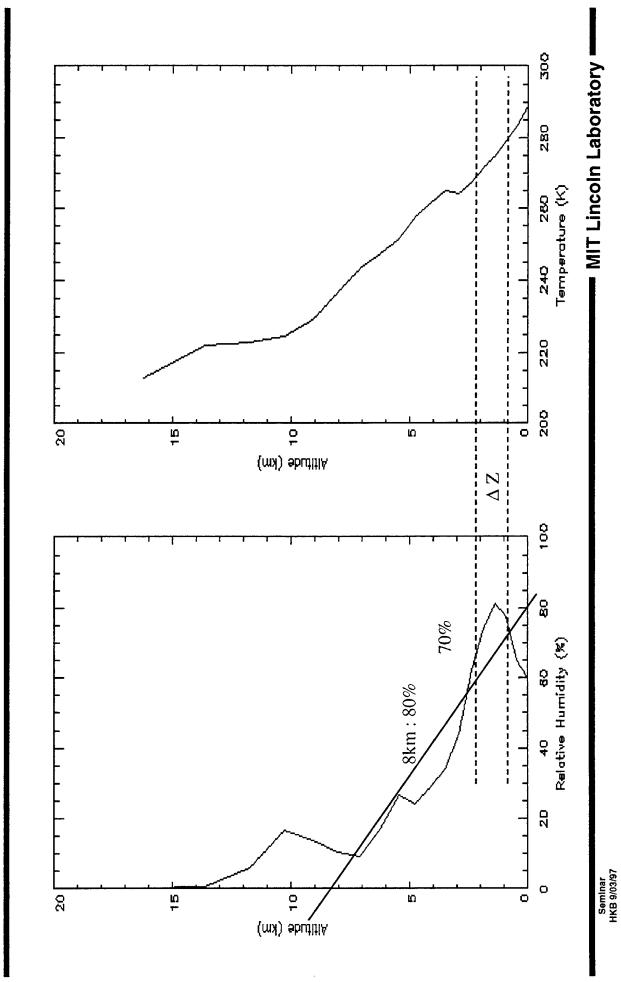
A Sample No-Cloud (Clear) Case

8km : 80%

Relative Humidity (%)

Altitude (km)
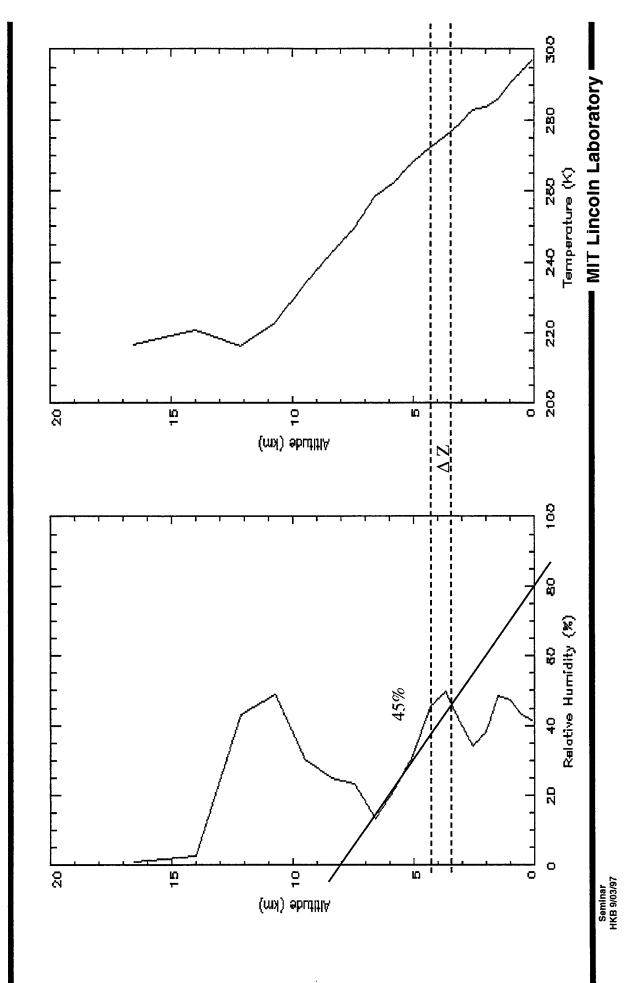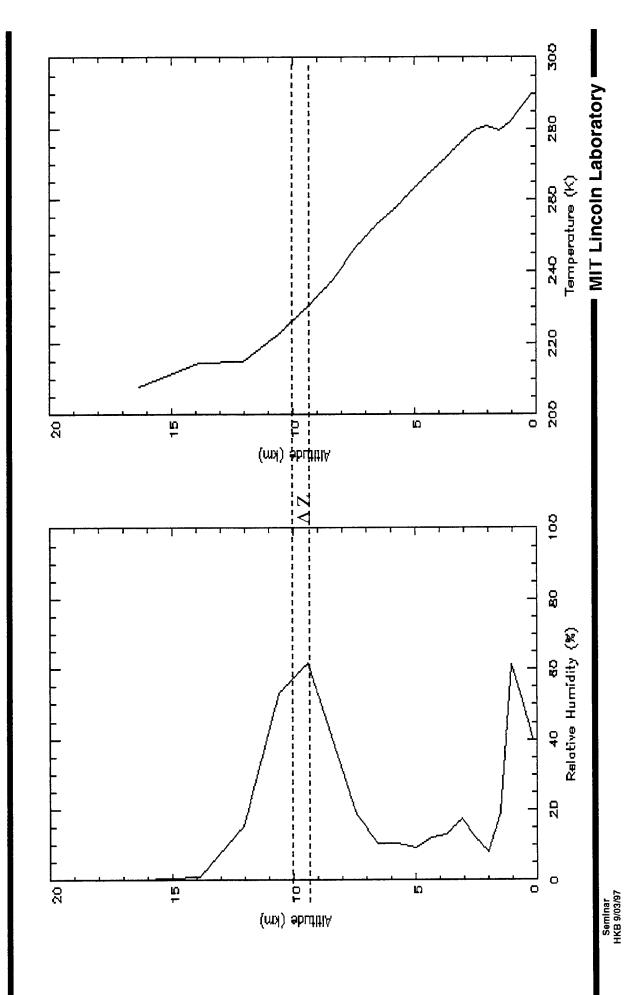
Temperature (K)

Altitude (km)

A Sample Low Cloud Case

A Sample Middle Cloud Case
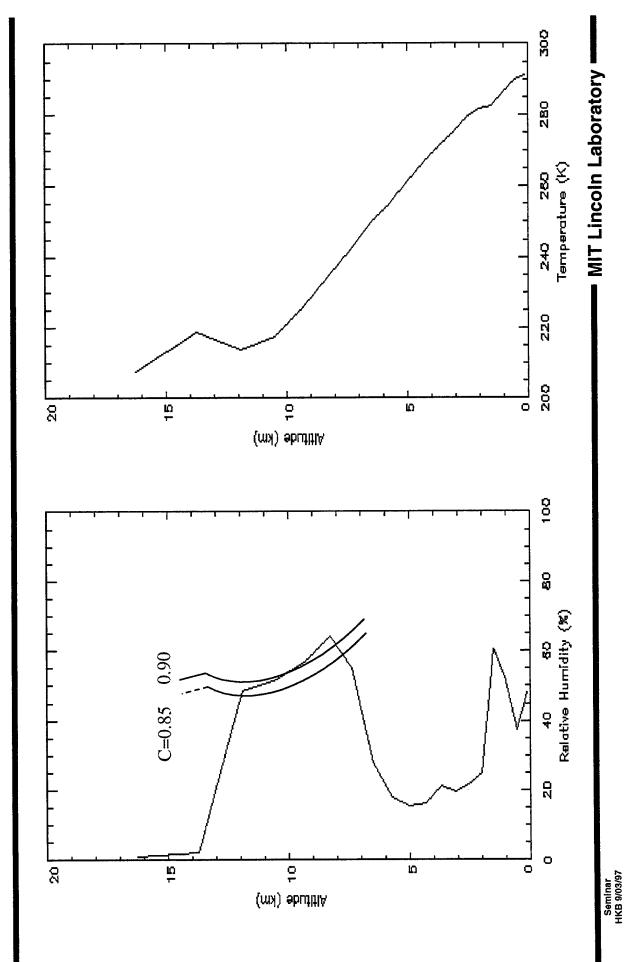
A Sample High Cirrus Case

436
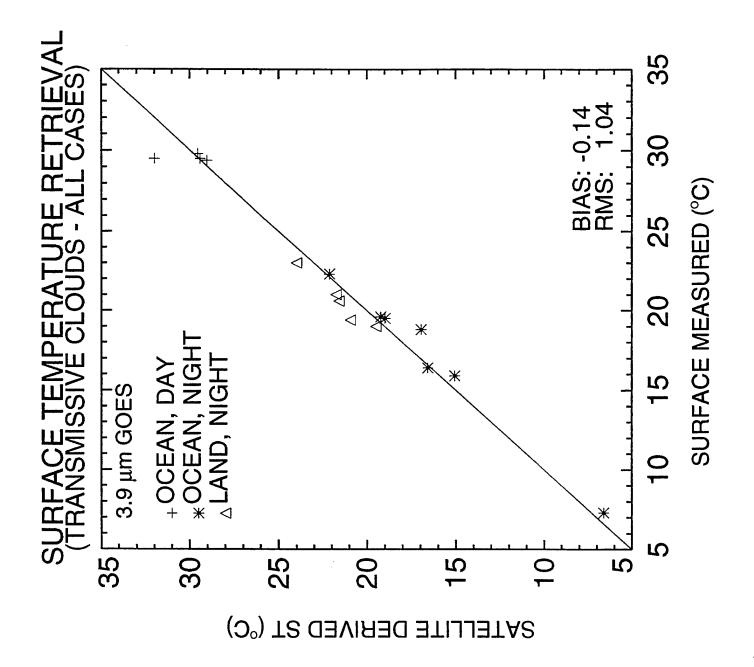
Diagnostic Test for Vertical Extent of Cirrus Cloud

MIT Lincoln Laboratory

SURFACE TEMPERATURE RETRIEVAL
(TRANSMISSIVE CLOUDS - ALL CASES)

3.9 μm GOES

+ OCEAN, DAY
* OCEAN, NIGHT
△ LAND, NIGHT

BIAS: -0.14
RMS: 1.04

SURFACE MEASURED (°C)

SATELLITE DERIVED ST (°C)

SURFACE TEMPERATURE RETRIEVAL
(NIGHTTIME, OCEAN, TRANSMISSIVE CLOUD)

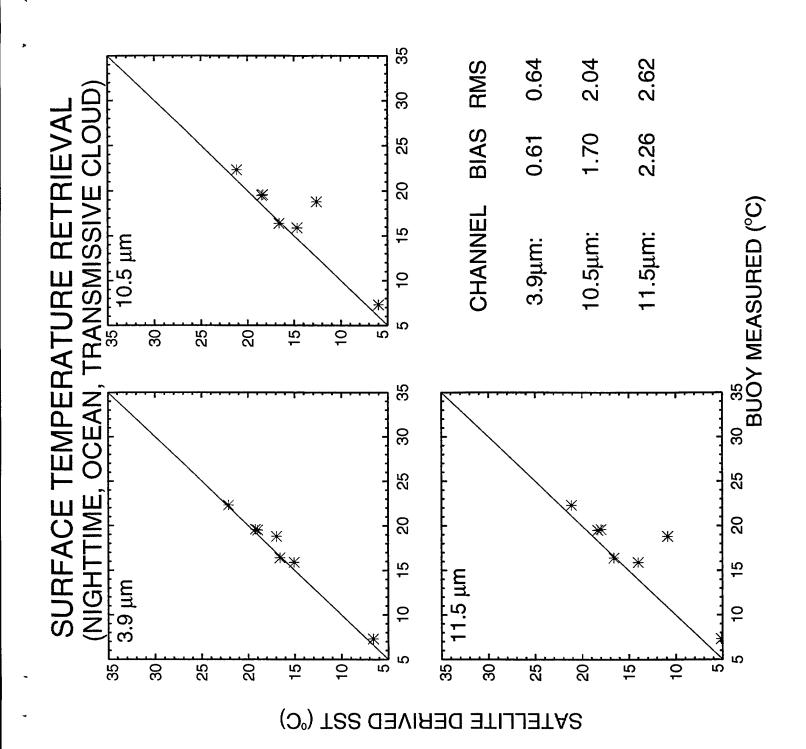| CHANNEL	BIAS	RMS
3.9μm:	0.61	0.64
10.5μm:	1.70	2.04
11.5μm:	2.26	2.62

MWIR Atmospheric Correction Algorithm

Summary

- New and innovative retrieval algorithm for surface radiance successfully developed and demonstrated

  - Approach utilizes existing "operational" products and state-of-science model

  - Various test cases (night/day, ocean/land)

- Significant results of MWIR atmospheric correction experiments

  - Improved accuracy of surface temp retrieval

    SST retrieval bias 0.1K, RMS 0.5K

MIT Lincoln Laboratory

MODTRAN4 and FASE: Potential for Climate-Change Modeling

G.P. Anderson, J.H. Chetwynd
PL/Geophysics Directorate, Hanscom AFB, MA 01731
781-377-2335, Fax 377-8900, 'ganderson@plh.af.mil'
A. Berk, L.S. Bernstein, P.K. Acharya
Spectral Sciences, Inc., Burlington, MA 01803
781-273-4770, Fax 270-1161, 'lex@spectral.com'
H.E. Snell
Atmospheric and Environmental Research, Cambridge, MA
617-549-2281, FAX 617-661-6479, 'snell@aer.com'

1. INTRODUCTION:

"Hyperspectral" is a relatively new descriptor for measurement techniques historically used by the atmospheric remote sensing communities. As opposed to "multi-spectral" sensing, which includes any instrument with a finite number of specific channels, filters, or bands, hyperspectral implies employing enough (usually contiguous) channels to provide redundant information on both the characteristics of the surface and the atmosphere when the instrument is configured for nadir viewing. This definition (Alex Goetz, Univ. of Colorado, private communication) can be contrasted with others, such as 'any instrument with better than 4 cm^{-1} resolution." This latter definition can be inadequate in the infrared spectral range because many overlapping molecular systems will not be sufficiently discriminated at such 'narrow' resolution. However, the 4 cm^{-1} is often much more than adequate in the visible, when typical resolutions of 10 nm (e.g. AVIRIS, Green et al., 1996) at 600 nm corresponds to a frequency resolution of over 200 cm^{-1}.

With the development of MODTRAN4 (Bernstein, et al., 1996), a flexible tool for applications of realistic hyperspectral sensing is now available. While this version of MODTRAN is grounded in the prior series of AF radiative transfer band model (BM) algorithms (LOWTRAN, Kneizys, et al., 1980, 1983, 1988, through MODTRAN3, Berk et al., 1989, 1995), it is distinct in its ability to employ Beer's law ($T_v = \exp(-k_{v,i} n_i)$) to describe local layer, species-specific transmittance for input to the radiance calculations. While this capability is not always necessary, it allows appropriate handling of multiple scattering (m.s.) using existing non-BM algorithms (DISORT, Stamnes et al., 1988, and Isaacs et al., 1987). MODTRAN4, while maintaining the basic 2 cm^{-1} spectral resolution, can now complement the m.s. routines by introducing a Correlated-k (CK) capability which is expressly compatible with Beer's law formulations. MODTRAN4 also provides greatly improved predictive capabilities under cloudy and/or heavy aerosol loading conditions in both the visible and IR by allowing the explicit definition of water and ice cloud vertical profiles and spectral data, either by scaling and combining default model clouds or by redefining entirely new model clouds with micro-layering options.

It can be shown that this combination of improvements will permit rapid identification of atmospheric contaminants/signatures in window regions as well as accurate spectral calculations of heating/cooling rates in the presence of clouds for both thermal and solar spectral regimes. Finally, in the regions of molecular opacity, where weighting functions peak in the atmosphere, it is expected that MODTRAN4 can play a role in very quick 'primitive' retrievals, avoiding the large number of line-by-line (LBL) calculations necessary for initiating derivative (perturbation) matrices (Anderson et al., 1993). While the error estimates and residuals associated with a 2 cm^{-1} algorithm will be larger than those associated with LBL retrievals, the speed advantage for image processing might warrant this initial approach.

FASE (Snell et al., 1995 a,b) can now be used for thermal infrared hyperspectral sensing, most notably for atmospheric compensation for interferometer data taken from aircraft or satellite platforms. Based on the validation of the HIS (High resolution Interferometer Sounder), Wang et al, 1996, FASCOD3 proved capable of fitting the measurements within a few percent, given accurate sonde data. But, this paper equally showed that the high resolution measurements can actually reveal the state of the atmosphere, independent of sonde (Revercomb et al., 1993; Smith et al., 1995). This process is termed 'atmospheric compensation' when applied to hyperspectral

imaging. HIS is, of course, a 'soda straw' rather than an imager, but the inferences can be extrapolated to the next generation of instruments. Certainly surface properties can be ascertained (eg. the sea surface albedo in the Wang paper), and sea surface temperature can be readily retrieved.

2. ADDITION OF A CORRELATED-k CAPABILITY TO MODTRAN

Addition of a CK capability to MODTRAN (Bernstein et al., 1995) provides an accurate and fast means for evaluation of the effects of clouds and heavy aerosol loading on retrievals (both surface properties and species concentration profiles) and on atmospheric radiative heating/cooling calculations. These radiative transfer computations require coupling the effects of gaseous molecular absorption due primarily to water vapor, carbon dioxide, and ozone, with particulate multiple scattering due to volcanic aerosols, ice crystals, and water droplets. In order to adapt a band model approach for use in scattering calculations it is necessary to express the band model transmission function in terms of a weighted sum of Beer's law exponential terms. Thus, a method for determining the weighing factors and monochromatic absorption coefficients for the MODTRAN band model is required. An abbreviated discussion of the CK approach as tailored for integration into MODTRAN is given below; for a more complete discussion of the CK method the reader is referred to Lacis and Oinas (1991).

For simplicity, consider the problem of determining the average transmittance, as defined by Beer's law, for a homogeneous path over a finite spectral interval. The generalization to inhomogeneous paths is straightforward. The path transmittance can be exactly determined through evaluation of:

$$T(u) = \frac{1}{\omega_2 - \omega_1} \int_{\omega_1}^{\omega_2} d\omega \; \exp(-k(\omega)u) \quad ,$$

where ω is frequency, $k(\omega)$ is the monochromatic absorption coefficient, and u is absorber column density. The basis of the CK approach is that evaluation of $T(u)$ by integration over frequency can be replaced by an equivalent integration over the distribution of absorption coefficient values f(k) in the spectral interval

$$T(u) = \int_0^{\infty} dk \, f(k) \exp(-ku) \quad .$$

The distribution function f(k) is not smooth or monotonic; it generally consists of a series of sharp spikes which reflects the sharp line structure of $k(\omega)$. It then becomes more computationally convenient to work with the smooth and monotonic cumulative probability distribution function

$$g(k) = \int_0^{k} d'k \, f(k') \quad .$$

where k(g) is given by the inverse of g(k), $k(g) = g^{-1}(k)$.

The MODTRAN band model for a single species is based on four parameters: (1) the integrated line strength S in a spectral interval $\Delta\omega$ ($\Delta\omega = 1$ cm^{-1} in MODTRAN), (2) the effective number of equivalent lines n (non-integer values of n are acceptable) in the interval, (3) the average pressure broadening Lorentz line width γ_L, and (4) the Doppler line width γ_D. These parameters are determined directly from the 1996 HITRAN parameter line compilation (Rothman et al., 1996).

3. INITIAL VALIDATION OF MODTRAN4 MULTIPLE SCATTER SOLAR

Development of MODTRAN4 was necessary because MODTRAN3 predictions of multiple scatter solar radiances in spectral regions where non-continuum molecular absorption is important are inaccurate. This scenario cannot be validated by comparisons to FASCODE (Clough et al., 1988) because of the lack of solar scattered contributions. Thus, initial validation of MODTRAN4 multiple scatter solar calculations were made directly to measurements.
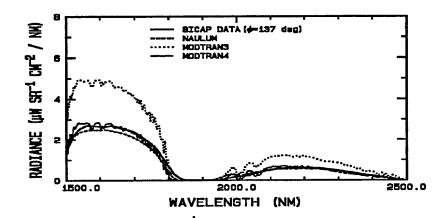
Figure 1: A comparison between SICAP measurements and model predictions for a solar illuminated cloud top. See text.

For example, Figure 1 illustrates a comparison of calculated radiance predictions to airborne measurements (Malherbe et al., 1995) performed by ONERA and CELAR using SICAP, a circular variable filter cryogenic spectrometer (1500 - 5500 nm, 2% spectral resolution). The aircraft altitude was 3.0 km, the cloud top was 2.5 km, the sensor line-of-sight (LOS) zenith angle was 104°, and the solar zenith and relative azimuth angles were 48° and 137°, respectively. Three sets of calculations are shown: (1) results from NAULUM (Malherbe et al., 1995), a new radiative transport model developed at ONERA, (2) MODTRAN3 calculations without the CK approach, and (3) MODTRAN4 calculations performed with the CK approach. The MODTRAN4 cloud model upgrade enabled the cloud profile and spectral data to be explicitly entered for both the MODTRAN3 and MODTRAN4 calculations. Both MODTRAN calculations were performed using a simpler two-stream multiple scattering model (Isaacs et al., 1987); the discrete ordinate model in MODTRAN, DISORT (Stamnes et al., 1988), was run with 8-streams over a limited spectral sub-region and produced similar results. The fit is excellent, but if the sun is in the near line of sight (eg. 11°), the fit would not properly capture the forward scattering lobe.

4. COOLING RATES IN THE PRESENCE OF CLOUDS

An important part of model development is continual comparison with measurements and theoretical predictions. In recent years the ARM community participants, particularly Clough and colleagues, have undertaken the extension of the work originally begun by F. Luther and R. Ellingson, as represented in the dedicated issue of *J. Geophys. Res., 96*, May 1991. The cooling rate discussions therein have been augmented by more recent studies by Clough et al., 1992, Bernstein et al., 1996, and Kimball, 1992, for instance. In Figure 2a the cooling due to H_2O alone, in the 0-3000 cm-1 spectral range is represented, including a 0.5 km thick cirrus cloud centered at 6.5 km. The atmosphere is sub-arctic winter; integrated results can be seen in 2b. This result is preliminary, but MODTRAN4 now allows for the inclusion of such clouds with multiple scattering and micro-layering. Initial results show a clear dependence on the mode of implementing the cloud within the code, with as much as a 0.7K/day difference (MOD3 vs. MOD4) from that shown if 2b, as well as 0.5K/day difference between separate MOD4 calculations. Certainly much additional theoretical work needs to be done, but without good measurements, the impact of cloud cooling will remain uncertain.
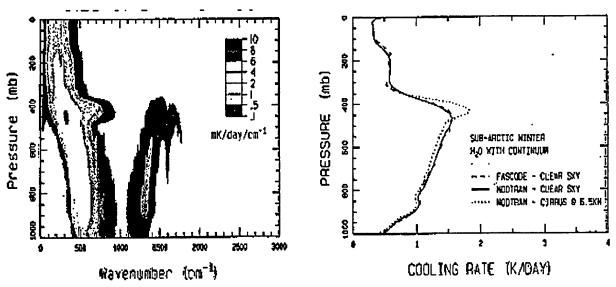
Figure 2: Spectral and integrated cloud cooling for a SAW atmosphere, with an embedded thin cirrus.

5. ACKNOWLEDGMENTS

6. REFERENCES

Anderson, G.P., J.H. Chetwynd, J.-M. Thériault, P.K. Acharya, A. Berk, D.C. Robertson, F.X. Kneizys, M.L.Hoke, L.W. Abreu, E.P. Shettle, 'MODTRAN2: Suitability for Remote Sensing", *Proc. of SPIE, 1954, Remote Sensing,* 1993.

Berk, A., "Upgrades to the MODTRAN Layer Cloud/Rain Models," Rpt. No. SSI-SR-56, Spectral Sciences, Inc., 99 S. Bedford St., Burlington, MA, 1995..

Berk, A., L. S. Bernstein, and D. C. Robertson, "MODTRAN: A Moderate Resolution Model for LOWTRAN7," Rep. GL-TR-89-0122, Air Force Geophys. Lab., Bedford, MA, 1989. ADA214337

Bernstein, L. S., A. Berk, D. C. Robertson, P. K. Acharya, G. P. Anderson, and J. H. Chetwynd, "Addition of a Correlated-*k* Capability to MODTRAN," Proceeding of the 1996 IRIS Targets, Backgrounds, and Discrimination Mtg, 1996.

Bernstein, L.S., A. Berk, P.K. Acharya, D.C. Robertson, G.P. Anderson, J.H. Chetwynd, L.M. Kimball, "Very Narrow Band Model Calculations of Atmospheric Fluxes and Cooling Rates Using the MODTRAN Code," In press, *J.Atm.Sci.,* Oct. 1996.

Clough, S. A., F. X. Kneizys, G. T. Anderson, E. P. Shettle, J. H. Chetwynd, L. W. Abreu, and L. A. Hall, 1988, "FASCODE3 Spectral Simulation" Proceedings of the International Radiation Symposium, Lenoble and Geleyn, Deepak Publishing.

Clough, S.A., M.J. Iacono, J.-L. Moncet, "Line-by-Line Calculations of Atmospheric Fluxes and Cooling Rates: Applications to Water Vapor", *J. Geophys. Res., 97,* 15761, 1992.

Isaacs, R. G., W. C. Wang, R. D. Worsham, and S. Goldenberg, 1987, "Multiple Scattering LOWTRAN and FASCODE Models," *Applied Optics, 26,* 1272-1281.

Kimball, L.M., "Investigation of Atmospheric Heating and Cooling Balance Using MODTRAN3", *AFOSR Summer Faculty Report,* 1995.

Kneizys, F.X., Shettle, E.P., Gallery, W.O., Chetwynd, J.H., Abreu, L.W., Selby, J.E.A., Fenn, R.W., McClatchey, R.A., **Atmospheric Transmittance/Radiance: Computer Code LOWRAN 5,** AFGL-TR-80-0067, AD A058643, 1980.

Kneizys, F.X., Shettle, E.P., Gallery, W.O., Chetwynd, J.H., Abreu, L.W., Selby, J.E.A., Clough, S.A., Fenn, Atmospheric Transmittance/Radiance: Computer Code LOWRAN 6, AFGL-TR-83-0187, AD A137796, 1983.

Kneizys, F.X., Shettle, E.P., Chetwynd, J.H., Abreu, L.W., Anderson, G.P., Gallery, W.O, Selby, J.E.A., Clough, S.A.., Users Guide to LOWRAN 7, AFGL-TR-88-0177, 1988. ADA206773

Lacis, A. A., and V. Oinas, "A description of the Correlated K Distribution Method for Modeling Nongray Gaseous Absorption, Thermal Emission, and Multiple Scattering in Vertically in Homogeneous Atmospheres," *J. Geophys. Res., 96*, 9027 - 9063, 1991.

Malherbe, C., P. Simoneau, A. Boischot, G. Durand, J. Deschamps, and G. Gregoire, 1995, "Radiative Transfer Model in a Cloudy Atmosphere: A Comparison with Airborne Cumulus Measurement," Proceedings of the SPIE Conference on Passive IR Remote Sensing of Clouds and the Atmosphere III.

Revercomb, H.E., F.A. Best, R.G. Dedecker, T,P,Dirkx, R.A. Herbsleb, R.O. Knuteson, J.F. Short, W.L. Smith, Atmospheric Emitted Radiance Interferometer (AERI) for ARM, *Proceedings of Fourth Symposium on Global Change Studies*, 46-49, American Meterorological Society, 1993.

Rothman, L. S. et al., 1996, "The HITRAN Molecular Database: Edition of 1996," Released as a CD-Rom, June, 1996. ('rothman@plh.af.mil')

Smith, W.L., H.E. Revercomb, R.O. Knuteson, F.A. Best, R. Dedecker, H.B. Howell, and H.M. Woolf, Cirrus Cloud Properties Derived from High Resolution Infrared Spectrometry during FIRE ii. Part I: The High Resolution Interrferometer Sounder (HIS) Systems, *Journal of the Atm. Sciences, 52*, 4238-4245, 1995.

Snell, H.E., G.P. Anderson, J. Wang, J.-L. Moncet, J.H. Chetwynd, and S.J. English, Validation of FASE (FASCODE for the Environment) and MODTRAN3: Updates and Comparisons with Clear-Sky Measurements, *Proceedings of Passive Infrared Remote Sensing of Clouds and the Atmosphere III, SPIE, 2578*, 194-199, 1995.

Snell, H.E., J.-L. Moncet, G.P. Anderson, J.H. Chetwynd, S. Miller, and J. Wang, FASCODE for the Environment (FASE), *Proceedings of Atmospheric Propagation and Remote Sensing IV, SPIE, 2471*, 88-95, 1995.

Stamnes, K., S. C. Tsay, W. J. Wiscombe, and K. Jayaweera, "Numerically Stable Algorithm for Discrete-Ordinate-Method Radiative Transfer in Multiple Scattering and Emitting Layered Media," *Applied Optics, 27*, 2502-2509, 1988.

ACHARYA, P.K.   2,22,23,43,73,236,245,430
ADLER-GOLDEN, S.   236
ALEXIS, Q.   8,127
ALLRED, C.L.   36
ALWINE, R.   42
ANDERSON, G.P.   2,9,21,22,23,43,73,138,210,236,254,441
ARMSTRONG, P.   19,36,192
AYER, S.A.   41

BAS, C.F.   33,360
BAUMBACK, M.   27,292
BERK, A.   2,22,23,43,73,236,254,441
BERNSTEIN,L.S.   22,23,43,236,254,430
BINGHAM, G.   17,165
BLUMBERG, W.A.M.   2,19,36,73,192
BOISHOT, A.   39,397
BROWN, J.   21,210
BROWN, P.D.   101
BUNTZEN, R.   27,292
BURKE, H-H.K.   28,40,306,430
BURROWS, J.   15

CAMPBELL, J.   42
CAUDIL, T.R.   41
CHETWYND, J.H.   9,23,43,89,138,236,254,441
CHEUNG, A.S-C   5
CLOUGH, S.A.   90,101
CORNETTE, W.M.   2,35,73,368
COX, G.   5
COY, S.L.   36

DELANNOY, A.   39,397
DEWAN, E.M.   21,210
DIONNE, C.   27,292
DIRAND,H.   39,397
DODD, J.A.   19,192
DUPREE, S.   42
DURAND, G.   39,397

EDWARDS, M.M.   41
EGAN, W.G.   8,127
ESMOND, J.R.   5

FARNHAM, K.   19,192
FIELD, R.W.   36
FISHER, J.   27,292
FLAMANT, P.H.   39,397

GALLERY, W.	10,21,29,146,169
GARDINER, H.A.B.	18,19,20,21,169,192,200,210
GIBSON, J.	18,19,21,169,192,210
GILLESPIE, P.	34
GOEDE, A.	15
GOETZ, A.F.H.	26,282
GOLDMAN, A.	101
GRIFFIN, M.K.	11,38,387
GROSSBARD, N.	21,210
GRUNNINGER, J.	21
HARADA,L.K.	31
HARRISON, L.	25,278
HEGBLOM, E.	21,210
HEIDEBRECHT, K.B.	26,282
HOGAN, D.	10,29,146
HUTCHISON,K.D.	325
IMAJO, T.	5
ITO, K.	5
JACOBSON, M.P.	36
JEONG, L.	2,44,73
JORDAN, M.P.	28,40,306,430
KENDRA, M.	19,20,192,200
KEREKES, J.	28,306
KILLINGER, D.K.	13
KINDEL, B.	26,282
KNEIZYS, F.X.	2,73
KUNTZ, M.	7,112
LANDRY, J.C.	101
LEARNER,.R.C.M.	5
LEUNG, K. W-S.	5
LING, A.G.	11,38,387
LIPSON, S.	19,36,192
LIPTON, A.E.	11,38,387
LOCKWOOD, R.B.	36
MALHERBE, C.	39,397
MAKHLOUF, U.B.	21,200,210
MARUSA, S.	30,325
MATSUI, T.	5
McCANN, A.	34
MERTZ, F.C.	35,368
MICHALSKY, J.	25,278
MILLER, S.	9,14,138
MIN, Q-L.	25,278
MLAWER, E.	6,101
MLYNCZAK, M.	17,165
MONCET, J.L.	14
MOZER, J.B.	41
MULLER, C.	15
MURCRAY, F.J.	101
MURRAY, J.E.	5
NADILE, R.M.	17,165

A

Michael Abel Ball Aerospace 2875 Presidential Drive, Fairborn, OH 45431 (937) 320-4161 mabel@ball.com
Len Abreu Abreu Consulting (508) 256-6334 LAaruba@aol.com
Ronald Alley Jet Propulsion Lab. (818) 354-0751 ron.alley@jpl.nasa.gov
Will Arkinson Harvard University
Peter Armstrong Stewart Radiance Laboratory (617) 377-7380 psa@pldac.plh.af.mil
Prabhat Acharya Spectral Sciences Inc. (617) 273-4770

B

Christophe Bas ARL/PSU (814) 86-0851 cfb104@psu.edu
Michael Batey WITS, bldg. 485, M/S 5M98, 16800E. Centre Tech Parkway, Aurora, CO (303 306-8151 mlbatey@lcgate.hac.com
Alexander Berk Spectral Sciences, Inc. (617) 273-4770 lex@spectral.com
Rosier Bernard ONERA BP72, 92322 Chatilion FRANCE 331 69 93 63 60 rosier@ONERA.FR
Larry Bernstein Spectral Sciences Inc. (617) 273-4770 larry@spectral.com
K.H. Bhaunani Radex, Inc. 3 Preston Ct. Bedford, MA (617) 275-6767
Olga Lado-Bordowsky ENSSAT/University ladobord@merlin.enssat.fr
Art Boright Boeing (206) 393-1006 Arthur.L.Boright@Boeing.com
Hsiao-hua K. Burke MIT/Lincoln Lab. (617) 981-7979 Fax (617) 981-7271 burke@ll.mit.edu

C

Tom Caudill PL/GPOR (617) 377-2943 caudill@plh.af.mil
Kelly Chance SAO (617) 495-7389 kchance@cfa.harvard.edu
Ken Chen Commercial Remote Sensing Program, Stennis Space Center (610) 688-2497 kchen@wpogate.ssc.nasa.gov
Jim Chetwynd PL/GPOC (617) 377-2613 chetwynd@plh.af.mil
Dwight Clark Lockheed Martin (415) 424-3214
Shepard A. Clough AER clough@aer.com
William M. Cornette NIMA 4600 Sangamore Road, D-33, Bethesda, MD 20816 (301) 227-3492 Cornettew@nima.mil

D

Gil Davidson Photometrics (617) 935-6500 gil.davidson@photometrics.com
Richard Davis NASA Langley Research Center M/S 474, Hampton, VA 23681-0001 (757) 864-1647 r.c.davis@larc.nasa.gov

Noreen Dimond PL/GPBP Hanscom AFB, MA (617) 377-3608
Jim Dodd Stewart Radiance Lab (617) 377-4190 dodd@pldac.plh.af.mil
James Duff Spectral Sciences, Inc. (617) 273-4779 duff@spectral.com

E

Walter Egan City University of New York (718) 441-6210 egan@ycvay.york.cuny.edu

F

Martin Fair Dera, Farnborough, UK 4412 52 39 63 72 mlfair@dra.hmg.gb
Vincent Falcone GPOR (617) 377-4029 vfalcone@arcuni.plh.af.mil
Gerald Felde Phillips Laboratory/GPOR, Hanscom AFB, MA (617) 377- 3136
felde@arcuni.plh.af.mil
Harry Finkle MIT/LL fink@ll.mit.edu
Shalom Fisher NRL (202) 767-3914

G

Peggy Gardiner Visidyne, Burlington, MA (617) 273-2820
William O. Gallery AER, Inc. (617) 349-2284
Paul Gehred USAF WL/DOW DSN 785-1978 gehredpa@88abw.wpafb.af.mil
Adrian George Mission Research Corporation, Nashua , NH ageorge@mrcuh.com
James R. Gillis Boeing , P.O. Box 3999 MSEH-05, Seattle WA 98124-2499 (253) 773-
4721 james.r.gillis@boeing.com
De Toma Giuliana LASP detoma@ackerman.colorado.edu
Melanie Gouveia TASC (617) 942-0080 x2367 mjgoveia@tasc.com
Donald Grantham Phillips Laboratory (617) 377-2982 grantham@plh.af.mil
Mike Griffin PL/GPO griffin@arcxsz.plh.af.mil

H

Kathy Heidebrecht CSES/CIRES University of Colorado (303) 492-1866
kathy@cses.colorado.edu
Michael Hoke PL/GPOS (617) 377-3614
Karen Hopke Hughes Aircraft Co. P.O. Box 902, M/S B210, El Segundo, CA 90245
(310) 616-6559 kehopke@ccgate.hac.com
Haijun Hu Harvard Unviersity (617) 495-5922 haijun@huarp.harvard.edu
Martin Hunter PL/GPOS martinh@plh.af.mil

I

Precila Ip Mission Research Corp. 1 Tara Blvd, Ste 302, Nashua. NH (603) 891-0070 ext 222 pip@mrcnh.com

J

K

David Keith Harvard University (617) 495-5922 Keith @hvard.harvard.edu
Bruce Kindel University of Colorado (303) 492-6782 kindel@kwoma.colorado.edu
Sarah Harrell Klein MIT Lincoln Lab. (617) 981-3035
Martin Kuntz Research Center Karlsrube Germany 49 72 47 82 45 10
kuntz@imk.kk.de

L

Alan Ling Radex, 3 Preston Ct. Bedford, MA 01730 (617) 275-6767
Ling @ziggy.radex.plh.af.mil
Steven Lipson Phillips Laboratory PL/GPOC, Hanscom AFB, MA (617) 377-3626
lipson@plh.af.mil
Alan Lipton PL/GPOR (617) 377-2941 lipton@plh.af.mil
Ron Lockwood PL/GPOS (617) 377-7380

M

Steve Marusa Lockheed Martin Valleyforge, PA (610) 354-6706
smarusa@wf.lmms.lmnca.com
Bob McClatchey (617) 271-1480
Steven Miller PL/GPOC, Hanscom AFB, MA (617) 377-2807
Qilong Min SUNY at Albany, ASRC (518) 437-8742 min@asrc.cestm.albany.edu
Eli Mlawer AER (6170349-2226 mlawer@aer.com
Joel Mozer PL/GPOF (617) 377-2945 mozer@plh.af.mil
Christian Muller BISA christian.muller@omo.be

N

Michelle Najarian SciTec Inc. 100 Wall Street, Princeton, NJ 08540 (609) 921-3892
x255 mnajarian@scitec.com
Meg Noah MRC 1 Tara Blvd. Suite 302, Nashua, NH (603) 891-0070 ext. 240

O

Michael O'Brien ARL/Penn State University (814) 863-0851 mxo107@psu.edu
Bob O'Neil PL/GPOC (617) 377-4775 oneil@pldac.plh.af.mil

P

C.R. Philbrick ARL/Penn State University (814) 865-2975
Dick Picard PL/GPO picard@plh.af.mil
Simoneau Pierre ONERA BP72 Chatillon 92322 FRANCE simoneau@onera.fr
Eldon Puckerin Trent University (705) 748-1654 epuckerin@trentu.ca

Q

R

David Robertson Spectral Sciences dave@spectral.com
Ron Rodney WL/DOWA WPAFB (937) 255-1978 Ext. 4034 rodneyrl@aa.wpafb.af.mil
Harold Roth PL/GP
Larry Rothman PL/GPOS (617) 377-2336 rothman@plh.af.mil

S

Keith Sashegyi Naval Research Lab. (202) 767-3350 sashegyi@atmos.nrl.navy.mil
Steve Schmidt Los Alamos Natl Lab. (505) 667-1815 scs@lanl.gov
John Schroeder Ontar Corporation (508) 689-9622 johnschr@aol.com
Guy Seeley PL/GPOF, Radex, Inc. (617) 377-6069
John Selby Northrop Grumman Corp. (516) 575-6608 john_selby@atdc.northgrum.com
Alan R. Shaffer DOD (703) 455-0610 shaffear@acq.osd.mil
Scott D. Shannon Boston University Center for Remote Sensing (617) 884-5582
sshannon@bu.edu
Eric P. Shettle NRL (202) 404-8152 shettle@poamb.nrl.navy.mil
Richard Shirkey ARL (505) 678-5470 rshirkey@arl.mil
Joan Spind MIT Lincoln Laboratory (617) 981-3742 spinde@ll.mit.edu
Ned Snell AER (617) 547-6207 snell@aer.com
Ryan Spackman Harvard University (617) 495-5922 spackman@huarp.harvard.edu
Robert Spurr Smithsonian Astrophysical Obs. 60 Garden Street, Cambridge, MA 02138
(617) 496-7819 rspurr@gome.harvard.edu
Espen Stark Norwegian Defense Research 47 63 80 72 82 espen.stark@th.no
William Stoner SAIC, Suite 130, 20 Mall Road, Burlington, MA (617) 221-7603
wstoner@bos.saic.com

T

Andy Tooth Sowerby Research Center, Filton Bristol UK

U

V

W

Zhengming Wan UCSB (805) 893-4541 wan@jcess.ucsb.edu
Sally Westmoreland Photon Research Associates (619) 455-9741 sjw@photon.com
Alan Wetmore Army Research Lab. (301) 394-2499 awetmore@arl.mil
Bill Wilcox WJ Schafer (508) 256-2070 bwilcox@wjsa.com
Jeremy Winick PL/GPOC (617) 377-3619 winick@plh.af.mil
John Wise PL/GPOB (617) 377-4277
Beiying Wu Research, ACD, NCAR, Boulder, CO 80307 beiying@acd.ucar.edu

X

Y

Tatsuya Yokota NIES, Japan 81 29 85 02 550 yoko@nies.go.jp
Kouichi Yoshino Harvard University (617) 495-2796 yoshino@cfa.harvard.edu

Z

Kenneth Zabel Amtec Corporation (205) 842-2013 kzabel@rttc.redstone.army.mil
Al Zachor ARC (508) 263-1931 zachor@pldoc.af.mil
Daniel Zhou Utah State University (801) 755-4410 daniel.zhou@sdl.usu.edu
Michael Zugger Penn State University, University Park, PA 16803